

**MECHANICAL AND DYNAMIC  
BEHAVIOR OF ADDITIVELY  
MANUFACTURED POLYMER  
NANOCOMPOSITES**

Thesis

Submitted in partial fulfillment of the requirements for the degree of

**DOCTOR OF PHILOSOPHY**

by

**SUMODH KUMAR**



DEPARTMENT OF MECHANICAL ENGINEERING  
NATIONAL INSTITUTE OF TECHNOLOGY KARNATAKA,  
SURATHKAL, MANGALORE – 575025

OCTOBER, 2024

## DECLARATION

I hereby *declare* that the Research Thesis entitled “MECHANICAL AND DYNAMIC BEHAVIOR OF ADDITIVELY MANUFACTURED POLYMER NANOCOMPOSITES” which is being submitted to the National Institute of Technology Karnataka, Surathkal in partial fulfillment of the requirements for the award of the Degree of Doctor of Philosophy in Department of Mechanical Engineering is a *bonafide report of the research work carried out by me*. The material contained in this Research Thesis has not been submitted to any University or Institution for the award of any degree.

Register Number : 197142ME026

Name of the Research Scholar : SUMODH KUMAR

Signature of the Research Scholar : *Sumodh Kumar*

Department of Mechanical Engineering

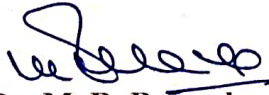
Place : NITK, Surathkal

Date : *22/10/2024*

## C E R T I F I C A T E

This is to *certify* that the Research Thesis entitled “MECHANICAL AND DYNAMIC BEHAVIOR OF ADDITIVELY MANUFACTURED POLYMER NANOCOMPOSITES” submitted by Mr. SUMODH KUMAR (Register Number: 197142ME026) as the record of the research work carried out by him, is *accepted as the Research Thesis submission* in partial fulfillment of the requirements for the award of degree of **Doctor of Philosophy**.

### Research Guide



**Dr. M. R. Ramesh**

Professor

Department of Mechanical Engineering, School of Mechanical & Materials Engg.  
NITK, Surathkal



**Dr. Mrityunjay Doddamani**

Associate Professor

IIT Mandi



Chairman – DRPC

Date: 22-10-2024



## **ACKNOWLEDGEMENT**

I want to extend my sincere gratitude to Dr. M. R. Ramesh, Professor, Department of Mechanical Engineering, NITK, Surathkal and Dr. Mrityunjay Doddamani, Associate Professor, School of Mechanical and Materials Engineering, IIT Mandi, for their invaluable constructive guidance and encouragement extended throughout my study. I want to thank Research Progress Assessment Committee members, Prof. G. C. Mohan Kumar and Dr. Anandhan Srinivasan, for their valuable inputs.

I would like to thank Prof. S. M. Murigendrappa, Head of the Department of Mechanical Engineering and all the faculty members of the Department of Mechanical Engineering for their support throughout this research work. I want to thank Dr. P. Jeyaraj and Prof. Narendranath of the Department of Mechanical Engineering, NITK, for their valuable suggestions and the experimental resources provided for my research work.

The constant grace of my Late parents, Laljhari Devi (Mother) and Rampukar Ram (Father), and the constant encouragement and support of family members, Shri Suman Kumar Ram (elder brother) and Shrimati Sangita Devi (sister-in-law), to pursue higher studies have made it possible for me to reach this stage. I wish to thank all my family members for their love, help, and encouragement. I want to give special thanks to my dear wife, Mrs. Geeta Kumari, for her core hearted constant support and encouragement, which made my research work complete without any obstacles. I would also like to thank my dear daughters Saanvi Kumari and Saanya Kumari, for their constant love and support, which helped me complete my research smoothly. Thanks a lot to my family for being with me on this research journey.

I express my sincere thanks to Dr. Dileep Bonthu, Dr. Bharath H S, Dr. Sailesh R, Dr. Praveen Jayachandran, Dr. Sateeshkumar Kanakannavar, Mrs. Nidhi Ojha, Mr. Sanjay Suresh Sutar, and the Advanced Manufacturing Lab research team for their help and kind cooperation extended throughout this research work. Thanks to all my friends and well-wishers for their constant help, encouragement, and understanding.

## ABSTRACT

Rapid production of high quality components without any additional tools is the key to cost reduction in industrial applications. The present work deals with the additive manufacturing of polymer nanocomposite and their graded variants using fused filament fabrication (FFF) technology based 3D printing process. High Density Polyethylene (HDPE) is used as a matrix, and functionalized MWCNTs are used as a filler material in this work. The development of nanocomposite (NC) with lightweight functionalized MWCNTs serves the purpose of reduction in weight with enhanced properties. The functionalized MWCNTs (0.5%, 1%, 3%, and 5% by weight) are blended with the HDPE to develop functionalized MWCNTs/HDPE NCs in the form of pellets, which are further characterized through scanning electron microscopy (SEM), melt flow index (MFI), and thermogravimetric analysis (TGA). Then, these developed NCs are utilized to extrude NC filaments for 3D printing. The extruded NC filaments are characterized for quality and printability, which are further utilized in 3D printing of NC and functionally graded nanocomposite (FGNC) samples. The 3D printed NCs and FGNCs are comprehensively characterized for prints quality through various techniques such as SEM, rheology, XRD, and density, and finally subjected to the tensile, flexural, compression, hardness, impact, mechanical buckling, free vibration, and thermal buckling. Also, the waste NC filament is investigated for its recycling potential.

The SEM analysis revealed the uniform distribution of the functionalized MWCNTs in the HDPE in the developed nanocomposites, extruded nanocomposite filaments, and the 3D printed samples, confirming the suitability of the processing parameters used in the blending, extrusion, and 3D printing. It also revealed the seamless and strong layer bonding in the 3D printed NCs and FGNCs. The rheology findings also confirm the uniform distribution of the fillers qualitatively. It is observed that complex viscosity ( $\eta^*$ ) for the NCs slightly increases as the functionalized MWCNTs content increases up to 0.5%, and then dramatically increases for 5% (almost two orders) at the low frequency by maintaining a steeper graph, confirming the good

dispersion of the MWCNTs in the HDPE matrix. The complex viscosity ( $\eta^*$ ), storage modulus ( $E'$ ), and loss modulus ( $E''$ ) of the 3D printed NCs and FGNCs increase while the damping factor ( $Tan\delta$ ) decreases as the functionalized reinforcement content rises.

The MFI of the developed NCs (H0.5-H5) showed a decreasing trend with increase in the MWCNTs content, confirming the inclusion of the fillers in the matrix. The MFI decreases in the 14.52%-51.60% range for the H0.5- H5 NCs compared to the HDPE. The thermal stability of the developed NCs increases with the addition of the filler. The highest thermal degradation temperature is observed for H5 NC (479.07 °C). The density of the filaments and the specimens decreases with the increase in the MWCNTs content. The highest density reduction of 16.06% and 15.58%, respectively, is observed in the H5 filament and the respective H5 print compared to the pure HDPE. The density of the FGNCs was also found to decrease with layer gradation. The FGNC-2 exhibited the highest weight-saving potential of 12%.  $T_{Melt}$  of the filaments and the specimens increases with an increase in the MWCNT content, while  $T_{Cryst}$  increases up to 0.5% and 1% for the filaments and the specimens, respectively, then decreases.  $\alpha_{Cryst}$  is higher for the filaments and the specimens than the neat HDPE. The XRD results also revealed the higher crystallinity of the NCs than the pure HDPE.

A tensile study of the extruded filaments, NC, and FGNC prints revealed that the modulus and strength increase with the addition of the MWCNTs. The highest tensile modulus and strength are observed for the H5 NC filament, which is 105% and 30% higher than the pure HDPE filament. For the printed NC specimens, the modulus increases by 15.89%, 19.41%, 44.87%, and 81.43% in the H0.5, H1, H3, and H5 NC specimens, respectively, compared to the pure HDPE specimens. The highest modulus is registered for the H5 NC specimen (~81.5%). Further, it is noted that the tensile modulus of the printed specimens is higher than the respective filaments. The tensile modulus of the printed H-H5 NC specimens increased by 15.42%, 13.97%, 13.96%, 15.47%, and 2.38% compared to the respective filaments. The highest tensile strength (UTS) is registered for the H5 (16.6 MPa), 12.16% higher than the pure

HDPE. It is noted that the H5 NC specimen has the highest modulus and strength among all the NC specimens, 81.43%, and 12.16%, respectively, higher than the HDPE. Further, the FGNCs are also tested for tensile. It is seen that their modulus and strength increase with the layer gradation. The enhancements in the moduli are 55.15% and 90.41% for the FGNC-1 and the FGNC-2 compared to the pure HDPE, respectively. Moreover, the FGNCs exhibited higher moduli than their respective homogeneous NCs, showing the potential to replace the NCs. The FGNCs showed higher strength than the respective homogeneous NCs, 23.75% and 37.12%, respectively, higher strength than the HDPE are noted for the FGNC-1 and FGNC-2. The tensile properties of the NCs are compared with the existing composites, where it is found that the 3D printed NC sample exhibited the highest tensile strength compared to the other fillers reinforced HDPE composites.

The printed NCs and FGNCs are also investigated for the flexural responses. It is observed that the flexural modulus and strength of the NC specimens increase with the MWCNTs increase. The highest modulus and strength, 24.71% and 22.23% are noted for the H5 NC print compared to the neat HDPE. It is noticed that the specific strength and modulus of the printed NC specimens increase with the filler loadings. The H5 specimen showed the highest specific modulus and strength, 47.62% and 44.73% higher than the pure HDPE. For the FGNCs, the flexural moduli and strength are also noted to increase with the layer grading. The highest flexural strength and moduli are exhibited by the FGNC-2, which is 28.57% and 26.83% higher than the pure HDPE. The FGNC-2 also exhibited the highest specific strength and modulus, 46.16% and 44.14%, respectively, higher than the pure HDPE. The flexural behavior of the NCs and the FGNCs was also studied numerically, and the experimental findings were found to match well with the FEA results.

The compression, hardness, and impact studies are also conducted on the printed NCs and FGNCs, which revealed an increasing trend of compressive modulus and yield strength with the increased MWCNTs content. The highest compressive modulus and yield strength are found for the H5 NC, which are, respectively, 44.89% and 9.28% higher than the pure HDPE. In the FGNCs, the layer gradation also notes a similar

increasing trend. The FGNC-1 and FGNC-2 exhibited 35.75% and 61.14% higher modulus than the pure HDPE with the highest of the FGNC-2. The yield strengths of the FGNC-1 and the FGNC-2 are 8.89% and 11.56% higher than the pure HDPE with the maximum FGNC-2. The hardness and the impact strength of the NCs and FGNCs also increase with the filler content. The highest hardness and impact strength are noted for the H5 NC among all the NCs, while in the case of the FGNCs, are for the FGNC-2. The FGNC-2 exhibited the highest hardness and impact strength, respectively 76.80% and 119.99% higher than the pure HDPE.

Mechanical, thermal, and dynamic loading causes instability, leading to the failure of the structure. Therefore, the printed NCs and FGNCs are also investigated for mechanical buckling, free vibration, and thermal buckling behavior. Results revealed that the NCs and the FGNCs buckling strength increases with the increased MWCNTs content. The highest critical buckling load ( $P_{cr}$ ) is noted for the H5 NC among the NCs, which is 79.03% (by DTM) and 79.13% (by MBC method) compared to the HDPE. The  $P_{cr}$  of the FGNC-1 and the FGNC-2, calculated from DTM and MBC methods, are 54.38% and 91.34% higher than the pure HDPE. It is noted that the H5 NC and FGNC-2 displayed the highest buckling strength among the 3D printed NCs and FGNCs. The  $P_{cr}$ , calculated from DTM, MBC, and VCT methods, exhibited good agreement. The natural frequency of the NCs and the FGNCs increases with the MWCNTs loading while decreases with increasing compressive load. Their damping factor showed a decreasing trend with the filler loading while observed to be increasing with a rise in the compressive load. The experimental and numerical findings are observed to be in very good agreement. The property chart reveals the superior performance of the H5 NC and the FGNC-2 compared to thermosetting composites.

Thermal buckling studies of the NCs and the FGNCs under various heating conditions revealed that the critical buckling temperature ( $T_{cr}$ ) and the deflection due to heating is very sensitive to heating type. The  $T_{cr}$  is noted as the highest in case-3 and the lowest in case-2. The maximum deflection is observed in case-2, while no significant difference is observed in case-1 and case-3. The  $T_{cr}$  of the NCs and FGNCs increases,

while the deflection decreases due to the addition of the MWCNTs and their gradation. The highest  $T_{cr}$  is observed for the H5 NC (11.16% higher than the pure HDPE) and FGNC-2 (19.06% higher than the pure HDPE). The lowest deflection is observed for the H5 NC (53.33% lower than the pure HDPE) and the FGNC-2 (73.34% lower than the pure HDPE), indicating enhanced thermal stability. It is seen that the H5 NC exhibited the superior performance among all the NCs, while the FGNC-2 showed the best performance between the FGNC-1 and FGNC-2. Moreover, the FGNCs exhibited the superior performance to all the homogeneously reinforced NCs.

In addition to comprehensive studies on the 3D printed NCs and FGNCs, this work also considered the study on the recycling potential of the waste polymers, which is increasing in the environment and causing many hazardous environmental problems. In this study, the waste extruded nanocomposite filaments that get wasted during filament extrusion are collected and examined for recycling potential. The waste filaments of the functionalized MWCNTs/HDPE NCs (H1 composition) are recycled to obtain the useful NC filaments for utilization in 3D printing. These NC filaments are further tested to check their potential for 3D printing. The samples are 3D printed using the recycled filaments, and subjected to density, XRD, and tensile tests to examine their recycling potential. The recycled filaments and the respective prints showed enhanced density, crystallinity, and tensile properties with respect to the extrusion cycle. After third extrusion cycle, no enhancement in the properties is found. The tensile strength and modulus of 1x, 2x, and 3x prints are 63.82%, 67.11%, and 67.76%, and 45.63%, 55.34%, and 97.81%, respectively, higher than the W/UR print. The highest tensile strength and modulus are observed for 3x print, which is 67.76% and 97.81%, respectively, higher than the W/UR print. This study revealed that the H1 NC filament can be recycled (extruded) three times to achieve property enhancement. The H1-3x print exhibited superior tensile strength and modulus among all the recycled prints. Through such an approach, the environmental pollution due to the plastic waste generated by 3D printing industries can be substantially lowered, in addition to expanding the filament material options for the FFF community. A similar route can also be explored for the other NCs (0.5%, 1%, 3%, and 5 wt.%), increasing

application areas across various engineering fields such as structural, marine, aerospace, and automobile.

The efforts presented in this research exhibited the potential of the 3D printed NCs and the FGNCs to be utilized as integrated and jointless functional components in a wide spectrum of engineering applications such as marine, automobile, aerospace, construction, defense, electronics, and naval in addition to increasing the novel materials options for 3D printing industries.

**Keywords:** *Functionalized MWCNTs; High density polyethylene; 3D printing; Nanocomposites; Functionally graded nanocomposites; Polymer nanocomposites; Thermal properties; Mechanical properties, Physical properties; Buckling; Free vibration.*

## TABLE OF CONTENTS

DECLARATION	
CERTIFICATE	
ACKNOWLEDGEMENT	
ABSTRACT	
CONTENTS.....	I
LIST OF FIGURES.....	V
LIST OF TABLES.....	IX
ABBREVIATION.....	XI
NOMENCLATURE.....	XIII
1 INTRODUCTION.....	1
1.1 Additive manufacturing.....	1
1.2 AM process chain.....	2
1.3 Classification of AM processes.....	3
1.4 Fused filament fabrication.....	3
1.5 Selection of filler and matrix.....	4
1.6 Polymer nanocomposites and their applications.....	7
1.7 Functionally graded materials and their applications.....	8
1.8 Polymer manufacturing methods.....	10
1.9 Literature review.....	11
1.10 Motivation.....	40
1.11 Objectives and scope of the work.....	41
1.12 Thesis outline.....	42
2 MATERIALS AND METHODS.....	43
2.1 Constituent Materials.....	43
2.1.1 Matrix.....	43
2.1.2 Filler.....	44
2.2 Nanocomposite development.....	45
2.3 Nanocomposite filament extrusion.....	47
2.3.1 Recycling of nanocomposite filament.....	50
2.3.2 Filament regularity check and density measurement.....	51

2.4	3D printing of NCs and FGNCs .....	51
2.5	Obtaining suitable 3D printing parameters .....	57
2.6	Melt flow Index .....	58
2.7	Density measurement .....	59
2.8	Differential scanning calorimetry.....	59
2.9	Thermogravimetric analysis .....	60
2.10	Rheology .....	60
2.11	X-ray diffraction.....	60
2.12	Tensile test.....	60
2.13	Flexural investigation.....	61
2.13.1	Experimental.....	61
2.13.2	Numerical.....	61
2.14	Hardness .....	62
2.15	Impact test .....	62
2.16	Compression test .....	63
2.17	Mechanical buckling .....	63
2.18	Free vibration .....	65
2.19	Vibration correlation technique.....	67
2.20	Numerical analysis of mechanical buckling and free vibration .....	67
2.21	Coefficient of thermal expansion .....	68
2.22	Thermal buckling .....	68
2.23	Microstructural analysis .....	70
3	BASIC MATERIAL CHARACTERIZATION .....	71
3.1	Blended nanocomposites.....	71
3.1.1	Scanning electron microscopy .....	71
3.1.2	Melt flow index.....	72
3.1.3	Thermogravimetric analysis.....	73
3.2	Extruded nanocomposite filaments and 3D printed samples .....	74
3.2.1	SEM .....	74
3.2.2	Rheology .....	76
3.2.3	Density .....	78
3.2.4	DSC.....	80
3.2.5	XRD .....	82
3.3	Coefficient of thermal expansion .....	84
3.4	Conclusion.....	85

4	TENSILE BEHAVIOUR .....	89
4.1	Tensile responses of the nanocomposite filaments .....	89
4.2	Tensile results of the printed specimens .....	92
4.2.1	Tensile responses of the NCs .....	92
4.2.2	Property map .....	94
4.2.3	Tensile responses of the FGNCs .....	96
4.3	Conclusion.....	100
5	FLEXURAL BEHAVIOR.....	103
5.1	Experimental investigation.....	103
5.1.1	Flexural responses of the NCs .....	103
5.1.2	Flexural responses of the FGNCs .....	105
5.2	Numerical investigation .....	108
5.3	Conclusion.....	111
6	COMPRESSION, HARDNESS AND IMPACT BEHAVIOUR.....	113
6.1	Compression responses of the NCs .....	113
6.2	Compression responses of the FGNCs.....	115
6.3	Hardness and impact responses .....	118
6.4	Conclusion.....	119
7	MECHANICAL BUCKLING AND FREE VIBRATION BEHAVIOUR .....	121
7.1	Mechanical buckling studies .....	121
7.1.1	Comparison of the experimental and numerical buckling load .....	123
7.2	Free vibration investigations .....	124
7.2.1	Comparison of the experimental and numerical natural frequency .....	131
7.3	$P_{cr}$ estimation using VCT .....	132
7.4	Property map .....	133
7.5	Conclusion.....	134
8	THERMAL BUCKLING .....	137
8.1	Thermal buckling results .....	137
8.1.1	Effect of various non-uniform heating on $T_{cr}$ .....	137
8.1.2	Effect of various non-uniform heating on deflection.....	141
8.1.3	Effect of addition of functionalized MWCNTs and their gradation on $T_{cr}$ .....	141
8.1.4	Effect of addition of functionalized MWCNTs and their gradation on deflection .....	143
8.2	Conclusion.....	145

9	RECYCLING POTENTIAL OF NANOCOMPOSITES .....	147
9.1	Filament regularity and quality check .....	147
9.2	XRD of the recycled nanocomposite filaments and the prints.....	149
9.3	Tensile test of the NC filaments .....	150
9.4	3D printing using recycled NC filaments.....	152
9.5	Tensile test of the 3D printed samples .....	153
9.6	Property map .....	155
9.7	Conclusions .....	157
10	SUMMARY AND CONCLUSIVE REMARKS .....	159
	SCOPE OF FUTURE WORK .....	166
	REFERENCES .....	167
	LIST OF PUBLICATIONS .....	181
	BIO-DATA .....	183

## LIST OF FIGURES

Figure 1.1 Process chain in AM.....	3
Figure 2.1. (a) Representative images of the as-received HDPE granules and its (b) SEM image.....	44
Figure 2.2. (a) Representative image of the as-received functionalized MWCNTs powder and its (b) SEM image. ....	45
Figure 2.3. (a) Representative image of the Brabender, (b) mechanism of blending and (c) the developed H5 nanocomposite.....	47
Figure 2.4. Extruded H5 nanocomposite filaments. ....	48
Figure 2.5. Schematic representation of the single screw extruder. ....	49
Figure 2.6. Experimental setup of the single screw extruder used in the current work. ....	49
Figure 2.7. Representative images of (a) W/UR filament, (b) pellets of W/UR filaments and (c) H1-3X recycled filament. ....	51
Figure 2.8. (a) Thickness of each graded layer ( $hc$ ), printing direction, and nozzle used for FGNCs printing and (b) 3D Printed FGNC-2 sample. ....	54
Figure 2.9. Schematic representation of FFF 3D printer. ....	55
Figure 2.10. Representative image of the FFF 3D printer used in the current work. ..	55
Figure 2.11. Different challenges in 3D printing, (a)-(b) extrusion problems, (c) proper extrusion of material, (d)-(e) rubbing problems, (f) defect free print and (g)-(h) over heating issues. ....	58
Figure 2.12. Melt flow indexer. ....	59
Figure 2.13. (a) FE model and (b) simply supported boundary condition.....	62
Figure 2.14. Experimental setup showing (a) pre-buckling, (b) post-buckling and (c) buckled/deflected shape of the 3D printed sample. ....	64
Figure 2.15. (a) DTM and (b) MBC for calculating $P_{cr}$ from load-deflection curve. 64	
Figure 2.16. (a) Experimental setup and (b) the schematic representation of free vibration test.....	66
Figure 2.17. DEWESoft software showing FRF, mode shape and mode circle in the experimental modal analysis.....	67

Figure 2.18. Representative image of in-house experimental set up for thermal buckling test. ....	69
Figure 2.19. Representative images of different types of non-uniform heating, and the corresponding IR heater position and the temperature variation. ....	70
Figure 3.1. SEM images of the developed H5 nanocomposite, showing uniform distribution and network structure of the functionalized MWCNTs. ....	71
Figure 3.2. MFI of the blended nanocomposites. ....	72
Figure 3.3. TGA responses of MWCNT/HDPE NCs (a) weight loss (%) with temperature and (b) variation of decomposition temperature with MWCNTs content. ....	73
Figure 3.4. SEM image of the extruded H5 nanocomposite filament, showing uniform distribution and network structure of the functionalized MWCNTs. ....	75
Figure 3.5. SEM images of the FGNC-2 3D printed sample: (a) thickness showing seamless diffusion of each printed layer, (b) cross-section of freeze-fractured sample showing seamless materials diffusion and porous free printing, and (c) uniform distribution and network structure of the functionalized MWCNTs in the H5 layer of FGNC-2 (magnified image of the marked region of Figure 3.5b).....	75
Figure 3.6. Rheology results: (a) complex viscosity, (b) storage modulus, (c) loss modulus, and (d) damping of 3D printed HDPE, NCs, and FGNCs. ....	78
Figure 3.7. Micrographs of the freeze fractured H3 specimen at (a) lower and (b) higher magnifications.....	80
Figure 3.8. DSC curves of the filaments (a), (b) and the printed samples (c), (d).....	82
Figure 3.9. XRD responses of (a) the filaments and (b) the prints. ....	83
Figure 4.1. Representative (a) experimental set up for the filament tensile test, tensile stress-strain graph of (b) the neat HDPE and (c) the H0.5-H5 NC filaments.....	90
Figure 4.2. Representative SEM images of (a) the H5 NC and (b) H0.5 NC filaments. ....	92
Figure 4.3. (a) Tensile stress-strain graph of the printed NC specimens and (b) SEM image of the tensile tested H5 specimen. ....	94
Figure 4.4. Tensile (a) strength and (b) modulus of HDPE composites (Adhikary 2011, Beesetty et al. 2020, Bharath Kumar et al. 2016, H S et al. 2020, Jayavardhan M. L. 2017, Patil et al. 2019). ....	96

Figure 4.5. (a) Experimental test set up, (b) tensile results, (c) tested sample showing top, thickness, and fracture surfaces, and (d)-(g) SEM images of the fractured surface of the FGNC-2 sample.....	99
Figure 5.1. Representative (a) experimental set up for the flexural test (b) flexural stress-strain graph of the printed NCs and (c) SEM image of the flexural tested H5 NC.....	104
Figure 5.2. (a) Schematic representation of three-point bending test, (b) experimental setup, (c) flexural results, and (d)-(e) SEM images of the tested FGNC-2 sample, showing MWCNTs uniform distribution and their networks.....	107
Figure 5.3. Specific flexural properties of 3D printed FGNCs: (a) specific modulus and (b) specific strength.....	107
Figure 5.4. FE plots of (a) stress distribution in X-direction, (b) von-Mises stress distribution, and (c) mid-point deflection of the NCs and FGNCs.....	110
Figure 6.1. The compressive properties of the 3D printed NCs.....	114
Figure 6.2. Representative SEM images of freeze-fractured as 3D printed and post tested H5 sample.....	115
Figure 6.3. Compressive responses of the 3D printed FGNCs.....	117
Figure 6.4. SEM images of the pre and post tested FGNC-2 sample showing (a)-(b) compression, (c) brittle fracture and (d) FGNC-2 without crack.....	118
Figure 7.1. Load-deflection curve of 3D printed (a) neat HDPE, (b) NC and (c) FGNC.....	122
Figure 7.2. Comparison of experimental and numerical load-deflection curves of 3D printed (a) neat HDPE, (b) H0.5, (C) H1, (d) H3, (e) H5, (f) FGNC-1 and (g) FGNC-2.....	124
Figure 7.3. The FRF plots of the 3D printed (a) H5 NC and (b) FGNC-2 under no load conditions.....	126
Figure 7.4. Variation of the natural frequency with the axial compressive load of 3D printed (a) neat HDPE, (b) H0.5, (c) H1, (d) H3, (e) H5, (f) FGNC-1 and (g) FGNC-2.....	128
Figure 7.5. Variation of damping ratio with the increase in compressive load of 3D printed (a) neat HDPE, (b) H0.5, (c) H1, (d) H3, (e) H5, (f) FGNC-1 and (g) FGNC-2.....	130

Figure 7.6. Representative plots of the VCT to evaluate $P_{cr}$ of 3D printed (a) HDPE and NC, and (b) FGNCs.....	132
Figure 7.7. Comparison of the $P_{cr}$ of the 3D printed (a) HDPE and NC, and (b) FGNC samples calculated using DTM, MBC and VCT methods. ....	133
Figure 7.8. Representative plot of buckling load of different composites as a density function (Bharath 2020, Dileep 2021, Rajesh 2017, Waddar 2018).....	134
Figure 8.1. Thermal load vs deflection curves of the 3D printed (a) HDPE, (b) NC and (c) FGNC under case-1 heating. ....	138
Figure 8.2. Thermal load vs deflection curves of the 3D printed (a) HDPE, (b) NC and (c) FGNC under case-2 heating. ....	139
Figure 8.3. Thermal load vs deflection curves of the 3D printed (a) HDPE, (b) NC and (c) FGNC under case-3 heating. ....	140
Figure 8.4. Effect of various non-uniform thermal loads on $T_{cr}$ of (a) H5 NC and (b) FGNC-2.....	141
Figure 8.5. Effect of addition of the functionalized MWCNTs and their gradation on $T_{cr}$ in case-1 heating condition. ....	143
Figure 8.6. Effect of addition of the functionalized MWCNTs and their gradation on deflection in case-1 heating condition. ....	144
Figure 9.1. Representative images of the 3D printed freeze-fractured H1-3x print at (a) lower and (b) higher magnifications.....	148
Figure 9.2. The XRD pattern of the recycled NC (a) filaments and (b) the prints. ...	149
Figure 9.3. Representative (a) tensile stress-strain plot of the NC filaments and (b) SEM image of the H1-3x recycled filament. ....	151
Figure 9.4. Challenges encountered in 3DP of recycled filaments.....	153
Figure 9.5. Tensile tested samples showing (a) brittle failure and (b) fractured surfaces in brittle mode. ....	154
Figure 9.6. Representative (a) tensile stress-strain graph of the 3D printed samples and (b) SEM image of the tensile tested H1-3x printed sample. ....	155
Figure 9.7. Comparison of tensile (a) strength and (b) modulus of different HDPE composites with H1-3x composite (Adhikary 2011, Beesetty 2020, Bharath 2020, Bharath Kumar 2016, Jayavardhan 2017, Patil 2019). ....	156

## LIST OF TABLES

Table 1.1. The seven AM categories as per ASTM F42.....	6
Table 1.2. Literature Review. ....	12
Table 2.1. Typical properties of the HDPE of HD50MA180* grade. ....	43
Table 2.2. Typical properties of the functionalized MWCNTs*. ....	45
Table 2.3. Specifications of the single screw extruder. ....	50
Table 2.4. Printing parameters used in the current work. ....	54
Table 2.5. Specifications of the FFF 3D printer. ....	56
Table 3.1. Physical properties of the samples.....	79
Table 3.2. Thermal properties of the samples.....	81
Table 3.3. XRD responses of the filaments and the prints.....	84
Table 3.4. CTE responses of the 3D printed samples.....	85
Table 4.1. Tensile results for the filaments and the prints. ....	91
Table 4.2. Specific mechanical properties of the NC specimens.....	94
Table 4.3. Tensile results of the printed FGNCs. ....	99
Table 5.1. Flexural properties of the printed NCs. ....	104
Table 5.2. Flexural properties of the 3D printed FGNCs. ....	108
Table 5.3. Specific flexural properties of the 3D printed FGNCs. ....	108
Table 5.4. Comparison between experimental and numerical results. ....	110
Table 6.1. Compressive properties of the 3D printed NCs.....	114
Table 6.2. Compressive responses of the 3D printed FGNCs. ....	117
Table 6.3. Rockwell hardness and impact strength of the 3D printed materials. ....	119
Table 7.1. Critical buckling load ( $P_{cr}$ ) of 3D printed samples. ....	122
Table 7.2. Effect of compressive load on the natural frequency (Hz) of 3D printed samples.....	128
Table 7.3. Effect of compressive load on damping factor of 3D printed samples.....	130
Table 7.4. Comparison between numerical and experimental natural frequency of 3D printed samples under no-load conditions. ....	131
Table 8.1. Thermal buckling responses of the prints. ....	140
Table 9.1. Density of the recycled filaments and the prints.....	148
Table 9.2. XRD responses of the recycled filaments and the prints. ....	150

Table 9.3. Tensile responses of the recycled NC filaments and the prints. .... 152

## ABBREVIATION

ASTM	: American Society for Testing and Materials
Flmt	: Filament
W/UR	: Waste/Unrecycled
FEM	: Finite Element Method
HDPE	: High Density Polyethylene
MWCNT	: Multi-Walled Carbon Nanotubes
Spmn	: Specimen
Specimen	: 3D printed Part
UTS	: Ultimate Tensile Strength
AM	: Additive Manufacturing
CTE	: Coefficient of Thermal Expansion
NC	: Nanocomposite
FGNC	: Functionally Graded Nanocomposite
FEA	: Finite Element Analysis
3D	: Three Dimensional
3DP	: 3D Printing
DAQ	: Data Acquisition System
DSC	: Differential Scanning Calorimetry
DTM	: Double Tangent Method
MBC	: Modified Budiansky Criteria
FFF	: Fused Filament Fabrication

MFI	: Melt Flow Index
TGA	: Thermogravimetric analysis
PMC	: Polymer Matrix Composite
SEM	: Scanning Electron Microscope
UTS	: Ultimate Tensile Strength
VCT	: Vibration Correlation Technique

## NOMENCLATURE

$\omega$	Angular natural frequency	rad/s
$\epsilon$	Damping factor	-
$f$	Natural frequency at applied load, P	Hz
$f_n$	Natural frequency at no- load	Hz
$\alpha$	Angle between $\omega$ 's	°
$T_{cr}$	Critical buckling temperature	°
$P_{cr}$	Critical buckling load	N
$\rho_H$	HDPE density	kg/m <sup>3</sup>
$\rho_c$	Composite density	kg/m <sup>3</sup>
$\rho_{CNT}$	MWCNT density	kg/m <sup>3</sup>
$\rho_{exp}$	Experimental density	kg/m <sup>3</sup>
$\rho_{th}$	Theoretical density	kg/m <sup>3</sup>
$W_H$	Weigh fraction of HDPE	%
$W_{CNT}$	Weigh fraction of MWCNTs	%
$\bar{d}$	Recycled filament mean diameter	mm
$\sigma$	Standard deviation	mm
$n$	No. of samples	-
$T_{Cryst}$	Crystallization temperature	°C
$T_{Melt}$	Melting temperature	°C
$\alpha_{cryst}$	Degree of crystallinity	%
$b_f$	Final width at yield point	mm
$b_i$	Initial width	mm
$E$	Young's modulus	MPa
$\rho$	Density	kg/m <sup>3</sup>

$P$	Load	N
$L$	Span length	mm
$m$	Slope	-
$d$	Thickness	mm
$w$	Width	mm

# 1 INTRODUCTION

## 1.1 Additive manufacturing

Long Island, New York, has a geologic foundation of metamorphic rock dating back 200-350 million years, followed by a layer formed during the Cretaceous Period 72-100 million years ago. The early substrate was covered by clay, gravel, and sand due to glacial activities. It now houses a new technology, composite and additive manufacturing, reflecting Earth's layering and additive geologic process (Zhang et al. 2019). The progressive advancement and rapid growth in the manufacturing sector are driving the realization of the next-generation manufacturing process, which relies on innovative materials and technologies for economic success in a country. Over the past few decades, the additive manufacturing (AM), also known as 3D printing (3DP), has revolutionized the manufacturing industry. This technology allows building objects layer-by-layer directly from digital models, enabling unprecedented customization and design flexibility. The AM was initiated in 1980 with the invention of stereolithography (SLA) by Charles Hull, which laid the groundwork for the modern 3D printing (González 2019). Since then, it has evolved rapidly, encompassing various new techniques such as fused filament fabrication (FFF), selective laser sintering (SLS), and direct metal laser sintering (DMLS), among others. Each method utilizes a different process and materials, such as plastic, metal, and ceramics. The AM is revolutionizing the product design and construction, offering opportunities for customization, improved performance, multi-functionality, and lower manufacturing costs. The printing technologies have developed exceptionally in accuracy, speed, material property, and manufacturing cost (Raviv et al. 2014). However, a limited range of the AM materials limits the potential of 3D printing for different applications. The composites combine a matrix with reinforcing materials and have gained popularity due to their enhanced mechanical properties and versatility. To fully realize the potential of the AM technology, the efforts are needed to integrate the AM with the composites, allowing for the development of high-strength and high-stiffness lightweight components without expensive tooling like in conventional processes. This could strengthen the clean energy economy and shift the design-to-manufacture process. The history of the composite is found back to 1500

B.C., when Egyptian and Mesopotamian settlers used a mixture of mud and straw to create durable building materials. The straw was used to reinforce pottery and boats, while the mud served as a matrix or resin. Further, in 1200 A.D., Genghis Khan introduced the stronger bows made from the composite materials like wood, bone, and animal glue. Later on, Thomas Edison used the carbon fibers for light bulbs in the late 1800s. Owens Corning developed the first Fiber Reinforced Plastic (FRP), now known as fiberglass, in 1935. In 1946, the first commercial composite boat hull was made. Goldsworthy introduced the first fiberglass surfboard. Goldsworthy invented pultrusion, accelerating manufacturing for pipes and poles. In the 1960s, fiber was used on aeroplanes by George Lubin (Zhang et al. 2019). Initially, the AM was used for rapid prototyping, but now it has accelerated the product development life cycle, and has been progressively being used in different engineering applications such as aerospace, construction, automotive, electronics, marine, defense, and medical industries for manufacturing and deployment in service (Kumar 2022).

## **1.2 AM process chain**

The AM process starts with the conversion of an imagination/idea into a solid computer aided design (CAD) model, which is obtained by design software (such as AutoCAD, Creo, Solid works, and CATIA), 3D laser scanning, or Computer Topographic (CT) scanning technique, which is further saved in .STL (Stereolithography/Standard Tessellation Language) format (Domingo-Espin et al. 2015). In the next process, the .STL file is sliced in slicing software (such as Simplify3D). This slicing software is the interface between the computer and the 3D printer. It also allows for setting various process parameters such as layer height, infill percentage, raster angle, raster pattern, build orientation, and support structure geometry. After slicing and setting the required parameters, the file is converted into G-code, the identifying language for the 3D printer to process the material. The G-code file is fed into the machine, and the printing is initiated. The printer deposits the material on the bed layer-by-layer, as the software defines. The printed part is then removed from the bed, and the post-processing steps, like priming, are carried out. The different AM processes have different procedures to remove the additional structure from the printed part because they use different methods and materials.

However, all the processes share a common feature: the fabrication of the part directly from a 3D CAD model using a fast, accurate, highly automated, and flexible process. The AM process is presented in Figure 1.1 (Chen et al. 2017).

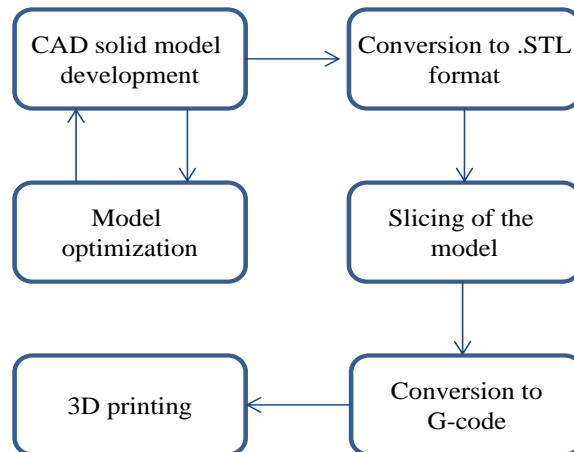


Figure 1.1 Process chain in AM.

### 1.3 Classification of AM processes

Industrial companies like Electro Optical System (EOS) in Germany, Arcam (Sweden), MCP Tooling technologies (UK), and Optomec, Stratasys, and Z Corporation in the USA, have introduced various AM processes to the commercial market. The ASTM F42 committee classifies these processes into seven areas. The various AM methods and their detailed information are presented in Table 1.1. Out of them, there are four methods Selective laser sintering (SLS), Stereolithography (SLA), Multi-jet/Polyjet modeling (MJM), and FFF, which are extensively used for polymer processing (Kazmer 2009).

### 1.4 Fused filament fabrication

The FFF 3D printing is the most widely utilized AM technology for creating thermoplastic polymer/composite products due to its lower lead time and tooling cost, simple and easy process, easier filaments availability, and most importantly, the ability to produce complex geometry and integrated components (Ojha 2023, 2024), finding applications in the fabrication of automobile, aircraft, spacecraft, medical devices, and marine structures/parts (Jagadeesh 2022, Kumar 2022). This FFF technology was developed by S. Scott Crump in 1980 and later commercialized in 1990 (Tucker et al. 2014) by Stratasys Inc company, which he co-founded. It uses

thermoplastic materials as feedstock material in filament form with varying diameters from 1.75 mm to 3 mm, depending upon the diameter of the nozzle used in the 3D printer. The filament is unwound from a spool and pulled into an extrusion nozzle using a controlled drive mechanism. The heated nozzle provides enough heat to melt the plastic material, resulting in semi-molten strands. These strands are then layered on a hot bed using the numerically controlled nozzle movement to obtain a 3D physical object. This FFF technology supports different thermoplastic polymers such as polycaprolactone (PCL), polyetherimide (PEI), polymethylmethacrylate (PMMC), polycarbonate (PC), polylactide (PLA), acrylonitrile butadiene styrene (ABS), polyamide (PA), polybutylene terephthalate (PBT), polypropylene (PP), and HDPE (Patil et al. 2019). It can also print their composites, which are generally reinforced by the glass micro balloons (GMBs), Al<sub>2</sub>O<sub>3</sub> powder, iron particles, fly ash cenospheres, glass fiber, carbon fiber, nano clay, carbon black, graphene, and carbon nanotubes (CNTs) (Kumar 2022).

### **1.5 Selection of filler and matrix**

The warpage is a prevalent problem in the FFF 3D printing of thermoplastic polymers/their composites because of their thermal instability (H S et al. 2020), which can be improved by incorporating fillers with low thermal expansion coefficient (CTE). The CNTs are brittle with less CTE and can improve thermal and dimensional stability; hence, they can eliminate the warpage issue in the polymer printing. Moreover, the CNTs have very high mechanical properties. They have excellent elastic modulus (1 TPa), high electrical conductivity ( $10^5$ - $10^7$  S/m), high thermal conductivity (3000 W/mK), having the ability to enhance mechanical, thermal, and electrical properties even if a minimal amount ( $\leq 5$  %) is incorporated in the matrix (Kumar 2022), and hence the CNT is utilized in the current work as a filler. Any matrix cannot be integrated with any filler. They must be compatible; only then, the property enhancement can be achieved, which is the main aim of developing a composite, be achieved. With the CNTs, thermoplastic polymers like PLA (Zhao 2022), ABS (Akar 2022), PU and PC (Liu et al. 2020), polystyrene (PS) and PP (Beesetty et al. 2020), and polyethylene (PE) (Stan et al. 2019) are compatible.

The HDPE is a highly utilized industrial polymer, having very attractive properties such as good wear resistance, low friction coefficient, high impact strength, high strength, and moderate stiffness (Kumar 2022). Moreover, it is a very commonly utilized polymer from home to engineering applications. It is mostly used in chemical, packaging, and household goods manufacturing industries (Bharath et al. 2021, Chrissafis et al. 2007, Chrissafis et al. 2009, H S et al. 2020). With the HDPE, the fillers like graphite nanofibers (Di et al. 2003), carbon (Fouad et al. 2011), nano clay (Beesetty et al. 2020), glass microballoons (GMBs) (Doddamani 2020, Jayavardhan et al. 2018), fly ash cenospheres (Kumar et al. 2016, Kumar 2016), wood flour (Adhikary 2011), and the CNTs (Amoroso et al. 2020) are compatible. Thus, it is confirmed from the literature that the CNTs and the HDPE are compatible, and therefore, can be combined with each other to develop composite. Since the CNTs are found on nanoscale, therefore, the CNT/HDPE based composite would be known as polymer nanocomposite (PNC). The CNT/HDPE PNCs have great significance in the noise spectroscopy and transport devices (Barone 2011), gears (Dabees 2021), thermistors (Zeng 2014), and the structural and consumer products (Zeng 2014).

Table 1.1. The seven AM categories as per ASTM F42.

Process Type	Brief Description	Technology Utilized	Companies	Materials
Direct Energy Deposition (DED)	Focused thermal energy is used to fuse material by melting as the material is being deposited	Laser Metal Deposition (LMD)	POM (USA), Optomec (USA)	Metals
Powder Bed Fusion (PBF)	Thermal energy selectively fuses region of powder bed	Selective Laser Sintering (SLS), Electron Beam Melting (EBM), Selective Heat, Sintering (SHS) and Direct Metal Laser Sintering (DMLS)	EOS (Germany), Arcam (Sweden), 3Dsystem (USA)	Polymers, Metals
Material Extrusion (ME)	Material is selectively dispensed through a nozzle or orifice	Fused Filament Fabrication (FFF)	Bits from bytes, Stratasys (Israel)	Polymers
Binder Jetting (BJ)	A liquid bonding agent is selectively deposited to join powder material	Plaster Based 3D Printing (PP), Powder Bed and Inkjet Head (PBIH)	3D system (USA), ExOne (USA)	Metals, polymers, foundry sand
Sheet Lamination	Sheets of material are bonded to form an object	Ultrasonic Consolidation, Laminated Object Manufacturing (LOM)	Mcor (Ireland), Fabrisonic (USA)	Metals, paper
Material Jetting (MJ)	Droplets of build material are selectively deposited	Multi-Jet Modeling (MJM)	3D system (USA), Objet (Israel)	Waxes, polymers
Vat Photo Polymerization	Liquid photopolymer in a vat is selectively cured by light-activated polymerization	Digital Light Processing (DLP), Stereolithography (Gupta and Nagorny),	EnvisionTEC (Germany), 3D system (USA)	Photopolymers

## **1.6 Polymer nanocomposites and their applications**

The polymer nanocomposites (PNCs) are the composites in which the reinforcement phase is of nano size ( $1 \text{ nm} = 10^{-9} \text{ m}$ ) and the matrix is a polymer (Camargo et al. 2009). The physical, mechanical, and thermal properties of the PNCs are improved by a strong molecular connection between the nanofiller and the polymer resin (Venkatesan et al. 2014). Among the other matrix based NCs, the PNCs have drawn a lot of attention from the researchers because of their customized material properties that are suited to electrical and electronic industries (printed circuits and electric components), automotive sectors (body exterior, interior parts, and under-the-hood), food packaging (containers, films), construction (panels, shaped extrusions), cosmetics, beverages, aerospace, biomedical, and military applications (Beesetty et al. 2020, Boran et al. 2017). The composite comprises at least two or more materials, which gives better material properties than the individual materials (Kumar 2022). The reinforcement and matrix are the two phases in the composite. However, a third phase, as voids, can also be found in a composite (Bharath 2020). The void phase is crucial for the energy absorption applications. The matrix phase is continuous, whereas the reinforcement phase is discontinuous in the composite. The matrix phase keeps the reinforcement/fibers in the desired orientation and spacing, protecting them from the abrasion and environment. The reinforcements used in the composites are usually fibers or particulates, often stronger, stiffer, and harder than the matrix. The composites are well-known for their exceptional stiffness and strength, provided by the composite's reinforcing phase. The composites are divided into three categories based on the matrix phase: ceramic matrix composite (CMC), metal matrix composite (MMC), and polymer matrix composite (PMC). The metals have moderate stiffness and strength but are ductile; the ceramics have high stiffness and strength but are brittle, while the polymers have low stiffness and strength. In the PMC and MMC, the strong interfacial bond is desirable so that the strength and stiffness can be enhanced, where the matrix phase uses shear loading at the interface to convey loads from the matrix to the fibers. The PMCs, also known as polymer composites in short, are well-known for their high stiffness and strength properties. The polymer composites are of two types based on thermosets and thermoplastics matrix used. The thermosets are the

low viscosity resins that react and cure during processing, resulting in an intractable solid. A thermoplastic is a high-viscosity resin heated beyond the melting point to be processed. Because thermosets are set up and cured during processing, they cannot be reused after reheating. The thermoplastics can be reheated beyond their melting temperature for further processing and can be used for different applications (Campbell 2010). The common thermoplastic polymers used in the industries in the form of matrix are acrylonitrile butadiene styrene (ABS) (Rabbi et al. 2020, Zhang et al. 2017), polylactic acid (PLA) (Arivazhagan et al. 2014, Spoerk et al. 2017), polyetherimide (PEI) (Ajinjeru 2018), polycarbonate (PC) (Domingo-Espin et al. 2015) polymethylmethacrylate (PMMA) (Espalin et al. 2010), polycaprolactone (PCL) (Stansbury et al. 2016), polyamide (PA) (Calvert et al. 2008, Tellis et al. 2008), polypropylene (PP) (Carneiro et al. 2015, Rahim et al. 2019, Silva et al. 2017) and their blends (Przybytek et al. 2018), polybutylene terephthalate (PBT) (Gómez et al. 2021, He et al. 2020), and the HDPE (Chatkunakasem et al. 2018, Ganesan et al. 2021, Gupta et al. 2019). The common fillers used to reinforce these thermoplastic polymers are the hollow microspheres such as fly ash cenospheres, glass micro balloons (Patankar et al. 2009, Patankar et al. 2010, Patil et al. 2019, Patil et al. 2019, Shutov et al. 1986, Shutov 1986, Singh et al. 2018), iron particles (Mastoid et al. 2004),  $Al_2O_3$  powder (Singh et al. 2016), nano clay-like montmorillonite (MMT) (Beesetty et al. 2020), glass fiber (Toutanji et al. 2000), carbon black (Yuan et al. 2010), carbon fiber (Brenken et al. 2018, Rizkalla et al. 2008), graphene (Sreenivasulu et al. 2018, Verma et al. 2014), and the carbon nanotubes (Amoroso et al. 2020, Mora et al. 2020). The reinforced polymer composites find a various sets of applications from the automotive, medical, marine, electronics, space, and aerospace to the several daily life products (Kumar 2022).

### **1.7 Functionally graded materials and their applications**

The laminated composite, mostly used in the aerospace and high speed vehicle applications, shows delamination issues due to discontinuous stress distribution along the thickness. The functionally graded materials (FGMs) are the special composite materials in which the material properties (such as density, strength, modulus, etc.) vary in the thickness direction, which further results in the continuous stress

distribution as compared to the laminated composites (Tahir et al. 2021). Due to the smooth variation in the material properties, the FGMs find their significance in plates (Kim et al. 2013), beams (Li et al. 2017), panels (Huan et al. 2017), conical shells, and cylindrical shells (Sofiyev et al. 2014, Sofiyev 2019). The gradation in the FGMs is envisaged to meet some specific functional requirements. Their specific applications can be found in the biomedical applications such as bone and dental implants. The bone is integrated with the muscles through bone tissues in the human body, where the bone material should be stronger and stiffer from the inside and flexible from the outside to integrate with the bone tissues properly. Similarly, in the case of dental implants, a variable stiffness is required from the implant to the crown side. In automobile applications, the FGMs can be utilized in brake discs. During the break application, the frictional surface is subjected to a high friction, resulting in high wear and heat development. Therefore, the frictional surface of the disc must be highly resistant to wear and thermally conductive, which can be obtained by grading the material only. In addition to these, the FGMs can also be used in water purification. There, the porosity or the functional group can be varied to improve the removal of the contaminants. These variational properties can be obtained through gradation only, and hence the study on the FGMs is important. Additionally, the FGMs have a variety of engineering utilizations, including nuclear reactors, spacecraft, turbine rotors, gears, flywheels, the energy industry, defense, and the medical fields. The FGMs were initially utilized by Japanese in 1984 in an aerospace project to eliminate the discontinuous stress distribution of the laminated composites (Sayyad 2019). The variation in the material properties in the FGM results in continuous stress distribution compared to the laminated composites, which further eliminates the delamination problem in the FGM (Dileep 2021, Tahir 2021). The FGMs are generally developed by gas, liquid, plasma, and powder metallurgy based processes. However, they have still not been explored much with 3D printing (Dileep 2021). The traditional polymer fabrication methods require molding specific shapes and designs for each part, which consumes additional time and cost, making these processes expensive.

## **1.8 Polymer manufacturing methods**

Each material system has a unique combination of mechanical, physical, and processing characteristics. An appropriate manufacturing procedure must be chosen to transform the material into a final product without defects. In the twentieth century, the processes used to produce items out of composite materials shifted from labor-intensive, skilled labor operations to sophisticated microprocessor systems with automatically run equipment. Earlier, manual spray-up in open molds method and hand lay-up techniques were used in which raw components were mixed and cured at the room temperature. Due to the advantages such as high strength-to-weight and high stiffness-to-weight ratio, the polymer composites are being used in almost every sector of the global economy, including automotive, consumer goods, marine, biomedical, space, electronics, aerospace, and construction. The rapid increase of the product applications demands the expansion of materials technology, design methodologies, and the production procedures (Arza 2012). The manufacturing method for polymer nanocomposites must be carefully selected based on the ease of processing method, less manufacturing cost and time, no material wastage, and the design and development flexibility. Various traditional manufacturing methods are used to fabricate polymer composites/nanocomposites. They are resin transfer molding, vacuum assisted resin transfer molding, hand lay-up method, spray-up in mold method, autoclave, compression molding, and injection molding methods for the utilization in automotive, electrical, electronic, construction, aerospace, military, and biomedical applications (Beesetty et al. 2020). The compression and injection molding processes are more frequently used processes for the plastic production. Also, the injection molding is far better than the compression molding process in terms of production speed. Still, all these processes are mold-based, designed based on the product size and shape, which is time-consuming and costly. Also, the mold design and development for very complex shapes and geometries are very difficult, which limits the applications of these traditional methods and requires such a method which can break all these limitations and provide greater design flexibility. Recently, a very attractive and useful manufacturing method, known as additive manufacturing

method, has evolved, which can fabricate any complex geometry and jointless parts without using any mold at minimal cost and time (Kumar 2024).

### **1.9 Literature review**

The CNT based polymer nanocomposites are lightweight nanocomposites, which have great significance in weight-saving applications such as automobile, marine, defence, aerospace, and electronics. However, these applications require good mechanical, thermal, and dynamic performance to serve in these applications without any failure. Therefore, these properties must be enhanced depending on the modified material's microstructure. Before going for the composite fabrication, the minimum and maximum amount of the fillers that can be added into a matrix must be known. A higher amount of the fillers that can be added into a matrix causes agglomeration effect, significantly reducing the composite properties. Therefore, selecting the filler amount is very essential. Moreover, their distribution in the matrix is also crucial, as it significantly affects the material properties, and can be obtained through a proper processing of the materials. In order to obtain this information, a comprehensive literature is carried out on the materials, manufacturing methods, studies conducted, and their outcomes, which will give a complete update of the polymer composites and their manufacturing methods.

Table 1.2. Literature Review.

Author	Process	Parameters	Materials Used	Property Studied	Remarks
(Porter et al. 2017)	FFF	Infill angle, Outline perimeters, Layer thickness, Nozzle temperature	Polyvinylidene fluoride (PVDF)	Tensile and Piezo-electric coefficient.	<ul style="list-style-type: none"> <li>• Yield strength was highest when the infill pattern was parallel to the pulling axis and reduced with a decreasing infill angle.</li> <li>• Higher phase content was associated with lower nozzle temperature, high extrusion rate, and higher hot end voltage.</li> </ul>
(Yao et al. 2017)	FFF	Infill density	PLA+Polyacrylon itric (PAN)/ continuous carbon fiber	Tensile, Three Point Bending, Piezo-electric behavior.	<ul style="list-style-type: none"> <li>• Fiber reinforcement increased tensile and flexural strength by 70% and 18.7%, respectively.</li> <li>• 11.41% print time and 26.01% weight reduction were achieved by lowering infill density without</li> </ul>

					compromising tensile strength.
(Wang et al. 2017)	FFF (Makerbot Replicator 2X)	Extrusion temperature, Layer height	Polypropylene (PP)	Izod impact	<ul style="list-style-type: none"> <li>• Proper printing process can provide similar impact strength to conventional injection molded PP.</li> </ul>
(Zaldivar et al. 2017)	FFF (Stratasys FDM 400 mc)	Print orientation	ULTEM <sup>®</sup> 9085	Dynamic Mechanical Analysis, Full field strain (Direct Image Correlation), Thermal Mechanical Analysis (TMA)	<ul style="list-style-type: none"> <li>• Tensile strength varies in the 46%-85% range of reported values of Injection Molded ULTEM parts.</li> <li>• Failure strain for FFF parts ranged from 2%-7% and was also considerably lower than the failure strain typically attained for IMULTEM<sup>®</sup> parts (75 %).</li> </ul>
(Alaimo et al. 2017)	3DP	Filament thickness,	ABS	Anisotropic behavior, Tensile,	<ul style="list-style-type: none"> <li>• It is possible to improve i) fiber properties and ii)</li> </ul>

	(3NTR A4v3)	Filament width, Chemical composition (normal, chemically additivated supplied by Versalis S.P.A)		Shear strength.	fiber-to-fiber bonding strength and, consequently, the overall mechanical properties at macro-scale, particularly the yielding strength and the strain at failure.
(Tian et al. 2017)	3DP	Temperature	Poly lactide (PLA) + Carbon Fibres	Tensile, Flexural, Impact (Charpy).	<ul style="list-style-type: none"> <li>• 25% improvement of flexural strength compared to the originally 3D printed composites.</li> <li>• Material recovery rates for CFs (100%) and PLA matrix (73%) were achieved due to the unique character of 3D printed</li> </ul>

					carbon fiber reinforced thermoplastic polymer composites.
(Singh et al. 2017)	Extrusion	Barrel temperature, Die temperature, Screw speed (For pilot study), wt.% of Fe.	HDPE, LDPE + Fe, HDPE + Fe, LDPE.	Melt Flow Index (MFI), Mechanical properties, and shore D hardness.	<ul style="list-style-type: none"> <li>• Break strength 15.02 N/mm<sup>2</sup>, peak elongation 3.63 mm, and shore D hardness 34.35 for HDPE were observed.</li> <li>• Lowest porosity for 100% HDPE was observed.</li> </ul>
(Gardner et al. 2016)	FFF (Aleph Object, Co.)		CNT infused with ULTEM®.	Tensile and Electrical conductivity	<ul style="list-style-type: none"> <li>• Addition of CNT yielded a specific modulus of 19.5 GPa and a specific tensile strength of 317 MPa.</li> <li>• 1850% increase in the specific modulus and 287% improvement in the specific strength compared to neat</li> </ul>

					ULTEM®Sheet.
(Weng et al. 2016)	FFF	Heating temperature, Heating time, Microsphere%.	Poly wax mixed with hydrocarbon filled microspheres	Tensile, Compressive, Thermal, Dynamic Mechanical Analysis.	<ul style="list-style-type: none"> <li>• Compressive and Tensile strength increased by 52.2% and 25.4%, respectively at 2 wt.% microsphere heated at 140 °C for 120 s.</li> </ul>
(Dakshinamurthy et al. 2018)	FFF	Layer height, Raster angle, Raster width.	ABS	Dynamic Mechanical Analysis	<ul style="list-style-type: none"> <li>• % contribution of slice height and raster width on the viscoelastic properties of the FFF-RP components was found to be 55% and 31%, respectively.</li> </ul>
(Ning et al. 2016)	FFF	Infill speed, Raster angle, Nozzle temperature, Layer thickness.	ABS + 5 wt.% CFs	Tensile	<ul style="list-style-type: none"> <li>• 0, 90 raster angles have a more significant effect on the tensile properties than the -45 and +45 raster angles.</li> <li>• 25mm/s infill speed</li> </ul>

					<p>resulted in highest mean tensile properties.</p> <ul style="list-style-type: none"> <li>• Tensile properties first increased and then decreased with an inflection point at 220 °C nozzle temperature.</li> <li>• 0.15 mm layer thickness gave highest tensile properties.</li> <li>• Toughness and ductility reach highest mean values at 0.25 mm layer thickness.</li> </ul>
(Singh et al. 2016)	FFF (uPrint SE system)		Nylon-6: Matrix, Al <sub>2</sub> O <sub>3</sub> : Filler.	Wear	<ul style="list-style-type: none"> <li>• Composite filament has same MFI as that of standard FFF filament.</li> <li>• Significant enhancement in the wear resistance is found</li> </ul>

					due to reinforcement.
(Singh et al. 2016)	FFF	Barrel temperature, Screw speed, Take up speed	ABS-EG (Extrusion Grade)	Melt Flow Index (MFI), Tensile	<ul style="list-style-type: none"> <li>• In house FFF filament development.</li> <li>• Process parameters optimized for single screw extruder.</li> <li>• Fabrication cost of one cartridge is 16.27 U.S. dollar which saves around 93% on FFF part.</li> </ul>
(Mohamed et al. 2016)	FFF (Fortus 400mc)	Layer thickness, Air gap, Raster angle, Build orientation, Road width, Outline perimeters.	PC-ABS (Polycarbonate-ABS) blend	Dynamic Mechanical Analysis	<ul style="list-style-type: none"> <li>• FDM process parameters like air gap, raster angle, contours, layer thickness, build orientation, and road width significantly affect the loss modulus and the storage modulus.</li> <li>• Inappropriate selection of process parameters causes</li> </ul>

					incomplete filling, distortion, voids, and delamination, eventually leading to the manufactured part's poor mechanical performance.
(Singh et al. 2016)	FFF (uPrint SE system)	Wt.% of Nylon, Size of Al <sub>2</sub> O <sub>3</sub> , Wt.% of Al <sub>2</sub> O <sub>3</sub> , Particle size in equal proportion in weight (single, double, triple particle size)	Nylon-6 with Al <sub>2</sub> O <sub>3</sub> reinforced filament	Tensile	<ul style="list-style-type: none"> <li>• % elongation decreases as the particle size changes from single particle size to triple particle size.</li> <li>• Highest tensile properties are noted for double particle size.</li> </ul>
(Riddick et al. 2016)	FFF (Fortus 400 mc)	Build orientation, Direction	ABS	Tensile, Microstructure	<ul style="list-style-type: none"> <li>• Build direction-Horizontal (Min. tensile strength- 15.26 MPa, Raster angle</li> </ul>

					<p>90°, Max. tensile strength-32.60 MPa, Raster angle 0°).</p> <ul style="list-style-type: none"> <li>• Build direction–side (Min. tensile strength-24.24 MPa, raster angle 90°, max. tensile Strength-34.17 MPa, raster angle 0°).</li> <li>• Build direction-Vertical (Min. tensile strength-12.42 MPa, raster angle 90°, max. tensile strength-19.80 MPa, raster angle±45°).</li> </ul>
(Faes et al. 2016)	FFF (Dimension SST 1200es)	Build Orientation, Inter layer cooling time	ABS – m30	Tensile	<ul style="list-style-type: none"> <li>• Tensile strength and elongation at break are inversely proportional to interlayer cooling time.</li> </ul>

(Zou et al. 2016)	FFF (Dimension SST 1200es)	Build angle	ABS, ABS PLUS	Tensile, Isotropic and anisotropic property	<ul style="list-style-type: none"> <li>• The elastic modulus and the tensile strength of ABS PLUS material can be calculated by using isotropic models, including elastic and yielding models whereas for better precision or more accurate applications concerning printing orientations anisotropic model is recommended.</li> <li>• Fundamental models of anisotropic and isotropic (transversely isotropic) elasticity are set to determine the relation of elastic constants and printing angles.</li> </ul>
-------------------	----------------------------------	-------------	---------------	---	---

(Mohamed et al. 2016)	FFF (Fortus 400)	Air gap, Layer thickness, Build orientation, Raster angle, Road width, Outline perimeters	Polycarbonate/ABS blend	Flexural, Single and multi-objective (build time and material consumption).	<ul style="list-style-type: none"> <li>• Experiments were conducted to validate mathematical models, and results obtained by this confirmation show that models can accurately communicate the correlation between the process condition and experimental responses.</li> <li>• The models helped to reduce number of experiments by estimating feedstock material consumption, build time, and dynamic flexural modulus. Indirectly minimizes cost, time, and effort.</li> </ul>
-----------------------	------------------	---	-------------------------	---	---

					<ul style="list-style-type: none"> <li>• Actual and the estimated values vary from 0.233% to 1.604%.</li> </ul>
(Weng et al. 2016)	FFF (creator, flash forge, china)	Organic Modified Montmorillo nite (OMMT) wt.%	ABS and Organic Modified Montmorillonite (OMMT)	Tensile, Flexural, DMA, Thermal	<ul style="list-style-type: none"> <li>• With 5 wt.% of OMMT into ABS increased tensile strength of 3D printed samples from 27.5 MPa to 39.48 MPa.</li> <li>• The elastic modulus increased from 1.2 GPa to 3.6 GPa.</li> <li>• Increase in flexural strength from 42.69 MPa to 56.92 MPa.</li> <li>• Increase in the storage modulus of ABS from 1.1 GPa to 1.6 GPa.</li> </ul>
(Garg et al. 2015)	FFF	Composition (Wt.% of Iron	ABS, Fe-Nylon6.	Wear	<ul style="list-style-type: none"> <li>• As the Fe content in Nylon6 increases, the wear</li> </ul>

		(Fe) and Nylon)			<p>resistance also increases.</p> <ul style="list-style-type: none"> <li>• 60% Fe and 40% nylon6 composition shows higher wear resistance value than the neat ABS sample.</li> <li>• Coefficient of friction (<math>\mu</math>) increases with the addition of Fe in the composite.</li> <li>• The coefficient of friction (<math>\mu</math>) for Fe-Nylon composite is noted to be lower than the ABS, but it is highest for 60% Fe and 40% nylon6 composition.</li> </ul>
(Domingo-Espin et al. 2015)	FFF (fortus 400mc)	Build orientation	Polycarbonate (PC)	Tensile, Flexural	<ul style="list-style-type: none"> <li>• FFF part anisotropy not only depends on the build direction but also gets influenced by other parameters such as slice</li> </ul>

					height, nozzle diameter, and filament diameter.
(Tuan Rahim et al. 2015)	3DP (MakerBot Replicator 2X)	Material (neat, composite)	Polyamide (PA) +5 wt.% Hydroxyapatite (HA) +15 wt.% zirconium oxide fillers, Pure Polyamide 12, Commercial polyamide, Taulman 618, ABS with Cu and Fe particles.	MFI, Thermal Tensile, Porosity	<ul style="list-style-type: none"> <li>• New composite PA filled with 20 wt.% ZrO<sub>2</sub> and HA was successfully fabricated via 3D printer.</li> <li>• Strength of the new composite (PA12/ZrO<sub>2</sub>/HA) is 22.78 MPa, which is slightly lower than unfilled PA12 (26.54 MPa).</li> <li>• It has equal strength as that of commercial PA and Taulman 618 (21.49 MPa).</li> <li>• The obtained properties are weaker than those of the injection molding sample.</li> </ul>
(Tekinalp et al. 2014)	FFF (solidoo)	Method (CM,	ABS & CNT	Tensile,	<ul style="list-style-type: none"> <li>• 700% and 115% increase</li> </ul>

	dle 3)	FFF), carbon fiber wt.%.		Comparison with Compression molded (CM) specimen.	<p>in the tensile modulus and strength of the FFF sample compared to the CM sample.</p> <ul style="list-style-type: none"> <li>• Remarkable porosity is found in the printed samples, whereas no porosity is visible in the CM sample.</li> </ul>
(Lee et al. 2013)	FFF	Print orientation	ABS, ABS PLUS.	Fatigue, Property comparison between ABS and ABS Plus Sample.	<ul style="list-style-type: none"> <li>• Tensile strength of the ABS printed sample ranges from 50%-80% of the ABS wire data.</li> <li>• Tensile strength of the ABS PLUS printed sample ranges from 75%-80% of the ABS PLUS wire data.</li> <li>• Strain energy of the ABS printed sample ranges</li> </ul>

					<p>from 3.4%-19.7% of the ABS material.</p> <ul style="list-style-type: none"> <li>• Strain energy of the ABS PLUS printed sample ranges from 1.8%-7.4% of the ABS PLUS material.</li> </ul>
(Nikzad et al. 2011)	FFF (3000 machine)	Composition	ABS P400 – Iron Filler, ABS P400 – Copper filler.	Thermal conductivity, Heat capacity, Dynamic mechanical properties, Tensile	<ul style="list-style-type: none"> <li>• Iron and copper is used as metallic filler into the ABS to develop new composite feedstock filament.</li> <li>• Copper-ABS composite of 30 vol.% of the copper particle having 45µm size shows noticeable enhancement in the conductivity.</li> <li>• Iron-ABS composite of 30 vol.% of the iron particle having 45 µm size shows</li> </ul>

					<p>remarkable enhancement in the conductivity.</p> <ul style="list-style-type: none"> <li>• Iron-ABS composite of 10 vol.% of the iron particle tensile strength drops suddenly since no additives were used.</li> <li>• Additives could promote better interfacial bonding.</li> </ul>
(Mora et al. 2020)	FFF	<p>Bed Temperature, Nozzle temperature, Infill density, Extrusion width, Layer height, and Nozzle speed.</p>	<p>PLA, HDPE and MWCNTs</p>	<p>SEM, XRD, TGA and Electrical Conductivity.</p>	<ul style="list-style-type: none"> <li>• CNTs are uniformly dispersed and characterized by SEM and XRD.</li> <li>▪ Electrical conductivity increases with the increase in CNT content.</li> </ul>
(Stanciu et al. 2019)	FFF	<p>Bed</p>	<p>HDPE &amp;</p>	<p>Rheology,</p>	<ul style="list-style-type: none"> <li>• For MWCNT loadings up</li> </ul>

		<p>Temperature, Nozzle temperature, Infill density, Extrusion width, Layer height, and Nozzle speed.</p>	MWCNTs	<p>Mechanical and Electrical properties.</p>	<p>to 1 wt.%, the melt shear viscosity and activation energy of PP/MWCNT composites are not significantly affected by the addition of CNTs.</p> <ul style="list-style-type: none"> <li>• All PP/MWCNT composites displayed solid-like behavior at high shear rates.</li> <li>• PP/MWCNT filaments with good surface finish were extruded. However, the roughness of the PP/MWCNT filament increased with increasing CNTs loading, especially at 1 wt.%, due to CNTs agglomeration.</li> </ul>
--	--	--	--------	--	---

					<ul style="list-style-type: none"> <li>• Overall, the filaments and the 3D printed specimens exhibited good mechanical properties with good-interlayer adhesion.</li> <li>• Printing direction was found to have a significant effect on the tensile strength.</li> <li>• The MWCNTs loading was also affected the tensile strength but with a lower impact.</li> </ul>
(Zeng et al. 2014)	Melt-mixing and Hot pressing	Mixing temperature, speed, and time, Hot pressing temperature and pressure	HDPE & MWCNTs	Electrical and Thermal Properties	<ul style="list-style-type: none"> <li>• Electrical resistivity of the CNT/HDPE drastically decreases with an increase in the CNT addition, showing a typical percolation phenomenon</li> </ul>

					<p>due to the CNT network formation at low CNT loading (percolation threshold of 4 wt.%).</p> <ul style="list-style-type: none"> <li>• At elevated temperatures, all the composites exhibited sharp increase in the electrical resistivity (a typical PTC phenomenon), mainly attributed to the breakdown of interconnected CNT networks, resulting from volumetric expansion of the HDPE matrix in the melting process.</li> </ul>
(Amoroso et al. 2020)	Injection molding	Oven temperature & time, Barrel	HDPE & MWCNTs	Rheology, SEM, XRD, DSC & Tensile	<ul style="list-style-type: none"> <li>• Rheological, mechanical, microscopy, thermal and X-ray scattering techniques</li> </ul>

		temperature and screw speed, Mold temperature, Injection temperature & pressure.			<p>are used to determine the extent of MWCNTs dispersion and crystalline structure development in the composites of HDPE and MWCNTs at loadings up to 5 wt.% (2.82 vol.%).</p> <ul style="list-style-type: none"><li>• Oscillatory rheology measurements and SEM imaging confirmed the MWCNTs were highly dispersed in the HDPE matrix and a rheological percolation.</li><li>• Rheological percolation threshold was attained at an MWCNT loading between 0.1 wt.% and 0.3 wt.%.</li></ul>
--	--	--	--	--	---

(Dabees et al. 2020)	Injection molding	Mold temperature, Injection temperature & pressure.	HDPE & MWCNTs	Tensile, Flexural, Hardness, Impact & MFI	<ul style="list-style-type: none"> <li>• The nanocomposites' surface characterization using SEM revealed sound dispersion of the MWCNTs in the HDPE matrix until 2 wt.%, also detecting the presence of some regions devoid of the MWCNTs and some with aggregates at higher concentration (2.5 wt.%).</li> <li>• The MWCNT/HDPE nanocomposites exhibited higher decomposition temperature and thermal stability than neat HDPE.</li> <li>• The yield strength and the tensile strength increased almost linearly as the</li> </ul>
----------------------	-------------------	---	---------------	---	---

					<p>MWCNTs were introduced in the HDPE up to a concentration of 2 wt.%. There was a minor saturation in the increase of yield strength between the concentrations of 2 and 2.5 wt.% ascribed to the aggregation of the MWCNTs.</p>
(Sui et al. 2009)	Compression Molding	Molding Temperature, Twin screw extruder zones temperatures.	UHMWPE, HDPE & CNFs	DSC, XRD & Tensile	<ul style="list-style-type: none"> <li>The degree of crystallinity of the nanocomposites with the pretreated CNFs exhibited a decrease due to better interface adhesion compared to the nanocomposites loaded with same loading untreated CNFs.</li> </ul>

					<ul style="list-style-type: none"> <li>• The enhancement in the tensile strength of the nanocomposites containing 0.5 wt.% treated CNFs was four times higher (32%) than that of the nanocomposites, containing untreated CNFs (8%) over that of the pure polymer.</li> </ul>
(El Achaby et al. 2013)	Hot-press molding	Melt mixing temperature, Molding temperature	HDPE, MWCNTs & GNs	Morphology, Thermal, Rheology & Tensile	<ul style="list-style-type: none"> <li>• Morphology and melt rheology studies of the composites showed that the fillers were well distributed at nanoscale within the polymer matrix.</li> <li>• It was found that at the same filler content, in terms of rheological, thermal and tensile properties, the GNs</li> </ul>

					<p>perform better than the MWCNTs.</p> <ul style="list-style-type: none"> <li>• Young's modulus and tensile strength increases with filler content.</li> </ul>
(El Achaby and Qaiss 2013)	Injection Molding	Mold temperature, Injection temperature & pressure.	HDPE & MWCNTs	DSC & Tensile	<ul style="list-style-type: none"> <li>• CNT-HDPE composites showed a good enhancement in the mechanical properties with an increase of CNT %.</li> <li>• Melting point and oxidation temperature of the CNT-HDPE composites are not affected by the addition of the CNTs, but the crystallinity of composites increases.</li> </ul>
(Rajeshwari 2015)	Hot Compression	Molding Temperature,	HDPE & MWCNTs	Morphology, Hardness, Tensile	<ul style="list-style-type: none"> <li>• Microstructure analysis reveals that the MWCNTs</li> </ul>

	Molding	Twin screw extruder zones temperatures.		& Indentation	were homogeneously dispersed within the HDPE. <ul style="list-style-type: none"> <li>• Hardness, indentation, and elastic modulus increase with the CNT content.</li> </ul>
Carl G. et al. (2019)	3D Printing	Nozzle temperature, Bed temperature, nozzle diameter, Layer thickness, Layer width, Melt flow, Printing	HDPE	Tensile	<ul style="list-style-type: none"> <li>• When the specimen is 3D printed on the bed, the sample lifts up due to heat development, known as warpage.</li> <li>• This warpage mainly depends on the printing temperature, infill density, and layer height.</li> <li>• This problem is overcome by using SEBS build plate,</li> </ul>

		speed			which is compression molded and shows very good surface finish, good adhesion, and easily detachable properties.
(Liu et al. 2015)	Hot Molding Process	Melt mixing temperature, Molding temperature	HDPE, CNFs & GNPs	Tensile & Compression	<ul style="list-style-type: none"> <li>• Tensile and compressive strength increased with the filler content.</li> <li>• Tensile strength showed lower values compared to the compressive strength.</li> </ul>

Table 1.2 clearly shows that several works have been carried out on the polymer composites with different matrices and different fillers, fabricated by FFF AM process. However, the functionalized MWCNTs/HDPE based composites have still not been explored through any manufacturing method, limiting the potential of this material system for different applications. Also, no extrusion and 3D printing of the functionalized MWCNTs and the HDPE based novel materials has been done earlier, which are crucial from the manufacturing perspective to check their manufacturability for realizing actual products. The MWCNTs have very low density, and incorporating this into HDPE will make the composite lighter, which will be crucial for lightweight applications. Also, exploring the feasibility of this material system through 3D printing will be beneficial for fabricating complex geometry and jointless parts in one go. Many engineering applications need two different functions in the same component/structure simultaneously, which cannot be fulfilled by homogeneously reinforced or sandwich composites rather than the FGMs. The fabrication of polymer-based FGMs is very difficult when compared to conventional methods. However, it can be easily realized through 3D printing. The parts fabricated by 3D printing exhibit better performance than the other conventional manufacturing processes such as compression and injection molding (Beesetty et al. 2020, Jayavardhan 2017, Kumar 2016), which led to the selection of the 3DP for fabricating the functionalized MWCNTs/HDPE based materials. In most engineering applications, the components/structures are subjected to various loads like tensile, compression, flexural, impact, mechanical buckling, thermal buckling, and dynamic loads, developing different types of stresses in the member. These developed stresses must always be lower than the yield strength to avoid the failure of the components/structures, which are confirmed by their mechanical properties, and hence, their different property characterizations become very important. The current work aims at the feasibility of 3D printing of the functionalized MWCNTs/HDPE based NCs and FGNCs, and their characterizations for different static and dynamic behavior.

## 1.10 Motivation

The functionalized MWCNTs are very lightweight filler material with a very high aspect ratio. Their outer diameter is 10-30 nm, inner diameter 5-10 nm, length >10  $\mu\text{m}$  and surface area about 110-350  $\text{m}^2/\text{g}$ . Also, the MWCNTs have unique material properties, such as good acoustic insulating properties and excellent mechanical, thermal, and electrical properties. Adding a small amount of the functionalized MWCNTs can greatly improve the mechanical, thermal, electrical, and permeation barrier properties of a wide range of polymers and metals without increasing the product cost. Also, the CNTs have a very low coefficient of thermal expansion (CTE), having the great capability to enhance the thermal and dimensional stability, which will be very helpful in reducing warpage issue in 3D printing of the thermoplastic based samples (H S et al. 2020). The HDPE is extensively utilized as industrial thermoplastics, having exceptional mechanical and physical properties (Beesetty et al. 2020, Kanagaraj et al. 2007, Sepet et al. 2016) such as high impact strength, good wear resistance (abrasion and fatigue capabilities), low coefficient of friction, mild rigidity and stiffness (Tang et al. 2003), having great utility from our daily life products to different technical fields (Bharath et al. 2021, Chrissafis et al. 2007, Chrissafis et al. 2009, H S et al. 2020). 3D printing of the functionalized MWCNTs/HDPE NCs and FGNCs will provide greater design flexibility, requiring a variety of technical applications. The present work focuses on developing lightweight functionalized MWCNTs/HDPE NC filaments and concurrent 3DP of NCs and FGNCs for mechanical, thermal, and dynamic characterizations. The motivation for pursuing this topic is summarized as below.

- Reduction in polymer consumption
- Eco-friendly processing
- No limitations to designers.
- Durable and integrated components with complex geometries
- Zero tooling cost.
- Increasing load-bearing capacity of the polymer and making it suitable for various applications.

The objectives of the current work are outlined in the next section.

### **1.11 Objectives and scope of the work**

The literature on the development of functionalized MWCNTs/HDPE based NCs, and 3DP of NCs and FGNCs is scarce, as observed by the preceding literature review. As a result, the current study focuses on developing functionalized MWCNTs/HDPE based NC filaments and their potential in concurrent 3D printing of NCs and FGNCs. It requires a systematic study of the material system, knowledge of 3DP process parameters, and the required characterization methods.

The work proposed is achieved by the following objectives.

- Blending of the functionalized MWCNTs and the HDPE materials using Brabender with optimized parameters.
- Development of the functionalized MWCNTs/HDPE based nanocomposite feedstock filaments with necessary properties by optimizing temperature and speed of the extruder.
- To optimize 3D printing parameters for the functionalized MWCNTs/HDPE based NCs and FGNCs.
- To evaluate the microstructure-property correlations of the as printed and the tested samples for the microstructure-property correlations.
- To study the effects of weight fraction of the fillers and the investigations of the physical properties like density and weight-saving potential, basic characterizations of the materials like MFI, Rheology, DSC, TGA, and XRD, and the mechanical properties of the NCs (Tensile, Flexural, Compression, Impact, Hardness, Mechanical Buckling, Vibration, and Thermal Buckling) and FGNCs (Tensile, Flexural, Compression, Impact, Hardness, Mechanical Buckling, Vibration, and Thermal Buckling).

The scope of this research work includes the development of NCs by varying the functionalized MWCNTs (0.5%, 1%, 3%, and 5% by weight) in the HDPE matrix. The developed NCs are characterized for SEM, MFI, and TGA. Further, these NCs are used in NC filament extrusion for 3DP. The nanocomposite filaments are extruded using suitable parameters and then characterized for SEM, tensile, DSC, density, and XRD. Finally, the NC and FGNC samples are concurrently 3D printed using the extruded NC filaments for tensile, flexural, compression, impact, hardness, thermal buckling, free vibration, and mechanical buckling. Their print

characterizations are done using SEM and rheological analysis.

### **1.12 Thesis outline**

A systematic study of the selected objectives is presented. A brief skeletal structure of the thesis is presented here,

Chapter 1. A brief description of additive manufacturing, basis of material selection, polymer nanocomposites, functionally graded materials, and polymer manufacturing methods, including motivation, objectives, and scope of the current work.

Chapter 2. Materials used in the current research work, their typical properties, and details of the different processing and characterization methods.

Chapter 3. Discussion on the basic material characterizations.

Chapter 4. Discussion on the tensile behaviour of 3D printed NCs and FGNCs.

Chapter 5. Discussion on the flexural behaviour of 3D printed NCs and FGNCs.

Chapter 6. Discussion on the compression, hardness, and impact behaviour of 3D printed NCs and FGNCs.

Chapter 7. Discussion on the mechanical buckling and free vibration behaviour of 3D printed NCs and FGNCs.

Chapter 8. Discussion on the thermal buckling behaviour of the 3D printed NCs and FGNCs.

Chapter 9. Discussion on the recycling potential of the nanocomposites.

Chapter 10. Summary and conclusive remarks.

Finally, the key findings of the current work and the scope of the future work are presented.

## 2 MATERIALS AND METHODS

### 2.1 Constituent Materials

The current work uses the high density polyethylene (HDPE) thermoplastic polymer as a matrix and the functionalized multi-walled carbon nanotubes (MWCNTs) as fillers. The typical properties of the HDPE matrix and the functionalized MWCNTs are presented in the further sections.

#### 2.1.1 Matrix

The matrix material, HDPE of grade HD50MA180, was procured from Indian Oil Corporation Limited, Mumbai, India, as granules of ~3 mm diameter. The received HDPE material was in an untreated condition, and it is used in the same untreated condition. The typical properties of the as-received HDPE matrix material are given in Table 2.1. Figure 2.1 shows the representative image of the as-received HDPE granules and their microstructure. The spherulites/lamellas of different sizes and shapes are observed in the HDPE resin. These spherulites consist of amorphous and crystalline regions, providing ductility and brittleness to the polymer (Kumar 2022). The formation of the most crystalline areas during crystallization makes the polymer brittle, whereas it is ductile in the case of more amorphous regions.

Table 2.1. Typical properties of the HDPE of HD50MA180\* grade.

Property	Test Method	Typical Value	Unit
Melt Flow Index (190 °C/2.16 kg)	ASTM D 1238	20.0	gm/10 min
Density @ 23°C	ASTM D 1505	950	kg/m <sup>3</sup>
Tensile Strength at Yield	ASTM D 638	22	MPa
Elongation at Yield	ASTM D 638	12	%
Flexural Modulus	ASTM D 790	750	MPa
Hardness	ASTM D 2240	55	Shore D
Vicat Softening Point	ASTM D 1525	124	°C

*\*Supplier data sheet.*



Figure 2.1. (a) Representative images of the as-received HDPE granules and its (b) SEM image.

### 2.1.2 Filler

The filler material, functionalized MWCNTs, was procured in the form of powder from Adnano Technologies, Karnataka, India. The MWCNTs were functionalized with a carboxylic group (COOH). The typical properties of the as-received functionalized MWCNTs are given in Table 2.2. Figure 2.2 shows the representative image of the as-received functionalized MWCNTs and its SEM image. They are found to be entangled, randomly oriented, and form a very strong network. The MWCNT network helps transfer stress from the matrix to the fillers, further improving the mechanical properties. Moreover, they will also improve the electrical and thermal conductivities due to these network structures. The non-functionalized MWCNTs exhibit poor interfacial interaction with the matrix, which further limits their potential for reinforcement; hence, the functionalized MWCNTs have been used in the current study to reinforce HDPE (Dabees 2021).

Table 2.2. Typical properties of the functionalized MWCNTs\*.

Property	Typical Values
Purity	~ 99 %
Outer Diameter	10-30 nm
Inner Diameter	5-10 nm
Length	> 10 $\mu\text{m}$
Surface Area	110-350 $\text{m}^2/\text{g}$
CNT content	~ 95%-99 %
Bulk Density	140 $\text{kg}/\text{m}^3$
Chemical Formula	C
Physical Form	Very Light Powder, Fluffy
Odour	Odourless
Colour	Black

\*Supplier data sheet.

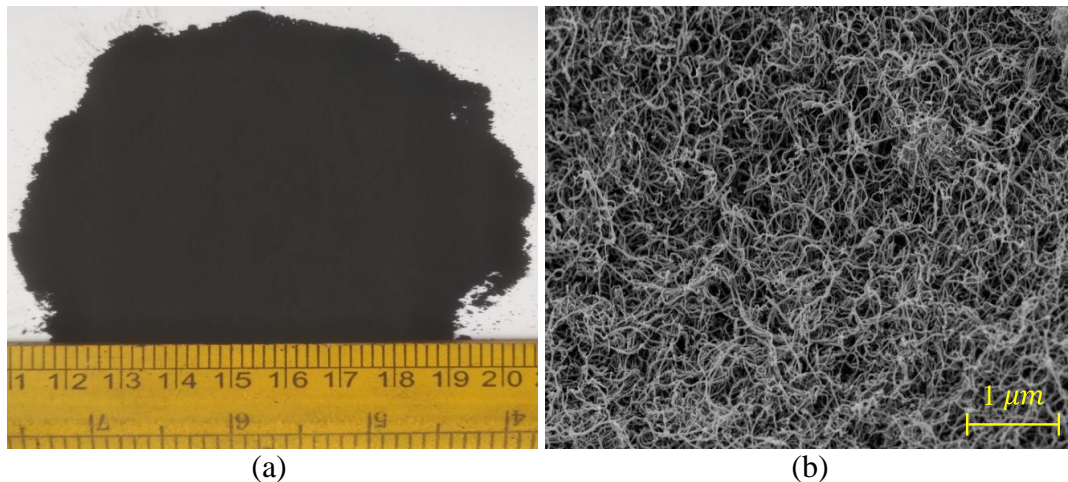


Figure 2.2. (a) Representative image of the as-received functionalized MWCNTs powder and its (b) SEM image.

## 2.2 Nanocomposite development

The nanocomposite of the HDPE and the functionalized MWCNTs are developed using a counter-rotating twin screw Brabender (model-16CME SPL, make-western company Keltron CMEI, Germany). A representative image of the Brabender is shown in Figure 2.3a. Initially, the functionalized MWCNTs are weighed and mixed manually into the HDPE granules. The mixture is placed in a hot air oven for 24 hours

at 100 °C to eliminate any moisture content. The blending temperature of the Brabender is set to 210 °C and left to stabilize. The warm mixture is fed through the Brabender's feeding zone (Figure 2.3b) after stabilizing the temperature, and the functionalized MWCNTs/HDPE nanocomposites (in pellet form) are obtained at the blending speed of 10 rpm. The functionalized MWCNTs are varied at 0.5%, 1%, 3%, and 5% by weight in the HDPE matrix, labelled as H0.5, H1, H3, and H5 for the further representation. The developed H5 nanocomposite is presented in Figure 2.3c. The filler loadings were selected based on the literature. The MWCNTs lower than 0.5% exhibit no significant viscoelastic behavior change, and higher than 5% result in non-uniform dispersion and agglomeration in the HDPE (Amoroso et al. 2020). The blending temperature and the speed are chosen based on the pilot study (Bharath Kumar et al. 2016). In the pilot study, an initial set of parameters is taken based on the literature/material properties, and the blending process is started. The developed nanocomposite is analysed for the filler distribution and interfacial bonding between the filler and the matrix through SEM to ensure the nanocomposite quality. If defects like improper filler distribution, agglomeration, or interfacial de-bonding are found in the developed nanocomposite, then the associated parameter is varied, and the process is repeated. This process continues till the proper nanocomposite is obtained (Kumar 2022). The utilized Brabender has two counter rotating type extruders (Figure 2.3b). The mechanical mixture of the HDPE and the functionalized MWCNTs are fed between the extruders, where it is subjected to shear stresses to achieve uniform filler distribution. These shear stresses are only responsible for properly compounding the constituent materials. An appropriate shear stress is required to properly compound the constituent materials, which can be obtained by regulating the blending speed. The blending speed of 10 rpm provides the appropriate shear action to the feed materials to compound them properly, which was obtained through a pilot study (Bharath Kumar et al. 2016).

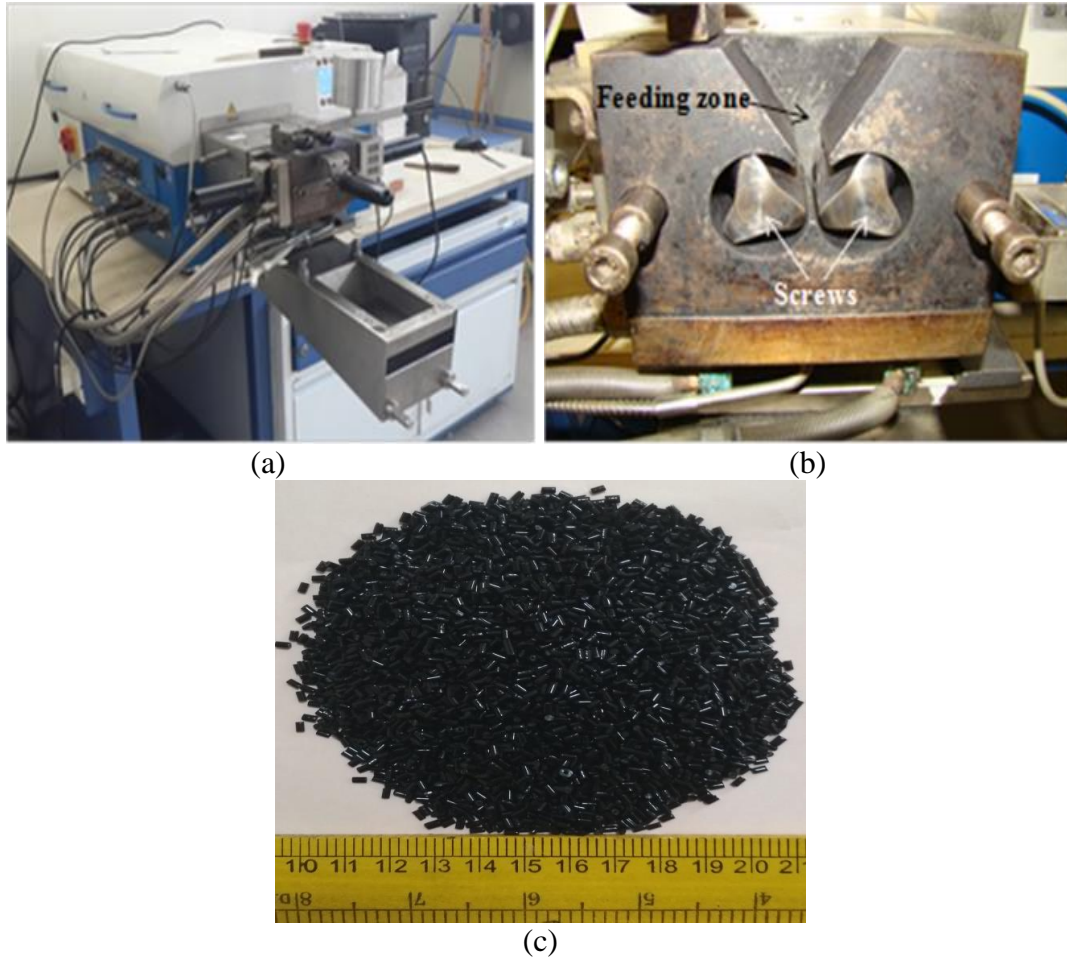


Figure 2.3. (a) Representative image of the Brabender, (b) mechanism of blending and (c) the developed H5 nanocomposite.

### 2.3 Nanocomposite filament extrusion

The extrusion is a continuous process preferably used to produce films, tubes, and filaments. It is accomplished by an extruder consisting of a feed zone, heating zone, die section, water bath, and take-off roller unit. In this process, the material is first fed into the hopper attached to a barrel with a single screw. Additionally, thermocouples and electric heaters are attached to this barrel. The material is fed into the hopper, which is guided by the single screw into the heating zone, where the thermocouples detect the barrel's current temperature. The material melts when it reaches the heating zone, and is forced out of the die by the action of a single screw. This material is pulled out of the die by the take-up unit and stretched, and then it is passed through a water bath to quench the extruded filament. In the current work, a single screw extruder of 25SS/MF/26 model, provided by Aasabi Machinery Pvt. Ltd., Mumbai, having screw flight length to its outside diameter ratio as 25:1, die

diameter of 2 mm, and three heating zones (feed, transition, and die) is used to extrude the nanocomposite filaments. The nanocomposite pellets are pre-heated at 85 °C for 24 hours. The barrel temperatures are fixed to 145-150-155-145 °C (H S et al. 2020) (from feed section–die section). The pre-heated nanocomposite pellets are fed into the hopper of the extruder, and the filament of  $2.80\pm 0.05$  mm is extruded by maintaining screw speed and the take-up unit speed to 25.1 rpm and 11.8 rpm, respectively. At least five samples are randomly cut from the different sections of the produced filament, and the diameter is measured using a micrometer screw gauge.  $2.85\pm 0.05$  mm filament is the most common filament used by manufacturers/industries (H S et al. 2020, Jayavardhan 2017) in a 0.8 mm nozzle 3D printer. The 3D printer (DE500, Deltasys E Forming, Belgaum) used in this study has a nozzle diameter of 0.8 mm, which takes the filaments of 2.85 mm. The H3 nanocomposite extruded filament having a constant diameter ( $2.85\pm 0.05$  mm) is shown in Figure 2.4. The extruded filaments (H-H5) are further used as the input material in the 3D printer to obtain the desired printed samples. The schematic representation of the single screw extruder and the currently used extrusion setup are shown in Figure 2.5 and Figure 2.6, respectively. The specifications of the single screw extruder used for filament extrusion are given in Table 2.3.



Figure 2.4. Extruded H5 nanocomposite filaments.

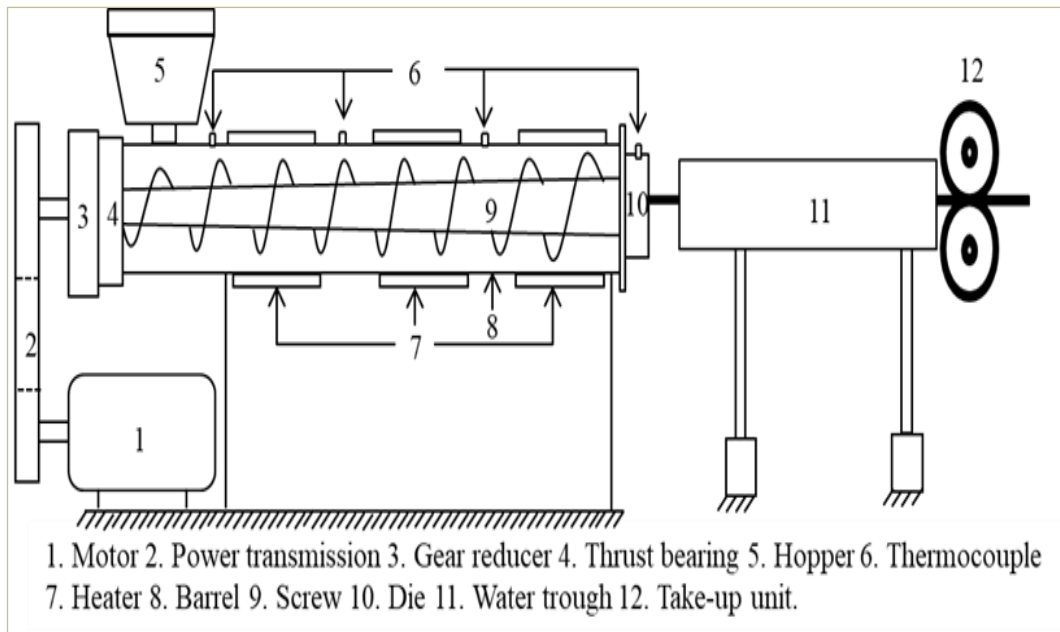


Figure 2.5. Schematic representation of the single screw extruder.



Figure 2.6. Experimental setup of the single screw extruder used in the current work.

Table 2.3. Specifications of the single screw extruder.

Specification	Details
Cooling	Water cooling
Die sizes	1.75 mm, 2.5 mm, and 3 mm
Drive	3 HP ACVF Drive, Max. RPM 60
Heaters	Ceramic in SS cover, 4 nos. with load up to 5 kW
Heating control panel	PID controllers with 5 zones, Accuracy $\pm 1^\circ\text{C}$ , Max. Temp. $450^\circ\text{C}$
Hopper	Min. 3 Kg, SS sheet with discharge chute
Make and Model	Aasabi Machinery (P) Ltd. Dombivli, Mumbai, India. (25SS/MF/26, L/D ratio of 25:1)
Pelletizer	Helical type, minimum 4" dia. $\times$ 4" L with 0.5 HP ACVF drive.
Screw	High tensile nitride hardened alloy steel to sustainable up to $450^\circ\text{C}$ , Dia. 25 mm with length 26D having uniform discharge.
Spooling arrangement	Take up rollers with 0.5 HP ACVF drive with height adjustments and castor wheels

### 2.3.1 Recycling of nanocomposite filament

There is a large amount of filament wastage while selecting/choosing the suitable extrusion parameters to obtain the filament's desired diameter. In this work, these waste filaments are recycled to reduce plastic waste in the environment. The waste filaments are collected, pelletized, and pre-heated in an oven at  $80^\circ\text{C}$  for 24 hours to avoid moisture content before the recycled filaments are extruded. The first-time extruded filament is designated as 1x filament. The 1x filament is pelletized and fed again to obtain a second-time extruded (2x) filament. The same method is repeated to get the third-time extruded filament, further designated as 3x filament. Figure 2.7 presents the waste extrusion filaments, waste filament pellets, and 3x recycled filament having a consistent diameter.

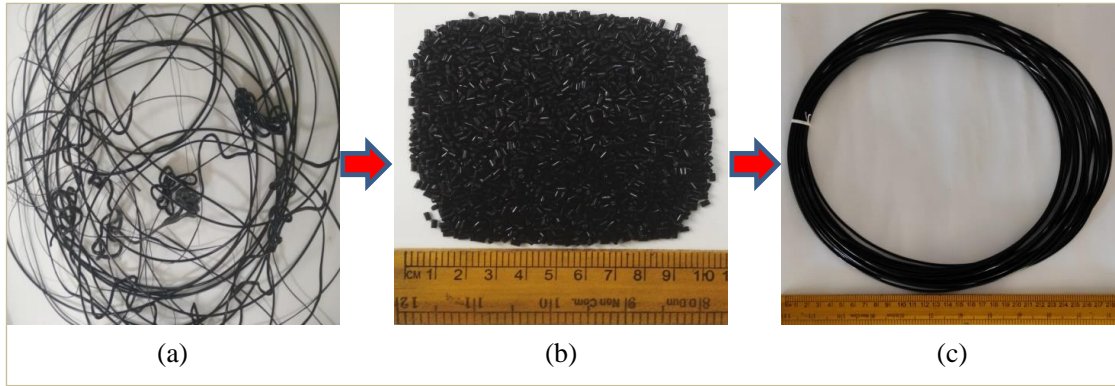


Figure 2.7. Representative images of (a) W/UR filament, (b) pellets of W/UR filaments and (c) H1-3X recycled filament.

### 2.3.2 Filament regularity check and density measurement

The regularity of the filament cross-section is checked by measuring its diameter and standard deviation. A minimum of five samples from different filament zones of extruded filaments are taken for diameter measurement. The mean/average diameter ( $\bar{d}$ ) is calculated using (Kumar 2022),

$$\bar{d} = \frac{\sum d_i}{n} \quad (1)$$

and the standard deviations ( $\sigma$ ) are estimated through (Kumar 2022),

$$\sigma = \sqrt{\frac{\sum (d_i - \bar{d})^2}{n}} \quad (2)$$

The measurement of the filament density and the prints are carried out using the ASTM D792-20. The theoretical density of the filaments and the prints are calculated with the help of the rule of mixture (Kumar 2022).

### 2.4 3D printing of NCs and FGNCs

In the current work, 3D printing, an emerging and cutting edge manufacturing method, is used for sample preparation. A commercial FFF technology based 3D printer (Aha 3D, Jaipur, India) with 2 nozzles ( $\varnothing$  0.8 mm) is used for 3D printing. The schematic representation of the FFF 3D printer is shown in Figure 2.9, while the FFF 3D printer set up with the console is shown in Figure 2.10. The detailed technical specifications of the FFF 3D printer are mentioned in Table 2.5. The 3D printer comprises two brass nozzles connected to the heating block, gear, and encoder unit. The gear and the encoder unit regulate the extrusion rate of the feedstock material coming through the nozzles. In the case of critical structures printing, one nozzle

builds the main part, while the second nozzle builds the support. The printing chamber consists of a fixed glass bed embedded with heating elements. The loading spools of the main part and the support materials are hung for easy access. The display unit of the machine keeps track of the printer head movement in the different X, Y, and Z directions with the help of the independent stepper motors. In the current work, the H-H5 extruded filaments are utilized for 3D printing of HDPE, NCs, and FGNCs. First, the CAD file of the sample is made and converted into .STL (stereolithography) file. The .STL file is sliced and transformed into G-code file with the help of slicing software (Simplify3D), and subsequently imported into the 3D printing machine. The suitable printing parameters, as presented in Table 2.4 (Kumar 2022, 2023, 2023, 2022), are set in the machine. Once the set nozzle temperature is reached and stabilized, the filament is loaded to initiate 3D printing of the NCs. The 3D printed samples are named H-H5 printed samples. The printing parameters are selected based on the defect-free prints. The defects such as raster gap, over extrusion, under extrusion, bulge formation, over-heating, warpage, voids, and surface roughness should not be present in the prints as they affect their mechanical properties. The prints are obtained by varying the defect-associated parameter and keeping the other parameters constant. As the defect is eliminated and confirmed through careful observation, the parameter is chosen as suitable. A similar procedure is followed for the other defect-associated parameters. Once the 3D printing of NCs is concluded, printing of FGNCs is initiated. Again, as mentioned earlier, the CAD file of the specimen has been prepared and converted into .STL file. Subsequently, the .STL file is sliced, and only the printing thickness for different gradations is defined for each nozzle (N1 and N2). The file is converted into G-code and imported to the 3D printer. The printing parameters are set, and then both of the nozzles are loaded with the appropriate filaments. 3D printing of two gradations is initiated. Once the two compositions are printed, the printer is paused for 30 seconds, the nozzle is moved up to a height of 10 mm for clearance between the nozzle tip and the print followed by loading of the third composition filament into the first nozzle. Then, the printing is resumed from the same position to get three different gradations. In the current study, two different graded nanocomposite variants (FGNC-1 and FGNC-2, shown in Figure 2.8a) are 3D printed using the suitable printing parameters,

mentioned in Table 2.4. The FGNC-1 represents H0.5-H1-H3 graded material, whereas the FGNC-2 represents H1-H3-H5 graded material. There are possibilities for many composite gradations, such as 2/3/4/5. Still, 3-composite gradations (near to average composition value) have been considered for the investigation in the current study. All the H-H5 NCs, FGNC-1, and FGNC-2 are 3D printed at room temperature with Y-orientation on Kraton™ SEBS FG1901 tape with 100% infill and permitted to cool up to the room temperature for obtaining warpage-free prints (Bharath 2020, 2020). The total thickness (h) of the FGNCs is divided by the number of compositions (c) to determine the thickness of each graded layer in the FGNCs (Kumar 2023). The top and the thickness views of the FGNC-2 flawlessly 3D printed sample are shown in Figure 2.8b. The 3D printed NCs and FGNCs are HDPE matrix based NCs, which encounters a very common issue known as warpage during printing of the samples. The warpage is due to excessive thermal stresses between the deposited layers, which can be minimized by optimizing the printing parameters (printing speed, bed temperature, and chamber temperature). Moreover, the warpage can be eliminated by choosing suitable filler material having a lower coefficient of thermal expansion (CTE), which further reduces the CTE of the composite, leading to less thermal stress, resulting in a reduced warpage (Kumar 2022). However, in this work, the warpage has been eliminated by optimizing the printing speed. The samples are printed using varying printing speeds (25-30 mm/s (Kumar 2022)), and the warpage was observed. No warpage was found at the printing speed of 30 mm/s. The printing speed is directly correlated to the thermal gradient between the deposited raster and the subsequent raster to be deposited, which becomes the primary reason for the thermal stresses between the layers. The higher printing speed provides less cooling time for the deposited raster before the next raster is deposited, leading to less temperature drop of the deposited raster, resulting in less temperature gradient, reducing the thermal stresses, and ultimately the less warpage.

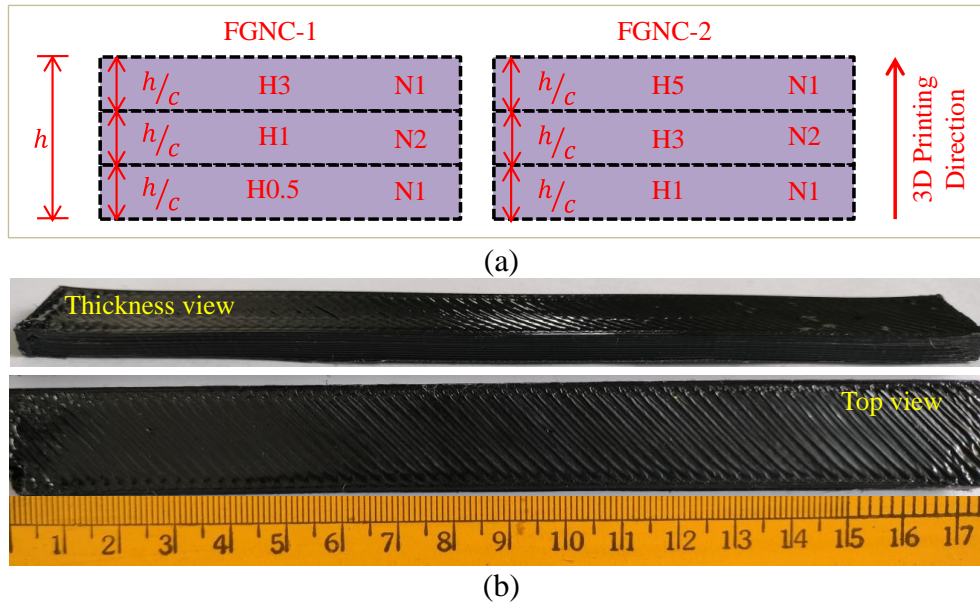


Figure 2.8. (a) Thickness of each graded layer ( $h/c$ ), printing direction, and nozzle used for FGNCs printing and (b) 3D Printed FGNC-2 sample.

Table 2.4. Printing parameters used in the current work.

Parameters	Values taken during experiment
Nozzle temperature ( $^{\circ}\text{C}$ )	200-220 [ <b>200</b> ] <sup>#</sup>
Layer height (mm)	0.30-0.50 [ <b>0.50</b> ]
Printing speed (mm/s)	25-30 [ <b>30</b> ]
Extrusion multiplier	0.90-1.0 [ <b>0.95</b> ]
No. of outlines	3
Raster angle	$\pm 45^{\circ}$
Raster pattern	Rectangular
Infill	100%

<sup>#</sup>Values in brackets represent optimized parameters.

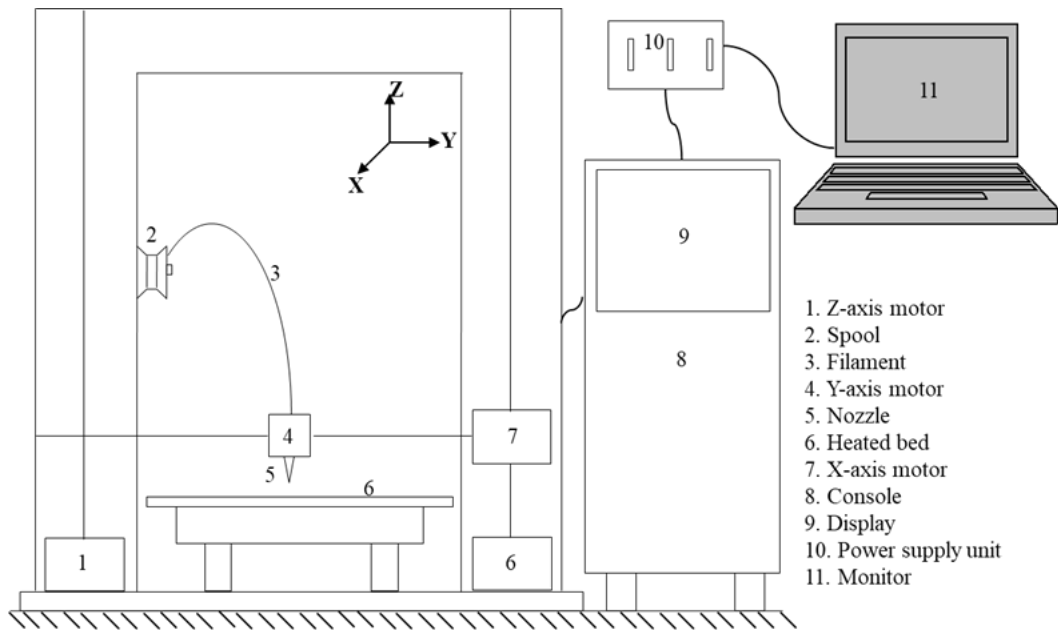


Figure 2.9. Schematic representation of FFF 3D printer.

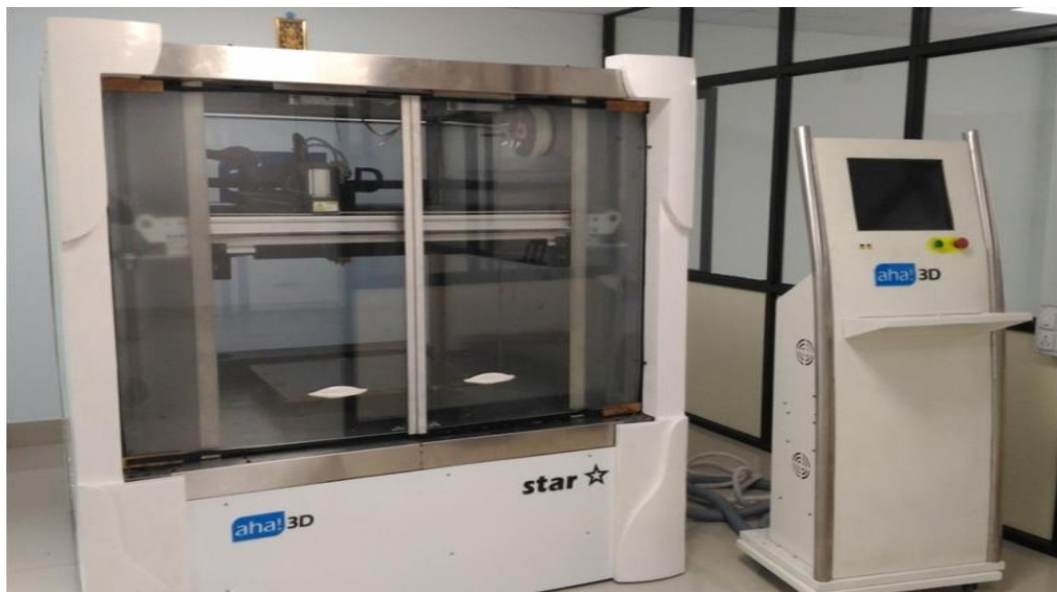


Figure 2.10. Representative image of the FFF 3D printer used in the current work.

Table 2.5. Specifications of the FFF 3D printer.

Specification	Details
Build chamber	Up to 100 °C
Build platform	Up to 150 °C
Build volume	500 × 500 × 500 mm <sup>3</sup>
Data import format	STL, AMF, OBJ
Filament diameter	3 mm (Standard)
Layer height	100 to 500 microns
Make and model	Aha 3D Innovations Pvt. Ltd., Jaipur, Model: Star
Maximum extrusion temp.	Basic tool head: 300 °C, Standard tool head: 500 °C
Number of extruders	2
Positional accuracy	50 micron (stepper), 20 microns (servo), 4 microns (dual servo)
Power requirement	220V AC, three phases
Printing materials	All engineering thermoplastic and Plastic Composites, ABS, HIPS, PC, Nylon, TPU, TPE, Carbon fiber composite, etc.
Rate of production	Basic tool head: up to 15 cm <sup>3</sup> /hr., Standard tool head: Up to 150 cm <sup>3</sup> /hr.
Screw	High tensile nitride hardened alloy steel to sustainable up to 450 °C. Suitable compression ratio (at least Dia. 25 mm with length 26D) having a uniform discharge at metering zone.
Technology	Fused Filament Fabrication (FFF)
Tool head cooling	Liquid cooled.
Workstation compatibility	Windows XP, Windows 7, Linux

## 2.5 Obtaining suitable 3D printing parameters

The suitable printing parameters are selected based on the defect-free prints. The defects such as raster gap, over extrusion, under extrusion, bulge formation, overheating, warpage, voids, and surface roughness, should not be present in the prints as they affect their mechanical properties. The non-uniform material flow, surface rubbing, over melting, surface roughness, etc., are some common issues observed during 3D printing. Therefore, a pilot experiment was conducted on the essential parameters such as extrusion multiplier, layer height, printing speed, and printing temperature to finalize the suitable printing parameters. The samples printed at 0.90, 1.0, and 0.95 extrusion multipliers, keeping nozzle temperature constant, are shown in Figure 2.11. It can be seen that the samples printed at 0.90 and 1.0 extrusion multipliers show the extrusion (Figure 2.11a) and over extrusion (Figure 2.11b) issues, respectively, whereas the sample printed at 0.95 extrusion multiplier shows a uniform flow of the material (Figure 2.11c). Therefore, a 0.95 extrusion multiplier is chosen for 3D printing all the samples. The inadequate distance between the nozzle tip and the specimen produces a surface rubbing, which can be resolved by selecting an adequate layer height. The samples are printed at 0.30 mm, 0.35 mm, and 0.50 mm layer height, respectively. The samples printed at 0.30 mm (Figure 2.11d) and 0.35 mm (Figure 2.11e) layer height showed the rubbing of the surface, whereas 0.50 mm (Figure 2.11f) layer height showed specimen without rubbing. The printing temperature is crucial for perfect specimens, and an improper selection of printing temperature leads to overheating issues. 3D printing at 210 °C and 220 °C nozzle temperatures led to overheating issues, as shown in Figure 2.11g and Figure 2.11h, respectively. The printed samples shown in Figure 2.11c and Figure 2.11f are the perfect specimens without any defects. Therefore, the parameters corresponding to these perfect samples are considered as suitable printing parameters, and all the functionalized MWCNTs/HDPE based NCs and FGNCs are 3D printed using the same suitable parameters, given in Table 2.4.

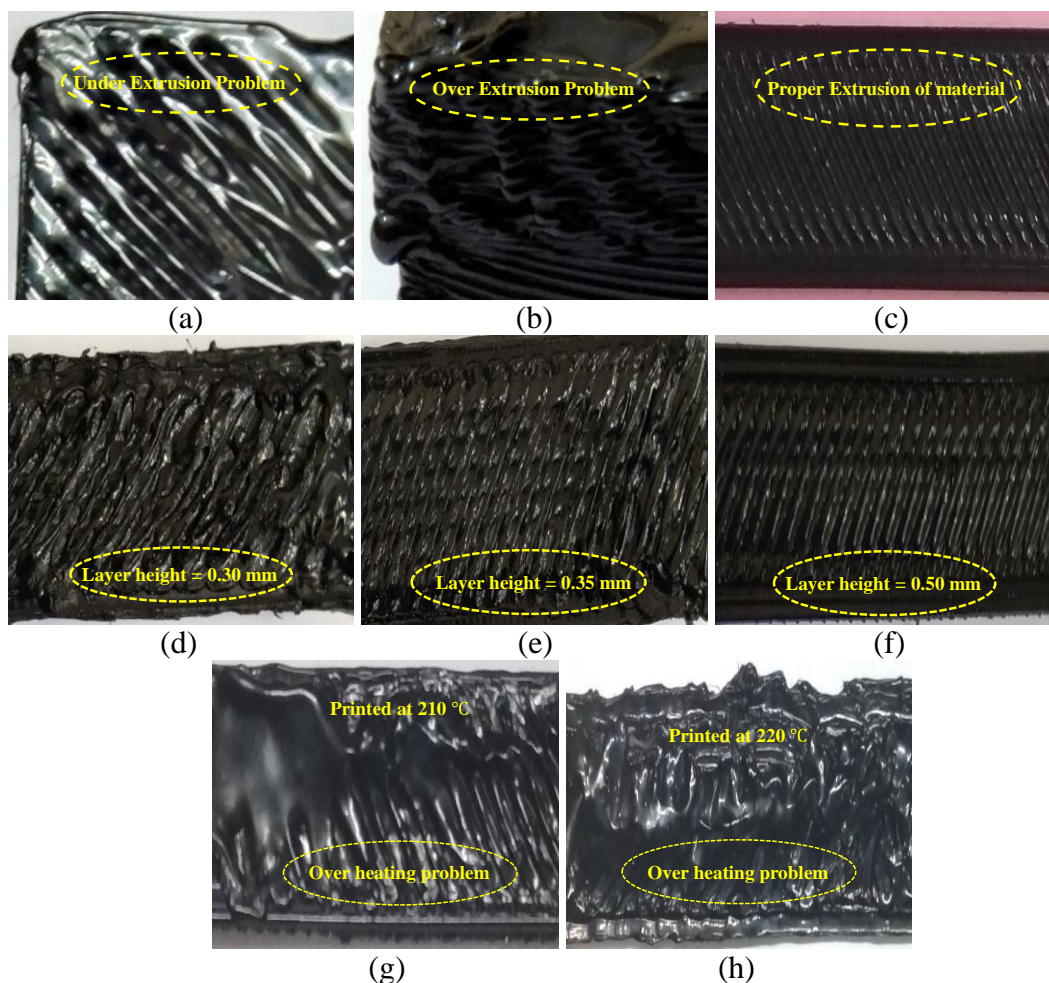


Figure 2.11. Different challenges in 3D printing, (a)-(b) extrusion problems, (c) proper extrusion of material, (d)-(e) rubbing problems, (f) defect free print and (g)-(h) over heating issues.

## 2.6 Melt flow Index

The addition of the functionalized MWCNTs into the HDPE matrix affects the melt viscosity of the nanocomposites, which further affects its melt flow behavior. The melt flow behavior of a material is measured through MFI (ASTM D1238-13). The current work uses Dynisco LMI5000 laboratory melt flow indexer (Figure 2.12) for the MFI measurement of the H-H5 nanocomposite pellets. Due to addition of the fillers, the melt viscosity of the nanocomposites increases while the MFI decreases as they are inversely proportional to each other (Beesetty et al. 2020). The extrusion multiplier is a crucial printing parameter in 3D printing. A proper value of the extrusion multiplier is required to print a quality product. The MFI estimation helps in setting the proper extrusion multiplier, which further helps achieve excellent quality prints (H S et al. 2020).

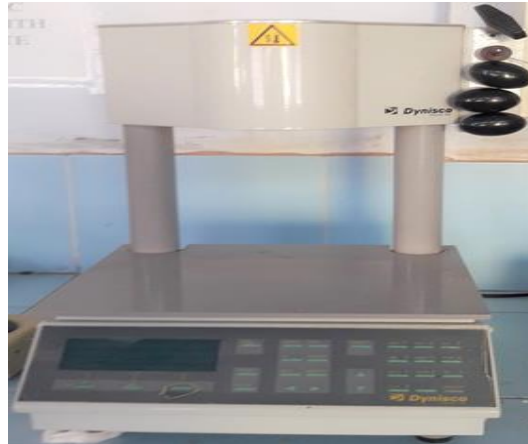


Figure 2.12. Melt flow indexer.

## 2.7 Density measurement

A material's density is a crucial property, which is useful when a composite's void content and weight saving potential are determined. The current work measures the density of the extruded filaments and the printed specimens using Contech analytical balance according to the ASTM D792-13 standard. At least five samples for each composition are tested, and the mean value of the H-H5 samples with their standard deviation is reported. Using the rule of mixture, the theoretical densities of all the compositions are calculated by

$$\frac{1}{\rho_c} = \frac{W_H}{\rho_H} + \frac{W_{CNT}}{\rho_{CNT}} \quad (3)$$

The density of the HDPE and the MWCNTs are considered 950 (Table 2.1) and 140 kg/m<sup>3</sup> (Table 2.2).

## 2.8 Differential scanning calorimetry

The differential scanning calorimetry (DSC) is performed to compute the crystallization and melting responses of the extruded filaments and the printed specimens using NETZSCH DSC 404F1 instrument. Approximately 10 mg of the sample is measured and kept in a 30  $\mu$ l Al crucible. The sample is heated from 25 °C-200 °C, and held at 200 °C for 3 min, then cooled from 200 °C-25 °C, held at 25 °C for 3 min, and again heated from 25 °C-200 °C. The cooling rate is maintained constant at 10 °C/min. The first heating cycle eliminates the residual thermal stresses developed in the prior processing steps. The DSC curve typically provides exothermic and

endothermic peaks.  $T_{Cryst}$  and  $T_{Melt}$  are determined from the cooling and the heating cycles, respectively.  $\alpha_{Cryst}$  is calculated using (Amoroso et al. 2020),

$$\alpha_{Cryst} = \frac{\Delta H_m}{(1-W_{CNT})\Delta H_m^*} \times 100 \quad (4)$$

where,  $\Delta H_m$  and  $\Delta H_m^*$  = heat of fusion of the samples and 100% crystalline HDPE polymer (293 J/g), respectively (Divya et al. 2013).

## 2.9 Thermogravimetric analysis

The thermogravimetric analysis (TGA) is carried out to estimate the thermal stability (degradation temperature) of the neat HDPE and the NCs using Exstar TG/DTA 6300 instrument as they undergo high temperature (nozzle temperature - 200 °C) during 3D printing. About 10 mg sample is kept in an aluminum pan and loaded in the chamber, where it is heated from 25 °C to 700 °C in a nitrogen environment at the rate of 10 °C/min (Dabees et al. 2021).

## 2.10 Rheology

The rheological investigation (dynamic oscillation frequency sweep) is performed at 150 °C (strain rate-5%) in the 0.1-10 Hz frequency range using a Discovery Hybrid Rheometer-2, TA instruments. The coupons are 3D printed with a thickness of 1 mm and a diameter of 25 mm to observe the effect of the functionalized MWCNTs on the viscoelastic behavior of the HDPE (H S et al. 2020).

## 2.11 X-ray diffraction

The crystallinity of the filaments and the printed samples is measured using Malvern PANalytical, Netherlands (Model-Empyrean 3rd Gen) fitted out with Cu  $\alpha$  radiation at 40 mA and 45 kV using a Nickel filter. The samples are scanned at a 2°/min speed from 10° to 80° ( $2\theta$ ) angle (Kumar 2022).

## 2.12 Tensile test

The tensile test (crosshead displacement rate-5 mm/min, initial load-0.1 MPa) of the filaments and the printed specimens is done as per the ASTM D638-14 standard using a Zwick Roell universal testing machine (UTM). The filament was fixed in the cardboards. In order to attach the sample to the cardboard, two channels-50 mm long and three filament diameters wide are cut through the top layer, leaving the corrugated

portion intact. The channels are then filled with epoxy, and the filament is laid across them with 10 mm ends that overhang the frame. By comparing the length of the overhanging before and after the test indicates if the filament has slipped through the same frame during the pulling phase, which did not happen in the present investigation. The covers are successively fastened on the channel's top using the same epoxy before testing (Bellini et al. 2003). An extensometer having a gauge length of 2-inch is used for the strain measurement. By tensile testing of the specimens, the yield point was confirmed. To measure the Poison's ratio, corresponding to the yield point, the longitudinal strain was measured using a 2- inch extensometer, and the specimen's final width was measured using a Vernier caliper. The lateral strain was calculated using the final width of the specimen using (5). Finally, the Poison's ratio was calculated using (6) for each composition and reported in the present study.

## 2.13 Flexural investigation

### 2.13.1 Experimental

A flexural test (cross head displacement rate-2.56 mm/min, preload-0.1 MPa) is performed on the printed samples (span length to depth ratio-16:1) according to the ASTM D790-17 standard. At least five samples for each composition have been tested for the filaments and the printed specimens, and the mean value of the H-H5 samples with the standard deviations is presented.

$$\text{Lateral strain} = \frac{b_f - b_i}{b_i} \quad (5)$$

$$\text{Poison's ratio} = - \frac{\text{Lateral strain}}{\text{Longitudinal strain}} \quad (6)$$

Flexural Modulus ( $E_f$ ) is computed using,

$$E_f = \frac{L^3 m}{4bd^3} \quad (7)$$

Flexural stress ( $\sigma_f$ ) is estimated using,

$$\sigma_f = \frac{3PL}{2bd^2} \quad (8)$$

### 2.13.2 Numerical

In the current study, the finite element method (FEM) has been used to analyse the flexural stresses and the deflections of the printed NCs (H0.5-H5) and the FGNCs

(FGNC-1 and FGNC-2) through ANSYS 2015. First, the NCs are simulated. The material is modelled using the material's elastic properties such as elastic moduli (H0.5→824, H1→849, H3→1030, and H5→1290 MPa (Kumar 2022)) and Poisson's ratio (H0.5→0.4587, H1→0.4559, H3→0.4486, and H5→0.4429 (Kumar 2022)). The meshing is carried out using SHELL 181 elements with 4 nodes and 6 DOF at each node with 3240 elements and 3439 nodes to obtain the FE model. The FE model of the flexural sample is shown in Figure 2.13a. Then, the boundary conditions and the load (as per the experiment) are applied to the FE model, as presented in Figure 2.13b, and the problem is solved. The same procedure is followed for the FGNCs. The stresses in the x-direction, Von-Mises stresses, and the deflection outcomes are extracted from the simulation and compared to the experimental data.

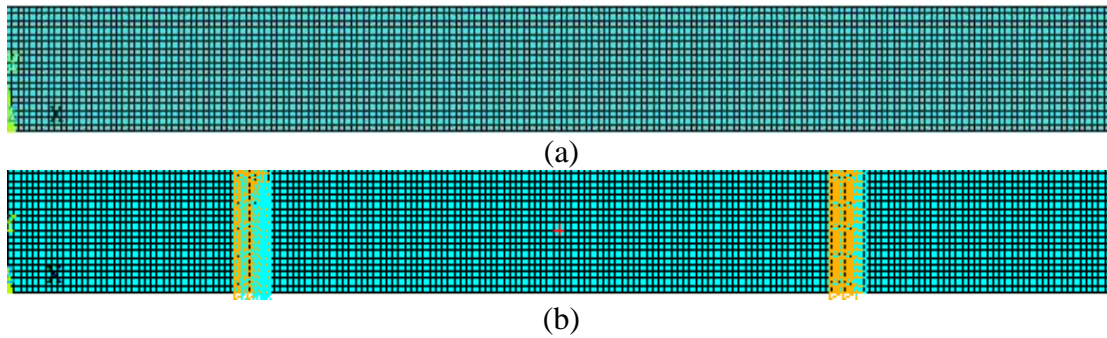


Figure 2.13. (a) FE model and (b) simply supported boundary condition.

## 2.14 Hardness

The Rockwell's hardness of the 3D printed specimens is estimated using a Zwick Rockwell hardness tester as per ASTM D785-08 (M scale, penetrator size-6.35 mm and major load-100 kg). The test specimen is placed on the Anvil, and the major load is released to obtain the hardness number. The sample's surface is maintained perpendicular to the tip of the indenter during testing (Saber-Samandari 2009).

## 2.15 Impact test

A Charpy impact test is performed on the 3D printed specimens of dimension  $55 \times 10 \times 10 \text{ mm}^3$  having a V-notch of  $45^\circ$  angle to estimate the material's toughness (Dabees 2021). The arm length and the weight of the pendulum are 40 cm and 2 kg, respectively. The sample is fixed in Anvil, and the weight is released freely from a height of 380 mm from the notch side.

## 2.16 Compression test

The specimens having dimensions of  $25 \times 25 \times 6 \text{ mm}^3$  are tested for the compression responses (ASTM C365/C365M-16) using a 20 kN load-cell Zwick Roell universal testing machine. The test specimen is fixed between the fixtures, all the parameters are set, and the test is performed at 0.5 mm/min. The specimens' yield strength is determined using the 0.2% offset technique, and the energy absorptions are computed using the equation below (Jeyachandran 2022, Kumar 2022). The results of the five specimens of each composition are taken for each test, and the mean value is reported.

$$\text{Energy absorption} = \int_0^{\epsilon} \sigma d\epsilon \quad (9)$$

where,  $\sigma$  = peak stress and  $\epsilon$  = peak strain.

## 2.17 Mechanical buckling

There is no specified ASTM standard for mechanical buckling experiments of 3D printed samples. Therefore, the specimens of 210 (span length)  $\times$  12.5 (width)  $\times$  4 (thickness)  $\text{mm}^3$  dimension are considered for the mechanical buckling investigations in accordance with Euler Bernoulli's beam theory (Bharath 2020, Dileep 2021). The buckling test is performed on a minimum of five samples for each configuration/composition using Tinius Olsen UTM (H75KS, UK, Load cell-50 kN). The experimental setting of the test is presented in Figure 2.14. The samples are fixed at both ends, and axial compressive load is gradually applied at 0.2 mm/min speed for conducting the test. The shift in buckling responses from the pre-buckling to the post-buckling is carefully investigated by 0.6 mm end-shortening (Bharath 2020). The test is stopped once the sample is buckled, and the load-deflection data are obtained. The  $P_{cr}$  is obtained using the load-deflection data from UTM through DTM and MBC approaches (Bharath 2020, Dileep 2021). In the DTM method, one tangent is drawn on the pre-buckling curve, and another is drawn on the post-buckling curve. The load corresponding to the meeting point of both tangents gives  $P_{cr}$  of the sample. In the MBC method, one tangent is drawn on the pre-buckling curve and another is drawn on the post-buckling curve then a bisector is drawn on the curve for the angle between the two tangents. The load corresponding to the intersection point gives the  $P_{cr}$ . The graphical approaches, the DTM and the MBC methods to calculate  $P_{cr}$ , have been presented in Figure 2.15. The similar procedure is used for testing all the 3D printed

NCs and FGNCs. The results from the DTM and MBC methods and the comparison between them are reported. The  $P_{cr}$  evaluated from the DTM and the MBC method is respectively assumed as the upper and lower critical buckling loads (Dileep 2021).

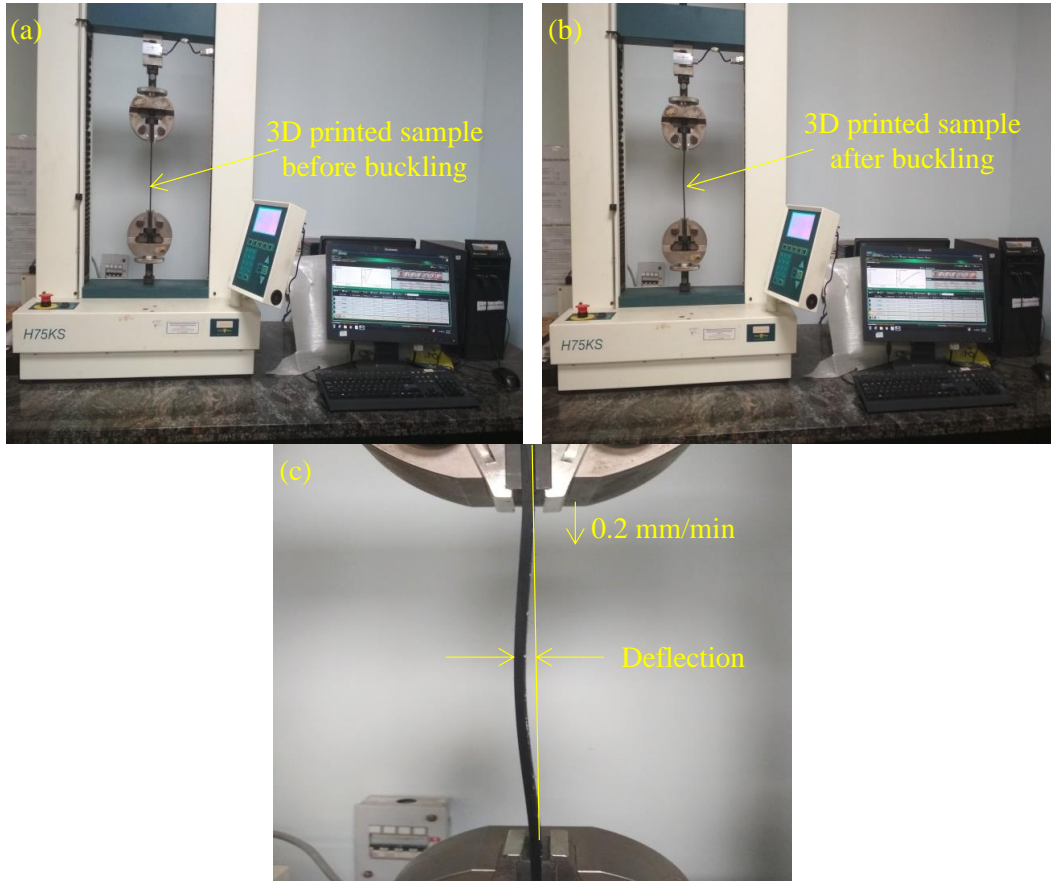


Figure 2.14. Experimental setup showing (a) pre-buckling, (b) post-buckling and (c) buckled/deflected shape of the 3D printed sample.

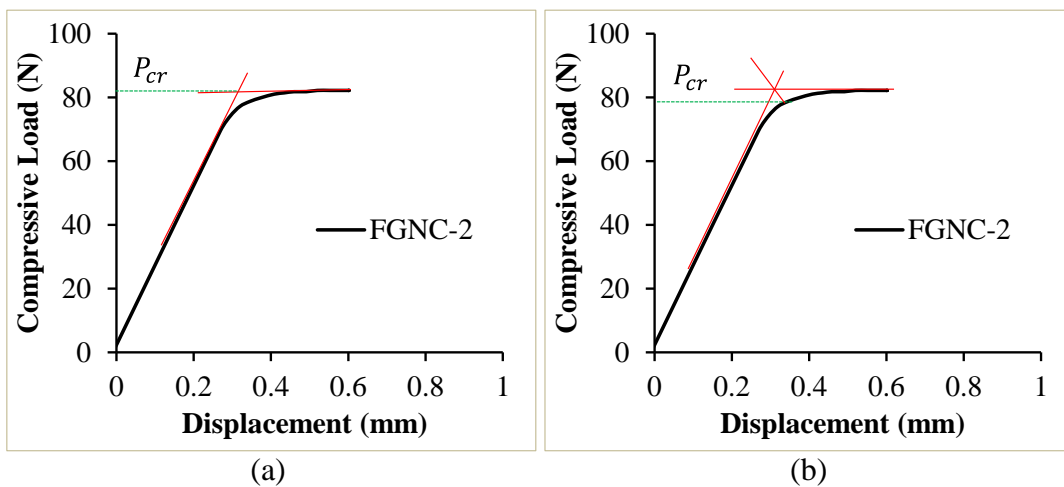
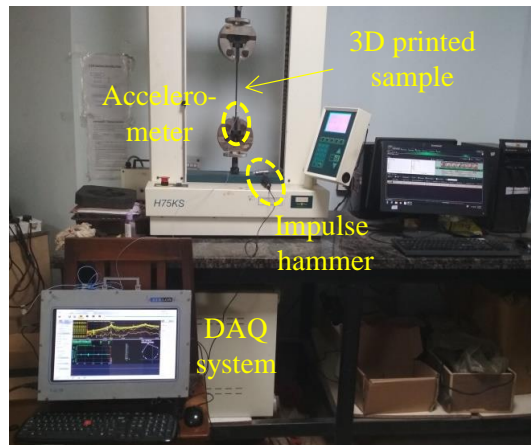


Figure 2.15. (a) DTM and (b) MBC for calculating  $P_{cr}$  from load-deflection curve.

## 2.18 Free vibration

The experimental modal analysis of the 3D printed HDPE, NCs, and the FGNCs, having the same dimension as used for buckling specimens, is conducted to estimate their first three natural frequencies ( $f_n$ ) and the corresponding damping factor. The experimental setup and the schematic representation of the free vibration test are shown in Figure 2.16. A uniaxial accelerometer (8778A500, sensitivity-10 mV/g) attached to the specimen with the help of bee's wax is utilized to capture the vibration signals generated by an impact hammer (9722A2000, Kistler, sensitivity-10 mV/N). The sample having ten marking points for excitation is clamped at both of the ends in the UTM, and the test is carried out with a 20 N force increment to analyse the natural frequencies along with the corresponding damping factor, with 2 min pause in between the test, for each load increment (Bharath 2020). The sample is tapped/hammered at all marked points under the particular loading condition, and the generated vibrations are captured using DEWESoft software. Ten channel-based data acquisition (DAQ), vibration results, and the time-dependent applied compressive load are fed to the DEWESoft as input data. The DEWESoft converts the time to frequency domain signals utilizing the Fast Fourier transformation method (Dileep 2021). This frequency response corresponding to the impulse excitation at several marked points captures FRF (frequency response function). The DEWESoft software renders frequency, associated mode shape, and the damping factor. The FRF, mode shape, and the mode circle obtained from the modal analysis (experimental) are presented in Figure 2.17. The modal damping factor is determined based on the circle fit approach using below equation (Dileep 2021).

$$\varepsilon = \frac{\omega_2^2 - \omega_1^2}{2\omega_0 \left[ \omega_2 \tan \frac{\alpha_2}{2} + \omega_1 \tan \frac{\alpha_1}{2} \right]} \quad (10)$$



(a)

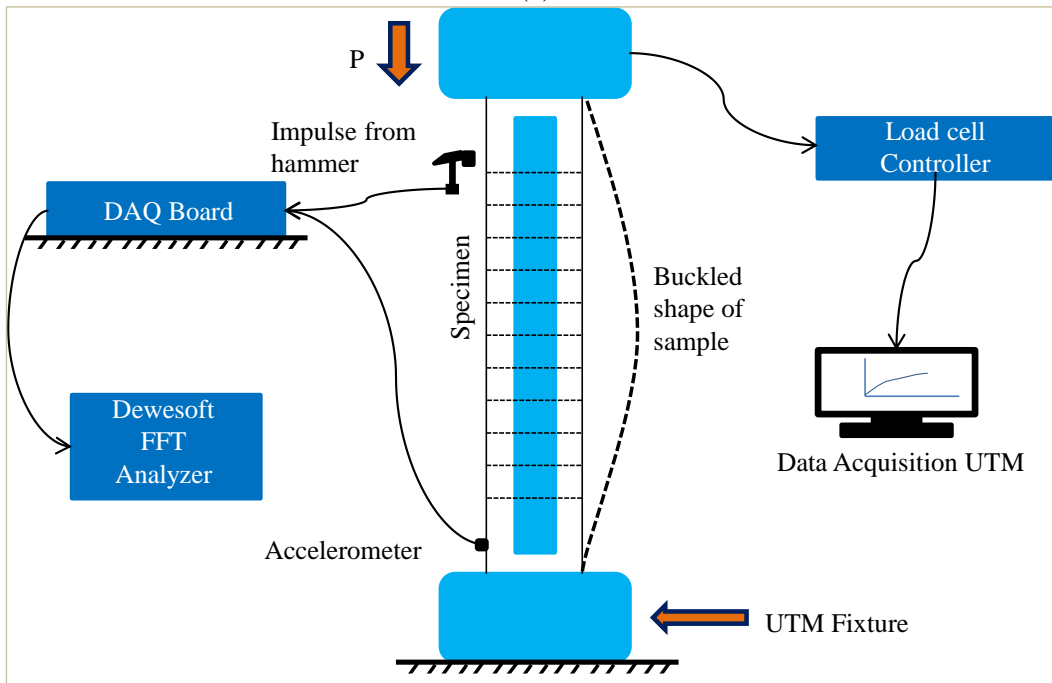


Figure 2.16. (a) Experimental setup and (b) the schematic representation of free vibration test.



Figure 2.17. DEWESoft software showing FRF, mode shape and mode circle in the experimental modal analysis.

## 2.19 Vibration correlation technique

The  $P_{cr}$  of the additively manufactured HDPE, NCs, and FGNCs are also estimated using the vibration responses through vibration correlation technique (VCT). The VCT is a non-destructive test for estimating the  $P_{cr}$  with the help of the vibration response. In the VCT, the experimental frequency is obtained corresponding to the load applied that is lower than the  $P_{cr}$ . The curve between the squared values of the fundamental frequency and the compressive load is plotted. Then, the plot is extrapolated using the second-order polynomial expression given in the below equation to evaluate the  $P_{cr}$  (Bharath 2020, Dileep 2021).

$$\left(\frac{f}{f_n}\right)^2 = 1 - \frac{P}{P_{cr}} \quad (11)$$

## 2.20 Numerical analysis of mechanical buckling and free vibration

The current work uses ANSYS software to perform the mechanical buckling and modal analysis of the 3D printed samples using finite element analysis (FEM). The material is first modelled using the elastic properties such as Poisson's ratio and elastic modulus. Then, the geometry of the sample is created and discretized into a number of elements to get a finite element model with the help of a 4-noded

SHELL181 element having 6 degrees of freedom (DOF) at each node and meshed with 212 elements and 270 nodes. The boundary condition (both ends clamped) and the compressive load are applied to the FE model, and the static analysis (linear) is performed. The eigenvalue buckling studies are carried out from which the primary buckling mode shape is deduced. The buckled form of the FE model is updated. The non-linear static analysis is further performed to obtain the non-linear load-deflection responses using the primary mode shapes with GIF (geometric imperfection factor - 0.0001 to 0.001). The numerical buckling loads are evaluated using the MBC and DTM methods, and compared with the corresponding experimental values. After the mechanical buckling analysis, a modal investigation is performed to simulate the free vibration of the 3D printed specimens. The densities are used for the modal analysis. Further, the same procedure is followed. A modal analysis is performed after the linear static analysis under no load condition. The first three  $f_n$  and the corresponding mode shapes are obtained, and compared with the experimental frequencies.

### **2.21 Coefficient of thermal expansion**

The CTE of the 3D printed samples of  $75 \times 12.7 \times 3 \text{ mm}^3$  dimension is measured using the dilatometer (CIPET, Chennai) as per the ASTM E228 standard. The thermal strain and dimensional stabilities of the 3D prints are qualitatively estimated through the CTE values.

### **2.22 Thermal buckling**

A thermal buckling test is conducted to analyse the buckling behavior of the printed HDPE and the nanocomposites under different non-uniform thermal loads. An in-house experimental setup (Figure 2.18) is developed for performing the thermal buckling test. In this experimental setup, the beam is subjected to clamped boundary conditions by fixing it in a steel frame and tightening it with the Allen bolts so that the motion at the beam ends is restricted due to the applied thermal load. The thermal load is applied using the 230 V/1000 W short-wave and single-tube infrared (IR) heaters. To subject the beam under non-uniform heating, the IR- heater is positioned at one end of the beam in case-1 (Left-edge heating), the centre of the beam in case-2 (centre heating), and at both ends of the beam in case-3 (Left and Right edge heating) as shown in Figure 2.19. To measure the lateral deflection of the beams MVL7 model

of linear variable differential transducer (LVDT) with  $\pm 25.4$  mm stroke length is used. This LVDT can operate between  $-50$  °C to  $125$  °C temperature range. The thermal sensors are fixed to the sample to measure the temperature at different positions as per the desired temperature profile study. The Lab view code is employed to control the on and off condition of the IR heater as per the set point and the current temperature reading. The temperature versus deflection data was taken as output using the NI9481 DAQ, and the  $T_{cr}$  is obtained corresponding to the point from where the beam loses its stiffness and starts deflecting.

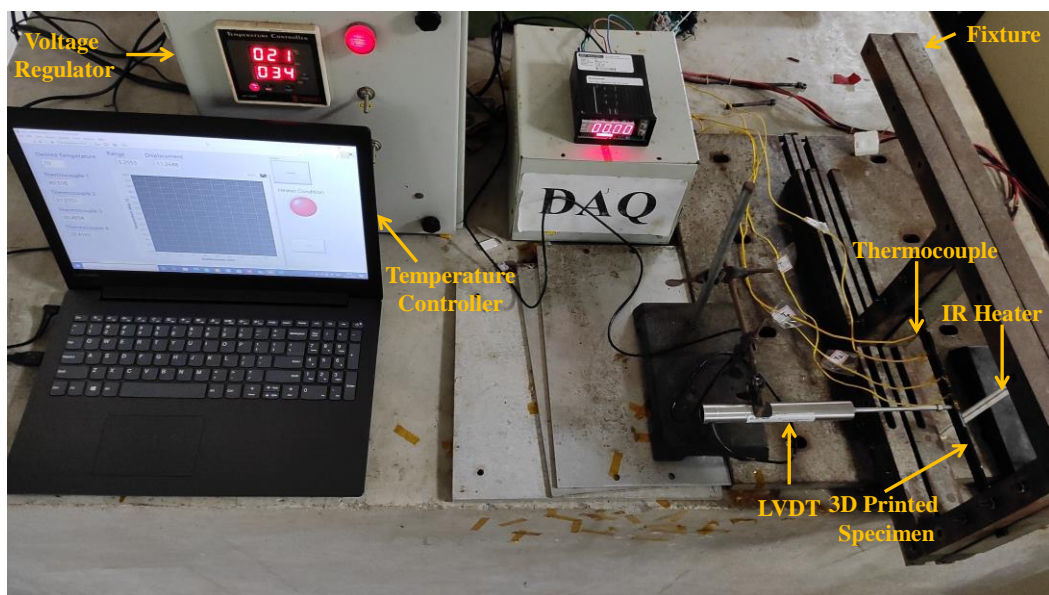


Figure 2.18. Representative image of in-house experimental set up for thermal buckling test.

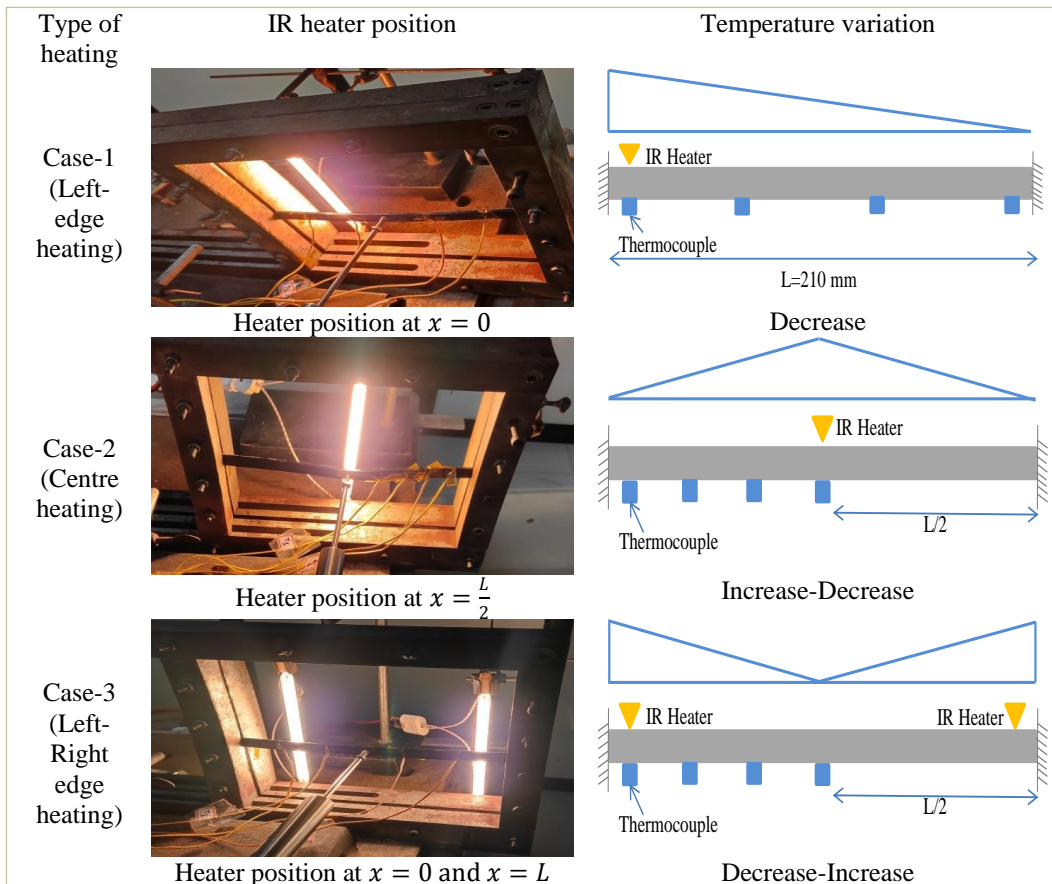


Figure 2.19. Representative images of different types of non-uniform heating, and the corresponding IR heater position and the temperature variation.

### 2.23 Microstructural analysis

The microstructure of the sample is analysed through scanning electron microscopy (SEM) (ZEISS, EVO MA18 SEM instrument). The samples were first gold sputtered, and then the images were taken. To show the distribution of the MWCNTs in the HDPE of the developed NCs, extruded filaments, and the 3D printed NCs and FGNCs, the sample is first freeze-fractured, and then the SEM images were taken on the fractured surface. The as printed samples are freeze-fractured and then analysed through the SEM. The tested samples are frozen in liquid nitrogen and then fractured (if not failed during the test) for the SEM analysis.

### 3 BASIC MATERIAL CHARACTERIZATION

#### 3.1 Blended nanocomposites

The functionalized MWCNTs and the HDPE are blended using a Brabender to develop nanocomposites. In any composite, the fillers are incorporated to enhance the matrix properties because the matrix is generally inferior in the performance in practical applications, while the fillers have superior properties than the matrix. To achieve the full potential of the fillers, they must be able to distribute homogeneously in the matrix. Therefore, in the first step, the developed nanocomposites are characterized for the filler inclusions and their distribution in the matrix.

##### 3.1.1 Scanning electron microscopy

The SEM technique is employed to examine the fillers' distribution/homogeneity in the developed nanocomposite. The SEM images of the developed H5 nanocomposite are presented in Figure 3.1. It is observed that the functionalized MWCNTs are homogeneously distributed in the HDPE. The HDPE resin surrounds the MWCNTs due to its functionalization. Generally, adding the CNTs into polymers renders their agglomeration (Dabees 2021). However, in the current study, no such agglomeration effect is observed up to the addition of 5% MWCNTs. The perfect distribution and coating of the functionalized MWCNTs without any agglomeration is attributed to the utilization of the suitable processing parameters (blending speed-10 rpm and temperature-210 °C) in the blending process.

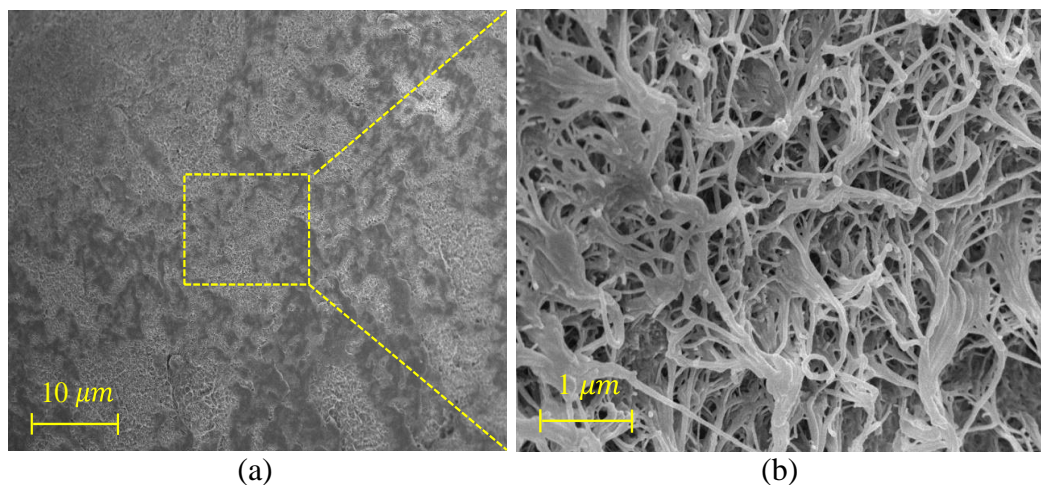


Figure 3.1. SEM images of the developed H5 nanocomposite, showing uniform distribution and network structure of the functionalized MWCNTs.

### 3.1.2 Melt flow index

The blended NCs have to be utilized in the extrusion and printing processes, which are, in fact, melting and cooling based processes, where the material has to melt and flow properly for successful extrusion and printing. Therefore, the feed material's melt flow behavior becomes crucial in the extrusion and 3D printing, which is examined by measuring its MFI values. The MFI value of the HDPE is 24.80 g/10 min, and for the H0.5-H5, it is observed as 21.20, 16.40, 15.20, and 12.00 g/10 min. The MFI variation with the MWCNTs is shown in Figure 3.2. The MFI reduces in the range of 14.52-51.60% for H0.5-H5 NCs compared to the HDPE. Adding the MWCNTs into the HDPE resists the polymer chain mobility and increases the melt viscosity. The melt viscosity is inversely proportional to the MFI; increased melt viscosity lowers the MFI value (Escócio et al. 2015). The MFI can be correlated to the material flow behavior through the nozzle in the 3D printer. An extrusion multiplier in the 3D printer controls the material flow through the nozzle. The lower MFI results in less material flow through the nozzle and vice versa. The lower MFI is compensated by increasing the extrusion multiplier. An appropriate value of the extrusion multiplier needs to be set for the proper amount of the material flow through the nozzle, especially for the NCs of higher filler loadings, to avoid under and over extrusion issues in specimens. The appropriate value of the extrusion multiplier is obtained using the measured MFI value of the NCs, which is further optimized through pilot study.

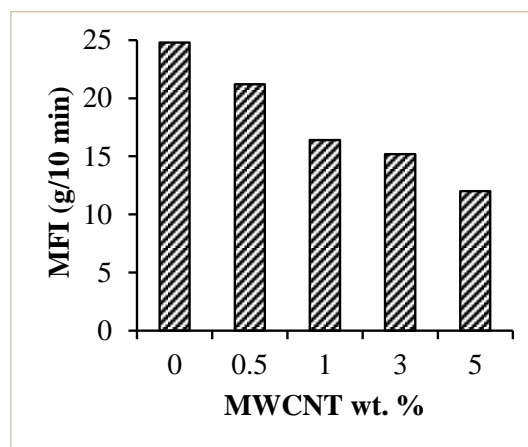


Figure 3.2. MFI of the blended nanocomposites.

### 3.1.3 Thermogravimetric analysis

The blended NCs have to be utilized in the filament extrusion, and the extruded filaments must be utilized in the sample printing. The filament extrusion and samples printing are carried out at very high temperatures, where the polymer matrix may degrade. A sudden loss in the weight of the material has been observed when the functional temperature crosses its material degradation temperature (Yu et al. 2010). Therefore, the material's degradation temperature is crucial to predict its degradation before it is used in the high temperature operations such as the extrusion and printing. The TGA thermograms of the neat HDPE and the NCs are presented in Figure 3.3a. The HDPE, H0.5, H1, H3, and H5 degradation temperatures are 396.68 °C, 439.23 °C, 446.80 °C, 466.53 °C, and 479.07 °C, respectively. Figure 3.3b shows that the degradation temperature of the NCs increases with the MWCNTs loading, which is ascribed to the inclusion of the stiffer MWCNTs. Moreover, the degradation temperature of the NCs is higher than the HDPE, which shows the enhancement in the thermal stability of the NCs (Dabees et al. 2021). The degradation of the neat HDPE and the NCs started at 395 °C and continued to around 480 °C (Figure 3.3a). The neat HDPE and the NC specimens have been printed at 200 °C nozzle temperatures (Table 2.4), which is lower than their degradation temperatures, confirming no material degradation during the 3D printing.

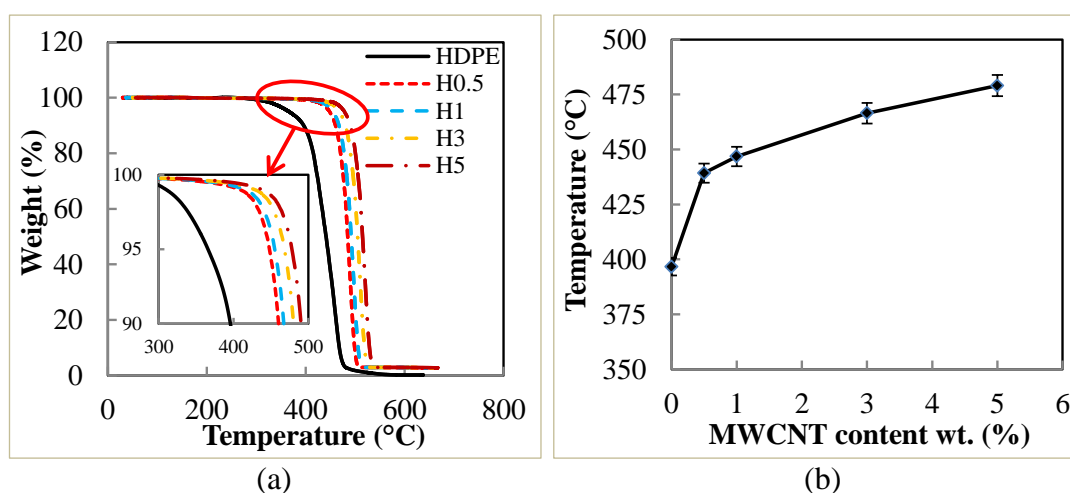


Figure 3.3. TGA responses of MWCNT/HDPE NCs (a) weight loss (%) with temperature and (b) variation of decomposition temperature with MWCNTs content.

## 3.2 Extruded nanocomposite filaments and 3D printed samples

### 3.2.1 SEM

The developed nanocomposites are utilized for extruding nanocomposite filaments, which are first characterized through the SEM before using in the printing process. The SEM image of the extruded H5 nanocomposite filaments is shown in Figure 3.4. A perfect coating, uniform distribution, and nicely formed network structures are found in the filaments, indicating the perfect selection of the extrusion parameters. The reorientation of the polymer chains and the fillers is possible due to the subsequent melting and cooling in the extrusion process. The change in the fillers and the polymer chains orientation can be ensured by measuring the density of the developed nanocomposite pellets (before extrusion product) and the extruded filaments (after extrusion product) as the orientation change affects the density. The density of the H0.5-H5 extruded filaments is found to be higher than the respective nanocomposite pellets (Kumar 2022), confirming the change in the density of the pellets and the filaments, which further confirms that the orientation of the fillers changes due to the subsequent cooling and melting in the extrusion process. Finally, the NC and FGNC samples are realized and characterized by the SEM to examine layer bonding/delamination, material diffusion, and the filler distribution. To check the outer layer bonding, the SEM is done on the thickness of the 3D printed FGNC-2 sample, while to examine the internal layer and material bonding, the sample is first frozen and then fractured to obtain its cross-section, which is then analysed through the SEM. The SEM images of the as printed FGNC-2 sample are presented in Figure 3.5. It is observed that each layer is seamlessly diffused into each other without voids and delamination, as observed in Figure 3.5a (SEM image of the deposited layers of the printed samples). Also, the fractured cross-section images show the seamless adhesion of the different layers and the materials (H1-H3-H5, Figure 3.5b). At the lower magnification, the MWCNTs are not visible (Figure 3.5b). Hence, the middle region of the H5 printed layer of the FGNC-2 sample (indicated in Figure 3.5b) is magnified, where the MWCNTs are observed in uniformly distributed and nicely formed network forms (Figure 3.5c). These 3D printed FGNC-2 sample

characteristics confirm the chosen parameters' suitability for the sample printing (Kumar 2023, 2022, 2023, 2022, 2023, 2023).

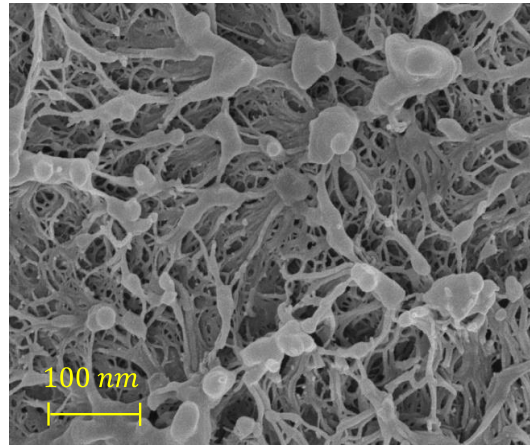


Figure 3.4. SEM image of the extruded H5 nanocomposite filament, showing uniform distribution and network structure of the functionalized MWCNTs.

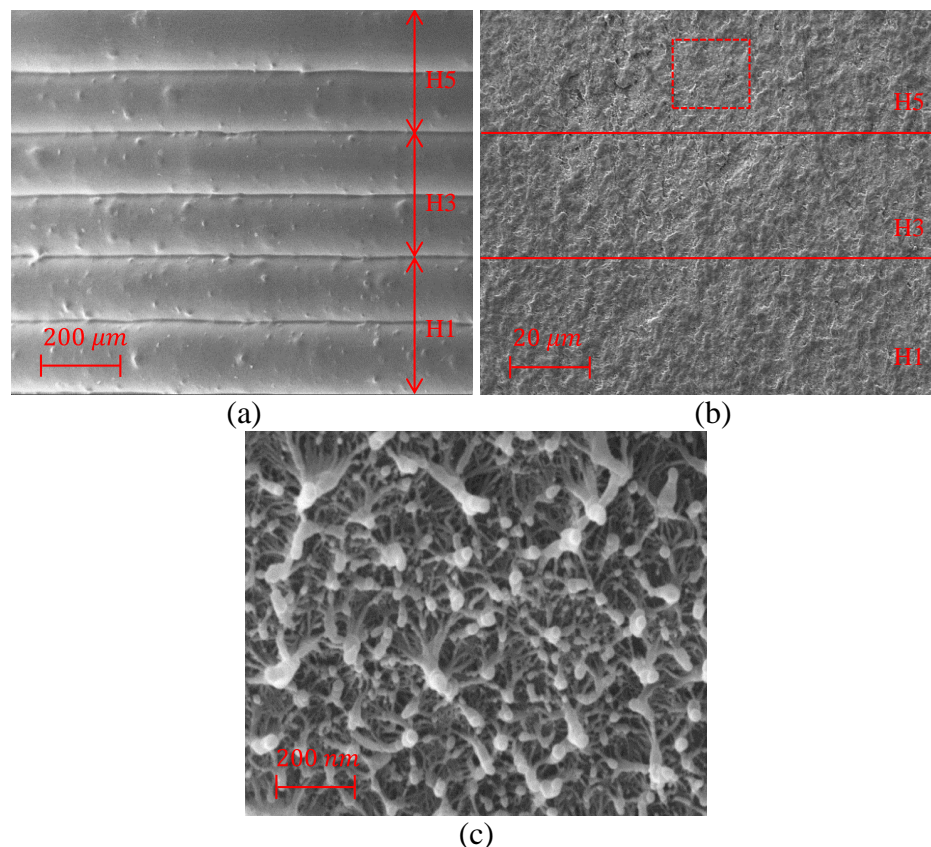


Figure 3.5. SEM images of the FGNC-2 3D printed sample: (a) thickness showing seamless diffusion of each printed layer, (b) cross-section of freeze-fractured sample showing seamless materials diffusion and porous free printing, and (c) uniform distribution and network structure of the functionalized MWCNTs in the H5 layer of FGNC-2 (magnified image of the marked region of Figure 3.5b).

### 3.2.2 Rheology

Generally, it has been observed that the researchers report only good SEM images to show the filler distribution, even if they are not distributed on the whole surface of the sample. Hence, another qualitative and reliable technique must be employed to show the fillers distribution in the matrix. Rheology is a material characterization technique that can be utilized to investigate the fillers homogeneity qualitatively. In this study, the rheology (frequency sweep) of all the printed NCs (H0.5-H5) and the FGNCs is performed for the qualitative analysis to assess the distribution of the filler (including up to which extent) and their rheological percolation. The fillers dispersion in a matrix is directly correlated to the change in  $\eta^*$  of the composite. In contrast, the dispersion's extent and the distribution correlate to the viscosity power law index at low frequency (the steeper the slope-the better the filler dispersion (Pötschke 2013)). The percolation threshold is estimated by the change in  $\eta^*$ ,  $E'$ , and  $E''$  of the composites concerning frequency (Amoroso et al. 2020). Due to the changes in the rheological behavior and the formation of the percolated system, the composites display pseudo-solid-like behavior, revealing a dramatic increase (several order) in  $\eta^*$  and  $E'$  at low frequency. The rheological responses of the HDPE, NCs, and FGNCs are shown in Figure 3.6. It is observed that  $\eta^*$  for the NCs slightly increases as the functionalized MWCNTs content increases up to 0.5% and then dramatically increases for 5% (almost two orders) at the low frequency by maintaining a steeper graph (Figure 3.6a), confirming the well dispersion of the MWCNTs in the HDPE. The increase in  $\eta^*$  with the filler loading can be attributed to the increased resistance (functionalized MWCNTs) to the polymer chain movement. For the FGNCs, the similar behavior of  $\eta^*$ , exhibiting a steeper graph, is obtained, showing the better filler distribution than the NCs, further improving their mechanical properties. In the 3D printing of the FGNCs, the higher filler content (HFC) layer is deposited on the lower filler content (LFC) layer. The LFC layer has more polymer content than the HFC layer. During the solidification process of the deposited layers, only the polymers participate in the layer adhesion, not the fillers. The more polymer participants, the more adhesion between the layers of the different compositions, and hence, the more strong layer bonding, which reflects through the shear viscosity and mechanical properties. Therefore, the  $\eta^*$  of the FGNCs is higher and stiffer than the NCs. The  $E'$  is the measure of the ability of a

material to store elastic energy. It was observed to be increased by four orders of the magnitude after the percolation threshold (0.5%) at low frequency, indicating the percolated network formation of the functionalized MWCNTs (Figure 3.6b), which further confirms their uniform distribution in the matrix (Amoroso et al. 2020). The  $E'$  and frequency curves tend to plateau at higher frequencies ( $>10$  rad/s), indicating the formation of the percolated networks of the MWCNTs in the matrix, resisting the polymer chains movement and rendering 'pseudo-solid-like' behavior (Amoroso et al. 2020). A significant improvement in the  $E'$  of the nanocomposites and their graded variants is observed with the inclusion of the MWCNTs compared to the HDPE at low frequency, attributing to the inclusion of the nano-sized and stiffer fillers in the matrix. Compared to the NCs, the FGNCs have shown an improved  $E'$ . This might be due to an effective stress transfer due to the material gradation. The  $E''$  is the measure of a material's ability to dissipate energy (Doddamani 2020), and observed to be increasing for the NCs at low frequency when the MWCNTs concentration increases (Figure 3.6c). The increase in the  $E''$  is governed by the uniform dispersion of the MWCNTs in the HDPE. The FGNCs also shows a similar behavior but exhibited to higher  $E''$  than the NCs due to the material gradation. The  $E''$  is just a representation of the viscous component of the viscoelastic material, but cannot show the energy dissipation potential of a material alone. The material's energy dissipation ability is represented by damping factor or loss factor (ratio of  $E''$  and  $E'$ ), as presented in Figure 3.6d. At the low frequencies, the damping of the prints decreases with the MWCNTs loading and the material gradation, respectively, due to increase in the filler inclusion, which has the ability to absorb more energy. The FGNCs are observed to have higher  $E'$  and  $E''$  and lower damping properties than the NCs, exhibiting superior viscoelastic behavior.

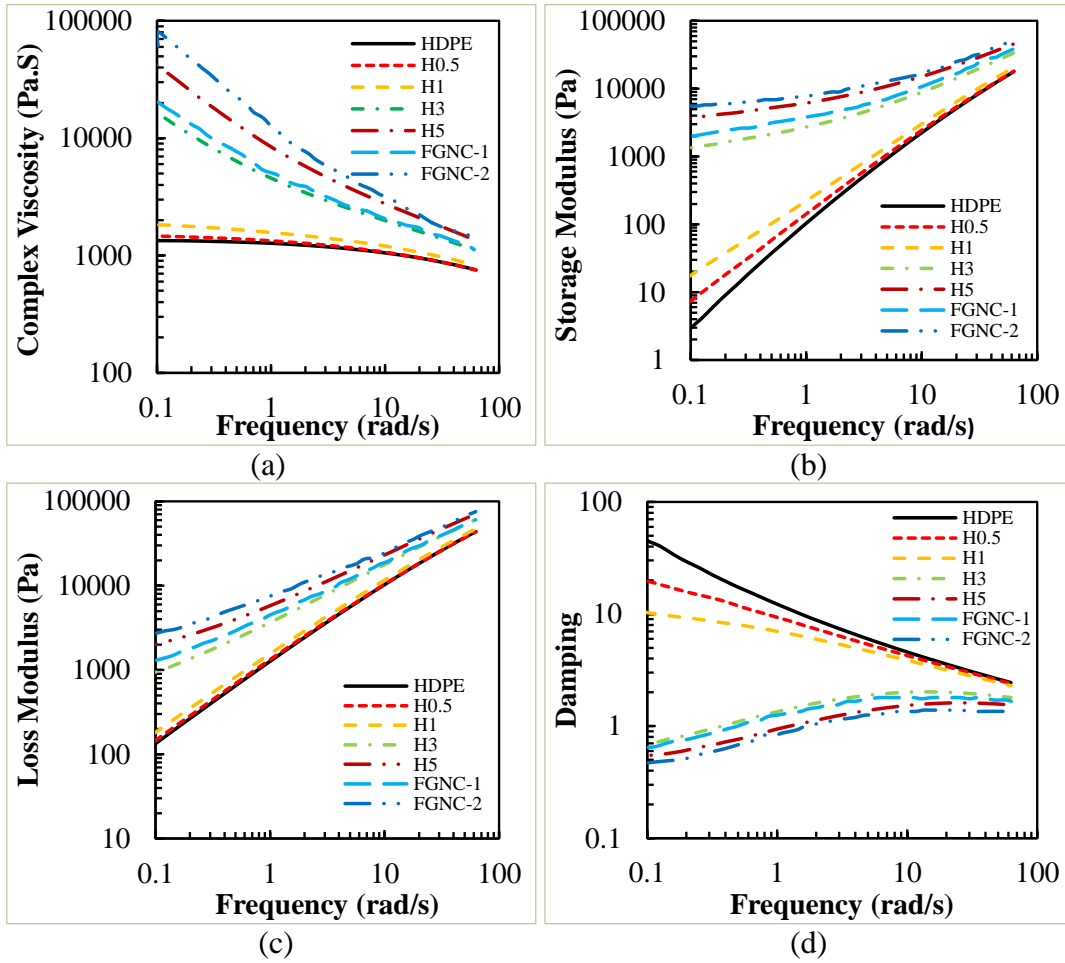


Figure 3.6. Rheology results: (a) complex viscosity, (b) storage modulus, (c) loss modulus, and (d) damping of 3D printed HDPE, NCs, and FGNCs.

### 3.2.3 Density

The quality of the filament is crucial for good quality prints. In this research, the filament quality is determined through the density, DSC, and the tensile test. The densities of the H-H5 filaments and the printed specimens are given in Table 3.1. Including the MWCNTs in the HDPE decreases the density of the filaments and the printed specimens. This is due to the MWCNTs having a lower density than the HDPE. The H5 has registered the lowest density among all the NCs for both filaments and the specimens, and it is 16.06% and 15.58%, respectively, lower than the HDPE. This is because of the highest content of the MWCNTs in the HDPE. The density of the printed samples is observed to be higher than the filaments. The printed specimens are allowed to cool to the room temperature after 3D printing, where they get enough time for crystallization. In contrast, the filaments are immediately quenched in a water bath after extrusion, with insufficient time for crystallization. The theoretical and

experimental densities of the H-H5 filaments and the printed specimens are very close, showing they are dense and free from the porosity (Beesetty et al. 2020). Figure 3.7 shows the micrographs of the printed freeze-fractured H3 specimens at lower and higher magnifications. It is visible that the specimens are dense and free from the porosity. The uniform distribution of the MWCNTs in the HDPE matrix is seen (Figure 3.7c). The experimental density of the printed FGNCs is mentioned in Table 3.1. It can be observed that the density of the pure HDPE is  $948.08 \pm 6.04 \text{ kg/m}^3$ , while for the FGNC-1 and FGNC-2, it is  $896.14 \pm 3.07$  and  $834.46 \pm 4.19 \text{ kg/m}^3$  respectively. It is observed that the density of the 3D printed FGNC samples decreases with the MWCNTs gradation than the HDPE. This is attributed to the increased MWCNTs gradation in the FGNC, which has a density lower than the HDPE. The weight saving potential of the 3D printed FGNC-1 and FGNC-2 are calculated to be 5.48% and 11.98%, respectively, compared to the HDPE. The 3D printed FGNC-2 sample exhibited the lowest density with the weight saving potential of  $\sim 12\%$ , showing its potential to improve the fuel efficiency of automotive, marine, and aerospace vehicles.

Table 3.1. Physical properties of the samples.

Composition	$\rho_{th}$ (kg/m <sup>3</sup> )	$\rho_{exp}$ (kg/m <sup>3</sup> )		Weight saving potential (%)	
		Filament	Specimen	Filament	Specimen
HDPE	950.00	947.12 $\pm$ 7.61	949.00 $\pm$ 9.45	-	-
H0.5	923.90	929.24 $\pm$ 5.36	931.57 $\pm$ 8.76	1.88	1.84
H1	898.04	898.32 $\pm$ 6.23	902.77 $\pm$ 4.48	5.15	4.87
H3	809.49	881.98 $\pm$ 8.71	886.35 $\pm$ 6.35	6.88	6.60
H5	736.84	795.03 $\pm$ 4.56	801.13 $\pm$ 2.12	16.06	15.58
FGNC-1	877.14	-	896.14 $\pm$ 3.07	-	5.48
FGNC-2	814.79	-	834.46 $\pm$ 4.19	-	11.98

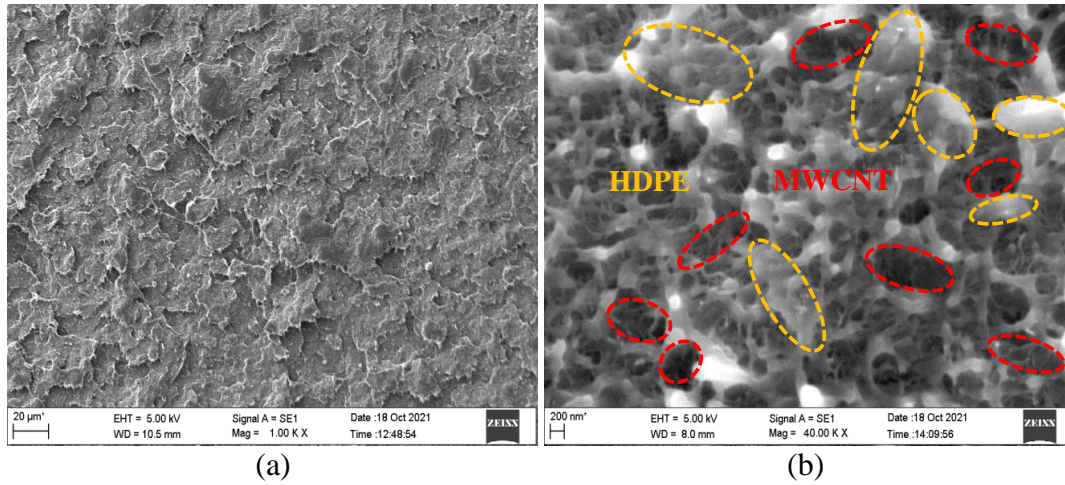


Figure 3.7. Micrographs of the freeze fractured H3 specimen at (a) lower and (b) higher magnifications.

### 3.2.4 DSC

The printing temperature is one of the crucial parameters in 3D printing, and it is decided based on the material's melting temperature. The thermal study is carried out using DSC, which provides  $T_{Melt}$ ,  $T_{Cryst}$  and  $\alpha_{Cryst}$ . Table 3.2 and Figure 3.8 list the DSC results and curves of the filaments and the printed specimens, respectively. For the filaments,  $T_{Cryst}$  increases with the MWCNTs addition up to 0.5 wt.% loading and then decreases for the higher loadings compared to the HDPE. During the cooling process, the nucleation of the HDPE melt begins on the MWCNTs surface. At low filler loadings,  $T_{Cryst}$  increases due to the heterogeneous nucleation effect while at the higher MWCNTs loadings,  $T_{Cryst}$  decreases because of the confinement effect of the MWCNTs network formation, which inhibits the nucleation of the polymers (Amoroso et al. 2020). All the filaments and the printed specimens have exhibited the higher  $T_{Cryst}$  compared to the HDPE, which indicates the strong interfacial interaction between the HDPE matrix and the MWCNTs (Beesetty et al. 2020). A similar trend is observed for the printed specimens. The only difference is that the  $T_{Cryst}$  increases up to 1 wt.% and then decreases for the higher MWCNTs loadings. No significant effect of the additional processing on the  $T_{Cryst}$  is observed for the filaments and the printed specimens. The  $T_{Melt}$  of the filaments and the printed specimens slightly increases with the filler loadings. This is due to the MWCNTs good dispersion in the HDPE, which resists the heat conduction to the crystallites until the heat flow is sufficient to melt them at higher temperatures (Amoroso et al. 2020). The higher  $T_{Melt}$  of the H5

filament and the printed specimen indicates that the MWCNTs are well dispersed in the HDPE at the higher loading as well. The  $\alpha_{Cryst}$  is determined from the second heating cycle and presented in Table 3.2. The  $\alpha_{Cryst}$  increases up to 1% filler content, and then decreases for the filaments and the printed specimens. At low filler loading (up to 1%), the MWCNTs act as heterogeneous nucleating agents (or external agents) for the HDPE matrix, increasing the  $\alpha_{Cryst}$ . At the higher loading, the MWCNTs make networks, which inhibits the crystal growth and limits the formation of large and uniform crystallites, resulting in a drop in the  $\alpha_{Cryst}$ . The printed samples exhibit the higher  $\alpha_{Cryst}$  than the filaments as the printed samples get a relatively higher time for the crystallization process than the filaments, which are directly quenched after the extrusion. The widening of the melting and the crystallization peaks with an increase in the MWCNTs can be due to the size distribution of the crystallites. The wider peak indicates a wider range of the crystallite sizes that melt at different temperatures. In comparison, the narrower peak indicates a narrower range of crystallite sizes that melts over a narrower temperature range (Xiang et al. 2014, Xiang et al. 2015). A similar trend is observed for the printed specimens as well.

Table 3.2. Thermal properties of the samples.

Composition	$T_{Cryst}$ (°C)		$\alpha_{Cryst}$ (%)		$T_{Melt}$ (°C)	
	Flmt	Spmn	Flmt	Spmn	Flmt	Spmn
HDPE	116.271	115.271	47.92	50.90	132.277	131.648
H0.5	118.114	118.628	52.68	52.91	133.668	132.311
H1	117.709	119.234	53.34	56.70	133.774	132.707
H3	115.842	117.046	51.82	53.11	135.118	133.218
H5	115.675	115.270	50.95	52.07	137.678	134.059

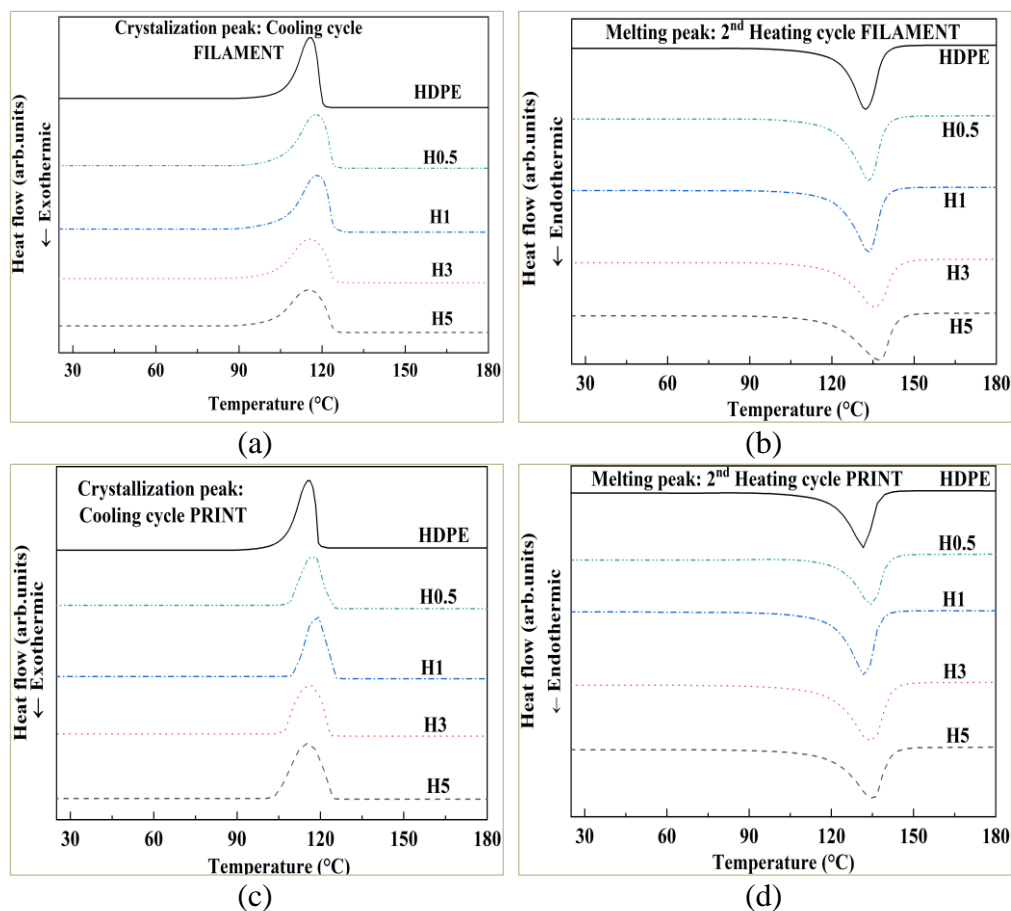


Figure 3.8. DSC curves of the filaments (a), (b) and the printed samples (c), (d).

### 3.2.5 XRD

The X-ray diffraction (XRD) is carried out for both the filaments and the prints to check their crystallinity behavior as the change in the crystallization behavior of the material influences the mechanical properties such as compressive strength and modulus (Amoroso 2020). The XRD pattern of the filaments and the prints are displayed in Figure 3.9, and the corresponding values are given in Table 3.3. The intensity of the NC filaments peaks is observed to be higher than the neat HDPE. It is also observed that there are two intense peaks for all the filaments. The peak values ( $2\theta$ ) of each filament signify the crystal structure (orthorhombic) in the (110) and (200) lattice planes (Doddamani 2020). A similar trend is observed for the prints, wherein the peaks are observed in almost the same positions, while an increase in the peak intensity is observed compared to the filaments. The highest peak intensity is observed for the H1 filament and the print, respectively. The sharpness of the peak shows the crystallinity, and an increase in the peak intensity is correlated to an

increase in the crystallinity. The degree of crystallinity of the NCs is higher for both the filaments and the prints compared to the HDPE filament and the print, respectively, and increases up to 1 wt.% of the MWCNTs. The fillers act like nucleating agents during the cooling cycle. The presence of the MWCNTs results in more crystal formation than the HDPE, leading to the higher crystallinity. However, a lower and large crystal formation occurs in the HDPE due to fewer impurities. The increase in the crystallinity can be attributed to the formation of fine and uniform crystallites. In contrast, a reduction in the crystallinity can be attributed to the prevention of large and uniform crystal formation due to the formation of the functionalized MWCNT network (Amoroso 2020). The H1 filaments and the prints have the highest crystallinity, which can be attributed to the finest and uniform crystal formation compared to all other filaments and prints. Furthermore, the degree of crystallinity of the 3D printed samples is more than that of the filaments due to the additional thermal heating and higher crystallization time in the 3DP process (Kumar 2022).

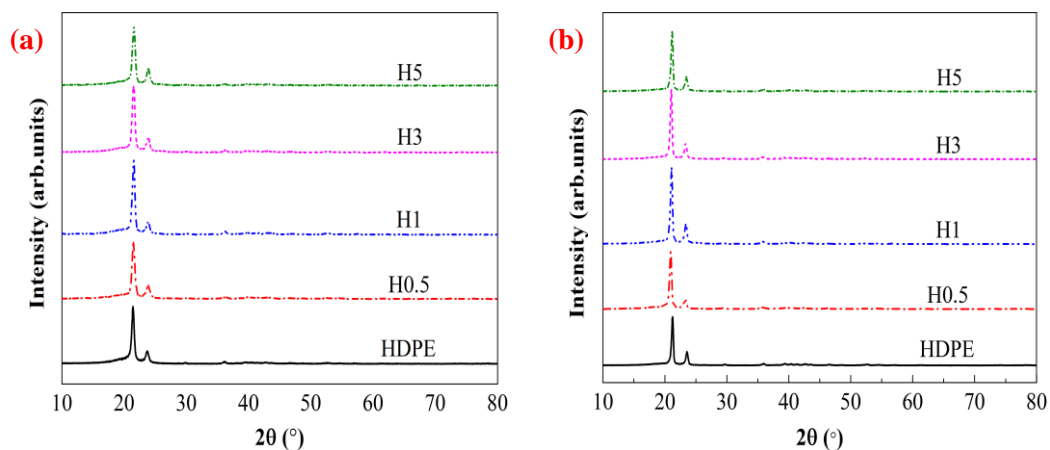


Figure 3.9. XRD responses of (a) the filaments and (b) the prints.

Table 3.3. XRD responses of the filaments and the prints.

Configuration	Filament Peak		3D Prints Peak		Degree of Crystallinity (%)	
	Position 2θ (°)		Position 2θ (°)		Filament	3D Prints
	1st peak	2nd peak	1st peak	2nd peak		
HDPE	21.426	23.710	21.24	23.55	64.389	73.504
H-0.5	21.504	23.842	20.95	23.21	65.278	75.062
H-1	21.557	23.868	21.05	23.42	68.414	78.059
H-3	21.583	23.920	21.19	23.42	67.729	77.661
H-5	21.531	23.894	21.08	23.39	65.528	75.619

### 3.3 Coefficient of thermal expansion

The coefficient of thermal expansion (CTE) is an important thermal property that signifies a material's thermal expansion capability. It plays a very important role in determining the warpage reduction in the polymer based 3D printing. All the 3D printed samples are tested for the CTE measurement to estimate the warpage reduction potential. The CTE responses of the printed samples are shown in Table 3.4. The CTE values of the NCs decreases with an increment in the MWCNTs. The CTE value of the HDPE is  $171 \times 10^{-6}/^{\circ}\text{C}$ , whereas the CTE value of the H5 is  $111 \times 10^{-6}/^{\circ}\text{C}$ . The reduction in the CTE of the H0.5-H5 is observed from 1.75%-35.09% compared to the pure HDPE. A significant reduction of 35.09% in the CTE value is observed for the highest composition H5 NC when compared to the HDPE, which clearly shows the potential of the functionalized MWCNTs to enhance the thermal and dimensional stability and thereby reduce the warpage issue. The gradation of the NCs also significantly decreases the CTE of the FGNCs. The reduction in the CTE of the FGNC-1 and FGNC-2 is observed from 40.35%-63.74%, respectively, compared to the pure HDPE. The maximum reduction in the CTE value is observed for the FGNC-2, which is 63.74% lower than the HDPE. The reason for the CTE reduction in the NCs is the strong and seamless interfacial interaction between the HDPE and the MWCNTs having the higher CTE as compared to the HDPE. In contrast, the seamless

adhesion between the two different compositions might lead to the CTE reduction in the FGNCs.

Table 3.4. CTE responses of the 3D printed samples.

Composition	CTE ( $\times 10^{-6}/^{\circ}\text{C}$ )
HDPE	171 $\pm$ 3.11
H0.5	168 $\pm$ 2.84
H1	165 $\pm$ 2.62
H3	159 $\pm$ 1.96
H5	111 $\pm$ 2.03
FGNC-1	102 $\pm$ 1.06
FGNC-2	62 $\pm$ 1.17

### 3.4 Conclusion

The functionalized MWCNTs are successfully mixed with the HDPE to develop the MWCNTs/HDPE based nanocomposites. The good quality nanocomposite filaments and flawless NC and FGNC samples are successfully realized through 3D printing. The processed materials are characterized through various techniques, of which, the results are summarized below.

#### *SEM*

- The SEM analysis revealed the uniform distribution of the functionalized MWCNTs in the developed nanocomposites, extruded nanocomposite filaments, and the 3D printed samples, confirming the suitability of the processing parameters used in the blending, extrusion, and the 3D printing obtained through a pilot study. It also revealed the seamless and the strong layer bonding in the 3D printed NC and FGNC samples.

#### *MFI*

- The MFI of the developed NCs decreases with the increase in the MWCNTs content, confirming the increase in the melt viscosity of the NCs, and hence the inclusion of the fillers. The MFI reduces 14.52%-51.60% for the H0.5-H5 NCs compared to the pure HDPE.

### TGA

- The degradation temperature of the developed NCs is higher than the neat HDPE, and increases with the MWCNTs loading. The HDPE, H0.5, H1, H3, and H5 degradation temperatures are 396.68 °C, 439.23 °C, 446.80 °C, 466.53 °C, and 479.07 °C, respectively.

### Rheology

- The rheology results confirm the uniform distribution of the fillers qualitatively. It is observed that the  $\eta^*$  for the NCs slightly increases as the functionalized MWCNTs content increases up to 0.5% and then dramatically increases for 5% (almost two orders) at the low frequency by maintaining a steeper graph, confirming the good dispersion of the MWCNTs in the HDPE.
- The  $\eta^*$ ,  $E'$ , and  $E''$  of the 3D printed NCs and FGNCs increase while damping decreases as the functionalized reinforcement content rises.

### Density

- The density of the filaments and the printed specimens decreases with the increases in the MWCNT content. The highest density reduction of 16.06% and 15.58%, respectively, is observed in the H5 filament and the respective specimen compared to the HDPE.
- The density of the FGNCs decreases with the MWCNTs gradation in the layer with the highest weight-saving potential of 12% for the FGNC-2.

### DSC

- The  $T_{Cryst}$  increases up to 0.5% and 1 wt.% of the MWCNTs for the filaments and the printed specimens, respectively, then decreases as compared to the neat HDPE.
- The  $T_{Melt}$  of the filaments and the printed specimens increases with the increase in the MWCNTs content.
- The  $\alpha_{Cryst}$  is found to be higher for the filaments and the printed specimens compared to the neat HDPE.

### XRD

- The crystallinity of the NC filaments and the prints is higher than that of the respective HDPE counterparts.

### *CTE*

- The CTE of the NC samples decreases with the addition and gradation of the MWCNTs.
- The highest reduction in the CTE is observed for the FGNC-2 and the H5 NC among all the NCs and FGNCs, showing the potential to reduce warpage issues.

Thus, the functionalized MWCNTs and the HDPE-based nanocomposites were successfully developed to realize the nanocomposite filaments and the 3D printed samples without any defects. The suitability of the processing parameters is confirmed through the SEM analysis. The developed nanocomposites, extruded filaments, and the printed samples are characterized for basic properties like MFI, DSC, XRD, TGA, and rheology, which help setting the appropriate processing parameters for realizing the defect-free samples.



## 4 TENSILE BEHAVIOUR

### 4.1 Tensile responses of the nanocomposite filaments

The feedstock filament is pulled through the drive roller of the 3D printer, where it is subjected to the frictional and normal forces. The frictional force develops the tensile stress, while the normal forces develop the compressive stress in the filament. The developed tensile stress may break/rupture the filament. In contrast, the compressive stress may deform the shape of the filament, which further causes improper movement of the filament through the roller. Therefore, the feedstock filament must have sufficient strength and stiffness to overcome the tensile stress and the associated deformation. The experimental setup for the filament tensile test is shown in Figure 4.1, and the respective results are shown in Table 4.1. The modulus increases by 17.37%, 20.94%, 44.80%, and 104.54% in respective H0.5, H1, H3, and H5 NC filaments compared to the HDPE filament. The highest modulus is found for the H5 NC (~105% more than the pure HDPE). The inclusion of the stiff functionalized MWCNTs in the neat HDPE is the reason for such a modulus enhancement. Moreover, the modulus of the composite depends upon the interfacial bonding between the matrix and the fillers. The stronger the interfacial bonding, the higher the  $T_{Melt}$  and the modulus (Amoroso et al. 2020). The DSC results (Table 3.2) showed the increased  $T_{Melt}$  of the NCs as compared to the HDPE, which confirms the strong interfacial bonding between the HDPE and the functionalized MWCNTs, and hence, an increase in the modulus of the NCs is observed. Figure 4.1b and Figure 4.1c represent the tensile stress-strain plots of the HDPE and the NC filaments, respectively. The HDPE filament showed more than 200% strains without any breakage due to the ductile behavior of the HDPE. The test is stopped due to limited stroke distance. The fracture strains of the H0.5, H1, H3, and the H5 NC filaments decreased severely compared to the pure HDPE. Including MWCNTs increases the brittleness of the HDPE, resulting in the fracture at a lower strain value. The tensile strength increases by 1.32%, 18.54%, 23.84%, and 29.14% in the H0.5, H1, H3, and H5, respectively, compared to the pure HDPE filament. The highest tensile strength is observed for the H5 (~30% more compared to the HDPE) filament due to the uniform distribution of the MWCNTs in the HDPE (Figure 4.2a) compared to the

H0.5 composite (Figure 4.2b). Another reason for this may be better bonding between the matrix and the filler in the H5 NC. The strength of the composites depends upon the interfacial bonding between the matrix and the filler, as well as the uniform distribution of the fillers in the matrix (Amoroso et al. 2020). Due to the uniform distribution of the fillers, the matrix can transfer the loads to all the fillers responsible for taking the loads in the composites. Hence, the load bearing capability of the composites increases. The strong interfacial interaction is confirmed by the increased  $T_{Melt}$  and the modulus of the NCs, whereas the uniform distribution of the functionalized MWCNTs in the HDPE is confirmed from the SEM image of the H3 freeze-fractured specimen (Figure 3.7). The elongation at the ultimate tensile strength (UTS) is registered highest for the H1 NC. The NC filaments show significantly lower fracture strength and strain than the pure HDPE due to the addition of the MWCNTs. The increased stiffness and strength ensure the shape retention and no rupture of the filaments while passing through the drive rollers. Hence, the filaments can be used for 3D printing of the samples, and can be utilized for different applications.

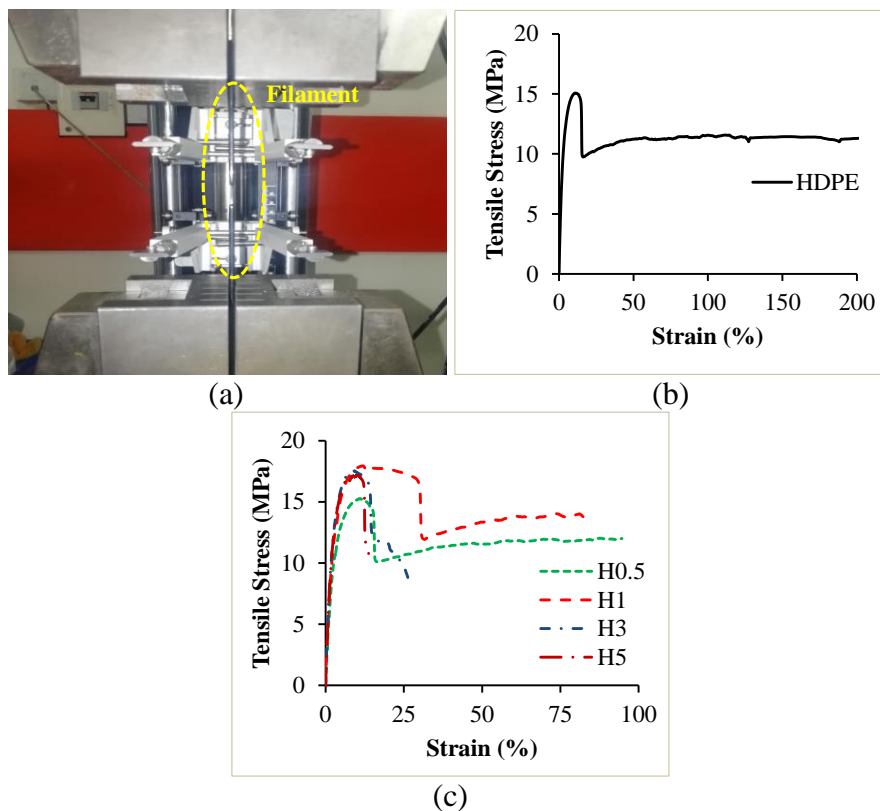


Figure 4.1. Representative (a) experimental set up for the filament tensile test, tensile stress-strain graph of (b) the neat HDPE and (c) the H0.5-H5 NC filaments

Table 4.1. Tensile results for the filaments and the prints.

Material	Tensile Modulus (MPa)		UTS (MPa)		Elongation at UTS (%)		Fracture Strength (MPa)		Elongation at Fracture Point (%)		Poison's Ratio
	Flmt	Spmn	Flmt	Spmn	Flmt	Spmn	Flmt	Spmn	Flmt	Spmn	Spmn
HDPE	616±13	711±11	15.1±0.14	14.8±0.22	10.9±0.17	8.9±0.33	-	13.44±0.21	-	139.12	0.4607
H0.5	723±16	824±17	15.3±0.31	15.2±0.29	10.8±0.24	7.6±0.25	11.98±0.10	15.23±0.32	94.57	7.25	0.4587
H1	745±11	849±23	17.9±0.23	15.5±0.38	11.6±0.15	4.0±0.43	13.75±0.06	11.59±0.22	±0.05	±0.08	±0.0008
H3	892±21	1030±20	18.7±0.22	16.2±0.41	8.9±0.32	4.8±0.27	9.03±0.09	16.10±0.34	83.35	6.42	0.4559
H5	1260±19	1290±15	19.5±0.36	16.6±0.20	8.6±0.40	7.6±0.23	10.78±0.13	13.06±0.40	±0.09	±0.03	±0.0009
									26.01	5.23	0.4486
									±0.12	±0.14	±0.0013
									13.74	3.30	0.4429
									±0.08	±0.20	±0.0002

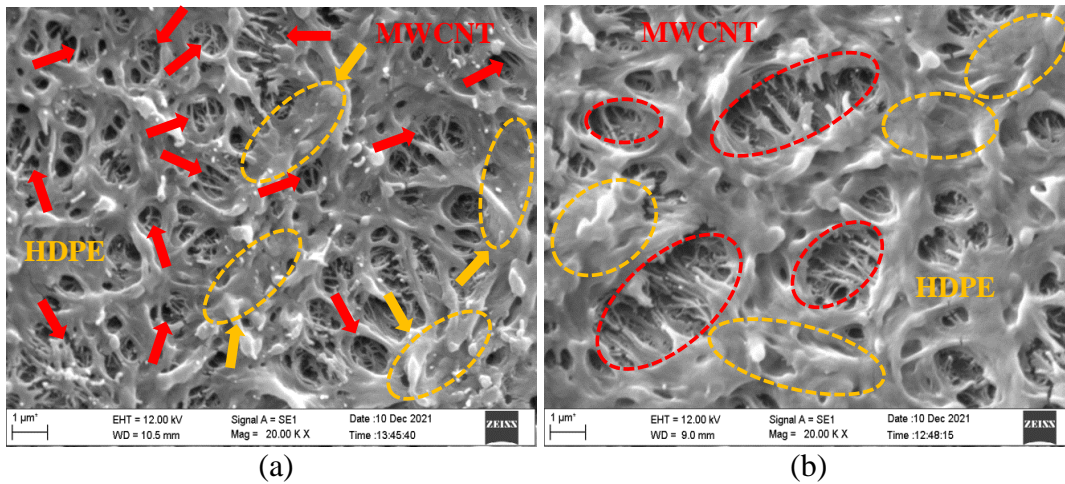


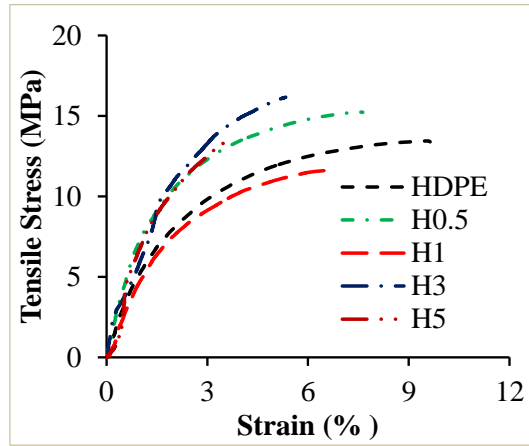
Figure 4.2. Representative SEM images of (a) the H5 NC and (b) H0.5 NC filaments.

## 4.2 Tensile results of the printed specimens

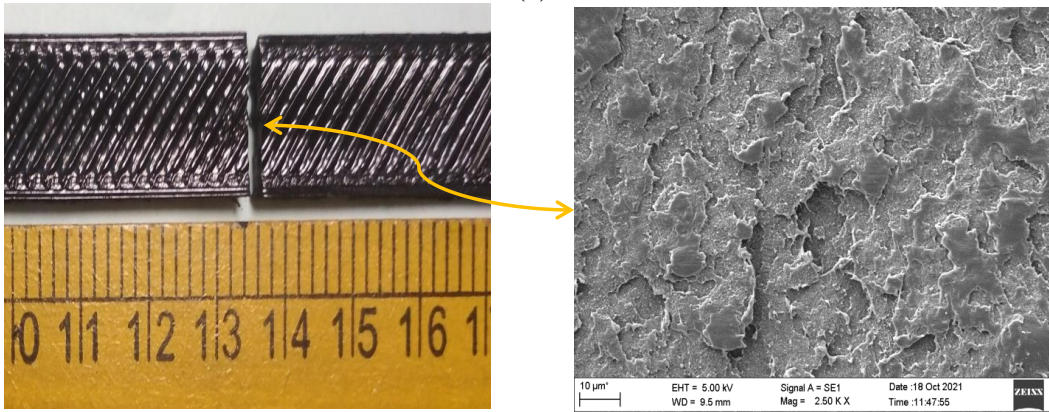
### 4.2.1 Tensile responses of the NCs

The tensile results of the printed H-H5 samples are shown in Figure 4.3a, and the respective values are shown in Table 4.1. All the specimens failed, typically in brittle mode. The HDPE extruded filament did not fail even after 200% strains, while the HDPE specimen failed at  $\sim 140\%$ , showing the change in behavior from the ductile to the brittle. The graph of the HDPE specimen is plotted up to 10% strains. The tensile modulus of the 3D printed NCs is enhanced with the MWCNTs addition (Table 4.1). The modulus increases by 15.89%, 19.41%, 44.87%, and 81.43% in the H0.5, H1, H3, and the H5 specimens, respectively, compared to the pure HDPE specimen. The highest modulus is registered for the H5 NC ( $\sim 81.5\%$ ). The modulus of the printed H-H5 specimens increased by 15.42%, 13.97%, 13.96%, 15.47%, and 2.38% compared to the respective filaments. This is due to the higher crystallization of the specimens compared to the filaments. The polymer chain realigns and crosslinks during 3D printing, leading to the higher crystallization, which is also observed in the DSC results. The highest tensile strength is registered for the H5 NC (16.6 MPa), which is 12.16% higher than the pure HDPE. This is because the H5 NC has the most effective load transfer between the filler and the matrix. The highest surface area of the HDPE rendered by the MWCNTs and the formation of the more MWCNTs networks might be the reason for the effective load transfer between them (Amoroso

et al. 2020, Beesetty et al. 2020). The micrograph of the tensile tested H5 NC is shown in Figure 4.3b. The strength of the filaments and the printed specimens are comparable. The elongation at the UTS for the printed specimens decreases with the MWCNTs content. This is attributed to an increase in the number of the MWCNTs in the HDPE. The highest fracture strength is observed for the H3, which is 19.79% more than the HDPE. The fracture strain decreases with the filler loadings. For the H5 NC, the UTS is substantially lower than the HDPE specimen. The poison's ratio decreases with the MWCNTs increase. This is because the increase in the MWCNTs in the HDPE results in the composites' brittleness, further decreasing the lateral strain. For the low-density 3D parts, a reduction in the strength and ductility is often observed especially in the non-surface modified hollow sphere (such as fly-ash cenospheres, GMB, etc.) embedded polymer matrices (H S et al. 2020, Patil et al. 2019). The reduction in the strength is due to presence of the porosity in the foams. The presence of the porosity reduces the load-bearing capability, and hence the strength of the foams. In the present study, the filler is functionalized MWCNTs, which are tubular and have a higher surface area. The higher experimental density of the NCs than the theoretical density (Table 3.1) confirms the absence of the matrix porosity; hence, the NCs' strength increases. However, the ductility of the NC specimens is decreasing due to brittleness caused by the functionalized MWCNTs addition. The specific mechanical properties are crucial for the weight-sensitive applications. The weight-saving potentials can be estimated through  $E/\rho^n$  (where  $n = 1, 2$  and  $3$ ). Table 4.2 presents the specific mechanical properties of the H-H5 specimens. The specific strength and modulus increase for the H-H5 as the MWCNTs content increases. This is attributed to the increase in the modulus and the strength values and the decrease in the density as filler loading increases. The H5 NC has shown the highest specific modulus and strength among all the NC specimens. The specific modulus and strength of the H5 are 114.67% and 32.90% higher compared to the HDPE, respectively, showing the great potential for the applications in the aerospace, automotive, marine, naval, biomedical, and the other structural components of integrated complex designs.



(a)



(b)

Figure 4.3. (a) Tensile stress-strain graph of the printed NC specimens and (b) SEM image of the tensile tested H5 specimen.

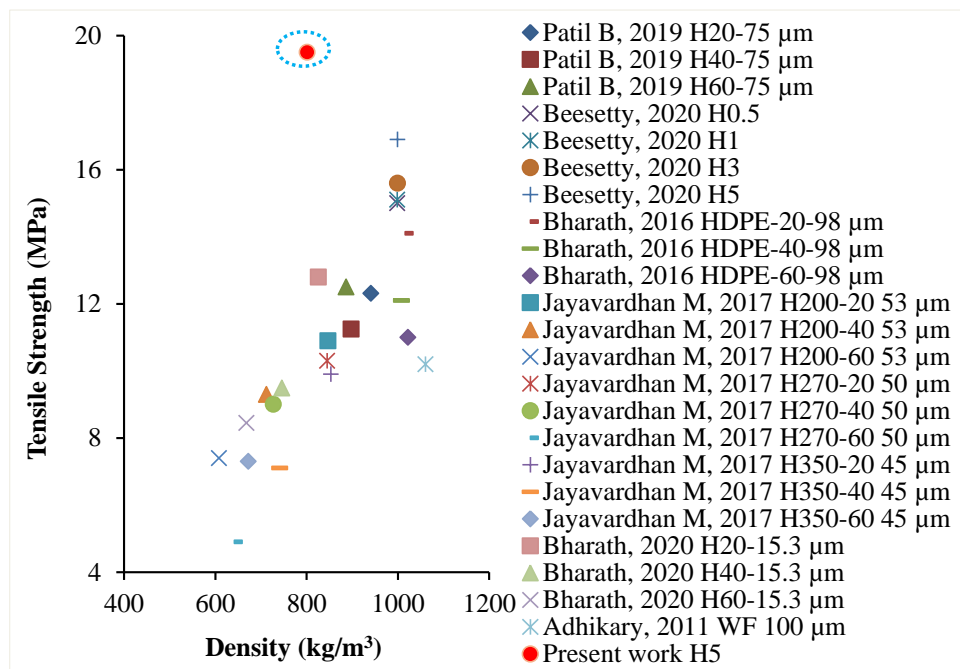
Table 4.2. Specific mechanical properties of the NC specimens.

Composition	$E/\rho$ (MPa/kg/m <sup>3</sup> )	$E/\rho^2$ (MPa/(kg/m <sup>3</sup> ) <sup>2</sup> × 10 <sup>-3</sup> )	$E/\rho^3$ (MPa/(kg/m <sup>3</sup> ) <sup>3</sup> × 10 <sup>-6</sup> )	Sp. Strength (MPa/ kg/m <sup>3</sup> × 10 <sup>-3</sup> )
HDPE	0.75	0.79	0.83	15.59
H0.5	0.88	0.95	1.02	16.32
H1	0.94	1.04	1.15	17.17
H3	1.16	1.31	1.48	18.28
H5	1.61	2.01	2.51	20.72

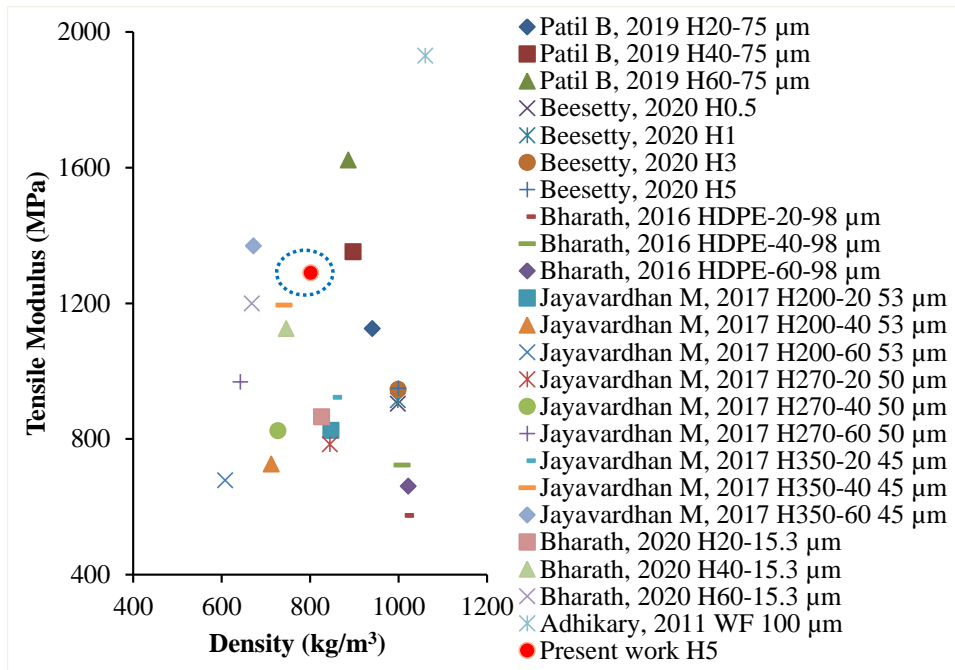
#### 4.2.2 Property map

Figure 4.4 (Adhikary 2011, Beesetty et al. 2020, Bharath Kumar et al. 2016, H S et al. 2020, Jayavardhan M. L. 2017, Patil et al. 2019) represents the tensile responses of the HDPE based composites against the composite density having different fillers

manufactured by the other manufacturing processes. The solid particle (wood flour) filled HDPE composite has shown the highest density and tensile modulus. The MWCNT/HDPE NC has a lower density than the fly ash cenospheres, nano clay, solid particles, and some compositions of the GMB based composites, showing great potential for the weight-sensitive applications. The density of the printed NCs lies in between the compression and injection molded foams. The printed NCs exhibit the higher tensile modulus except for the wood-based and the H60-75  $\mu\text{m}$  composites. Compared to the injection and compression molded composites, the tensile modulus of the 3D printed NCs is higher (Figure 4.4a). The 3D printed NCs exhibited the highest tensile strength compared to the other fillers reinforced HDPE composites with the solid particles-based composites (Figure 4.4b). The additively manufactured NCs exhibited the highest tensile strength compared to the injection and compression molded composites. Nonetheless, in the present work, the 3D printed H5 NC composition exhibited superior tensile strength than the composites with fillers like fly ash cenospheres, nano clay, GMB, and wood. The property plots reveal that the inclusion of the MWCNTs into the HDPE and the 3D printing of their NCs can be used to exploit a wide range of physical, mechanical, and thermal properties for various applications.



(a)



(b)

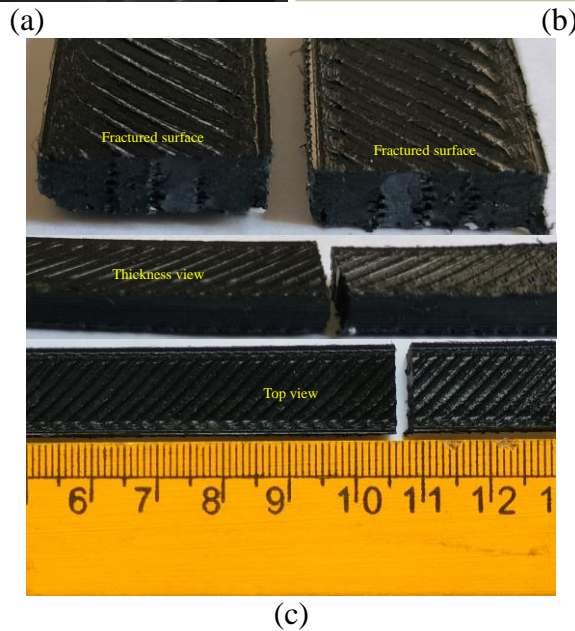
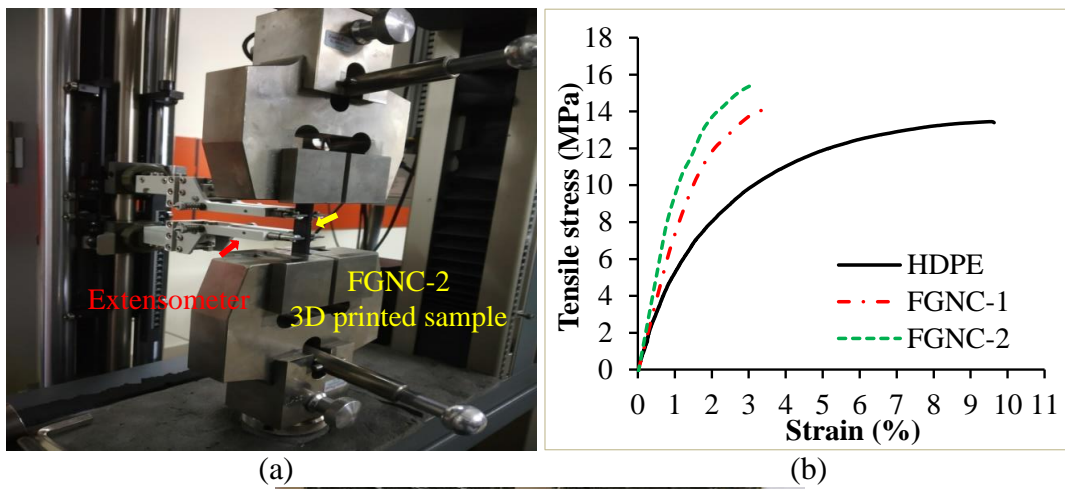
Figure 4.4. Tensile (a) strength and (b) modulus of HDPE composites (Adhikary 2011, Beesetty et al. 2020, Bharath Kumar et al. 2016, H S et al. 2020, Jayavardhan M. L. 2017, Patil et al. 2019).

#### 4.2.3 Tensile responses of the FGNCs

The tensile test of the FGNCs is performed to obtain the elastic properties such as moduli and Poisson's ratio, required for the material modelling in the numerical investigation of the bending behavior of the FGNCs. However, their tensile behavior is also discussed here in detail. There might be some conditions where structures/components designed for flexural loading may be subjected to the tensile loading, which may also fail due to the applied stress. Hence, the tensile behavior of the 3D printed FGNCs is also crucial for the practical applications. The experimental test setup and the obtained results are shown in Figure 4.5, while their corresponding data are given in Table 4.3. The modulus of the 3D printed HDPE, FGNC-1, and FGNC-2 are observed to be 709 MPa, 1100 MPa, and 1350 MPa, respectively (Table 4.1), showing the increasing trend with the increasing layer composition. The enhancements in the moduli are 55.15% and 90.41% for the FGNC-1 and FGNC-2 compared to the pure HDPE, respectively, showing the potential to replace them. Moreover, the H0.5, H1, H3, and H5 moduli are 824 MPa, 849 MPa, 1030 MPa, and 1290 MPa, respectively (Kumar 2022). It is noted that the moduli of the FGNCs are higher than the moduli of their respective homogeneous NCs, showing the potential to

replace the NCs as well. The tensile strength of the HDPE, FGNC-1, and FGNC-2 are observed to be 13.39 MPa, 16.57 MPa, and 18.36 MPa, respectively (Table 4.3). The FGNCs' strength is higher than the respective homogeneous NCs (H0.5, H1, H3, and H5→15.2, 15.5, 16.2, and 16.6 MPa, respectively (Kumar 2022)). The enhancements in the strength are 23.75% and 37.12%, respectively, compared to the pure HDPE. The enhancements in the moduli and strength are attributed to including the highly stiff and strong MWCNTs in each layer with their gradation. Moreover, a high composition layer will always have higher modulus and strength, and increasing layer composition provides smooth and continuous stress distribution, further enhancing the mechanical properties of the FGNCs. In addition, when the load is applied on the FGNCs, the maximum amount of the load is transmitted to the higher filler layer with the higher modulus and strength, and thus, it only takes the maximum load. Hence, until and unless the higher filler layer fails, the lower filler layers do not fail. Additionally, the lower filler layers provide additional support in the form of interfacial shear stress to the higher filler, further enhancing the overall stress bearing capability of the FGNCs compared to their respective homogeneous NCs. The fracture of the samples takes place at the ultimate point only, as clearly observed in Figure 4.5b, and hence, the fracture strength is approximately similar to the strength of the samples, as seen in Table 4.3. Furthermore, it is noted that all the 3D printed FGNC samples showed brittle failure as the maximum strain is <4%, while the pure HDPE also exhibited the brittle failure, but it was more ductile (up to 10%) than the FGNCs as observed in Figure 4.5b. The top, thickness, and the fractured surfaces of the failed (brittle mode) FGNC-2 sample have been shown in Figure 4.5c. The gaps between the rasters are observed in the 3D printed FGNC-2 sample, which might be the spot of the crack initiation. Moreover, in the pure HDPE, the chain molecules are bonded by the primary bond, which is more flexible and stronger than the secondary bonds. When the load is applied, the primary bond only bears the load, which shows flexibility through elasticity and then fails after plastic deformation. However, in the case of the nanocomposite, MWCNTs make a secondary bond with the HDPE, which is physical and weak. When the load is applied to it, the load is transmitted to the fillers by the matrix, and the interfacial bond between them (the secondary bonds) is only responsible for the failure; hence, the failure occurs in the brittle mode. The

ductile to the brittle transition in the FGNCs is because of the highly stiff and brittle MWCNTs incorporated in the HDPE. The fractured surface of the FGNC-2 sample is further analysed by the SEM, as shown in Figure 4.5d-g, which clearly shows the brittle failure due to the voids and cracks. The region 1 (R1) of the H5 layer is further magnified to observe the MWCNTs and their networks, and the clear visualization of the MWCNTs and the networks formed among them are seen in Figure 4.5g, which are responsible for the excellent moduli and strength of the FGNCs. Thus, the FGNC-2 exhibited the outstanding tensile modulus and strength, showing a great potential for the lightweight structural applications.



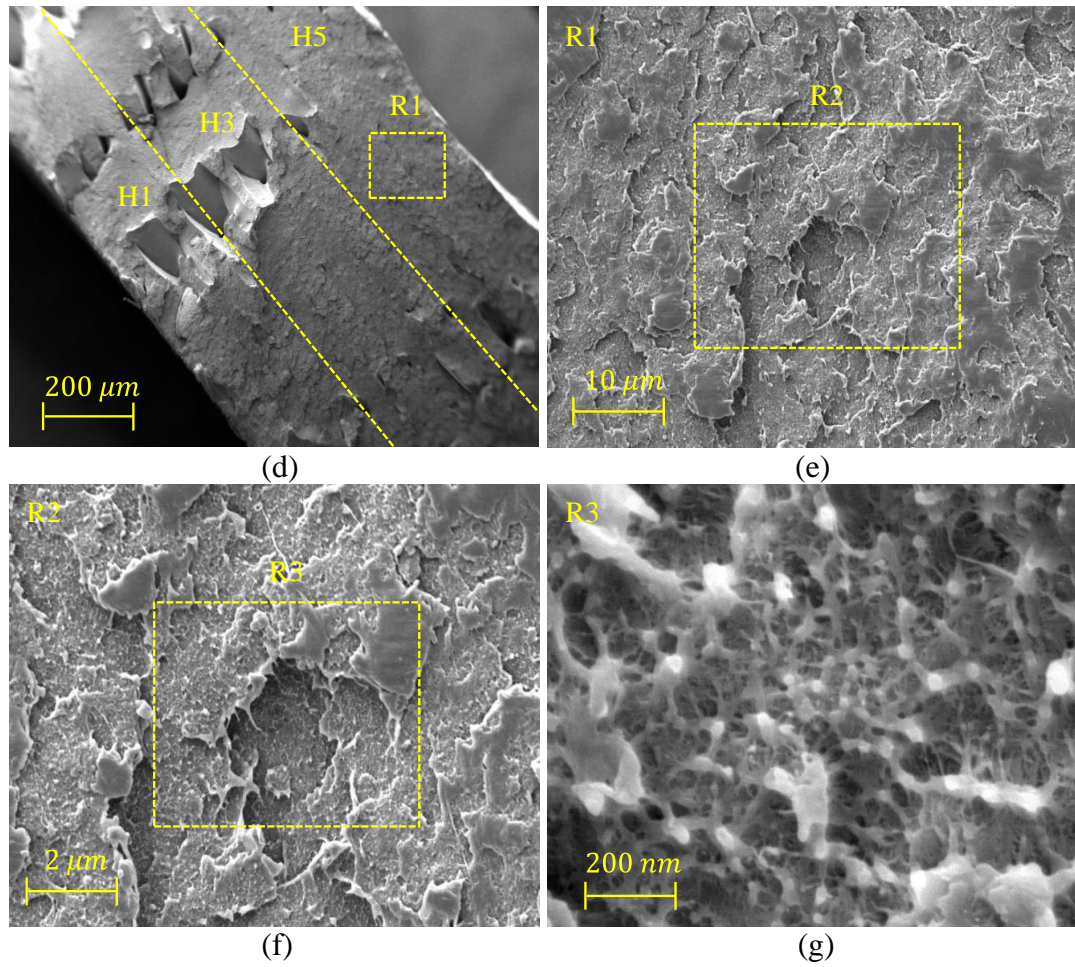


Figure 4.5. (a) Experimental test set up, (b) tensile results, (c) tested sample showing top, thickness, and fracture surfaces, and (d)-(g) SEM images of the fractured surface of the FGNC-2 sample.

Table 4.3. Tensile results of the printed FGNCs.

Composition	Modulus (MPa)	Strength (MPa)	Fracture strain (%)	Fracture strength (MPa)	Poisons' ratio
HDPE	709±07	13.39±1.12	9.63±0.78	13.39±1.41	0.4607±0.0011
FGNC-1	1100±10	16.57±1.31	3.35±0.82	16.55±1.67	0.4452±0.0004
FGNC-2	1350±13	18.36±1.03	3.18±0.90	18.30±1.09	0.4402±0.0007

### 4.3 Conclusion

The extruded NC filaments, printed NCs, and their graded variants (FGNCs) are tested for the tensile properties. The results are summarized below.

#### *Filaments*

- The tensile modulus and strength of the extruded filaments increase with the MWCNTs addition. The modulus increases by 17.37%, 20.94%, 44.80%, and 104.54% in the respective H0.5, H1, H3, and H5 NC filaments in comparison to the pure HDPE filament.
- The highest modulus is observed for the H5 NC (~105% more than the pure HDPE).
- Compared to the neat HDPE filament, the tensile strength increases by 1.32%, 18.54%, 23.84%, and 29.14% in the H0.5, H1, H3, and H5, respectively.
- The highest strength is observed for the H5 NC (~30% more compared to the HDPE) filament.

#### *3D Printed NCs*

- The modulus increases by 15.89%, 19.41%, 44.87%, and 81.43% in the H0.5, H1, H3, and H5 NC specimens, respectively, compared to the pure HDPE specimens.
- The highest modulus is registered for the H5 NC specimen (~81.5%).
- The modulus of the printed H-H5 specimens increased by 15.42%, 13.97%, 13.96%, 15.47%, and 2.38% compared to the respective filaments.
- The highest tensile strength is registered for the H5 NC (16.6 MPa), which is 12.16% higher than the pure HDPE.

#### *3D Printed FGNCs*

- The modulus of the FGNC-1 and FGNC-2 are 1100 MPa and 1350 MPa, respectively, showing the increasing trend with the increasing layer composition.
- The enhancements in the moduli are 55.15% and 90.41% for the FGNC-1 and FGNC-2 compared to the pure HDPE, respectively, showing the potential to replace them.
- The FGNCs exhibited the higher moduli than their respective homogeneous NCs, showing the potential to replace the NCs as well.

- The tensile strength of the FGNC-1 and FGNC-2 are observed to be 16.57 MPa, and 18.36 MPa, respectively.
- The FGNCs' strength is found to be higher than the respective homogeneous NCs. The enhancements in the strength are 23.75% and 37.12%, respectively, compared to the pure HDPE.

*Property map*

- The property map revealed that the 3D printed NC samples exhibited the highest tensile strength compared to the other fillers reinforced HDPE composites with solid particles-based composites.
- Additively manufactured NC exhibited the highest tensile strength compared to the injection and compression molded composites.
- The H5 composition exhibited the superior tensile strength than the composites with fillers like fly ash cenospheres, nano clay, GMB, and wood.

Thus, the tensile properties of the extruded NC filaments and the printed specimens are greatly enhanced due to the addition of the MWCNTs filler. These properties are crucial for the structural applications, where the structures are subjected to the tensile loading.



## 5 FLEXURAL BEHAVIOR

### 5.1 Experimental investigation

#### 5.1.1 Flexural responses of the NCs

The 3D printed NCs are tested for the flexural responses in 3-point bending mode to analyse their behavior under the transverse load as shown in Figure 5.1a. Figure 5.1b shows the flexural stress-strain plot of the H-H5 printed samples. It is clearly observed that the printed samples did not fail until the 10% strain. The printed NCs' flexural strength and modulus increase with the MWCNTs loadings (Table 5.1). The modulus increased by 12.55%, 15.83%, 21.81%, and 24.71%, while the strength increased by 12.70%, 20.63%, 21.43%, and 22.23% in the H0.5-H5, respectively when compared to the pure HDPE specimen. The H5 NC displayed the highest modulus and strength among all the NCs. The functionalized MWCNTs networks effectively restrict the matrix flow. The MWCNTs' larger surface area might bind the polymer chains together effectively, resulting in improved mechanical properties. Figure 5.1c shows the micrograph of the H5 NC post the flexural test. The MWCNTs are firmly embedded in the polymer matrix and show no evidence of the displacement. Due to their larger surface area, this could be attributed to the enhanced mechanical bonding between the polymer chains and the nanoscale MWCNTs (Beesetty et al. 2020). The specific strength and modulus of the specimens increased with the filler loadings. The H5 NC showed the highest specific modulus and strength, 47.62% and 44.73% higher than the pure HDPE. The NCs exhibited the superior flexural and tensile responses compared to the pure HDPE specimen. These printed NCs, particularly H5, may be a preferable material choice for geometrically complex components. Also, the H5 NC showed the great weight reduction potential, making it preferable for the lightweight applications. Furthermore, including the MWCNTs reduces the HDPE consumption to some extent. As shown in the current work, developing the NC filaments and their 3D printing feasibility expands the feedstock filament choices in the polymer-based AM community.

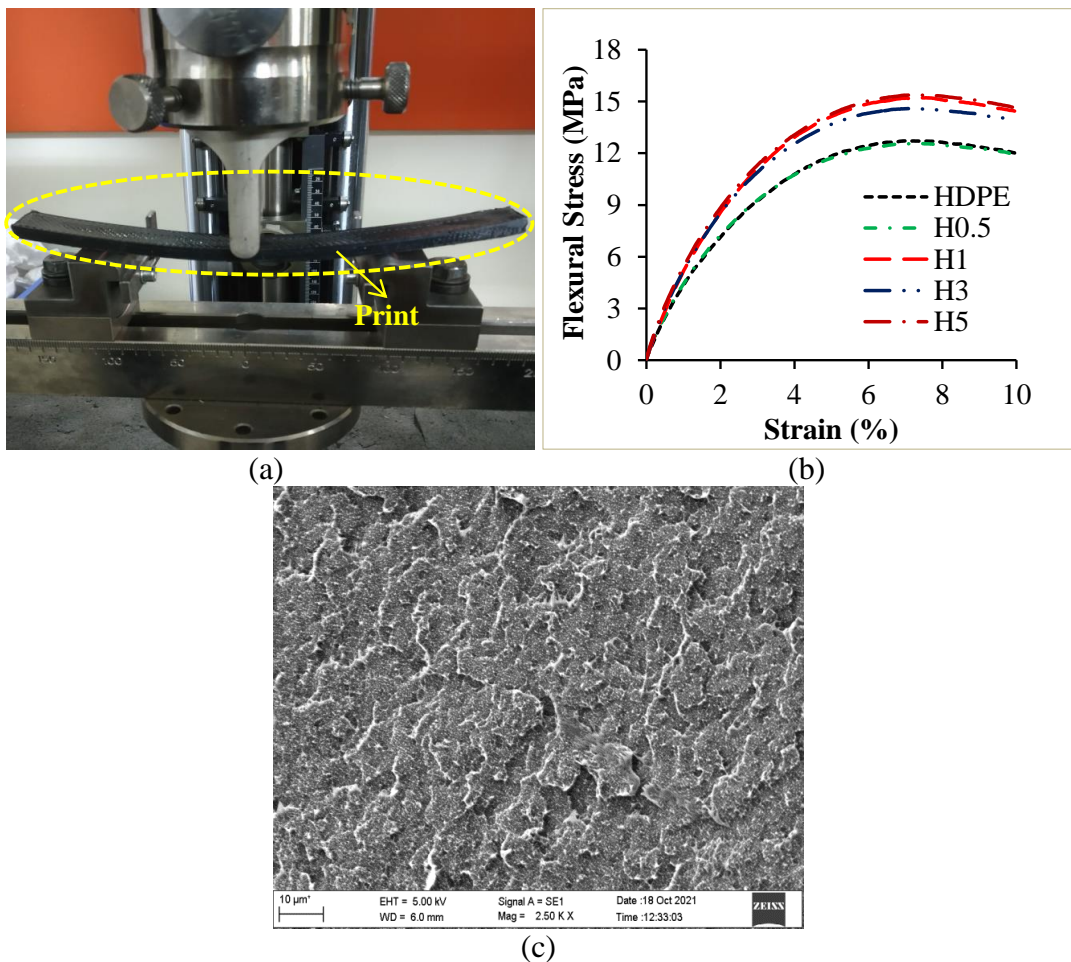


Figure 5.1. Representative (a) experimental set up for the flexural test (b) flexural stress-strain graph of the printed NCs and (c) SEM image of the flexural tested H5 NC.

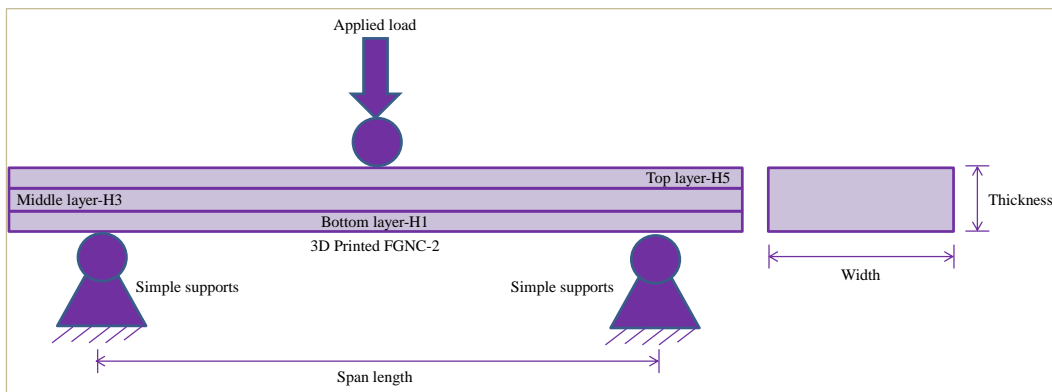
Table 5.1. Flexural properties of the printed NCs.

Composition	Modulus (MPa)	Strength (MPa)	Specific Modulus (MPa/kg/m <sup>3</sup> )	Specific Strength (MPa/kg/m <sup>3</sup> )
HDPE	518±11	12.6±0.5	0.546	13.28
H0.5	583±13	14.2±0.3	0.626	15.24
H1	600±12	15.2±0.2	0.665	16.84
H3	631±14	15.3±0.4	0.712	17.26
H5	646±12	15.4±0.3	0.806	19.22

### 5.1.2 Flexural responses of the FGNCs

The 3D printed FGNCs are also tested for the flexural responses in the 3-point bending mode, as shown in Figure 5.2a-b. The flexural responses of the 3D printed FGNCs are depicted in Figure 5.2c, while the corresponding values are presented in Table 5.2. It is noticed that none of the tested specimens fail until the maximum applied load (20 kN-load cell) or 10% flexural strain. The strength of the pure HDPE, FGNC-1 and FGNC-2 are 12.60 MPa, 15.34 MPa, and 16.20 MPa, while the modulus is observed to be 518 MPa, 635 MPa, and 657 MPa, respectively. It is observed that the strength and modulus of the FGNCs increase with the increasing MWCNTs content in the graded layer. The flexural moduli and strength of the FGNCs increase respectively by 21%-23% and 26%-29% more than the pure HDPE. The stress transfer mechanism in a pure and a composite material is entirely different. In the pure polymer, the applied stress is taken primarily by the molecular bonds of the polymer chains such as covalent bonds, which are primary bonds and strong, whereas, in the case of the composite, the applied stress is taken by the interfacial bonds between the matrix and the filler, which are secondary bonds such as Van der Waals forces. These Van der Waals forces might be stronger or weaker than the primary bonds depending upon the interaction between the fillers and the matrix materials. The modulus and strength of the composite depend on the interfacial bonds only. The strong interfacial bonds offer high strength and modulus in the composite, indicating the stronger Van der Waals forces between the matrix and the filler than the primary bonds. Moreover, the matrix flow is effectively restricted by the networks formed by the functionalized MWCNTs, enhancing the flexural properties (Beesetty et al. 2020). The micrographs of the FGNC-2 post the flexural test show that the HDPE effectively grips the functionalized MWCNTs (Figure 5.2d-e), which further shows the enhanced attraction between the HDPE chains and the nanoscale reinforcement, resulting in enhancements in the strength and moduli (Beesetty et al. 2020). The FGNC-2 exhibited the highest flexural properties such as modulus (26.83%) and strength (28.57%) due to the higher MWCNTs content in each graded layer capable of bearing more load than the FGNC-1. The specific flexural properties are crucial for the lightweight applications such as marine, aerospace, and automobile to improve fuel efficiency (H S et al. 2020). Therefore, the specific strength and modulus are also

presented in Table 5.3. The specific modulus and strength are found to enhance as the filler content rises in the graded layers, as observed in Figure 5.3. The FGNC-1 and 2's specific modulus is 29.67% and 44.14%, whereas the specific strength is 28.91% and 46.16% higher than the pure HDPE. The FGNC-2 showed the maximum specific modulus and strength, which are 44.14% and 46.16% higher than the HDPE. Further, the flexural moduli and the strength of the FGNCs are also compared with the corresponding homogeneous NCs. The moduli of the H0.5, H1, H3, and H5 are  $583 \pm 13.00$ ,  $600 \pm 12.00$ ,  $631 \pm 14.00$ , and  $646 \pm 12.00$  MPa, while the strength are  $14.20 \pm 0.3$ ,  $15.20 \pm 0.2$ ,  $15.30 \pm 0.4$ , and  $15.40 \pm 0.3$  MPa, respectively (Kumar 2022). The flexural properties such as moduli and strength of the FGNCs are higher than those of the corresponding homogeneous NCs. This may be attributed to the effective stress transfer between each layer of the FGNCs due to the seamless bonding between the graded layers during 3D printing. Moreover, the FGNC-2 exhibited the highest flexural properties due to the higher MWCNTs content in each graded layer, which made it capable of bearing more load than the FGNC-1. The specific strength of the H0.5, H1, H3, and H5 are 15.24, 16.84, 17.26, and 19.22 MPa/kg/m<sup>3</sup> × 10<sup>-3</sup>, while the specific moduli are 0.626, 0.665, 0.712, and 0.806 MPa/kg/m<sup>3</sup> (Kumar 2022). The specific flexural properties of the FGNCs are observed to be lower than the respective NCs due to their higher density. It is noticed that the 3D printed FGNCs exhibited the higher flexural moduli and strength than the homogeneously reinforced NCs, showing the better performance than the NCs, and hence can be applied instead of the NCs. Moreover, it can also be utilized where varying stiffness and strength are required.



(a)

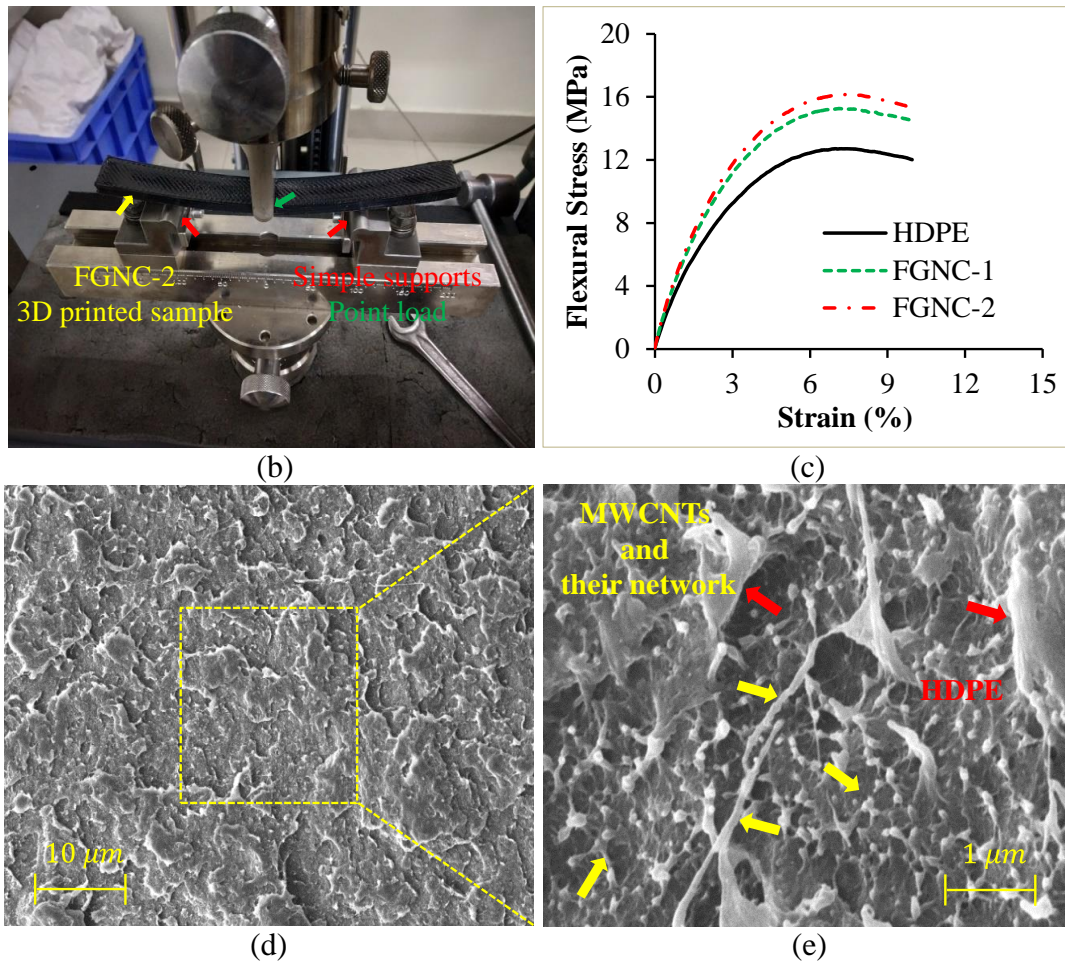


Figure 5.2. (a) Schematic representation of three-point bending test, (b) experimental setup, (c) flexural results, and (d)-(e) SEM images of the tested FGNC-2 sample, showing MWCNTs uniform distribution and their networks.

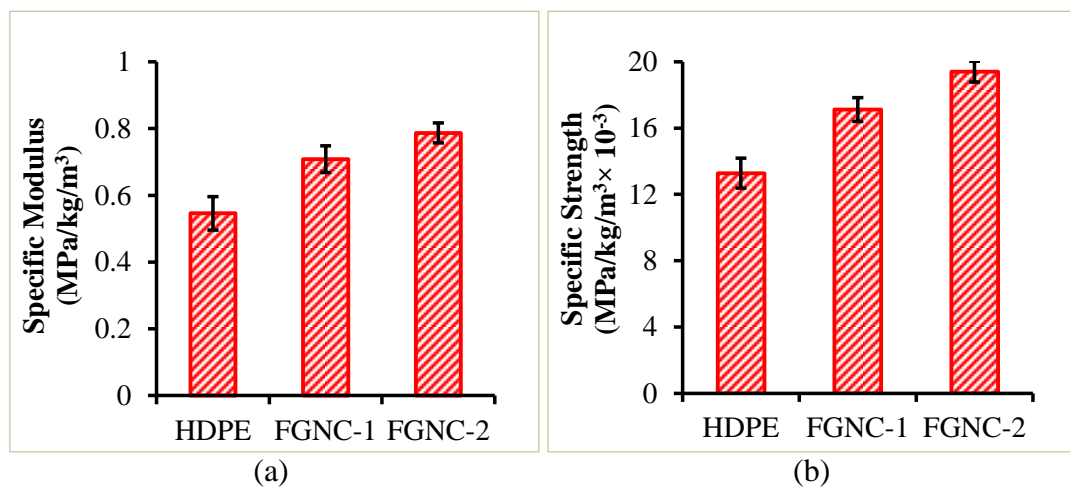


Figure 5.3. Specific flexural properties of 3D printed FGNCs: (a) specific modulus and (b) specific strength.

Table 5.2. Flexural properties of the 3D printed FGNCs.

Composition	Modulus (MPa)	Strength (MPa)
HDPE	518±11.00	12.60±0.5
FGNC-1	635±12.72	15.34±0.1
FGNC-2	657±09.43	16.20±0.2

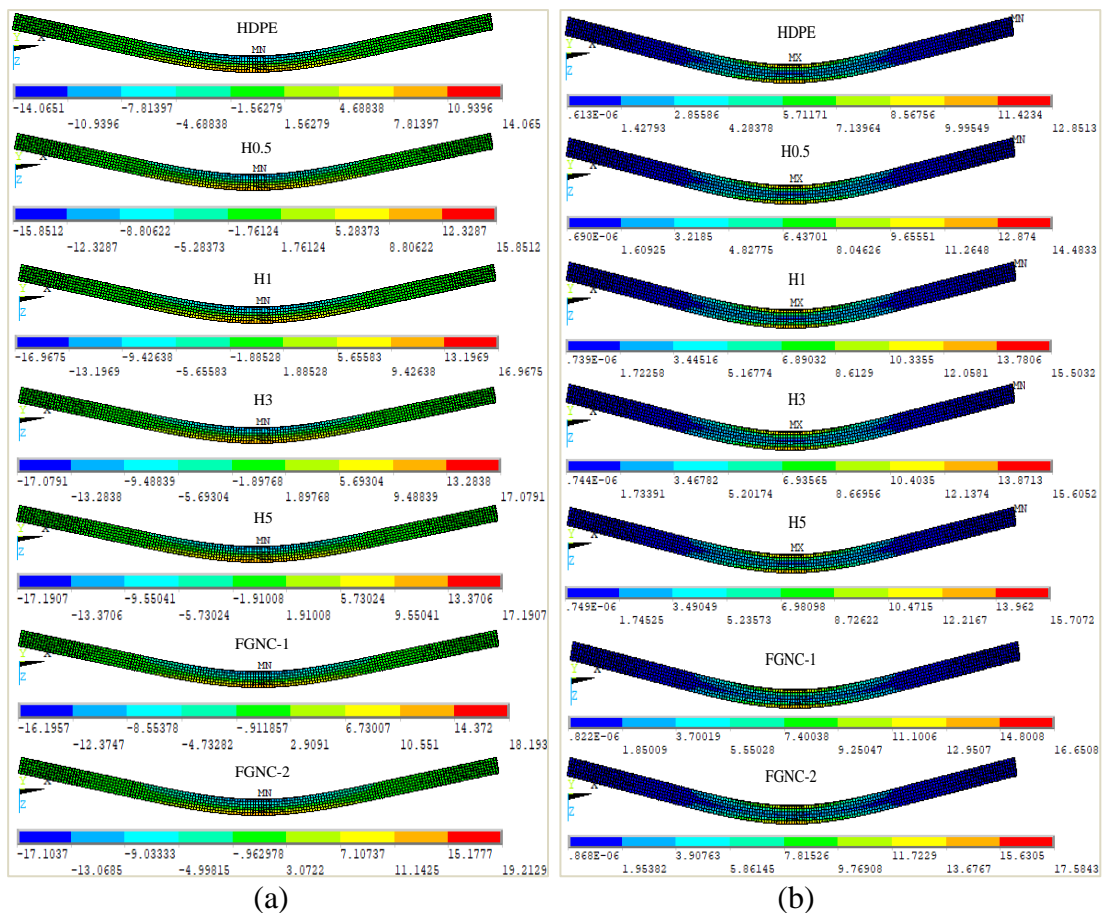
Table 5.3. Specific flexural properties of the 3D printed FGNCs.

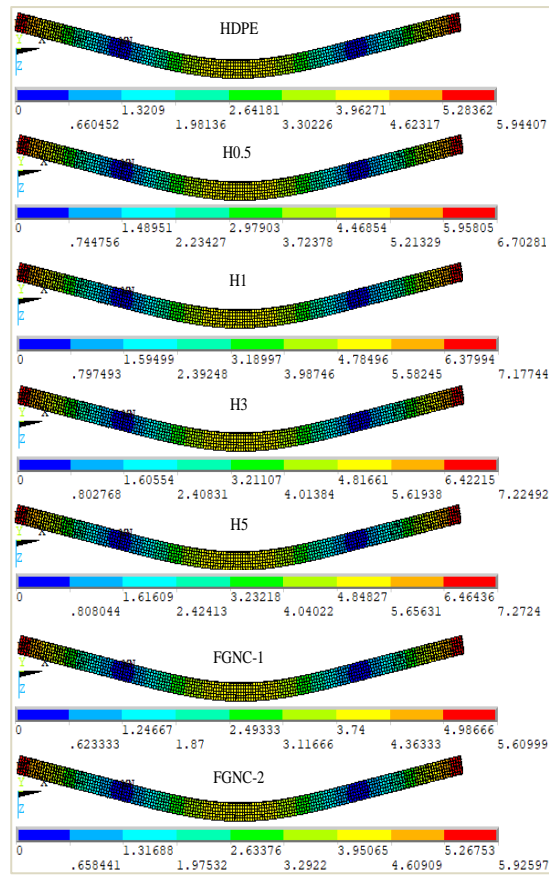
Composition	Specific modulus (MPa/kg/m <sup>3</sup> )	Specific strength (MPa/kg/m <sup>3</sup> × 10 <sup>-3</sup> )
HDPE	0.546±0.05	13.28±0.90
FGNC-1	0.708±0.04	17.12±0.71
FGNC-2	0.787±0.03	19.41±0.63

## 5.2 Numerical investigation

The numerical study helps in predicting and optimizing the results. It also helps in validating the experimental procedure and the results. In this work, the numerical analysis of the flexural properties is performed to validate the experimental flexural results of the 3D printed NCs and FGNCs. The maximum von Mises stress and the mid-point deflection values are utilized to validate the experimental flexural strength and the modulus, respectively. The stress distribution in the X-direction, the von Mises stress distribution, and the mid-point deflection are presented in Figure 5.4. For the NCs, it is noticed that the stress distribution in the X-direction in both tensile and compressive sides are equal (Figure 5.4a), which shows the similar stress distribution in both sides with respect to the neutral axis, confirming the flexural behavior of the homogeneous materials, while in the case of the FGNCs, the stress distribution is not the same. For the FGNCs, the stress distribution in the X-direction on the tensile side is higher than on the compressive side, showing their heterogeneous behavior and witnessing their neutral axis shift towards the composition with the higher modulus (Figure 5.4a). A similar behavior is observed in the previous study (Gupta 2008). The numerical outcomes of the flexural stresses and the deflection of the NCs and the FGNCs show a similar trend as experimental outcomes (Figure 5.4b-c). The comparison of the experimental and numerical results is displayed in Table 5.4. It is noticed that the FEA findings closely predict the experimental trend, with a %

difference of less than ~8% and 3.5% for the stresses and the mid-point deflections, respectively. The FE results overpredict the stresses and the mid-point deflections compared to the experimental results, which is attributed to some defects in the 3D printed NCs and FGNCs (Gupta 2008). Such FE simulation predictions convey information about the stress concentration of expensive experimental methodologies beforehand. Thus, the functionalized MWCNTs reinforced HDPE based 3D printed FGNCs showed the superior flexural behavior compared to the pure HDPE and the homogeneously reinforced NCs. The FGNC-2 exhibited the superior behavior, making it a preferred and promising choice for marine, aerospace, automotive, and biomedical applications, offering a variational stiffness as required by the envisaged applications.





(c)

Figure 5.4. FE plots of (a) stress distribution in X-direction, (b) von-Mises stress distribution, and (c) mid-point deflection of the NCs and FGNCs.

Table 5.4. Comparison between experimental and numerical results.

Composition	Stress (MPa)			Mid-point deflection (mm)		
	Experimental	FEA	% Difference compared to FEA results	Experimental	FEA	% Difference compared to FEA results
HDPE	12.60±0.5	12.85	1.94	5.73±0.21	5.94	3.53
H0.5	14.20±0.3	14.48	1.93	6.53±0.13	6.70	2.54
H1	15.20±0.2	15.50	1.93	6.98±0.17	7.18	2.78
H3	15.30±0.4	15.60	1.92	6.91±0.23	7.22	4.29
H5	15.40±0.3	15.70	1.91	7.09±0.16	7.27	2.47
FGNC-1	15.34±0.1	16.65	7.87	5.48±0.14	5.61	2.32
FGNC-2	16.20±0.2	17.58	7.85	5.71±0.11	5.92	3.55

### 5.3 Conclusion

The 3D printed NCs and FGNCs are investigated experimentally and numerically for the flexural properties. The results are summarized below.

- The flexural modulus and strength of the 3D NCs increase with the MWCNTs increase. The modulus increased by 12.55%, 15.83%, 21.81%, and 24.71%, while the strength increased by 12.70%, 20.63%, 21.43%, and 22.23% in the H0.5-H5 respectively, when compared to the pure HDPE sample.
- The H5 NC exhibited 24.71% and 22.23% higher modulus and strength, respectively, compared to the neat HDPE.
- Among all the 3D printed NCs, the H5 composition exhibited the superior mechanical properties.
- The specific strength and modulus of the NCs increased with the filler loadings. The H5 NC showed the highest specific modulus and strength among all the NCs, 47.62% and 44.73% higher than the HDPE.
- The flexural moduli and strength increase with the nanoscale filler loading in the graded layer.
- The highest flexural strength and moduli are exhibited by the FGNC-2, which are 28.57% and 26.83% higher compared to the HDPE, respectively.
- Further, the highest specific strength and modulus are exhibited by the FGNC-2, which are 46.16% and 44.14%, respectively, higher than the HDPE.
- The experimental findings matched well with the FEA results.

These flexural results of the 3D printed NCs will help design and develop integrated and complex geometrical functional and structural parts subjected to transverse load, while of the FGNCs will help in designing structures needing variational stiffness and strength features under the transverse load for different applications such as marine, automobile, aerospace, biomedical, electronics, and defense.



## 6 COMPRESSION, HARDNESS AND IMPACT BEHAVIOUR

### 6.1 Compression responses of the NCs

The 3D printed NCs are also tested for the compression behavior. Figure 6.1 depicts the compression responses with the numerical values in Table 6.1. It is found that the prints' compressive modulus increases with the loading of the functionalized MWCNTs. The modulus values of the 3D printed H0.5-H5 NCs are 12.81%, 18.71%, 23.32%, and 44.89% higher than the respective HDPE print. The highest modulus is observed for the H5 NC. It is also observed that the yield strength of the prints rises with the functionalized MWCNTs content. The yield strength of the H0.5-H5 prints is 1.07%, 3.89%, 7.04%, and 9.28% higher than the HDPE, respectively. The highest yield strength is observed for the H5 NC. The increase in the modulus is due to the strong interfacial adhesion between the HDPE and the functionalized MWCNTs. The strong interfacial interaction absorbs the higher amount of strain energy for the same amount of deformation within the elastic limit, which increases modulus. The strength increase is attributed to the uniform distribution of the functionalized MWCNTs in the HDPE, which helps in the effective compressive load transfer from the matrix to the fillers, resulting in higher load bearing capability of the composites. The prints' yield strain and the energy absorption decrease as the functionalized MWCNTs content increases, showing the reduction in ductility due to decrease in the HDPE proportion, which is responsible for the deformation in the composites. The peak stress of the 3D printed NCs (H0.5-H5) slightly increases, whereas the peak strain decreases with an increase in the functionalized MWCNTs content compared to the HDPE as the stiffer functionalized MWCNTs content increases. No layer delamination post 3DP (Figure 6.2a) is observed, indicating the chosen parameters' suitability for the functionalized MWCNT/HDPE NCs. The larger lamellas size of the as-3D printed H5 NC (Figure 6.2b) than the post compression tested H5 NC (Figure 6.2c) shows the compression phenomenon and ductile deformation in the 3D printed samples. The crystalline region is responsible for the ductile deformation, while the amorphous region is responsible for the brittle fracture in the HDPE. Only the ductile deformation was observed for all the 3D printed samples, showing two different deformation regions: the elastic and the plastic regions (higher deformation regions with low stress). Figure

6.2d-e shows the higher magnification SEM images of the tested H5 NC, showing no visible cracks. Due to addition of the stiffer functionalized MWCNTs in the HDPE, very less deformation was observed in the elastic region. In contrast, the higher deformation was observed in the plastic region due to the brittle fracture of the surfaces (Figure 6.2f), resulting in the decreased energy absorption. Due to the compressive load, the absence of crack, fracture, and fragmentation in the 3D printed samples clearly indicates the homogeneous functionalized MWCNTs dispersion in the HDPE (Figure 6.2g-i) (Jeyachandran 2022). The 3D printed NCs exhibited the superior compressive modulus, yield strength, and peak stress compared to the HDPE, exhibiting their potential for marine, naval, aerospace, military, medicals, food packaging, automobiles, and various engineering applications where the integrated jointless components are subjected to the compressive loads.

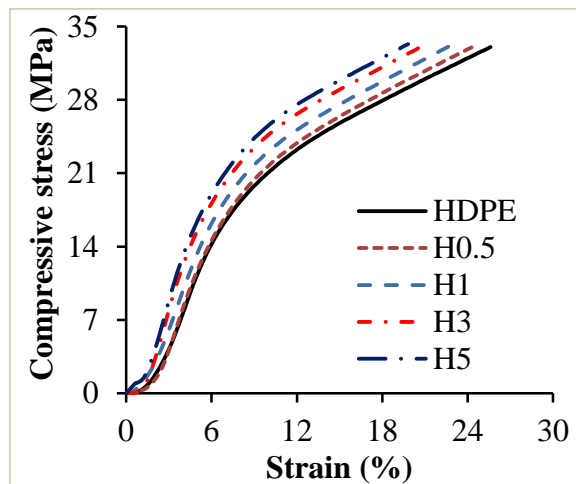


Figure 6.1. The compressive properties of the 3D printed NCs.

Table 6.1. Compressive properties of the 3D printed NCs.

Configuration	Compressive Modulus (MPa)	Yield strength (MPa)	Yield strain (%)	Peak stress (MPa)	Peak strain (%)	Energy absorption (MJ/m <sup>3</sup> )
HDPE	301.32±6.42	20.59±0.12	9.60±0.02	33.04±0.03	25.61±0.12	5.32±0.14
H0.5	339.93±5.36	20.81±0.24	9.29±0.03	33.19±0.04	24.51±0.04	5.10±0.11
H1	357.71±4.29	21.39±0.28	8.65±0.01	33.27±0.08	22.89±0.08	4.89±0.13
H3	371.60±7.10	22.04±0.19	8.04±0.04	33.29±0.19	21.02±0.09	4.58±0.09
H5	436.58±5.17	22.50±0.13	7.94±0.05	33.33±0.33	19.82±0.06	4.36±0.15

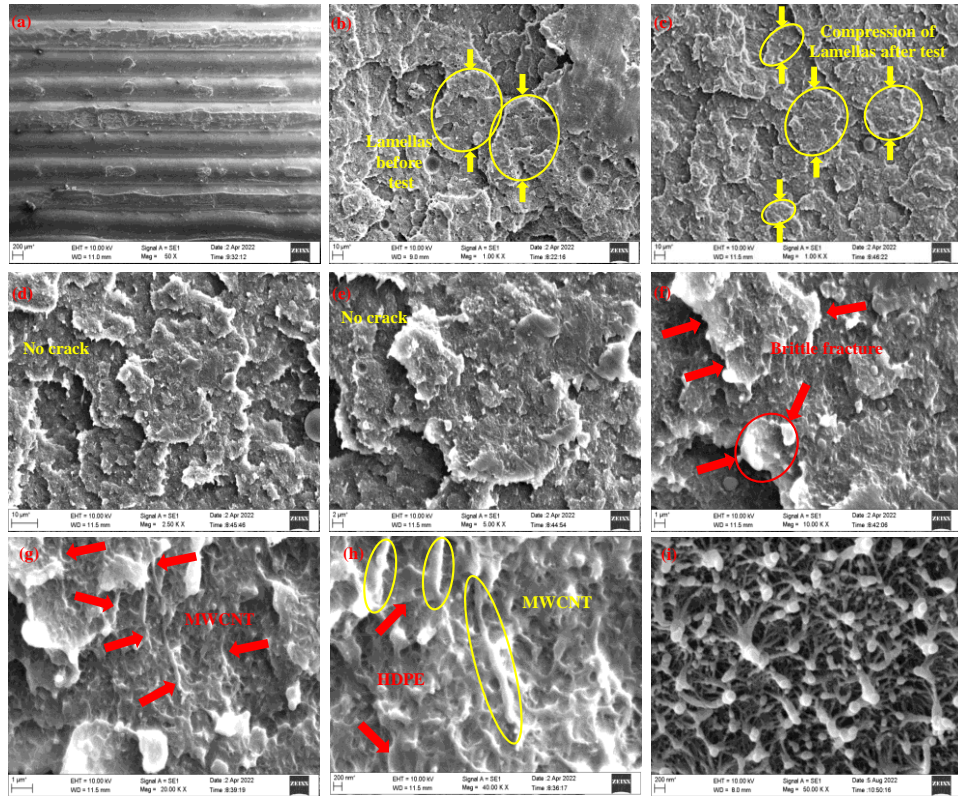


Figure 6.2. Representative SEM images of freeze-fractured as 3D printed and post tested H5 sample.

## 6.2 Compression responses of the FGNCs

The compression test is conducted on the 3D printed FGNCs also. The ductile deformation without any crack is predominantly observed in all the FGNCs during the compression test (Figure 6.3, Table 6.2). The FGNCs' compressive modulus is higher than the pure HDPE and increases as the content of the functionalized MWCNTs increases in each graded layer. The compressive modulus of the FGNC-1 and the FGNC-2 increases, respectively by 35.75% and 61.14% compared to the HDPE. The FGNC-2 (H1→H3→H5) exhibits the peak compressive moduli. The strong interface between the functionalized MWCNTs and the HDPE and the seamless/perfect bonding/diffusion between the layers lead to higher moduli. Moreover, the enhanced interfacial adhesion between the constituents and across the layered interfaces absorbs more strain energies for a given deformation within the elastic limit, raising the compressive modulus. The good diffusion of the layers into each other indicates the seamless/perfect bonding between them. Further, the homogeneous distribution and the strong interfacial bonding between the constituents increase the modulus. For the

same strain, the load-carrying capacity increases with the filler addition (Figure 6.3), indicating a rise in the modulus and yield strength. The yield strengths of the FGNC-1 and FGNC-2 are 8.89% and 11.56% higher than the HDPE. The FGNC-2 exhibited the highest yield strength owing to the homogeneous distribution of the functionalized MWCNTs in the HDPE, facilitating the effective load transfer and increasing load-taking capability. The yield strain and the energy absorption of the FGNCs decrease due to reduction in the matrix ductility, which is accountable for the composite deformation. The addition of the brittle and stiffer functionalized MWCNTs lowers the composite ductility. The peak stress also rises slightly while the peak strain falls as the content of the functionalized MWCNTs increases in each graded layer. A sudden drop in the stress at the peak point is observed. The previous studies also reveal the similar trend for the compressive properties of the composites (Dileep 2021, Jeyachandran 2022, Kumar 2022, Patil et al. 2019). The ductile deformation and the compression phenomenon of the FGNC-2 are shown in Figure 6.4. Figure 6.4a-b shows the SEM images of the FGNC-2 before and after the compression test. The size of the lamellas before the compression test is observed to be greater than the size post the compression test, which shows the ductile deformation. The amorphous and the crystalline regions of the HDPE are responsible for the brittle and ductile deformations, respectively. The ductile deformation is observed, revealing two different deformation zones: the elastic region, showing very less deformation due to inclusion of the functionalized and stiffer MWCNTs, and the plastic region, showing higher deformation zones due to the brittle fracture (Figure 6.4c) (Jeyachandran 2022, Kumar 2022). No cracks and fractures are observed in the FGNC-2 during and after the compression test (Figure 6.4d), reaffirming the homogeneous distribution of the functionalized MWCNTs in the HDPE. The compression responses of the 3D printed FGNCs are also compared with the 3D printed homogeneously reinforced NCs (Table 6.1 and Figure 6.1). The compressive modulus and strength of the FGNCs are higher than those of the respective NCs, exhibiting better performance than those of the NCs. This is attributed to the gradient of the different composite materials and the seamless bonding between them. Thus, the FGNCs have exhibited the superior mechanical properties, implying the possible potential usage requiring variational stiffness (Kumar 2022). The present work demonstrates the successful development of the 3D

printed FGNCs without manufacturing defects. The industries can use the parameters and methods for 3D printing of the FGNCs to develop different products/parts for specified applications. Moreover, these 3D printed FGNCs have been tested for the hardness, toughness, and compression responses. The results obtained can be used by design community for designing functional components/structures subjected to compressive load for various engineering applications.

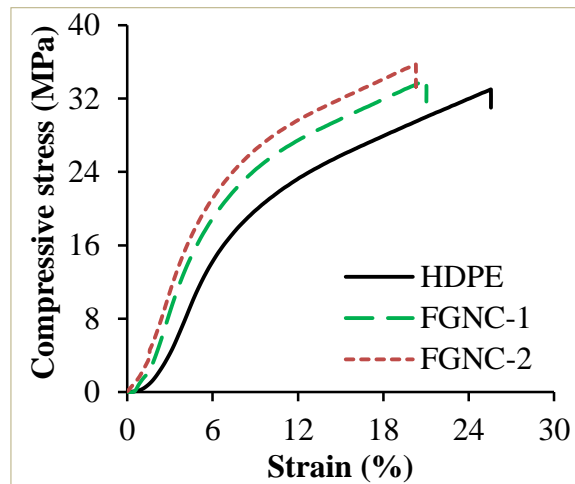
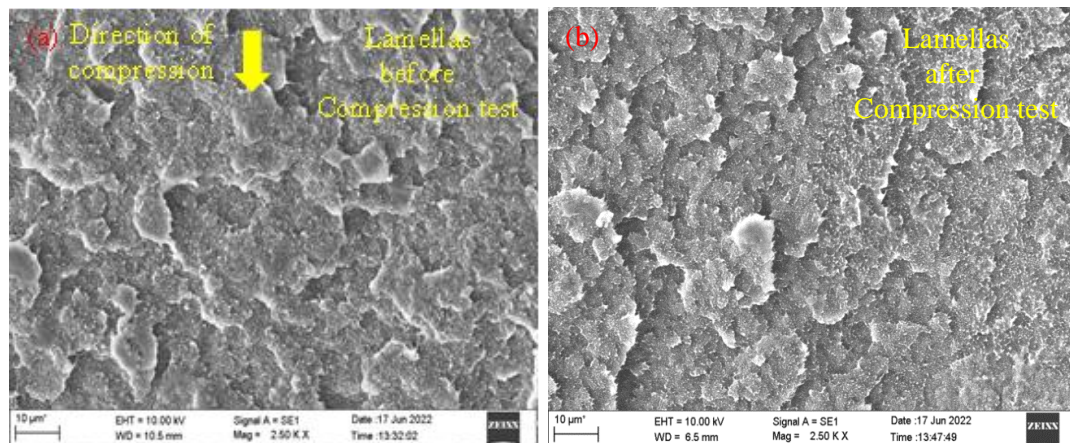


Figure 6.3. Compressive responses of the 3D printed FGNCs.

Table 6.2. Compressive responses of the 3D printed FGNCs.

Composition	Moduli (MPa)	Yield strength (MPa)	Yield strain (%)	Peak stress (MPa)	Peak strain (%)	Energy absorption (MJ/m <sup>3</sup> )
FGNC-1	409.03±2.01	22.42±0.13	8.02±0.01	34.08±0.01	21.03±0.02	4.61±0.11
FGNC-2	485.56±3.97	22.97±0.09	7.86±0.04	35.74±0.03	20.29±0.03	4.43±0.13



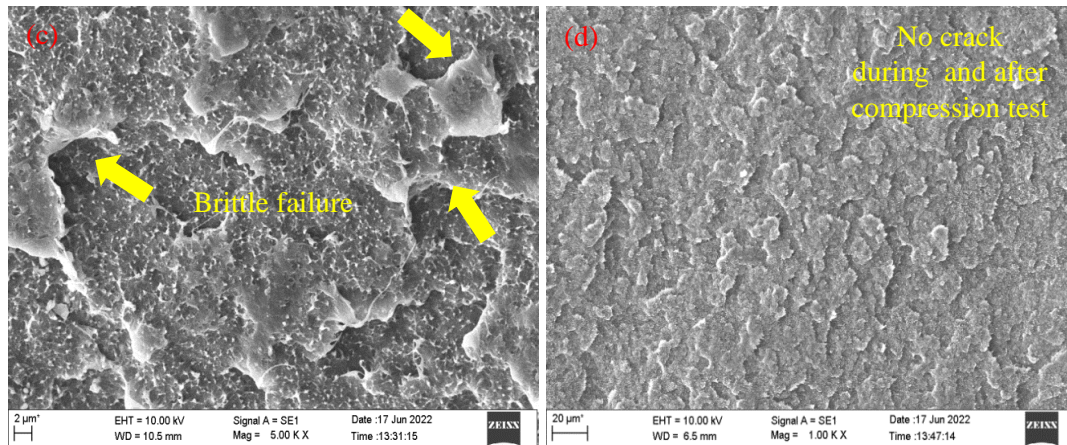


Figure 6.4. SEM images of the pre and post tested FGNC-2 sample showing (a)-(b) compression, (c) brittle fracture and (d) FGNC-2 without crack.

### 6.3 Hardness and impact responses

The hardness and impact tests are also conducted on the 3D printed NCs and the FGNCs. The hardness increases for the H0.5-H5 NCs from 44.15%-65.60% compared to the HDPE with increase in the MWCNTs (Table 6.3), possibly due to the homogeneous distribution of the MWCNTs providing a strengthening effect. The NCs' gradation improved the FGNCs' hardness from 66.80%-76.80% compared to the HDPE. The interfacial interaction/diffusion of the graded compositions enhances the toughness, hence the hardness. The impact strength of the H0.5-H5 NCs increased from 42.56%-89.25% compared to the HDPE with the increasing MWCNTs due to the increased toughness. The impact strength of the FGNCs increased from 104.49%-119.99% due to the toughness gradation. The gradation enables effective stress distribution among the layers. Furthermore, the seamless bonding between the two different compositions enhances the mechanical properties.

Table 6.3. Rockwell hardness and impact strength of the 3D printed materials.

Composition	Rockwell hardness (M scale)	Impact strength (kJ/m <sup>2</sup> )
HDPE	45.21±0.8	20.56±1.3
H0.5	65.17±1.0	29.31±0.4
H1	68.30±0.9	33.10±0.9
H3	70.91±1.2	35.26±1.4
H5	74.87±0.5	38.91±0.3
FGNC-1	75.41±0.6	42.12±0.7
FGNC-2	79.93±1.3	45.23±0.9

*M scale* → 100 kg major load, 6.35 mm indenting ball diameter.

#### 6.4 Conclusion

The compression, hardness, and impact studies are conducted on the 3D printed NCs and the FGNCs. The results drawn are given below.

- The MWCNTs addition increases the modulus and yield strength of the 3D printed NCs and the FGNCs. The highest compressive modulus and yield strength found for the H5 NC, respectively, are 44.89% and 9.28%, compared to the pure HDPE.
- The FGNCs' compressive modulus is found to be higher than the pure HDPE and increases as the content of the functionalized MWCNTs increases in each graded layer.
- The compressive modulus of the FGNC-1 and FGNC-2 increases, respectively by 35.75% and 61.14% compared to the pure HDPE. The FGNC-2 exhibited the peak compressive moduli.
- The yield strength of the FGNCs increases with the MWCNTs addition. The yield strengths of the FGNC-1 and FGNC-2 are found to be 8.89% and 11.56% higher than the HDPE. The FGNC-2 exhibited the highest yield strength owing to the homogeneous distribution of the functionalized MWCNTs in the HDPE.
- The FGNC-2 exhibited the highest hardness and impact strength, respectively 76.80% and 119.99% higher than the pure HDPE.

- All at once, 3D printed FGNCs help design and fabricate complex geometrical integrated functional parts for different applications requiring variational stiffness.

## 7 MECHANICAL BUCKLING AND FREE VIBRATION BEHAVIOUR

### 7.1 Mechanical buckling studies

The buckling test is conducted for the 3D printed HDPE, NCs, and FGNCs with no slipping at the clamped supports. The global buckling is observed in all the 3D printed samples with a maximum deflection at the middle of the span length. No separation between the 3D printed layers (delamination) was detected in the buckled specimen, which shows that all the specimens were 3D printed with the suitable 3D printing parameters (Table 2.4), having seamless and strong bonding between each layer. The load-deflection curves of the 3D printed HDPE, NC, and FGNC samples obtained through the buckling test are presented in Figure 7.1, and the corresponding calculated values of the  $P_{cr}$  using the DTM and MBC methods are presented in Table 7.1. It is found that the  $P_{cr}$  of the NCs increases with the functionalized filler addition than the HDPE (Figure 7.1a and Figure 7.1b). The  $P_{cr}$  of the H0.5, H1, H3 and H5 calculated from the DTM and MBC methods increases by 16.40%, 19.49%, 44.03% and 79.03%, and 15.95%, 18.81%, 43.90% and 79.13%, respectively than the pure HDPE. The maximum  $P_{cr}$  is observed for the H5 NC among all the NCs. The increase in  $P_{cr}$  of the 3D printed NCs is because of the MWCNTs into the HDPE, which results in a rise in the elastic modulus and structural stiffness. The rise in the elastic modulus increases the buckling strength, increasing the load carrying capacity of the 3D printed NCs. The highest  $P_{cr}$  of the H5 NC is due to the highest filling of the functionalized fillers into the HDPE. From Figure 7.1c, it is also found that the  $P_{cr}$  of the 3D printed FGNCs increases as the functionalized MWCNTs increase in each layer. The  $P_{cr}$  of the FGNC-1 and FGNC-2 calculated from the DTM and MBC methods increases by 54.38% and 91.34%, and 54.62% and 90.62%, than the HDPE. The highest  $P_{cr}$  is observed for the FGNC-2. The addition of the functionalized MWCNTs as the filler having higher modulus than the HDPE improves the stiffness, which further increases the buckling strength of the 3D printed FGNC (Dileep 2021). From Table 7.1, it is also observed that the  $P_{cr}$  obtained from the DTM is higher than the  $P_{cr}$  obtained from the MBC method, which clearly indicates that the DTM estimates higher  $P_{cr}$ , ~ 2% to 5% than the MBC method. The buckling analysis of all

the 3D printed NCs and FGNCs show that the buckling strength is higher for the H5 NC and the FGNC-2 among all the 3D printed NC and FGNCs, respectively.

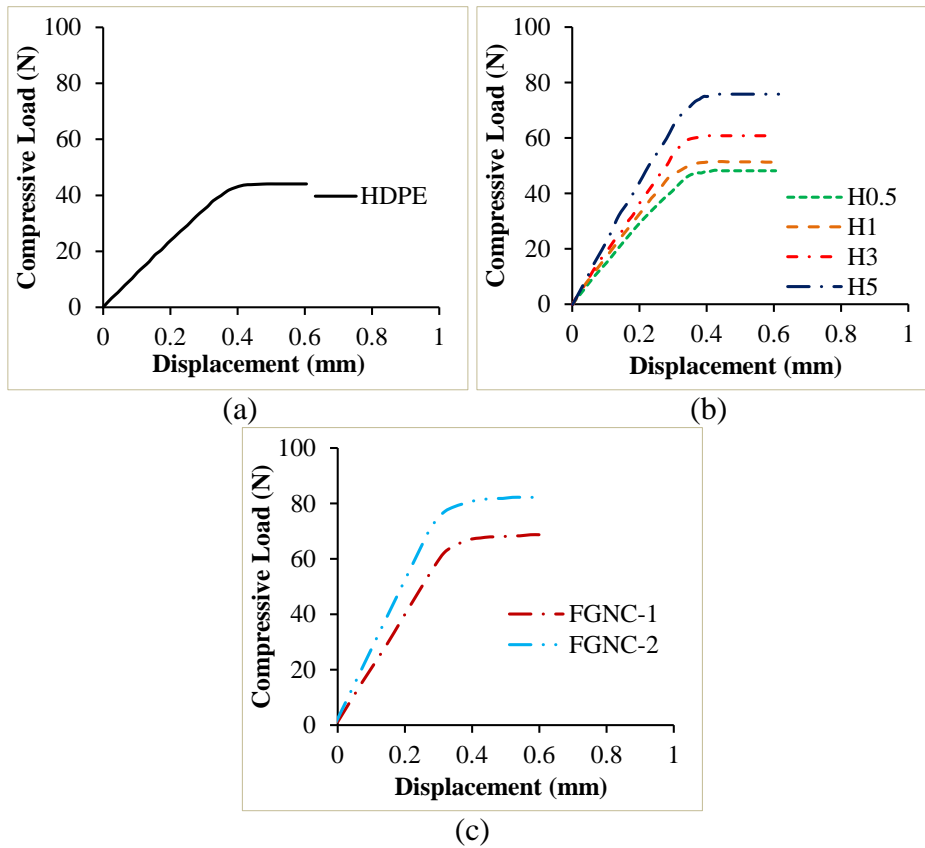


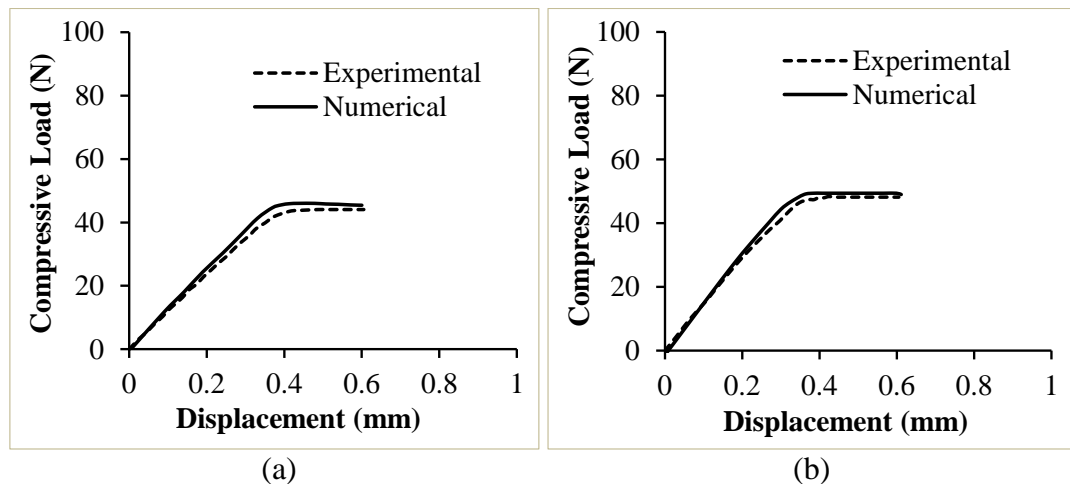
Figure 7.1. Load-deflection curve of 3D printed (a) neat HDPE, (b) NC and (c) FGNC.

Table 7.1. Critical buckling load ( $P_{cr}$ ) of 3D printed samples.

Composition	Critical Buckling Load, $P_{cr}$ (N)				Deviation of experimental with respect to numerical results (%)	
	Experimental		Numerical		DTM	MBC
	DTM	MBC	DTM	MBC		
HDPE	42.02±1.06	41.25±1.02	43.57	42.28	3.56	2.44
H0.5	48.91±1.11	47.83±0.98	50.59	48.76	3.32	1.91
H1	50.21±1.02	49.01±1.17	52.03	50.96	3.50	3.83
H3	60.52±1.54	59.36±1.38	62.31	61.15	2.87	2.93
H5	75.23±1.22	73.89±1.84	76.94	75.39	2.22	1.99
FGNC-1	64.87±1.03	63.78±1.23	65.88	65.37	1.53	2.43
FGNC-2	80.40±1.65	78.63±1.37	82.25	80.16	2.25	1.91

### 7.1.1 Comparison of the experimental and numerical buckling load

The experimental buckling results are validated by the numerical buckling results. In the numerical analysis, initially, a linear eigenvalue buckling analysis is carried out, from where; the buckled shape of the FE model is obtained. In order to perform the non-linear buckling analysis, the shape obtained through the linear buckling analysis is updated in the software, and then the static analysis is carried out. After this stage, the non-linear load-deflection curve is obtained. From the curve, numerical  $P_{cr}$  is obtained using the DTM and MBC methods for the comparison with the experimental values. Figure 7.2 compares the numerically obtained load-deflection curves with the experimentally obtained load-deflection curves. The numerically obtained  $P_{cr}$  values of all the 3D printed samples, and the % deviation in the numerical and experimental values are listed in Table 7.1. The trend of the numerically obtained  $P_{cr}$  values of all the 3D printed samples is same as experimentally obtained  $P_{cr}$  values. It is clearly observed that the numerically deduced  $P_{cr}$  is a little greater than the experimentally obtained values. This difference for both the DTM and MBC methods is found in the range of  $\sim 1.5\%$  to  $3.6\%$ . The earlier investigation revealed that the higher numerical values than the experimental ones might be due to air voids, porosity, and assumed GIF values (Dileep 2021, Gupta 2008). In the current study, the SEM analysis reveals no porosity and air voids in the 3D printed sample. Therefore, the difference in the numerical and experimental  $P_{cr}$  may be because of the assumed GIF values (Dileep 2021, Gupta 2008). It is also observed that the numerical results for all the 3D printed samples match well with the experimental results with a GIF value of 0.0008.



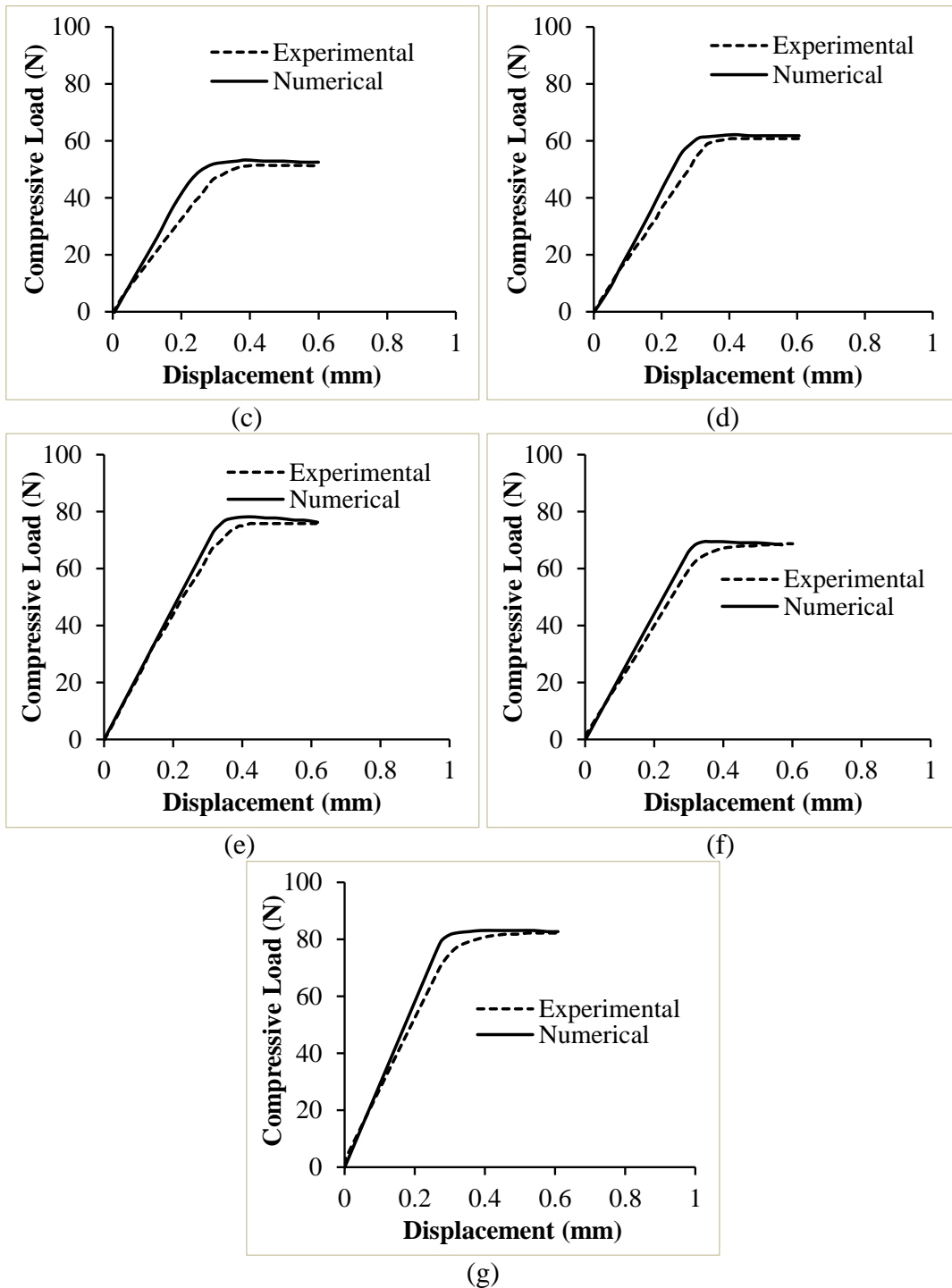


Figure 7.2. Comparison of experimental and numerical load-deflection curves of 3D printed (a) neat HDPE, (b) H0.5, (c) H1, (d) H3, (e) H5, (f) FGNC-1 and (g) FGNC-2.

## 7.2 Free vibration investigations

The axially compressive loaded components change their stiffness, further influencing the dynamic behavior (Bharath 2020). Therefore, studying free vibration is crucial for

designing components for dynamic applications. This work also investigates the free vibration behavior of the 3D printed neat HDPE, NCs and the FGNCs under no-loading and axial compressive loading conditions. The 3D printed samples are marked with ten points having equal distance (Figure 2.16b), and excited at each marked point with the help of an impact hammer. The associated FRF is measured with the use of an accelerometer. The typical FRF plots of the 3D printed H5 NC and FGNC-2 are presented in Figure 7.3. The first three natural frequency modes are identified from the FRF, and the corresponding values are taken. The graph between the natural frequency versus an axial compressive load of the 3D printed neat HDPE, NCs, and the FGNCs are presented in Figure 7.4. The corresponding outcomes are presented in Table 7.2. It is evident that the natural frequency corresponding to the first mode of the 3D printed NCs rises with the rise in the functionalized MWCNTs in the HDPE than the neat HDPE. The natural frequency of the 3D printed NCs increases in the range of 7.17%-41.14% compared to the HDPE. The increase in the natural frequency is due to the inclusion of the stiffer and functionalized MWCNTs in the neat HDPE, which increases the elastic modulus of the HDPE. The increase in the modulus of the HDPE matrix increases the stiffness, which further results in higher natural frequency. A similar trend has been found in the previous studies on isotropic composite columns and beams (Bharath 2020, Rajesh 2017). For the second and third modes, a similar trend for natural frequency is observed for the 3D printed NCs. It is also seen that the  $f_n$  corresponding to the 1<sup>st</sup> mode of the 3D printed NCs falls with the compressive load compared to the 3D printed neat HDPE. The same trend is found for the second and third modes. Due to application of the compressive load, the structure/component undergoes lateral deformation, which changes the mode shape of the structure. Due to change in the mode shape, the stiffness of the structural members reduces, which causes the decrease in the natural frequency. The similar trend is observed in Ref. (Bharath 2020). In the case of the 3D printed FGNCs, the  $f_n$  corresponding to the first mode is observed to be increasing with respect to the pure HDPE due to the increased stiffness of the 3D printed FGNCs compared to the HDPE. The 3D printed FGNCs natural frequency increases by 35.84%-46.20% compared to the HDPE. With a rise in the compressive loads, it is observed that the  $f_n$  of the 3D printed FGNC (FGNC-1 and FGNC-2) decreases compared to the HDPE. This can be attributed to the change in

the mode shape due to applying the compressive load, which reduces the stiffness and the natural frequency. The natural frequency of the additively manufactured HDPE, NCs and FGNCs are taken before and after the buckling. The similar trends are observed for post buckling (Table 7.2 and Figure 7.4). Figure 7.5 presents the damping factors of the 3D printed HDPE, NCs and FGNCs, showing the effect of the different compositions and axial compressive load. The corresponding damping factor values are presented in Table 7.3. The damping ratio of the 3D printed NCs falls with the rise in the MWCNTs% compared to the HDPE. This is due to increased stiffness due to the inclusion of the stiff and functionalized MWCNTs in the HDPE. It was also found that the damping ratio of the 3D printed NCs increases with the compressive load compared to the HDPE due to the stiffness loss, which, in turn, is caused by an increase in pre-stress. A similar observation is noted for the 3D printed FGNCs. A similar trend is also noted in Ref. (Dileep 2021).

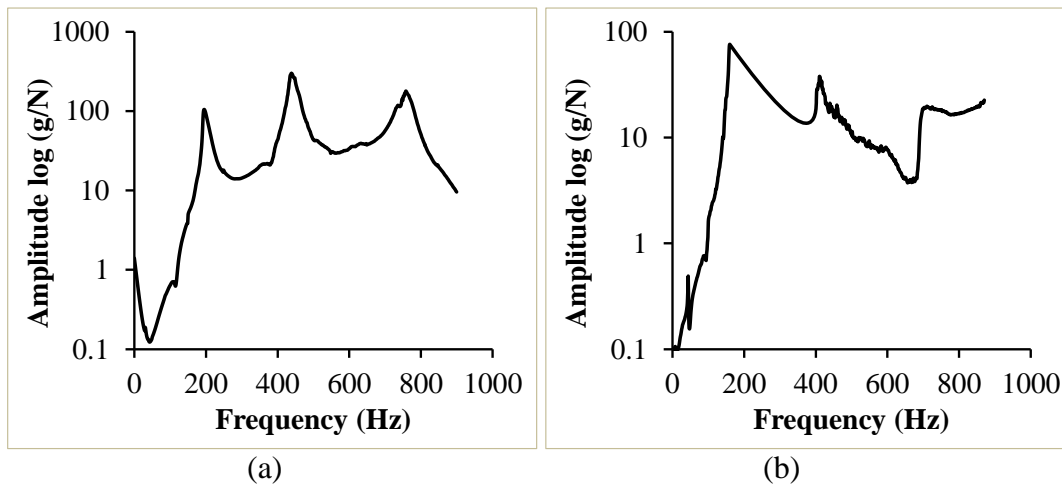
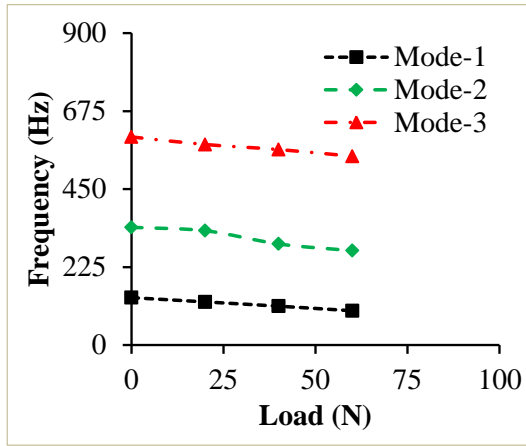
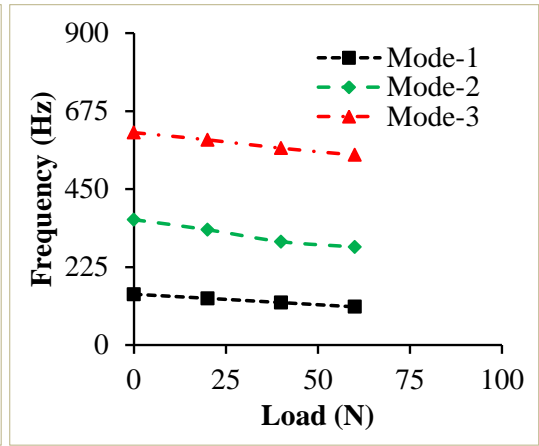


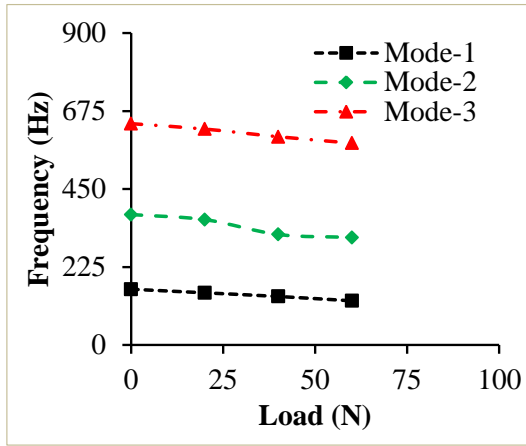
Figure 7.3. The FRF plots of the 3D printed (a) H5 NC and (b) FGNC-2 under no load conditions.



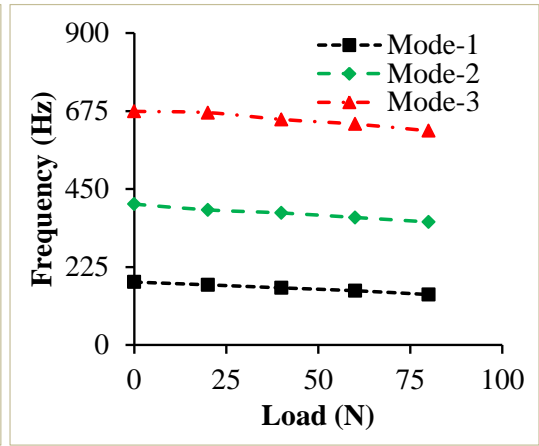
(a)



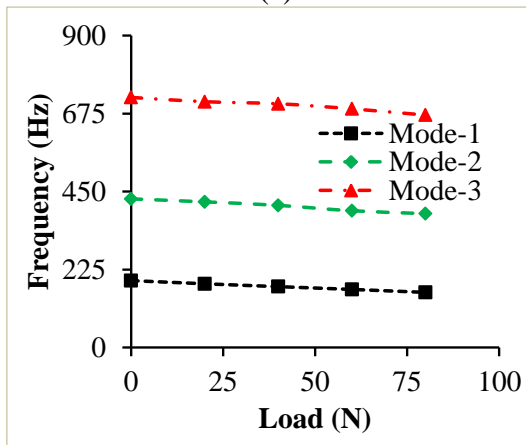
(b)



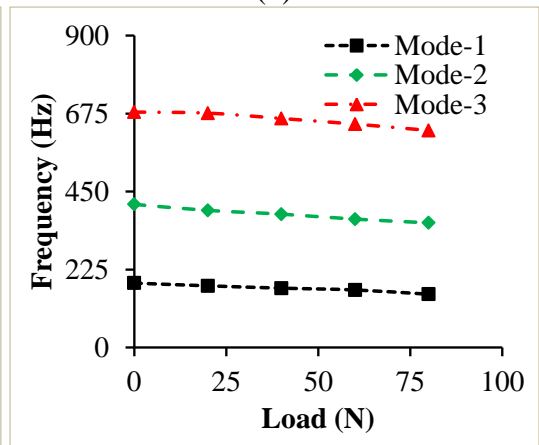
(c)



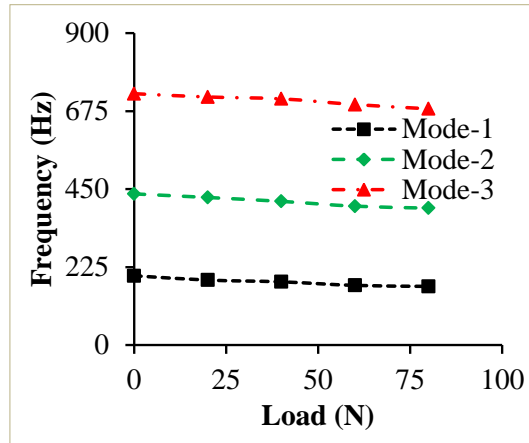
(d)



(e)



(f)

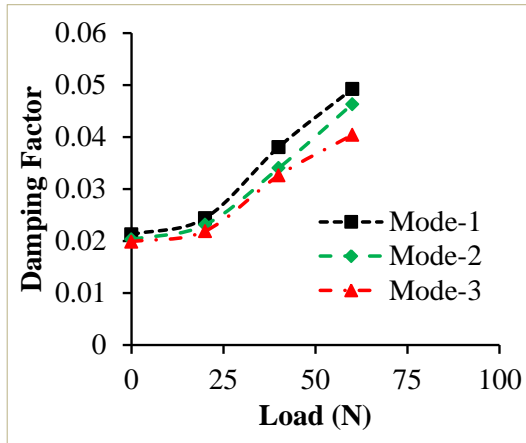


(g)

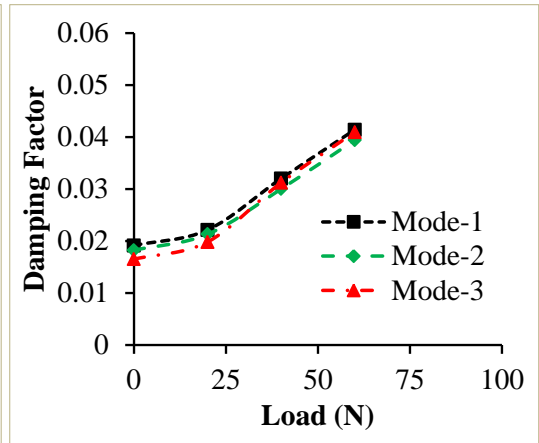
Figure 7.4. Variation of the natural frequency with the axial compressive load of 3D printed (a) neat HDPE, (b) H0.5, (c) H1, (d) H3, (e) H5, (f) FGNC-1 and (g) FGNC-2.

Table 7.2. Effect of compressive load on the natural frequency (Hz) of 3D printed samples.

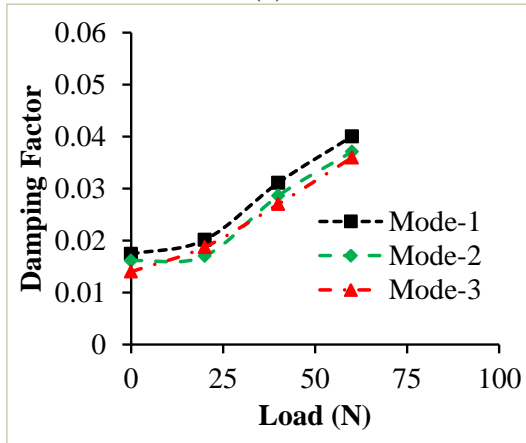
Composition	Mode	Load (N)					$P_{cr}$
		0	20	40	60	80	
HDPE	1	136.70	124.50	112.08	98.90	-	43
	2	339.66	329.80	291.60	272.20	-	
	3	600.55	578.73	564.09	544.83	-	
H0.5	1	146.50	134.75	122.43	110.19	-	49
	2	361.69	332.74	298.26	282.97	-	
	3	612.91	592.18	567.91	548.33	-	
H1	1	160.80	150.45	139.86	127.32	-	51
	2	376.24	361.61	318.80	310.17	-	
	3	638.56	622.99	600.85	582.38	-	
H3	1	181.37	173.45	164.64	156.53	145.37	62
	2	406.46	389.61	380.89	367.81	354.92	
	3	673.96	670.29	650.77	637.34	617.84	
H5	1	192.94	183.80	175.51	167.48	158.94	76
	2	428.79	420.14	410.04	394.52	386.22	
	3	721.58	709.20	703.24	688.63	670.51	
FGNC-1	1	185.69	177.90	171.16	165.97	153.61	65
	2	412.90	395.58	384.70	370.33	359.69	
	3	679.26	676.28	660.79	644.52	626.27	
FGNC-2	1	199.86	187.39	182.32	172.05	169.21	81
	2	436.13	425.74	414.53	400.63	395.06	
	3	725.23	715.75	710.33	693.89	681.59	



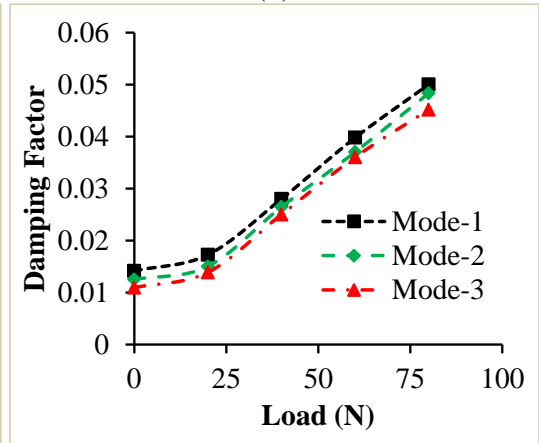
(a)



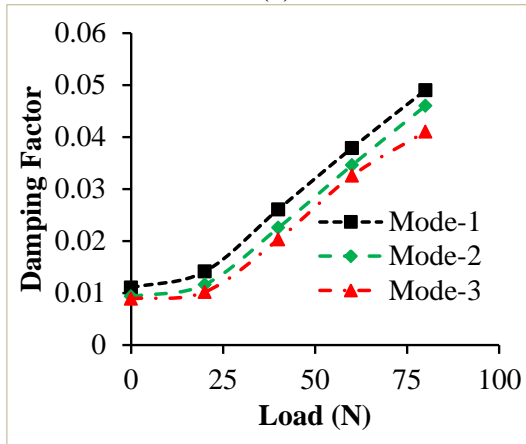
(b)



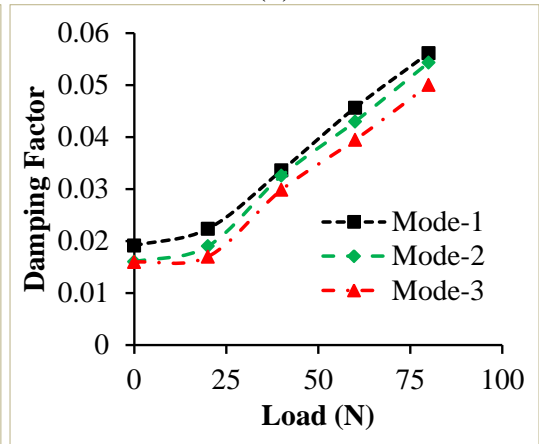
(c)



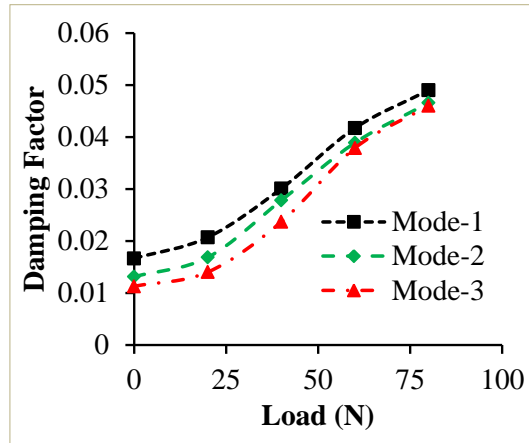
(d)



(e)



(f)



(g)

Figure 7.5. Variation of damping ratio with the increase in compressive load of 3D printed (a) neat HDPE, (b) H0.5, (c) H1, (d) H3, (e) H5, (f) FGNC-1 and (g) FGNC-2.

Table 7.3. Effect of compressive load on damping factor of 3D printed samples.

Composition	Mode	Load (N)					$P_{cr}$
		0	20	40	60	80	
HDPE	1	0.021258	0.024399	0.038069	0.049237	-	43
	2	0.020291	0.023121	0.034015	0.046326	-	
	3	0.019879	0.021912	0.032603	0.040413	-	
H0.5	1	0.019149	0.022142	0.032025	0.041395	-	49
	2	0.018225	0.021302	0.030021	0.039413	-	
	3	0.016506	0.019825	0.031224	0.040951	-	
H1	1	0.017418	0.020127	0.031129	0.040023	-	51
	2	0.016124	0.017041	0.028610	0.037071	-	
	3	0.014012	0.018753	0.027012	0.035957	-	
H3	1	0.014163	0.017261	0.028012	0.039782	0.050017	62
	2	0.012512	0.015023	0.026471	0.037014	0.048329	
	3	0.010952	0.013875	0.025012	0.036025	0.045182	
H5	1	0.011044	0.014127	0.026091	0.037896	0.049037	76
	2	0.009341	0.011625	0.022546	0.034578	0.046023	
	3	0.008902	0.010205	0.020320	0.032546	0.041039	
FGNC-1	1	0.019127	0.022361	0.033562	0.045648	0.056147	65
	2	0.016021	0.019010	0.030256	0.042990	0.054338	
	3	0.015956	0.016997	0.029846	0.039451	0.050007	
FGNC-2	1	0.016663	0.020705	0.030095	0.041730	0.049014	81
	2	0.013136	0.016859	0.027814	0.038900	0.046581	
	3	0.011295	0.014021	0.023694	0.037892	0.046001	

### 7.2.1 Comparison of the experimental and numerical natural frequency

The experimental vibration results are compared with the numerical vibration results. The difference between the numerical and experimental vibration results is displayed in Table 7.4. It is seen that the numerically obtained natural frequencies exhibited a similar trend as that of the experimental observations. Among all the 3D printed NCs, the H5 NC exhibited the highest natural frequency, whereas the FGNC-2 exhibited the highest natural frequency between the FGNC-1 and the FGNC-2 compared to the HDPE. The slight difference between the experimental and the numerical results is possibly due to the assumptions considered in the numerical investigations (Dileep 2021, Gupta 2008).

Table 7.4. Comparison between numerical and experimental natural frequency of 3D printed samples under no-load conditions.

Composition	Mode	Natural Frequency (Hz)		
		Experimental	Numerical	Difference (%)
HDPE	1	136.70	138.91	1.59
	2	339.66	359.24	5.45
	3	600.55	637.27	5.76
H0.5	1	146.50	147.32	0.56
	2	361.69	387.42	6.64
	3	612.91	640.09	4.25
H1	1	160.80	162.14	0.83
	2	376.24	400.11	5.96
	3	638.56	680.03	6.09
H3	1	181.37	182.70	0.73
	2	406.46	425.46	4.46
	3	673.96	706.89	4.66
H5	1	192.94	193.36	0.22
	2	428.79	450.19	4.75
	3	721.58	751.33	3.96
FGNC-1	1	185.69	188.17	1.32
	2	412.90	432.58	4.55
	3	679.26	700.62	3.05
FGNC-2	1	199.86	204.09	2.07
	2	436.13	457.25	4.62
	3	725.23	756.02	4.07

### 7.3 $P_{cr}$ estimation using VCT

The  $P_{cr}$  of the additively manufactured HDPE, NCs and FGNCs are also estimated using the vibration responses through VCT method. The VCT is a non-destructive test for estimating  $P_{cr}$  with the help of the vibration responses. In the VCT, the experimental frequency is obtained corresponding to the load applied that is lower than the  $P_{cr}$ . The curve between the squared values of the fundamental frequency and the compressive load is plotted. Then, the plot is extrapolated using the second-order polynomial expression (equation 11) to evaluate  $P_{cr}$  (Bharath 2020, Dileep 2021). Table 7.1 presents the  $P_{cr}$  values of the 3D printed HDPE, NC and FGNCs using the VCT. It is clearly observed that the  $P_{cr}$  calculated from the VCT also displays the similar trend as that of the DTM and MBC approaches. The comparison of the  $P_{cr}$  values of the 3D printed HDPE, NC and FGNCs, calculated from these three techniques are presented in Figure 7.7. It is clearly seen that the VCT overestimates the DTM and MBC methods (Bharath 2020, Dileep 2021). This comparative analysis helps in estimating the lower and upper limits of the  $P_{cr}$ .

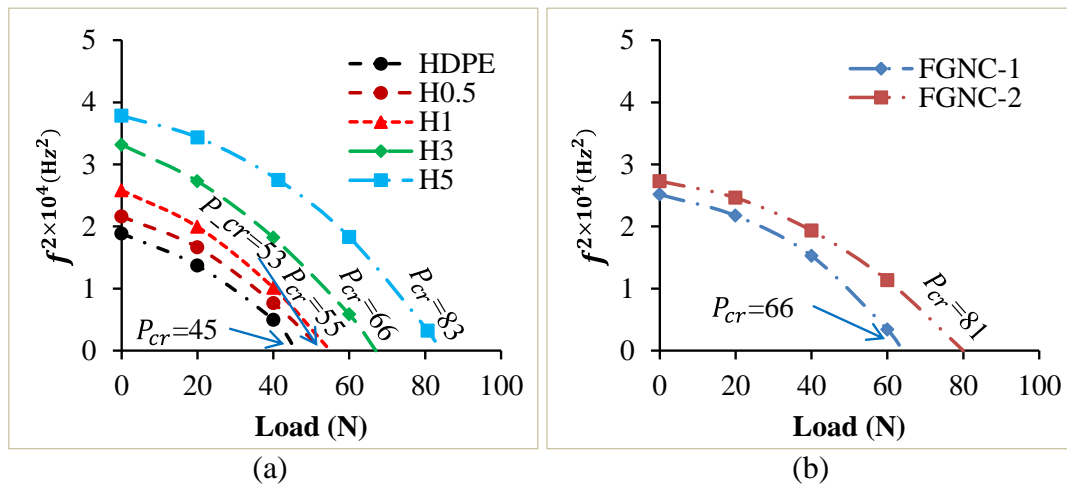


Figure 7.6. Representative plots of the VCT to evaluate  $P_{cr}$  of 3D printed (a) HDPE and NC, and (b) FGNCs.

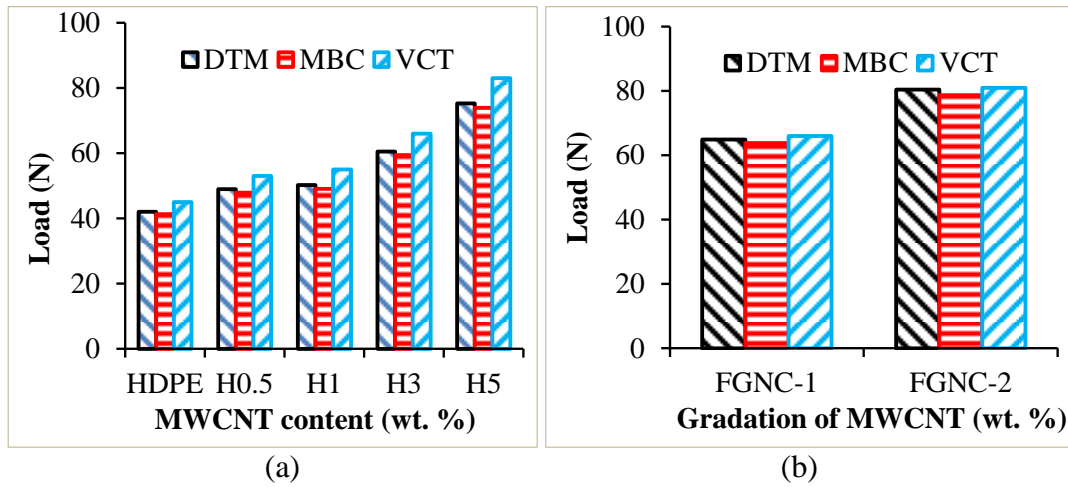


Figure 7.7. Comparison of the  $P_{cr}$  of the 3D printed (a) HDPE and NC, and (b) FGNC samples calculated using DTM, MBC and VCT methods.

#### 7.4 Property map

The density of the composites is a very crucial property that helps decide material for the lightweight applications. Therefore, the buckling strength and the density of the 3D printed NCs and FGNCs are compared against the available data. The 3D printed NCs and FGNCs are compared for density with the thermoplastic composites prepared by 3D printing and thermosetting composites prepared using the hand lay-up method (Bharath 2020, Dileep 2021, Rajesh 2017, Waddar 2018). Figure 7.8 shows the chart between different composites for buckling load and density. This comparative study shows that the 3D printed H5 NC and FGNC-2 have higher mechanical buckling strength than the B1 and B2 natural fiber reinforced composites prepared by the hand lay-up (Rajesh 2017). It is also found that the density of the 3D printed NCs and FGNCs is lower than the thermosetting foams and natural fiber reinforced composites (Rajesh 2017, Waddar 2018), making them suitable for the lightweight applications like marine and naval structures (Dileep 2021).

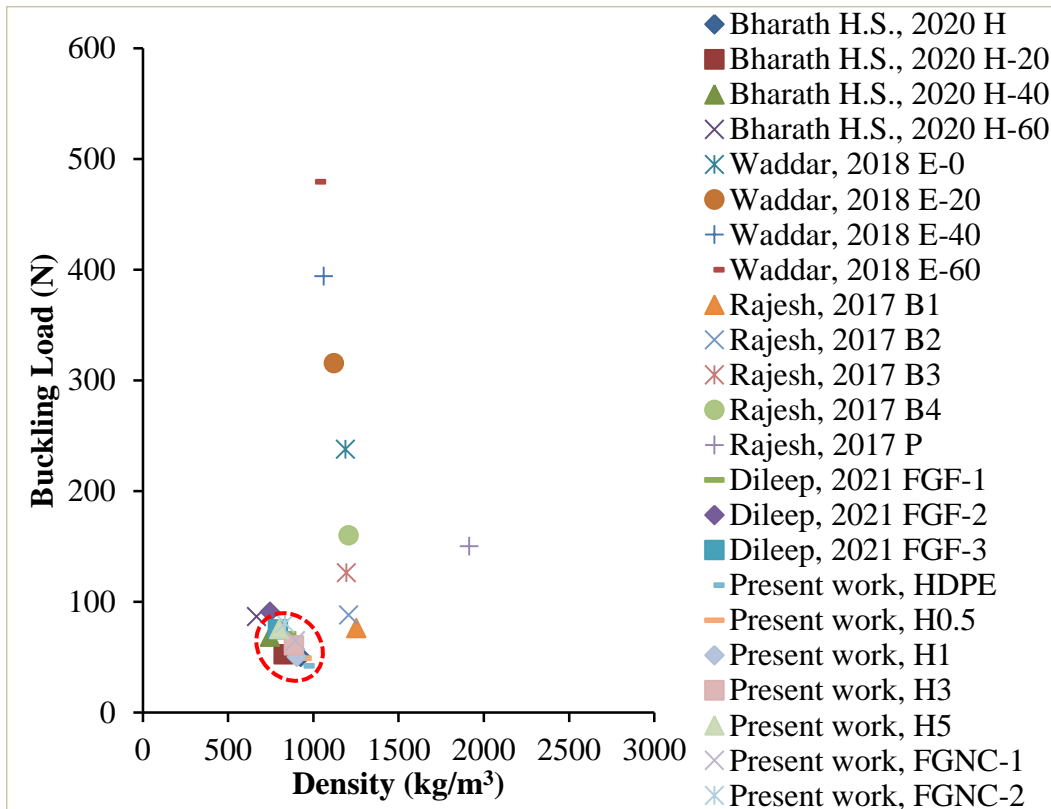


Figure 7.8. Representative plot of buckling load of different composites as a density function (Bharath 2020, Dileep 2021, Rajesh 2017, Waddar 2018).

## 7.5 Conclusion

The 3D printed NCs and FGNCs are also investigated for the buckling and dynamic responses. The results are summarized below.

- The buckling strength of the 3D printed NCs and FGNCs increases with the increased MWCNTs content.
- The  $P_{cr}$  of the H0.5, H1, H3, and H5, calculated from the DTM and MBC method, increased by 16.40%, 19.49%, 44.03% and 79.03%, and 15.95%, 18.81%, 43.90% and 79.13%, respectively, than the HDPE.
- The  $P_{cr}$  of the FGNC-1 and FGNC-2, calculated from the DTM and the MBC methods, increased by 54.38% and 91.34%, and 54.62% and 90.62%, respectively, than the HDPE.
- The H5 NC and the FGNC-2 displayed the highest buckling strength compared to the neat HDPE among the 3D printed NCs and FGNCs.
- The  $P_{cr}$  calculated from the DTM, MBC, and VCT methods exhibited good agreement.

- The natural frequency of the 3D printed NCs and FGNCs increases with the MWCNTs loading while decreasing with the increase in the compressive load.
- The damping factor of the 3D printed NCs and FGNCs decreases with the filler loading while observed to increase with a rise in the compressive load compared to the HDPE.
- The experimental and numerical findings are observed to be in very good agreement.
- The property chart reveals the superior performance of the H5 NC and FGNC-2 compared to thermosetting composites.

The concurrent 3D printing of the NCs and FGNCs for mechanical buckling and dynamic behavior is significant in designing and developing geometrically complex and integrated structures/components for static, dynamic, and weight-sensitive applications in automotive, aerospace, defense, and marine industries.



## 8 THERMAL BUCKLING

### 8.1 Thermal buckling results

#### 8.1.1 Effect of various non-uniform heating on $T_{cr}$

Buckling is a phenomenon in which a slender member loses its stiffness due to axial compressive load and fails below the yield point. And the thermal buckling refers to the loss of stiffness due to heating. The components or the structures may fail at any time before the yield point due to loss of the stiffness (buckling), which is, in fact, unpredictable. Therefore, studying the thermal buckling behavior is important for the safe design. In the current study, the HDPE, NCs and FGNCs are 3D printed and investigated for the buckling responses under various non-uniform heating cases. The temperature vs. deflection curves under non-uniform heating are presented in Figure 8.1-Figure 8.3, and the corresponding  $T_{cr}$  and the lateral deflection values are presented in Table 8.1. To investigate the effect of different non-uniform heating on the  $T_{cr}$ , the graph is plotted for the  $T_{cr}$  values in all heating conditions by considering one composition constant. Figure 8.4 presents the comparison of the  $T_{cr}$  in different non-uniform thermal loads for the H5 NC and FGNC-2. It can be clearly observed that the  $T_{cr}$  is the highest in case-3 and the lowest in case-2, while the  $T_{cr}$  in case-1 is higher than case-2 and lower than case-3. The same trend is observed for all the 3D printed FGNCs and NCs. The  $T_{cr}$  of any slender structure depends on “how much intensity of the heat is applied on the portion of the beam having the lowest stiffness.” The  $T_{cr}$  will be higher if the portion of the beam having lowest stiffness is subjected to the less intensity of the heat, whereas the  $T_{cr}$  will be lower if the portion of the beam having lowest stiffness is subjected to the high intensity of the heat. In case-3, the maximum intensity of the heat is applied at both ends, which are tightly clamped and have the highest stiffness. In this case, the temperature variation across the beam is like a decrease-increase type (Figure 2.19, case-3). It is clear that in this case, the central part of the beam is subjected to the lowest intensity of the heat compared to case-1 and case-2 (Figure 2.19), and hence the  $T_{cr}$  in case-3 is the highest. From Figure 2.19, it is also clear that the centre part of the beam is subjected to the maximum intensity of the heat in case-2, and thereby, the  $T_{cr}$  is the lowest in case-2.

In case-1, the central portion of the beam is subjected to a load higher than case-3 and lower than case-2. Thereby, the  $T_{cr}$  is lower than case-3 and higher than case-2. From this study, it is noticed that the  $T_{cr}$  is different in different heating cases, and can be concluded that the  $T_{cr}$  changes with change in heating type.

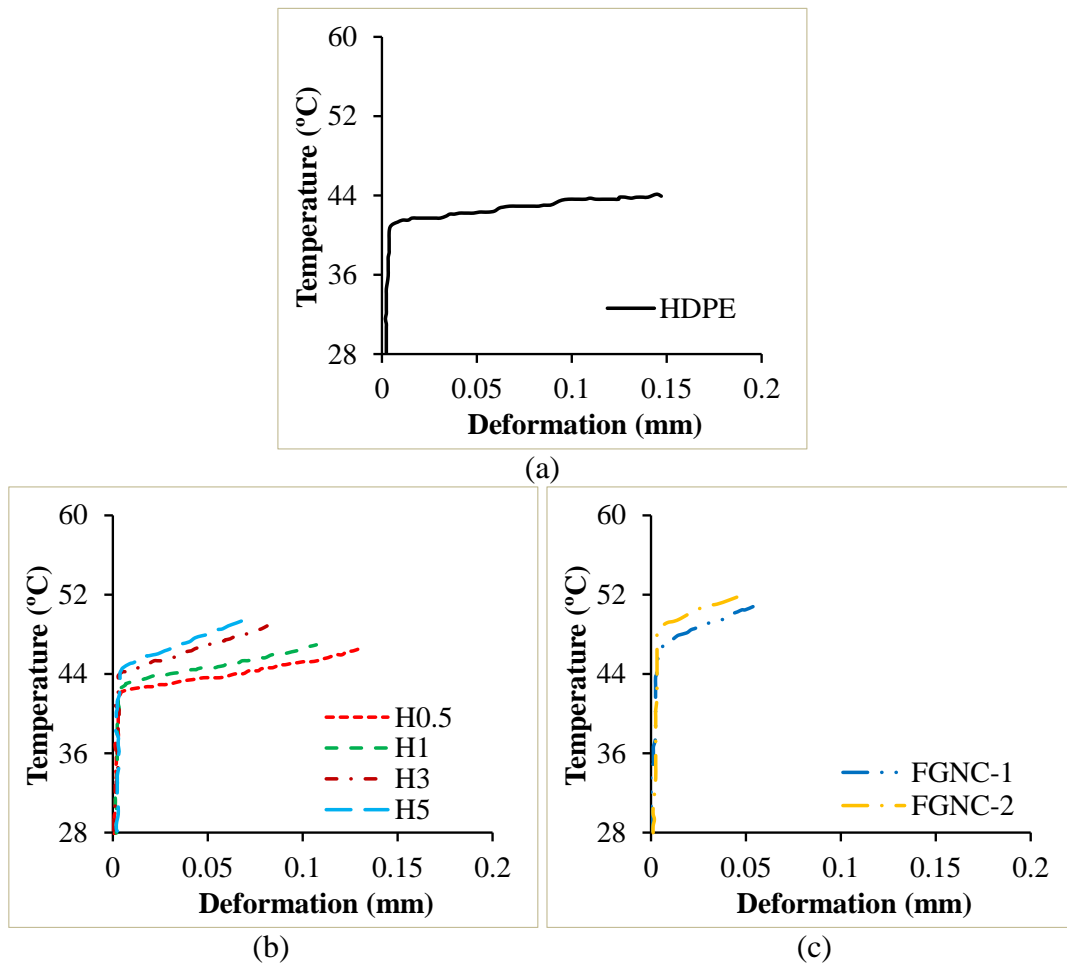
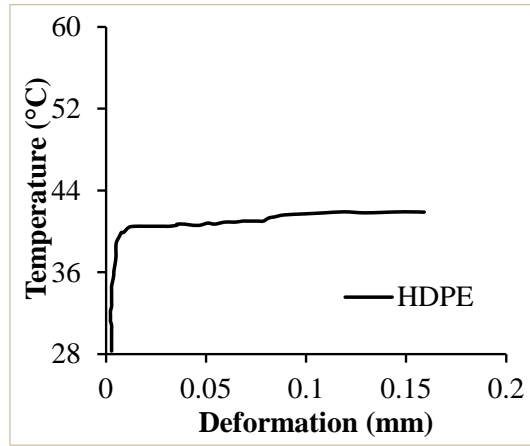
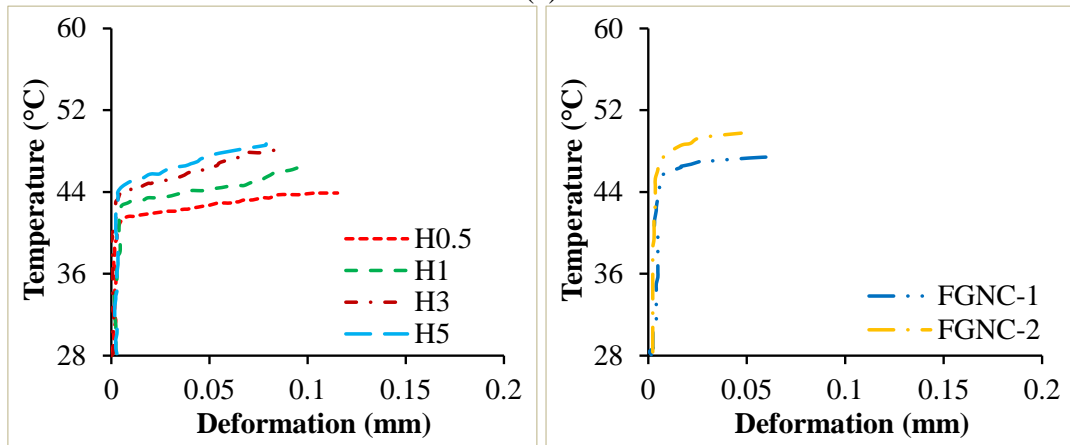


Figure 8.1. Thermal load vs deflection curves of the 3D printed (a) HDPE, (b) NC and (c) FGNC under case-1 heating.



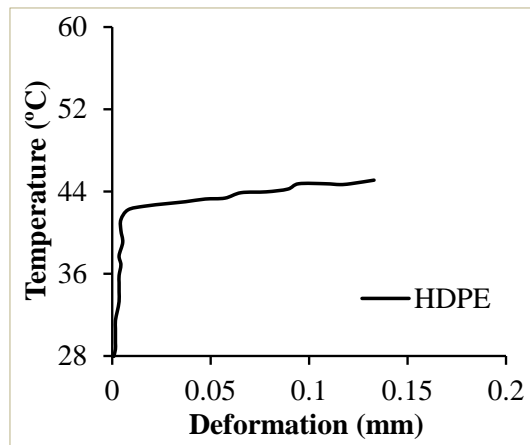
(a)



(b)

(c)

Figure 8.2. Thermal load vs deflection curves of the 3D printed (a) HDPE, (b) NC and (c) FGNC under case-2 heating.



(a)

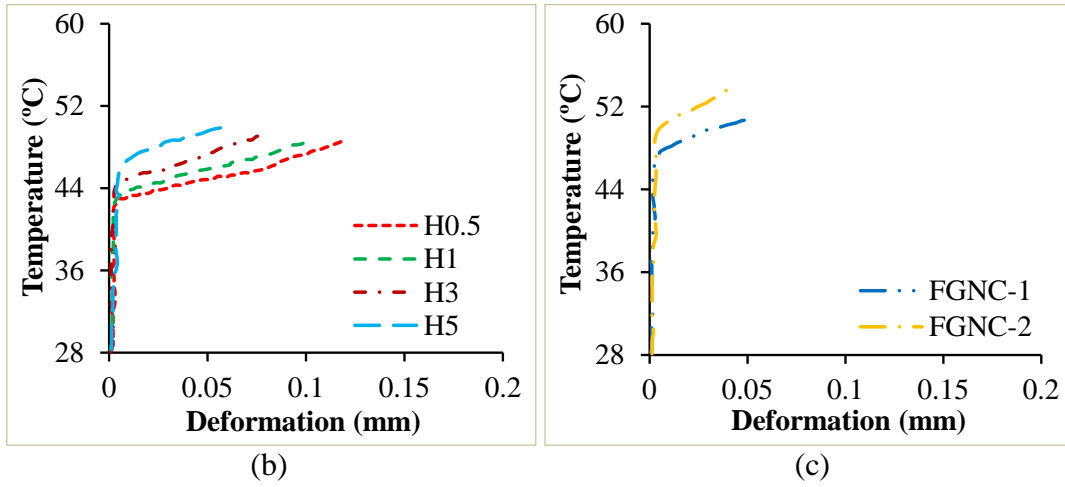


Figure 8.3. Thermal load vs deflection curves of the 3D printed (a) HDPE, (b) NC and (c) FGNC under case-3 heating.

Table 8.1. Thermal buckling responses of the prints.

Type of heating	Composition	Critical buckling temperature $T_{cr}$ (°C)	Deflection (mm)
Case-1	HDPE	41.32	0.15
	H0.5	41.82	0.13
	H1	42.73	0.11
	H3	44.33	0.08
	H5	45.93	0.07
	FGNC-1	47.45	0.05
	FGNC-2	49.19	0.04
Case-2	HDPE	39.89	0.16
	H0.5	40.31	0.11
	H1	41.62	0.10
	H3	42.53	0.09
	H5	44.08	0.08
	FGNC-1	46.20	0.06
	FGNC-2	48.06	0.05
Case-3	HDPE	42.21	0.13
	H0.5	43.63	0.12
	H1	44.30	0.10
	H3	45.98	0.08
	H5	47.92	0.06
	FGNC-1	49.60	0.05
	FGNC-2	51.77	0.04

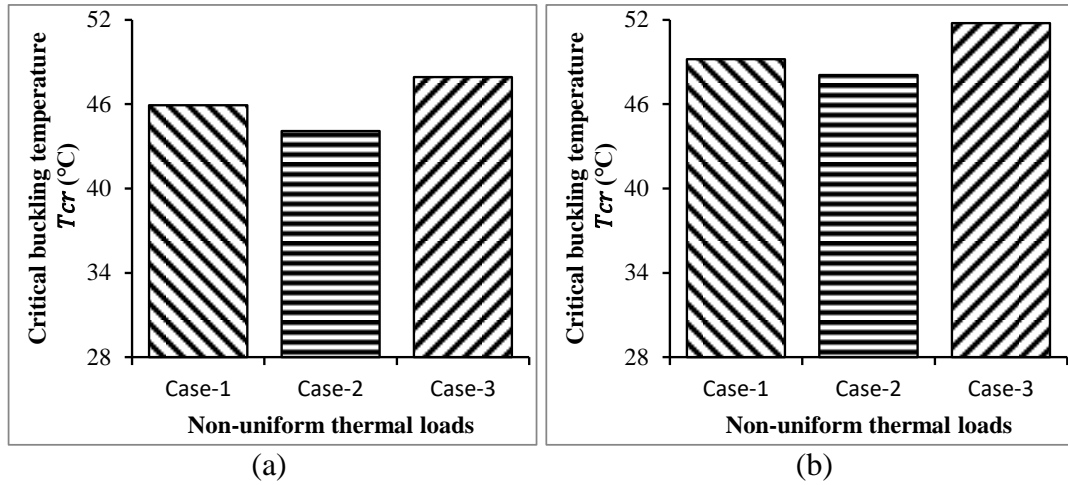


Figure 8.4. Effect of various non-uniform thermal loads on  $T_{cr}$  of (a) H5 NC and (b) FGNC-2.

### 8.1.2 Effect of various non-uniform heating on deflection

The deflection data corresponding to different non-uniform heating (Table 8.1) is also captured to investigate the impact of various non-uniform heating conditions on the deflection of the beam. It is noticed that the deflection is maximum in case-2, whereas no significant difference in the deflection is observed in case-1 and case-3. However, the deflection value is significantly less ( $<0.1$  mm). All the compositions (NCs and FGNCs) show the similar trend. The deflection of the beam in buckling depends on the position and intensity of the heat applied. The deflection will be higher if the highest intensity of the heat is applied to the portion of the beam with the lowest stiffness. In case-2, the highest heat intensity is applied at the central portion of the beam with the lowest stiffness; therefore, the deflection is the highest in this case. In case-1 and case-3, the highest intensity of the heat is applied at the fixed ends, which have the highest stiffness. That is the reason that the deflection is comparatively less in these heating conditions. The similar deflection trend is observed for all the 3D printed NCs and FGNCs. It is also noticed that the beam gets deflected from the position where heat is applied.

### 8.1.3 Effect of addition of functionalized MWCNTs and their gradation on $T_{cr}$

To investigate the impact of the addition of the functionalized MWCNTs and their gradation on  $T_{cr}$ , one heating condition is fixed, and then the effect is analysed. Figure 8.5 presents the influence of the MWCNTs addition and their gradation on  $T_{cr}$  in case-1 heating condition. It is clearly observed that the  $T_{cr}$  of the NCs rises by adding

MWCNTs (Figure 8.5a). The  $T_{cr}$  of the H0.5-H5 increases from 1.21%-11.16% compared to the pure HDPE. The highest  $T_{cr}$  (11.16% higher than the HDPE) is obtained for the H5 NC. The same trend is observed in the other heating conditions (case-2 and case-3). The elastic modulus of the NCs increases with the addition of the MWCNTs (Kumar 2022). In contrast, the CTE decreases (Table 3.4) with MWCNTs addition. The product of the elastic modulus and the CTE effectively increases with the addition of the MWCNTs, which enhances the buckling strength of the NCs. The enhancement in the buckling strength increases the  $T_{cr}$  of the NCs. Further, it is observed that the  $T_{cr}$  of the FGNCs also increases with the gradation of the functionalized MWCNTs (Figure 8.5b). The  $T_{cr}$  of the FGNC-1 to FGNC-2 increases from 14.83%-19.05% compared to the pure HDPE. The highest  $T_{cr}$  is obtained for the FGNC-2 (19.05% higher than HDPE). The same trend is observed in the other heating conditions (case-2 and case-3). In the case of the FGNCs, the CTE of the different compositions is different. The adjacent composition restricts the expansion at the interface due to varying CTE. Moreover, the CTE of the FGNCs decreases, whereas the modulus increases with the gradation of the functionalized MWCNTs (Table 3.4). Due to gradation of the material, the stress transfer becomes effective at the interface of the two compositions, which results in higher buckling strength. The higher buckling strength further results in the higher  $T_{cr}$ . From Figure 8.5c, it is clearly observed that the  $T_{cr}$  of the FGNCs is higher than the homogeneously reinforced NCs. The FGNC-1 and FGNC-2 both exhibited the higher  $T_{cr}$  than the H5 NC having highest content of the functionalized MWCNTs exhibiting the better performance of the FGNCs compared to homogeneously reinforced NCs.

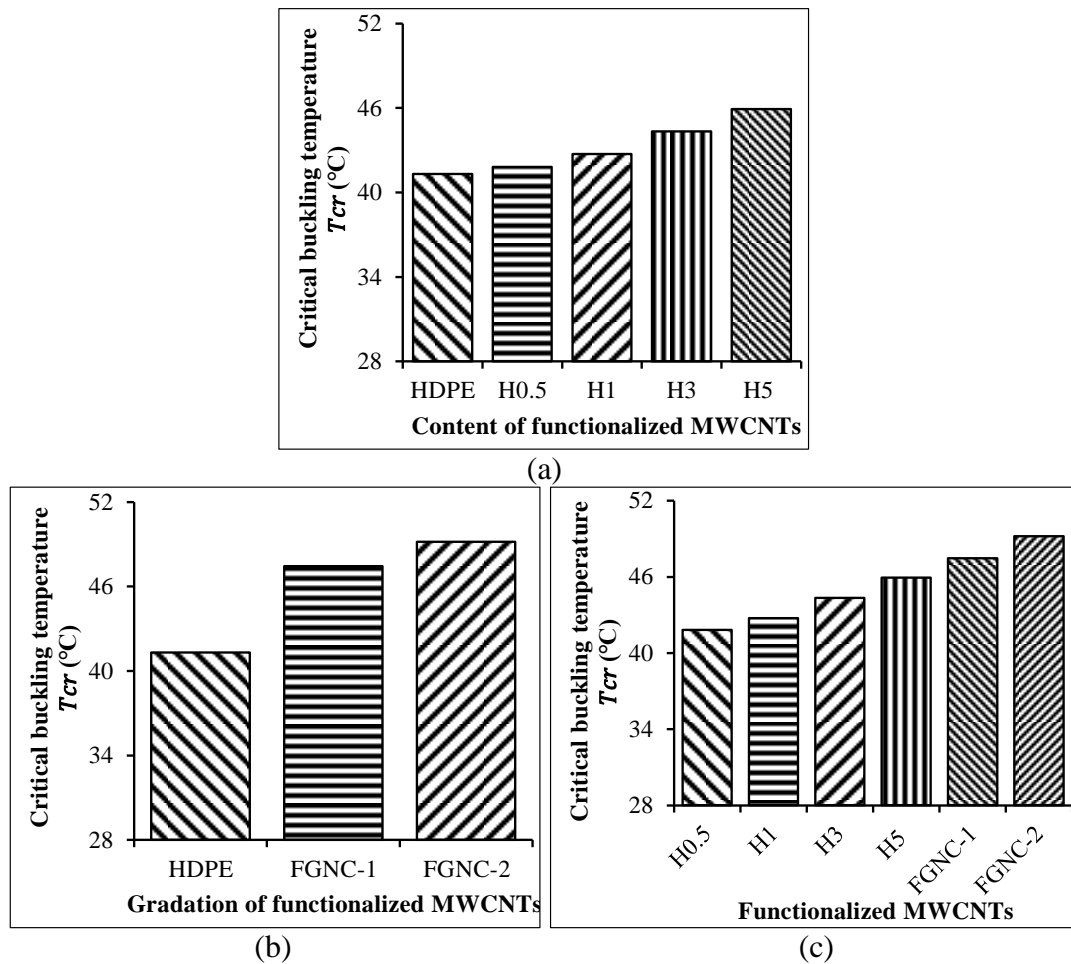


Figure 8.5. Effect of addition of the functionalized MWCNTs and their gradation on  $T_{cr}$  in case-1 heating condition.

#### 8.1.4 Effect of addition of functionalized MWCNTs and their gradation on deflection

One heating condition is fixed to investigate the influence of the addition of the functionalized MWCNTs and their gradation on the deflection, and then the effect is analysed. Figure 8.6 presents the influence of the addition of the functionalized MWCNTs and their gradation on the deflection of the beams in the case-1 heating condition. It is found that the deflection in the NCs decreases with the addition of the functionalized MWCNTs (Figure 8.6a). The deflection of the H0.5-H5 decreases from 13.33%-53.33 % compared to the pure HDPE. The reduction in the deflection in the NCs may be attributed to the increase in the elastic modulus of the NCs due to increase in the MWCNTs content, which further results in the increase in the stiffness of the beam. The higher the stiffness, the lower the deflection. A similar trend has also been observed in case-2 and case-3 heating conditions. The deflection of the FGNC-1

and FGNC-2 decreases from 66.67%-73.34 % compared to the pure HDPE. The highest reduction in the deflection is observed for the FGNC-2 (Figure 8.6b). Due to gradation of the different compositions and the suitability of the printing parameters, the interfacial bonding enhances the elastic modulus and further increases the stiffness of the FGNCs. The deflections of the NCs and FGNCs are plotted and presented in Figure 8.6c to compare the functional performance of the FGNCs to the homogeneously reinforced NCs. The deflection of the FGNCs is observed to be lower than the homogeneously reinforced NCs due to the higher stiffness of the FGNCs than the NCs, exhibiting that the FGNCs perform better than the homogeneously reinforced NCs.

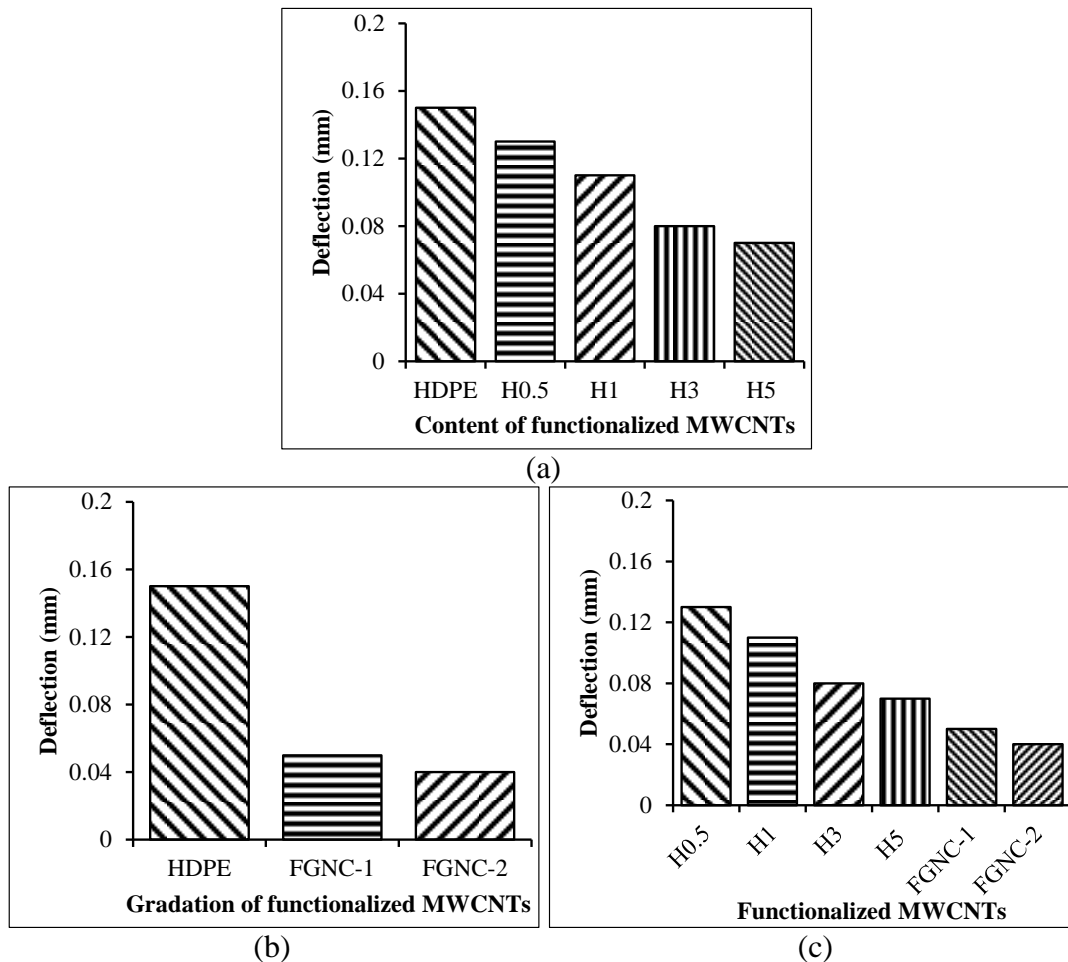


Figure 8.6. Effect of addition of the functionalized MWCNTs and their gradation on deflection in case-1 heating condition.

## 8.2 Conclusion

The 3D printed NCs and FGNCs are characterized for buckling responses under different non-uniform thermal loads, and the results are summarized below.

- The  $T_{cr}$  is the highest in case-3 and the lowest in case-2. The  $T_{cr}$  is observed to be sensitive to the type of heating.
- The maximum deflection is observed in case-2, whereas no significant difference in deflection is observed in case-1 and case-3.
- The  $T_{cr}$  of the NCs and FGNCs increases due to addition of the MWCNTs and their gradation, respectively. The highest  $T_{cr}$  is observed for the H5 NC (11.16% higher than HDPE) and the FGNC-2 (19.06% higher than HDPE).
- The deflection of the NCs and FGNCs decreases with the addition of the functionalized MWCNTs and their gradation. The lowest deflection is observed for the H5 NC (53.33% lower than HDPE) and the FGNC-2 (73.34% lower than HDPE).
- The H5 NC and FGNC-2 exhibited the superior performance among the NCs and FGNCs, respectively.
- The FGNCs exhibited the superior performance compared to all the homogeneously reinforced NCs as they have the higher  $T_{cr}$  than the NCs.

The findings of thermal buckling of this research exhibit the potential of the 3D printed NCs and FGNCs to be utilized as integrated and jointless functional components subjected to different thermal environments.



## 9 RECYCLING POTENTIAL OF NANOCOMPOSITES

### 9.1 Filament regularity and quality check

In this research, the recycling potential of the waste polymer nanocomposite is also investigated. Using the waste filaments (W/UR), nanocomposite filaments are extruded and characterized for the printability. The uniform regularity in the diameter of the extruded filaments is crucial for the uniform material to flow through the printer nozzles, resulting in good quality prints. The mean diameter and the standard deviation of the W/UR and the recycled filaments are listed in Table 9.1. The mean diameter of each filament is 2.73 mm, which shows the extrusion consistency. The standard deviation of the W/UR filament is higher (0.03 mm) than the recycled filaments (1x, 2x, and 3x), which shows that the W/UR filament has minor variations in the diameter than the 1x, 2x, and 3x filaments. The 2x and 3x (0.01 mm) filament diameters are lower than the 1x filament (0.02 mm), possibly due to the stiffening effect post the subsequent thermal cycles. Further, the decrease in the standard deviation may be due to the good arrangement of the polymer chains and the MWCNTs in the NCs. There is no change in the standard deviation of 2x and 3x recycled filaments, implying the saturation of the polymer chains and the fillers realignment. The higher diameter variations in the W/UR filament than the recycled filaments are due to the random alignment of the polymer chains and the MWCNTs. Further, when the filaments are recycled, the polymer chains and the MWCNTs undergo thermal processing, where they get aligned. Therefore, the filament cross-section reduces slightly, lowering the standard deviation further. Moreover, the variations in the filament diameter may also be due to matrix porosity. The matrix porosity in the recycled filament reduces the material's tensile strength (Bharath 2020). The presence of the porosity is determined through the density measurement of the sample. The density of the W/UR filament, recycled filaments, and the prints are listed in Table 9.1. The density of the recycled filaments (1x, 2x, and 3x) increases compared to the W/UR filament. It is also observed that the recycled filament density increases with each additional extrusion pass. The maximum density is observed to be for 3x recycled filament. In contrast, the densities of the 2x and 3x filaments are approximately the same, showing the delay in the realignment of the polymer chains

and the fillers. The same trend is observed for the prints as well. The print density is higher than the extruded counterparts, showing the additional alignment of the polymer chains with the fibers and the higher crystallization time in the printing process. The experimental density of the W/UR filament, recycled filament, and the 3D prints are higher than the theoretical density of the H1 NC, which shows no air voids/porosity in the sample. This can also be seen in the SEM image of the freeze-fractured H1-3x print. The lower magnification image of the H1-3x (Figure 9.1a) shows the matrix's air voids/porosity absence. In contrast, the higher magnification image (Figure 9.1b) shows the homogeneous dispersion of the functionalized MWCNTs in the HDPE.

Table 9.1. Density of the recycled filaments and the prints.

Particulars	$\bar{d}$ with $\sigma$ (mm)	$\rho_{th}$ (kg/m <sup>3</sup> )	$\rho_{exp}$ (kg/m <sup>3</sup> )	
			Filaments	Prints
W/UR	2.73±0.03	898.04	901.01±4.20	903.18±3.93
1x	2.73±0.02		948.42±4.40	950.27±2.48
2x	2.73±0.01		983.25±7.48	986.31±4.35
3x	2.73±0.01		985.13±9.61	991.43±5.12

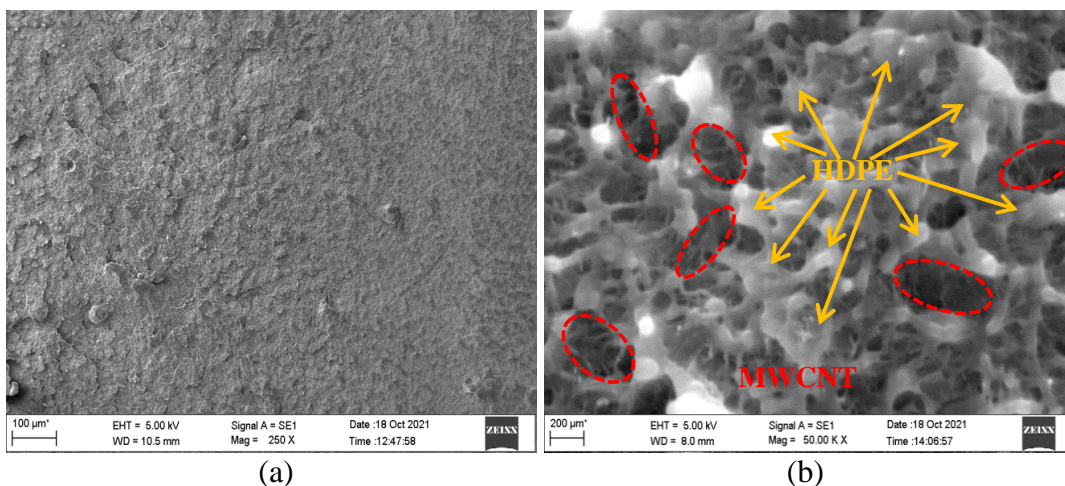


Figure 9.1. Representative images of the 3D printed freeze-fractured H1-3x print at (a) lower and (b) higher magnifications.

## 9.2 XRD of the recycled nanocomposite filaments and the prints

The polymer chains' and fibers' realignment influence the filaments' and prints' crystallinity. The XRD test is performed for the filaments and the prints to check the changes in their crystallinity. The XRD of the developed compositions and the associated prints are presented in Figure 9.2a-b, respectively, and the corresponding values are presented in Table 9.2. The peak intensity of the recycled filaments' increases compared to the W/UR filament. The peak intensity also increases with each extrusion cycle. The peak values (Table 9.2) show orthorhombic crystal structures at (110) and (200) lattice plane (Doddamani 2020). The similar observations are noted for the prints as well. The highest peak intensity is observed for the 3x filament and the print. The sharpness of the peak represents crystallinity. Therefore, the increase in the peak intensity can be correlated to the increase in the crystallinity. The degree of the crystallinity increases for the filaments and the prints compared to the W/UR filament and the print. It also increases with each extrusion cycle, as shown in Table 9.2. The increase in the peak intensity and the degree of crystallinity of the filaments and the prints may be due to the realignment of the polymer chains and the fillers while undergoing additional thermal processing. The degree of crystallinity of the prints is higher than the filaments owing to the thermal heating (additional) and the higher time of crystallization in the 3D printing.

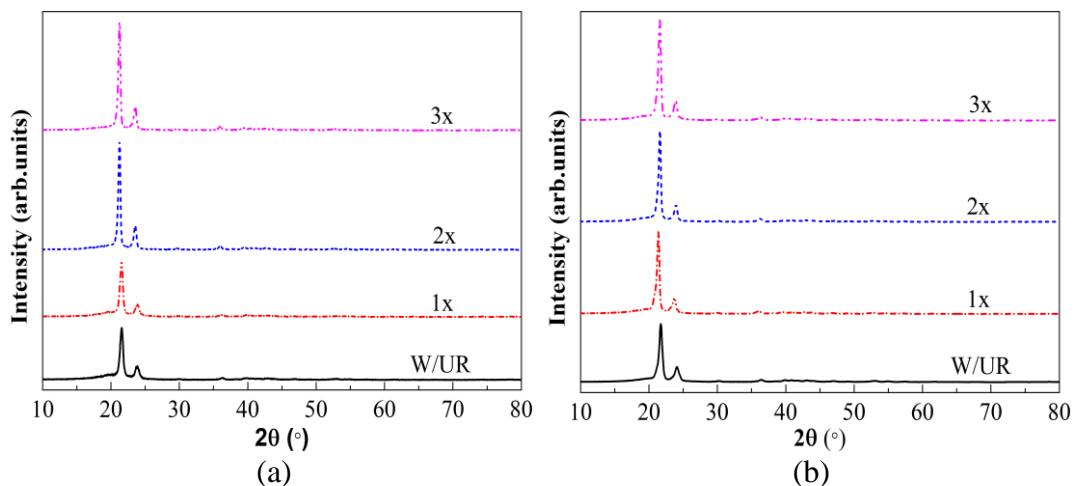


Figure 9.2. The XRD pattern of the recycled NC (a) filaments and (b) the prints.

Table 9.2. XRD responses of the recycled filaments and the prints.

Particulars	Filament Peak		3D Prints Peak		Degree of Crystallinity (%)	
	Position 2θ (°)		Position 2θ (°)		Filament	3D Prints
	1st peak	2nd peak	1st peak	2nd peak		
W/UR	21.23	23.63	21.32	23.42	59.04	68.35
1x	21.53	23.81	21.48	23.79	61.21	71.42
2x	21.15	23.52	21.51	23.91	62.89	73.33
3x	21.53	23.80	21.26	23.52	65.67	75.46

### 9.3 Tensile test of the NC filaments

The increase in the density and the crystallinity of the recycled filaments compared to the W/UR filament influences the mechanical properties. In this present work, the tensile test is performed on the recycled and the W/UR filaments to investigate their tensile properties. Moreover, the tensile test of the filaments is crucial to check their strength and stiffness so that they can be further utilized for 3D printing. The tensile responses of the recycled NC filaments are shown in Figure 9.3a and Table 9.3. The modulus of the recycled filaments (1x, 2x, and 3x) increases compared to the W/UR filament. The modulus of 1x, 2x, and 3x recycled filaments are 12.74%, 20.30%, and 23.12%, respectively, higher than the modulus of the W/UR filament. The polymer chains and the MWCNTs get realigned through the extrusion process, enhancing the adhesion between the filler and the matrix resulting in the higher modulus. The modulus of the recycled filaments also increases with each extrusion pass up to the 3<sup>rd</sup>; after that, no significant change is observed. The modulus of the 2x and 3x filaments are 6.70% and 9.20%, respectively, higher than the 1x filament, while the modulus of the 3x filament is 2.34% higher than the modulus of 2x filament, showing the property enhancement saturation. The highest modulus is observed for the 3x filament, 23.12% higher than the W/UR filament. The increased modulus in the recycled filaments with each extrusion pass is due to the additional realignment of the polymer chains due to further thermal processing. The yield strength (YS) and the ultimate tensile strength (UTS) of the recycled filaments are the same and higher than the W/UR filament. The values of YS and UTS for the 1x, 2x, and the 3x recycled filaments are 3.77%, 8.17%, and 9.43%, respectively, higher than the W/UR filament. The recycled filaments' YS and UTS also increase with each extrusion pass. The YS

of the 2x and 3x filaments are 4.24% and 5.45%, respectively, higher than the 1x filament, while the YS of the 3x filament is 1.16% higher than the YS of the 2x filament. The highest YS and UTS are observed for the 3x filament (9.43% higher than the W/UR filament). The YS increases due to the increased crystallinity (as observed in the XRD discussions), further increasing the filaments' elasticity (elastic region). The rise in the UTS is due to the cross-linking of the polymer chains, which enhances the load transfer capability. The SEM image of the 3x recycled tensile tested filament is shown in Figure 9.3b, showing the cross-linking and the good distribution of the functionalized MWCNTs as the better bonding between the constituents. The fracture strength of the 1x filament is observed to be the highest. The fracture strains of the recycled filaments (1x, 2x, and 3x) are higher than the W/UR filament, showing the increased ductility (due to more elongation) of the recycled filaments compared to the W/UR. It can also be observed that the fracture strains of the recycled (1x, 2x, and 3x) filaments are reducing with each extrusion pass. This is due to the increased brittleness in the recycled filaments while going through each extrusion pass. Overall, the tensile responses show the enhancement in modulus and the strength of the recycled filaments compared to the W/UR filaments, indicating that these filaments can be utilized in the 3D printer for components manufacturing for different applications.

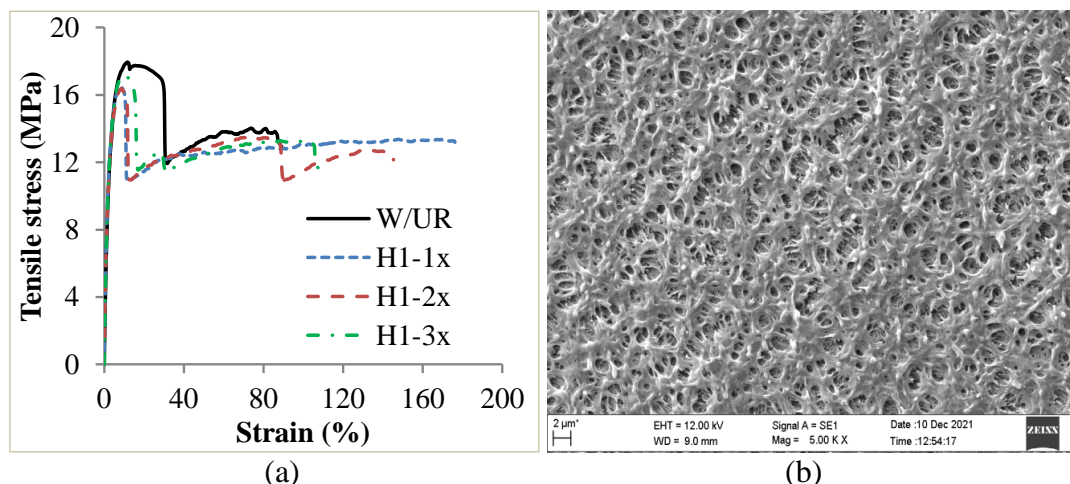


Figure 9.3. Representative (a) tensile stress-strain plot of the NC filaments and (b) SEM image of the H1-3x recycled filament.

Table 9.3. Tensile responses of the recycled NC filaments and the prints.

Number of cycles	Modulus (MPa)		Yield strength (MPa)		UTS (MPa)		Fracture strength (MPa)		Fracture strain (%)	
	Flmt	Print	Flmt	Print	Flmt	Print	Flmt	Print	Flmt	Print
W/UR	675	824	15.9	7.86	15.9	15.2	12.87	15.0	89.22	7.64
	±19	±26	±0.6	±0.4	±0.6	±0.5	±0.6	±0.9	±0.6	±3.31
1x	761	1200	16.5	12.7	16.5	24.9	12.94	24.5	176.3	12.17
	±12	±13	±0.1	±0.3	±0.1	±0.7	±0.3	±0.5	8	±2.23
2x	812	1280	17.2	10.37	17.2	25.4	12.15	25.0	145.3	5.07
	±17	±16	±0.3	±0.2	±0.3	±0.4	±0.2	3	6	±1.04
3x	831	1630	17.4	11.71	17.4	25.5	11.35	24.8	108.4	4.70
	±15	±23	±0.2	±0.3	±0.2	±0.3	±0.5	7	2	±2.06
								±0.2	±3.94	

#### 9.4 3D printing using recycled NC filaments

In order to achieve good prints quality, suitable printing parameters are required, which are obtained through the pilot studies shown in Table 2.4 (Kumar 2022, 2022). The samples 3D printed at respective extrusion multipliers of 0.90 and 1.0 showed the non-uniform flow of the material (Figure 9.4a). Bulge formation (Figure 9.4b) was observed when the samples were printed with the layer heights between 0.30 mm and 0.50 mm. There must be a proper clearance between the two layers to obtain bulge-free samples. The printing temperature is also very crucial for good quality prints. A higher printing temperature (220 °C) leads to overheating of the samples, and a lower printing temperature (190 °C) leads to improper flow of the melt materials, further influencing the quality of the prints. The samples printed at a higher speed (35 mm/s) increased the surface roughness (Figure 9.4c). The samples printed using the suitable parameters showed a good quality print (Figure 9.4d). The W/UR and the recycled filaments (1x, 2x, and 3x) are used as feedstock filaments to print the samples. The samples printed with the W/UR filament are named waste/unrecycled (W/UR) print, whereas the samples printed with the recycled filaments, 1x, 2x, and 3x, are designated as 1x, 2x, and 3x prints (recycled prints), respectively. After printing, the samples are tested for the density, XRD, and the tensile properties.

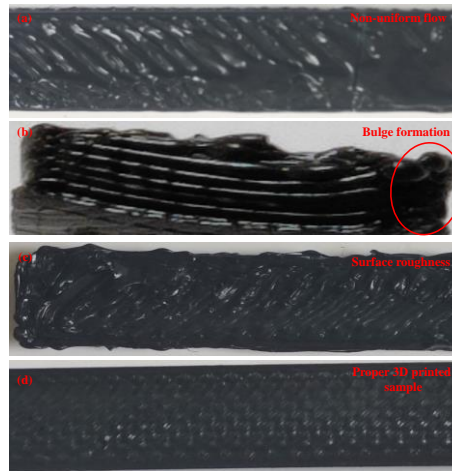


Figure 9.4. Challenges encountered in 3DP of recycled filaments.

### 9.5 Tensile test of the 3D printed samples

The printability of the W/UR and the recycled filaments is ensured through the tensile test of the filaments, which is then used to print tensile samples to check their property enhancement potential. The tensile tested samples exhibiting the brittle failure (Figure 9.5a), and the close-up image of the fractured surface (Figure 9.5b) are presented. The tensile responses of the prints are shown in Figure 9.6a, and the corresponding values are given in Table 9.3. The modulus of the recycled printed samples increases compared to the W/UR printed samples. The modulus of the 1x, 2x, and 3x printed samples are 45.63%, 55.34%, and 97.81%, respectively, higher than the W/UR printed sample. The increase in the modulus is due to the higher crystallinity and interfacial bonding. The modulus of the 2x and 3x prints are 6.67% and 35.83%, respectively, higher than the 1x print, while the moduli of the 3x print is 27.34% higher than the modulus of the 2x print. The highest modulus is noted for the 3x print, 97.81% higher than the W/UR print. The modulus of the printed samples has been observed to be higher with respect to the corresponding modulus of the filaments. The modulus of the W/UR, 1x, 2x, and 3x prints have been increased by 22.07%, 57.69%, 57.63%, and 96.15%, respectively, compared to the modulus of the respective filaments. This is due to the additional thermal processing of the filaments in 3D printing process, where the polymer chains are again aligned in addition to the filler functionalization. The recycled printed samples' YS are higher than the W/UR prints. The highest YS is observed for the 1x print and is 61.58% higher than the W/UR print. No significant effect in the YS of the printed samples is observed

compared to the YS of the respective filaments. The UTS of the recycled prints (1x, 2x, and 3x prints) also increases compared to the UTS of the W/UR print. The UTS of 1x, 2x, and 3x prints are 63.82%, 67.11%, and 67.76%, respectively, higher than the W/UR print. The highest UTS is observed for the 3x print, 67.76%, which is higher than the W/UR print. There is no significant change in the UTS of the W/UR filament and the print, whereas the UTS of the recycled prints is observed to be increasing with the extrusion cycles. The UTS of the 1x, 2x, and 3x prints are 50.91%, 47.67%, and 46.55%, respectively, higher than the 1x, 2x, and 3x filaments. The increase in the UTS may be attributed to the rise in the load transfer capability due to additional cross-linking of the polymer chains when they undergo recycling. The fracture strength of the recycled print is higher than the W/UR print. The fracture strength of the prints is higher than the filaments, and the values are 16.55%, 89.33%, 106.01%, and 119.12% higher for the W/UR, 1x, 2x, and 3x prints, respectively, for their respective filaments. The highest fracture strength and strain are observed for the 2x and 1x print, 66.87% and 59.29%, respectively, higher than the W/UR print. The printed samples undergo the additional extrusion recycling cycle when printed using a 3D printer, where they get more aligned and cross-linked, thereby enhancing the modulus and strength. It is observed that the 3x print is the best sample with the highest modulus, YS, UTS, and the fracture strength. The SEM of the tensile-tested 3x printed sample is shown in Figure 9.6b.

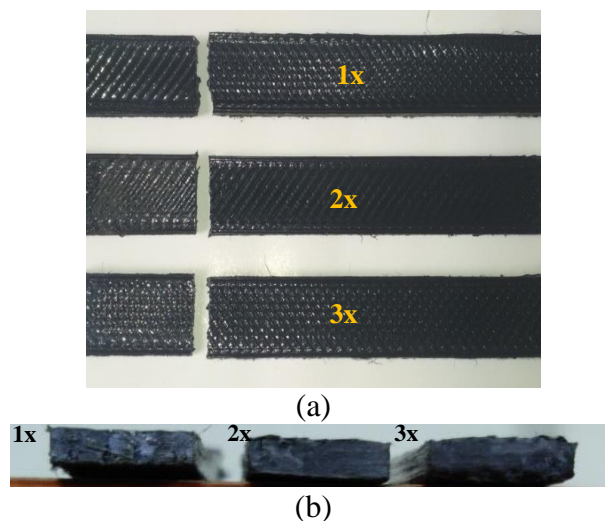


Figure 9.5. Tensile tested samples showing (a) brittle failure and (b) fractured surfaces in brittle mode.

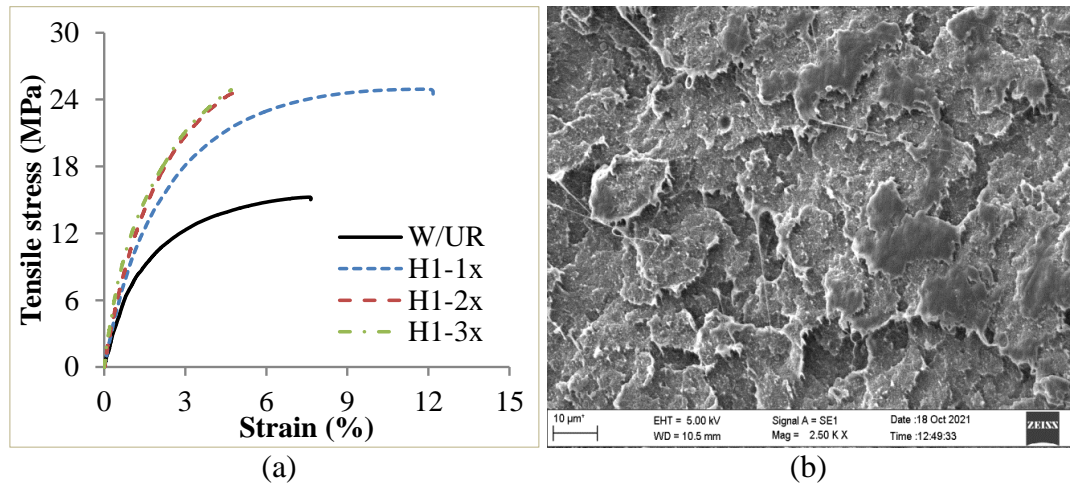
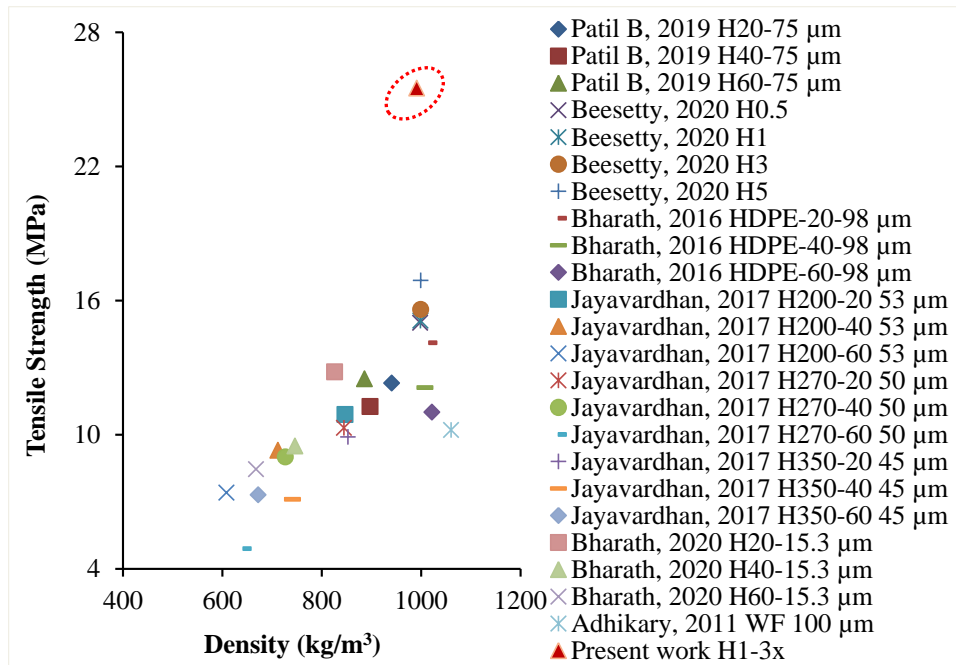


Figure 9.6. Representative (a) tensile stress-strain graph of the 3D printed samples and (b) SEM image of the tensile tested H1-3x printed sample.

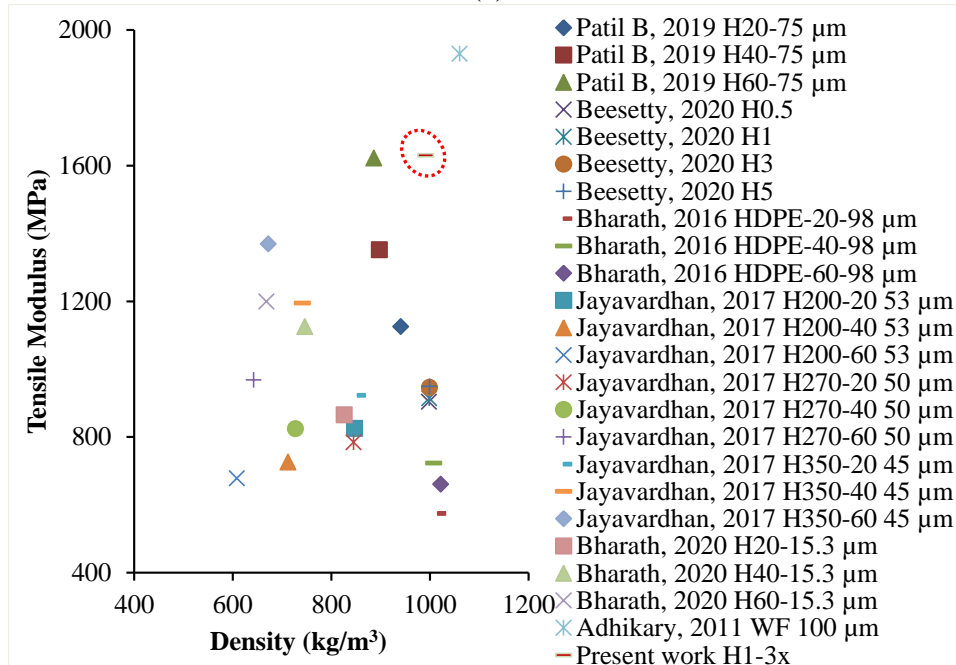
## 9.6 Property map

The tensile modulus and strength (Adhikary 2011, Beesetty 2020, Bharath 2020, Bharath Kumar 2016, Jayavardhan 2017, Patil 2019) of the H1-3x printed sample (which is an HDPE based composite) of the present study are compared with the different HDPE based composites reinforced with various fillers and manufactured by the different methods against the density of the composites. The tensile modulus and strength have been presented in Figure 9.7. The density of the H1-3x printed sample is lower than the nano-clay/HDPE composites (Beesetty 2020) and fly-ash cenospheres/HDPE composites (Bharath Kumar 2016). The H1-3x print exhibited the highest modulus (Figure 9.7a), except for the solid particle-filled HDPE composite. This highest modulus of the H1-3x sample may be due to the good distribution of the MWCNTs in the HDPE and the enhanced interfacial bonding between the HDPE and the functionalized MWCNTs. Compared to the other HDPE composites, the highest tensile strength (Figure 9.7b) is observed for the H1-3x printed sample. The highest tensile strength shows that the MWCNTs are well oriented in the HDPE, helping in the effective (highest) load transition from the HDPE to the MWCNTs. The property plot shows that the H1-3x print is stronger than the other HDPE composites filled with fillers like nano clay, GMB, fly ash cenospheres, and wood flour. Moreover, the H1-3x printed sample shows the superior tensile modulus than the HDPE composites with GMB, nano-clay, and fly ash cenospheres. Thus, the study of the property map reveals that the MWCNT/HDPE NCs recyclability potential can be effectively and

efficiently exploited through the 3D printing method to achieve a wider range of tailored physical and mechanical responses for various applications.



(a)



(b)

Figure 9.7. Comparison of tensile (a) strength and (b) modulus of different HDPE composites with H1-3x composite (Adhikary 2011, Beesetty 2020, Bharath 2020, Bharath Kumar 2016, Jayavardhan 2017, Patil 2019).

## 9.7 Conclusions

The waste filaments of the functionalized MWCNTs/HDPE NCs are recycled to obtain the useful NC filaments for 3D printing. The recycled NC filaments are further tested for density, crystallinity, and tensile properties to check their potential for 3D printing. The samples are 3D printed using the recycled filaments and subjected to density, XRD, and tensile tests to realize their potential for various applications. The results are summarized below.

- The density of the recycled filaments and the prints rises compared to the W/UR ones.
- The crystallinity of the recycled filaments and prints increases compared to the W/UR ones.
- The tensile strength and the modulus of the recycled filaments increase compared to the W/UR filament. The highest tensile strength and modulus are found for the H1-3x recycled filament.
- The tensile strength and modulus of the recycled prints increase compared to the W/UR printed sample. The highest tensile strength and modulus are observed for the H1-3x print.
- The H1-3x print exhibited the superior tensile strength and modulus among all the recycled prints.

The present work successfully illustrated the recycling of the nanocomposite waste filaments to minimize the plastic waste. Through such an approach, as presented in this paper, the environmental pollution due to the plastic waste generated by 3D printing industries can be substantially lowered, in addition to the expanding the filament material options for the FFF community. The H1 NC was printed without any warpage using the suitable printing parameters. Therefore, a similar route can be explored for the other NCs (0.5%, 1%, 3%, and 5 wt.% of the functionalized MWCNTs in the HDPE), increasing the applications across various engineering fields such as structural, marine, aerospace, and automobile.



## 10 SUMMARY AND CONCLUSIVE REMARKS

### Summary

The functionalized MWCNTs (0.5%, 1%, 3%, and 5% by weight) are incorporated in the highly utilized industrial HDPE thermoplastic polymer to develop their respective nanocomposites (NCs). These nanocomposites are subjected to SEM, MFI, and TGA to check the distribution of the fillers in the matrix, melt flow, and the thermal degradation behaviour of the developed NCs. Later, these NCs are used for the NC filament extrusion, which are subjected to SEM, tensile, DSC, and XRD to investigate their quality and printability. These extruded NC filaments can be utilized in the commercial FFF 3D printers for lightweight applications. Various NC and FGNC samples are 3D printed using these NC filaments for various studies. Initially, micrographic analysis is performed on the 3D printed samples to visualize their layers, interface bonding, and the filler distribution. The 3D printed NCs and FGNCs are further characterized by a comprehensive property required to design various components in the different applications. The outcomes of the current work are also compared with those of the previously published works through property maps. The property charts are useful for the industrial practitioners in selecting the correct material and manufacturing method for the envisaged applications.

### Conclusion

The major conclusions of the present work are summarized below.

#### *Processing of the materials*

- The functionalized MWCNTs are successfully mixed with the HDPE to develop nanocomposites using the optimized parameters.
- The MWCNTs/HDPE based excellent quality filaments are successfully extruded to be utilized in 3D printing.
- Utilizing the extruded filaments, flawless NC and FGNC samples are successfully 3D printed.

#### *SEM analysis*

- The SEM analysis revealed the uniform distribution of the functionalized MWCNTs in the HDPE in the developed nanocomposites, extruded

nanocomposite filaments, and the 3D printed samples, confirming the suitability of the processing parameters used in the blending, extrusion, and 3D printing. It also revealed the seamless and the strong layer bonding in the 3D printed NCs and FGNCs.

#### *Melt flow behaviour*

- The MFI of the developed NCs decreases with the increase in the MWCNTs content, confirming the increase in the melt viscosity of the developed NCs. It also confirms the inclusion of the fillers. The MFI reduces 14.52%-51.60% for the H0.5-H5 NCs compared to the pure HDPE.

#### *Thermal degradation behavior*

- The degradation temperature of the NCs increases with the addition of the filler, and is found to be higher than the neat HDPE.
- The HDPE, H0.5, H1, H3, and H5 degradation temperatures are 396.68 °C, 439.23 °C, 446.80 °C, 466.53 °C, and 479.07 °C respectively.

#### *Rheological behavior*

- The rheology results also confirm the uniform distribution of the fillers qualitatively. It is observed that the  $\eta^*$  for the NCs slightly increases as the functionalized MWCNTs content increases up to 0.5% and then dramatically increases for 5% (almost two orders) at the low frequency by maintaining a steeper graph, confirming the well dispersion of the MWCNTs in the HDPE.
- The  $\eta^*$ ,  $E'$ , and  $E''$  of the 3D printed NCs and FGNCs increase while damping decreases as the functionalized reinforcement content rises.

#### *Density*

- The density of the filaments and the printed specimens decreases with the increases in the MWCNT content. The highest density reduction of 16.06% and 15.58%, respectively is observed in the H5 filament and the respective printed specimen compared to HDPE.
- The density of the FGNCs decreases with the MWCNTs gradation in the layer. The highest weight-saving potential is observed for the FGNC-2, which is 12%.

### *DSC analysis*

- The  $T_{Cryst}$  increases up to 0.5% and 1 wt.% of the MWCNTs for the filaments and the printed specimens, respectively, then decreases compared to the neat HDPE.
- The  $T_{Melt}$  of the filaments and the printed specimens increases with the increase in the MWCNTs content.
- The  $\alpha_{Cryst}$  is higher for the filaments and the specimens compared to the neat HDPE. The crystallinity of the NC filaments and the prints is higher than that of the respective HDPE counterparts.

### *Tensile behavior of the filaments and the prints*

- The tensile modulus and strength increase with the addition of the MWCNTs. The modulus increases by 17.37%, 20.94%, 44.80%, and 104.54% in the respective H0.5, H1, H3, and H5 NC filaments compared to the HDPE filaments. The highest modulus is observed for the H5 NC (~105% more than the HDPE).
- Compared to the neat HDPE filament, the tensile strength increases by 1.32%, 18.54%, 23.84%, and 29.14% in the H0.5, H1, H3, and H5. The highest strength is observed for the H5 (~30% more than HDPE) NC filament.
- The modulus increases by 15.89%, 19.41%, 44.87%, and 81.43% in the H0.5, H1, H3, and H5 NC, respectively, compared to the pure HDPE specimens. The highest modulus is registered for the H5 NC (~ 81.5%). The tensile modulus of the 3D printed H-H5 specimens increased by 15.42%, 13.97%, 13.96%, 15.47%, and 2.38% compared to the respective filaments.
- The highest tensile strength (UTS) is registered for the H5 NC (16.6 MPa), which is 12.16% higher than the pure HDPE. The H5 NC showed the highest modulus and strength among all the NC specimens, 81.43% and 12.16%, respectively, which is higher than the HDPE.
- The modulus of the FGNC-1 and FGNC-2 are 1100 MPa and 1350 MPa, respectively, showing an increasing trend with the increasing layer composition. The enhancements in the moduli are 55.15% and 90.41% for the FGNC-1 and FGNC-2 compared to the pure HDPE, respectively, showing the potential to replace them.

- The H0.5, H1, H3, and H5 moduli are 824 MPa, 849 MPa, 1030 MPa, and 1290 MPa, respectively. The FGNCs exhibited the higher moduli than their respective homogeneous NCs, showing the potential to replace the NCs also.
- The tensile strength of the FGNC-1 and FGNC-2 are observed to be 16.57 MPa, and 18.36 MPa, respectively. The FGNCs' strength is higher than the respective homogeneous NCs. The enhancements in the strength are 23.75% and 37.12%, respectively, compared to the pure HDPE.

#### *Property map*

- The property map revealed that the 3D printed NCs exhibited the highest tensile strength compared to the other fillers reinforced HDPE composites with solid particles-based composites.
- The Additively manufactured NCs exhibited the highest tensile strength compared to the injection and compression molded composites.
- The H5 composition exhibited the superior tensile strength than the composites with fillers like fly ash cenospheres, nano clay, GMB, and wood.

#### *Flexural behavior of the prints*

- The flexural modulus and strength of the printed specimens increase with the MWCNTs increase. The modulus increased by 12.55%, 15.83%, 21.81%, and 24.71%, while the strength increased by 12.70%, 20.63%, 21.43%, and 22.23% in the H0.5-H5 respectively, when compared to the pure HDPE specimen.
- The H5 NC exhibited 24.71% and 22.23% higher modulus and strength, respectively as compared to the neat HDPE. Among all the 3D printed NCs, the H5 composition exhibited the superior mechanical properties.
- The specific strength and modulus of the 3D printed specimens increased with the filler loadings. The H5 NC showed the highest specific modulus and strength among all the NCs, 47.62% and 44.73% higher than the HDPE.
- The flexural moduli and strength increase with the nanoscale filler loading in the graded layer. The highest flexural strength and moduli are exhibited by the FGNC-2, which are 28.57% and 26.83% higher compared to the pure HDPE, respectively.

- The highest specific strength and modulus are exhibited by the FGNC-2, which are 46.16% and 44.14%, respectively, higher than the HDPE.
- The experimental findings matched well with the FEA results.
- These flexural results of the printed NCs will help design and develop integrated and complex geometrical functional and structural parts, while the FGNCs will help in designing structures needing variational stiffness and strength features for different applications such as marine, automobile, aerospace, biomedical, electronics, and defense.

*Compression, hardness, and impact behavior of the prints*

- The MWCNTs addition increases the compressive modulus and the yield strength of the NCs. The highest compressive modulus and yield strength found for the H5, respectively, are 44.89% and 9.28%, compared to the HDPE.
- The FGNCs' compressive modulus is higher than the HDPE, and increases as the content of the functionalized MWCNTs increases in each graded layer.
- The compressive modulus of the FGNC-1 and FGNC-2 increases, respectively by 35.75% and 61.14% compared to the HDPE. The FGNC-2 exhibited the peak compressive moduli.
- The yield strength of the FGNCs increases with the addition of the MWCNTs. The yield strengths of the FGNC-1 and FGNC-2 are found to be 8.89% and 11.56% higher than the HDPE. The FGNC-2 exhibited the highest yield strength owing to the homogeneous distribution of the functionalized MWCNTs in the HDPE.
- The hardness and the impact strength of the FGNCs increase with the increase in the MWCNTs in the graded layers. The FGNC-2 exhibited the highest hardness and impact strength, respectively 76.80% and 119.99% higher than the HDPE.

*Buckling and free vibration behavior of the prints*

- The buckling strength of the 3D printed NCs and FGNCs increases with the increased MWCNTs content.
- The  $P_{cr}$  of the H0.5, H1, H3, and H5, calculated from the DTM and MBC method, increased by 16.40%, 19.49%, 44.03% and 79.03%, and 15.95%, 18.81%, 43.90% and 79.13%, respectively, than the HDPE.

- The  $P_{cr}$  of the FGNC-1 and FGNC-2, calculated from the DTM and MBC methods, increased by 54.38% and 91.34%, and 54.62% and 90.62%, respectively, than the HDPE.
- The H5 and FGNC-2 displayed the highest buckling strength among the 3D printed NCs and FGNCs.
- The  $P_{cr}$  calculated from the DTM, MBC, and the VCT methods exhibited good agreement.
- The natural frequency of the 3D printed NCs and FGNCs increases with the MWCNTs loading, while decreases with the increase in the compressive load.
- The damping factor of the 3D printed NCs and FGNCs decreases with the filler loading while observed to be increasing with the rise in the compressive load compared to the neat HDPE.
- The experimental and numerical findings are observed to be in very good agreement.
- The property chart reveals the superior performance of the H5 NC and FGNC-2 compared to thermosetting composites.

#### *Thermal buckling behavior*

- The  $T_{cr}$  is the highest in case-3 and the lowest in case-2. The  $T_{cr}$  is observed to be sensitive to the type of heating.
- The maximum deflection is observed in case-2, whereas no significant difference in deflection is observed in case-1 and case-3.
- The  $T_{cr}$  of the NCs and FGNCs increases due to the addition of the MWCNTs and their gradation, respectively. The highest  $T_{cr}$  is observed for the H5 NC (11.16% higher than the HDPE) and the FGNC-2 (19.06% higher than the HDPE).
- The deflection of the NCs and FGNCs decreases with the addition of the functionalized MWCNTs and their gradation. The lowest deflection is observed for the H5 NC (53.33% lower than the HDPE) and FGNC-2 (73.34% lower than the HDPE).
- The H5 NC and FGNC-2 exhibited the superior performance among the NCs and FGNCs.

- The FGNCs exhibited the superior performance compared to all the homogeneously reinforced NCs, as they have the higher  $T_{cr}$  than the NCs.

*Recycling potential of the nanocomposites*

- The waste filaments of the functionalized MWCNTs/HDPE NCs are successfully recycled to obtain useful NC filaments for 3D printing. Samples are successfully 3D printed using these recycled nanocomposite filaments and tested to realize their potential for various applications.
- The density of the recycled filaments and the prints rises compared to the W/UR filament and print.
- The crystallinity of the recycled filaments and the prints increases compared to the W/UR filament and print.
- The tensile strength and modulus of the recycled filaments increase compared to the W/UR filament. The highest tensile strength and modulus are found for the H1-3x recycled filament.
- The tensile strength and modulus of the recycled prints increase compared to the W/UR printed sample. The highest tensile strength and modulus are observed for the H1-3x print.
- The H1-3x print exhibited the superior tensile strength and modulus among all the recycled prints.
- The H1 NCs have been printed without any warpage using suitable printing parameters. Therefore, a similar route can be explored for other NCs (0.5%, 1%, 3%, and 5 wt.% of the functionalized MWCNTs in the HDPE matrix), increasing the applications across various engineering fields such as structural, marine, aerospace, and automobile.
- The present work successfully illustrated the recycling of nanocomposite waste filaments to minimize plastic waste. Through such an approach, as presented in this paper, the environmental pollution due to plastic waste generated by 3D printing industries can be substantially lowered, in addition to expanding the filament material options for the FFF community.

*The current work successfully demonstrated the development of the functionalized MWCNTs (0.5%, 1%, 3%, and 5% by weight) and HDPE based NCs, their filament*

*extrusion, and 3D printing of the nanocomposites and the functionally graded nanocomposites using FFF 3D printer. The behaviour of these 3D printed NCs and FGNCs under various mechanical, thermal, and dynamic loads was analysed. The results revealed that the NCs and FGNCs' strength, modulus, hardness, mechanical, thermal, and dynamic stabilities could be greatly enhanced by incorporating the functionalized MWCNTs. The results also revealed that the FGNCs can be chosen for the greater performance than the plain NCs.*

### **SCOPE OF FUTURE WORK**

The current work successfully demonstrated the nanocomposite development, filament extrusion, and 3D printing of the nanocomposites and the functionally graded nanocomposites using FFF 3D printer using appropriate processing parameters. The behaviour of these 3D printed NCs and FGNCs under various loads is explored. This present study can be further carried out by considering these 3D printed NCs and FGNCs as core materials in sandwich construction that can be 3D printed simultaneously for the higher performance as compared to the conventionally manufactured counterparts' lightweight applications. Also, this study is limited to incorporating the functionalized MWCNTs up to 5 wt.% only. This filler level can be further increased in the HDPE matrix to realize the greater potential of the MWCNTs, and then those highly filler loaded composites can be tried printing to check the printing feasibility. Further, their plain, graded, and the sandwich composites with plain and graded cores can be 3D printed to achieve the high performance composites for various engineering applications.

## REFERENCES

- Adhikary, K. B., Park, Chul B, Islam, MR Rizvi, Ghaus M (2011). "Effects of lubricant content on extrusion processing and mechanical properties of wood flour-high-density polyethylene composites." 24(2), 155-171.
- Adhikary, K. B., Park, Chul B, Islam, MR, Rizvi, Ghaus M. (2011). "Effects of lubricant content on extrusion processing and mechanical properties of wood flour-high-density polyethylene composites." *Journal of Thermoplastic Composite Materials*, 24(2), 155-171.
- Ajinjeru, C., Kishore, Vidya Lindahl, John Sudbury, Zeke Hassen, Ahmed Arabi Post, BrianLove, Lonnie Kunc, Vlastimi Duty, Chad (2018). "The influence of dynamic rheological properties on carbon fiber-reinforced polyetherimide for large-scale extrusion-based additive manufacturing." 99(1), 411-418.
- Akar, A. O., Yildiz, Umit Hakan, Tirkes, Seha, Tayfun, Umit, Hacivelioglu, Ferda (2022). "Influence of carbon nanotube inclusions to electrical, thermal, physical and mechanical behaviors of carbon-fiber-reinforced ABS composites." *Carbon Letters*, 1-12.
- Alaimo, G., Marconi, S., Costato, L. and Auricchio, F. (2017). "Influence of meso-structure and chemical composition on FDM 3D-printed parts." *Composites Part B: Engineering*, 113, 371-380.
- Amoroso, L., Heeley, E. L., Ramadas, S. N. and McNally, T. (2020). "Crystallisation behaviour of composites of HDPE and MWCNTs: The effect of nanotube dispersion, orientation and polymer deformation." *Polymer*, 201, 122587.
- Amoroso, L., Heeley, E. L., Ramadas, S. N. and McNally, T. J. P. (2020). "Crystallisation behaviour of composites of HDPE and MWCNTs: The effect of nanotube dispersion, orientation and polymer deformation." 201, 122587.
- Amoroso, L., Heeley, Ellen L, Ramadas, Sivaram Nishal, McNally, Tony (2020). "Crystallisation behaviour of composites of HDPE and MWCNTs: The effect of nanotube dispersion, orientation and polymer deformation." 201, 122587.
- Arivazhagan, A., Saleem, A., Masood, S., Nikzad, M., Jagadeesh, K. J. A. J. o. E. and Sciences, A. (2014). "Study of dynamic mechanical properties of fused deposition modelling processed ULTEM material." 7, 307-315.
- Arza, S. (2012). *Fillers Encyclopedia of Polymer Science and Technology*. 4<sup>th</sup> edition, John Wiley & Sons, New York.
- Barone, C., Pagano, S, Neitzert, HC (2011). "Transport and noise spectroscopy of MWCNT/HDPE composites with different nanotube concentrations." *Journal of Applied Physics*, 110(11), 113716.

Beesetty, P., Patil, B. and Doddamani, M. J. C. S. (2020). "Mechanical behavior of additively manufactured nanoclay/HDPE nanocomposites." 247, 112442.

Beesetty, P., Patil, Balu, Doddamani, Mrityunjay. (2020). "Mechanical behavior of additively manufactured nanoclay/HDPE nanocomposites." *Composite Structures*, 247, 112442.

Bellini, A. and Güçeri, S. (2003). "Mechanical characterization of parts fabricated using fused deposition modeling." *Rapid Prototyping Journal*, 9(4), 252-264.

Bharath, H., Bonthu, Dileep, Prabhakar, Pavana, Doddamani, Mrityunjay. (2020). "Three-dimensional printed lightweight composite foams." *ACS Omega*, 5(35), 22536.

Bharath, H., Bonthu, Dileep, Prabhakar, Pavana, Doddamani, Mrityunjay (2020). "Three-dimensional printed lightweight composite foams." *ACS omega*, 5(35), 22536.  
Bharath, H., Sawardekar, Akshay, Waddar, Sunil, Jeyaraj P, Doddamani, Mrityunjay (2020). "Mechanical behavior of 3D printed syntactic foam composites." *Composite Structures*, 254, 112832.

Bharath, H. S., Bonthu, D., Gururaja, S., Prabhakar, P. and Doddamani, M. (2021). "Flexural response of 3D printed sandwich composite." *Composite Structures*, 263, 113732.

Bharath Kumar, B., Doddamani, Mrityunjay, Zeltmann, Steven E, Gupta, Nikhil, Gurupadu, S. Sailaja, RRN. (2016). "Effect of particle surface treatment and blending method on flexural properties of injection-molded cenosphere/HDPE syntactic foams." *Journal of Materials Science*, 51(8), 3793-3805.

Bharath Kumar, B., Zeltmann, S. E., Doddamani, M., Gupta, N., Gurupadu, S. and Sailaja, R. J. J. o. A. P. S. (2016). "Effect of cenosphere surface treatment and blending method on the tensile properties of thermoplastic matrix syntactic foams." 133(35).

Bharath Kumar, B. R., Doddamani, M., Zeltmann, S. E., Gupta, N., Ramesh, M. R. and Ramakrishna, S. (2016). "Processing of cenosphere/HDPE syntactic foams using an industrial scale polymer injection molding machine." *Materials & Design*, 92, 414-423.

Boran, S., Kiziltas, A., Erbas Kiziltas, E., Gardner, D. J., Rushing, T. S. J. P. E. and Science. (2017). "Nanoclay reinforced polyethylene composites: Effect of different melt compounding methods." 57(3), 324-334.

Brenken, B., Barocio, E., Favaloro, A., Kunc, V. and Pipes, R. B. J. A. M. (2018). "Fused filament fabrication of fiber-reinforced polymers: A review." 21, 1-16.

- Calvert, P. D., Bliss, C., Szivek, J., Margolis, D., Tellis, B. and Vaidyanathan, R. (2008). "Trabecular scaffolds created using micro CT guided fused deposition modeling."
- Camargo, P. H. C., Satyanarayana, K. G. and Wypych, F. J. M. R. (2009). "Nanocomposites: synthesis, structure, properties and new application opportunities." 12(1), 1-39.
- Campbell, F. C. (2010). *Structural composite materials*: ASM international.
- Carneiro, O. S., Silva, A., Gomes, R. J. M. and Design. (2015). "Fused deposition modeling with polypropylene." 83, 768-776.
- Chatkunakasem, P., Luangjuntawong, P., Pongwisuthiruchte, A., Aumnate, C. and Potiyaraj, P. (2018). *Tuning of HDPE properties for 3D printing*. Paper presented at the Key Engineering Materials.
- Chen, F., Mac, G. and Gupta, N. (2017). "Security features embedded in computer aided design (CAD) solid models for additive manufacturing." *Materials & Design*, 128, 182-194.
- Chrissafis, K., Antoniadis, G., Paraskevopoulos, K., Vassiliou, A., Bikiaris, D. J. C. s. and technology. (2007). "Comparative study of the effect of different nanoparticles on the mechanical properties and thermal degradation mechanism of in situ prepared poly ( $\epsilon$ -caprolactone) nanocomposites." 67(10), 2165-2174.
- Chrissafis, K., Paraskevopoulos, K., Tsiaoussis, I. and Bikiaris, D. J. J. o. A. P. S. (2009). "Comparative study of the effect of different nanoparticles on the mechanical properties, permeability, and thermal degradation mechanism of HDPE." 114(3), 1606-1618.
- Dabees, S., Tirth, V., Mohamed, A. and Kamel, B. M. (2020). "Wear Performance and Mechanical Properties of MWCNT/HDPE Nanocomposites for Gearing Applications." *Journal of Materials Research and Technology*.
- Dabees, S., Tirth, V., Mohamed, A., Kamel, B. M. J. J. o. M. R. and Technology. (2021). "Wear performance and mechanical properties of MWCNT/HDPE nanocomposites for gearing applications." 12, 2476-2488.
- Dabees, S., Tirth, Vineet, Mohamed, Alaa, Kamel, Bahaa M. (2021). "Wear performance and mechanical properties of MWCNT/HDPE nanocomposites for gearing applications." *Journal of Materials Research and Technology*, 12, 2476-2488.
- Dakshinamurthy, D. and Gupta, S. (2018). "A study on the influence of process parameters on the viscoelastic properties of ABS components manufactured by FDM process." *Journal of The Institution of Engineers (India): Series C*, 99(2), 133-138.

Di, W., Zhang, G., Xu, J., Peng, Y., Wang, X. and Xie, Z. J. J. o. P. S. P. B. P. P. (2003). "Positive-temperature-coefficient/negative-temperature-coefficient effect of low-density polyethylene filled with a mixture of carbon black and carbon fiber." 41(23), 3094-3101.

Dileep, B., Doddamani, Mrityunjay (2021). "Compressive response of 3D printed graded foams." *Composites Part C: Open Access*, 6, 100181.

Dileep, B., Prakash, Rohith, Bharath, HS, Jeyaraj P, , Doddamani, Mrityunjay (2021). "Dynamic behavior of concurrently printed functionally graded closed cell foams." *Composite Structures*, 275, 114449.

Divya, V., Pattanshetti, V., Suresh, R. and Sailaja, R. J. J. o. P. R. (2013). "Development and characterisation of HDPE/EPDM-g-TMEVS blends for mechanical and morphological properties for engineering applications." 20(2), 1-11.

Doddamani, M. (2020). "Dynamic mechanical analysis of 3D printed eco-friendly lightweight composite." *Composites Communications*, 19, 177-181.

Doddamani, M. J. C. C. (2020). "Dynamic mechanical analysis of 3D printed eco-friendly lightweight composite." 19, 177-181.

Doddamani, M. J. M. R. E. (2020). "Influence of microballoon wall thickness on dynamic mechanical analysis of closed cell foams." 6(12), 125348.

Domingo-Espin, M., Puigoriol-Forcada, J. M., Garcia-Granada, A.-A., Llumà, J., Borros, S. and Reyes, G. (2015). "Mechanical property characterization and simulation of fused deposition modeling Polycarbonate parts." *Materials & Design*, 83, 670-677.

Domingo-Espin, M., Puigoriol-Forcada, J. M., Garcia-Granada, A.-A., Llumà, J., Borros, S., Reyes, G. J. M. and Design. (2015). "Mechanical property characterization and simulation of fused deposition modeling Polycarbonate parts." 83, 670-677.

El Achaby, M. and Qaiss, A. (2013). "Processing and properties of polyethylene reinforced by graphene nanosheets and carbon nanotubes." *Materials & Design*, 44, 81-89.

Escócio, V. A., Pacheco, E. B. A. V., Silva, A. L. N. d., Cavalcante, A. d. P. and Visconte, L. L. Y. J. I. J. o. P. S. (2015). "Rheological behavior of renewable polyethylene (HDPE) composites and sponge gourd (*Luffa cylindrica*) residue." 2015.

Espalin, D., Arcaute, K., Rodriguez, D., Medina, F., Posner, M. and Wicker, R. J. R. P. J. (2010). "Fused deposition modeling of patient-specific polymethylmethacrylate implants."

Faes, M., Ferraris, E. and Moens, D. (2016). "Influence of inter-layer cooling time on the quasi-static properties of ABS components produced via fused deposition modelling." *Procedia Cirp*, 42, 748-753.

Fouad, H., Elleithy, R., Al-Zahrani, S., Ali, M. A.-h. J. M. and Design. (2011). "Characterization and processing of high density polyethylene/carbon nano-composites." 32(4), 1974-1980.

Ganesan, S., Hemanandh, J., Raja, K. S. and Purusothaman, M. (2021). Experimental investigation and characterization of HDPE & LDPE polymer composites *Advances in Industrial Automation and Smart Manufacturing* (pp. 785-799): Springer.

Gardner, J. M., Sauti, G., Kim, J.-W., Cano, R. J., Wincheski, R. A., Stelter, C. J., Grimsley, B. W., Working, D. C. and Siochi, E. J. (2016). "3-D printing of multifunctional carbon nanotube yarn reinforced components." *Additive Manufacturing*, 12, 38-44.

Garg, H. K. and Singh, R. (2015). "Comparison of wear behavior of ABS and Nylon6—Fe powder composite parts prepared with fused deposition modelling." *Journal of Central South University*, 22(10), 3705-3711.

Gómez, C., Mira, J., Carrión-Vilches, F. J. and Cavas, F. J. M. (2021). "Dynamic moduli of polybutylene terephthalate glass fiber reinforced in high-temperature environments." 14(3), 483.

González, R. (2019). "Brief history of additive manufacture and the effect of patents." *J American Scientific Research Journal for Engineering, Technology, and Sciences*, 54(1), 56-67.

Gupta, N., Gupta, Sandeep Kumar, Mueller, Benjamin J (2008). "Analysis of a functionally graded particulate composite under flexural loading conditions." *Materials Science and Engineering: A*, 485(1-2), 439-447.

Gupta, N., Gupta, Sandeep Kumar, Mueller, Benjamin J (2008). "Analysis of a functionally graded particulate composite under flexural loading conditions." *Materials Science Engineering: A*, 485(1-2), 439-447.

Gupta, N., Zeltmann, S. E., Luong, D. D. and Doddamani, M. (2019). Testing of foams *Handbook of mechanics of materials* (pp. 2083-2122): Springer Singapore.

H S, B., Bonthu, D., Prabhakar, P. and Doddamani, M. (2020). "Three-Dimensional Printed Lightweight Composite Foams." *ACS omega*, 5(35), 22536-22550.

He, H., Zhan, Z., Zhu, Z., Xue, B., Li, J., Chen, M. and Wang, G. J. J. o. A. P. S. (2020). "Microscopic morphology, rheological behavior, and mechanical properties of polymers: Recycled acrylonitrile-butadiene-styrene/polybutylene terephthalate blends." 137(4), 48310.

Huan, D. T., Tu, T. M., Quoc, T. H. J. V. J. o. S. and Technology. (2017). "Analytical solutions for bending, buckling and vibration analysis of functionally graded cylindrical panel." 55(5), 587-587.

Jagadeesh, P., Puttegowda, Madhu, Rangappa, Sanjay Mavinkere, Alexey, Karfidov, Gorbatyuk, Sergey, Khan, Anish, Doddamani, Mrityunjay, Siengchin, Suchart. (2022). "A comprehensive review on 3D printing advancements in polymer composites: technologies, materials, and applications." *The International Journal of Advanced Manufacturing Technology*, 121(1), 127-169.

Jayavardhan, M. and Doddamani, M. J. C. P. B. E. (2018). "Quasi-static compressive response of compression molded glass microballoon/HDPE syntactic foam." 149, 165-177.

Jayavardhan, M., Kumar, BR Bharath, Doddamani, Mrityunjay, Singh, Ashish K, Zeltmann, Steven E, Gupta, Nikhil (2017). "Development of glass microballoon/HDPE syntactic foams by compression molding." *Composites Part B: Engineering*, 130, 119-131.

Jayavardhan M. L., B. K. B. R., Doddamani Mrityunjay, Singh Ashish K., Zeltmann Steven E., Gupta Nikhil. (2017). "Development of glass microballoon/HDPE syntactic foams by compression molding." *Composites Part B: Engineering*, 130, 119-131.

Jayavardhan, M. K., BR Bharath, Doddamani, Mrityunjay, Singh, Ashish K, Zeltmann, Steven E, Gupta, Nikhil (2017). "Development of glass microballoon/HDPE syntactic foams by compression molding." 130, 119-131.

Jeyachandran, P., Bontha, Srikanth, Bodhak, Subhadip, Balla, Vamsi Krishna, Doddamani, Mrityunjay (2022). "Quasi-static compressive behavior of bioactive glass reinforced high density polyethylene composites." *Materials Letters*, 311, 131557.

Jeyachandran, P., Bontha, Srikanth, Bodhak, Subhadip, Balla, Vamsi Krishna, Doddamani, Mrityunjay (2022). "Quasi-static compressive behavior of bioactive glass reinforced high density polyethylene composites." 311, 131557.

Kanagaraj, S., Varanda, F. R., Zhil'tsova, T. V., Oliveira, M. S., Simões, J. A. J. C. S. and Technology. (2007). "Mechanical properties of high density polyethylene/carbon nanotube composites." 67(15-16), 3071-3077.

Kazmer, D. O. (2009). *Plastics manufacturing systems engineering*: Hanser Publications.

Kim, J. and Reddy, J. J. C. S. (2013). "Analytical solutions for bending, vibration, and buckling of FGM plates using a couple stress-based third-order theory." 103, 86-98.

Kumar, B. B., Doddamani, M., Zeltmann, S. E., Gupta, N., Gurupadu, S. and Sailaja, R. J. J. o. m. s. (2016). "Effect of particle surface treatment and blending method on flexural properties of injection-molded cenosphere/HDPE syntactic foams." 51(8), 3793-3805.

Kumar, B. B., Doddamani, Mrityunjay, Zeltmann, Steven E, Gupta, Nikhil, Ramesh, MR, Ramakrishna, Seeram (2016). "Processing of cenosphere/HDPE syntactic foams using an industrial scale polymer injection molding machine." *Materials & Design*, 92, 414-423.

Kumar, B. B. D., Mrityunjay, Zeltmann, Steven E, Gupta, Nikhil, Ramesh, MR, Ramakrishna, Seeram. (2016). "Processing of cenosphere/HDPE syntactic foams using an industrial scale polymer injection molding machine." *Materials Design*, 92, 414-423.

Kumar, S., M. R, Ramesh, Doddamani, Mrityunjay. (2022). "Compressive behavior of 3D printed MWCNT/HDPE nanocomposites." *Composites Communications*, 101317.

Kumar, S., Ojha, Nidhi, Ramesh, MR, Balan, ASS, Doddamani, Mrityunjay (2024). "Shape memory behavior of 4D printed CF/PEKK high temperature composite under subsequent thermomechanical cycles." *Materials Letters*, 366, 136567.

Kumar, S., Ramesh, M. R., Doddamani, Mrityunjay. (2023). "Investigation on hardness, impact, and compression responses of additively manufactured functionally graded nanocomposites." *Composites Communications*, 101545.

Kumar, S., Ramesh, MR, Doddamani, Mrityunjay. (2022). "Compressive behavior of 3D printed MWCNT/HDPE nanocomposites." *Composites Communications*, 35, 101317.

Kumar, S., Ramesh, MR, Doddamani, Mrityunjay (2023). "Recycling potential of MWCNTs/HDPE nanocomposite filament: 3D printing and mechanical characterization." *Journal of Material Cycles and Waste Management*, 1-11.

Kumar, S., Ramesh, MR, Doddamani, Mrityunjay, Rangappa, Sanjay Mavinkere, Siengchin, Suchart. (2022). "Mechanical characterization of 3D printed MWCNTs/HDPE nanocomposites." *Polymer Testing*, 107703.

Kumar, S., Ramesh, MR, Doddamani, Mrityunjay, Rangappa, Sanjay Mavinkere, Siengchin, Suchart. (2022). "Mechanical characterization of 3D printed MWCNTs/HDPE nanocomposites." *Polymer Testing*, 114, 107703.

Kumar, S., Ramesh, MR, Jeyaraj, P, Doddamani, Mrityunjay (2023). "Buckling and dynamic responses of 3D printed nanocomposites and their graded variants." *Composite Structures*, 316, 117031.

Kumar, S., Ramesh, MR, Jeyaraj, P, Powar, Satvasheel, Doddamani, Mrityunjay (2023). "Buckling behavior of non-uniformly heated 3D printed plain and functionally graded nanocomposites." *Polymer Composites*, 44(9), 5450-5463.

Lee, J. and Huang, A. (2013). "Fatigue analysis of FDM materials." *Rapid Prototyping Journal*.

Li, X., Li, L., Hu, Y., Ding, Z. and Deng, W. J. C. S. (2017). "Bending, buckling and vibration of axially functionally graded beams based on nonlocal strain gradient theory." 165, 250-265.

Liu, Y., Asare, E., Porwal, H., Barbieri, E., Goutianos, S., Evans, J., Newton, M., Busfield, J. J. C., Peijs, T., Zhang, H. and Bilotti, E. (2020). "The effect of conductive network on positive temperature coefficient behaviour in conductive polymer composites." *Composites Part A: Applied Science and Manufacturing*, 139, 106074.

Liu, Y., Hu, Y., Liu, T., Ding, J. and Zhong, W. (2015). "Mechanical behavior of high density polyethylene and its carbon nanocomposites under quasi-static and dynamic compressive and tensile loadings." *Polymer Testing*, 41, 106-116.

Mastoid, S. and Song, W. J. M. D. (2004). "Development of new metal/polymer materials for rapid tooling using fused deposition modeling." 25(7), 587-594.

Mohamed, O. A., Masood, S. H. and Bhowmik, J. L. (2016). "Mathematical modeling and FDM process parameters optimization using response surface methodology based on Q-optimal design." *Applied Mathematical Modelling*, 40(23-24), 10052-10073.

Mohamed, O. A., Masood, S. H., Bhowmik, J. L., Nikzad, M. and Azadmanjiri, J. (2016). "Effect of process parameters on dynamic mechanical performance of FDM PC/ABS printed parts through design of experiment." *Journal of materials engineering and performance*, 25(7), 2922-2935.

Mora, A., Verma, P. and Kumar, S. (2020). "Electrical conductivity of CNT/polymer composites: 3D printing, measurements and modeling." *Composites Part B: Engineering*, 183, 107600.

Mora, A., Verma, P. and Kumar, S. J. C. P. B. E. (2020). "Electrical conductivity of CNT/polymer composites: 3D printing, measurements and modeling." 183, 107600.

Nikzad, M., Masood, S. and Sbarski, I. (2011). "Thermo-mechanical properties of a highly filled polymeric composites for fused deposition modeling." *Materials & Design*, 32(6), 3448-3456.

Ning, F., Cong, W., Jia, Z., Wang, F. and Zhang, M. (2016). *Additive manufacturing of CFRP composites using fused deposition modeling: effects of process parameters*. Paper presented at the ASME 2016 11th International Manufacturing Science and Engineering Conference.

- Ojha, N., Kumar, Sumodh, Ramesh, MR, Balan, ASS, Doddamani, Mrityunjay (2023). "Influence of subsequent thermomechanical cycles on shape memory behavior of 4D printed PEKK." *Materials Letters*, 352, 135213.
- Ojha, N., Kumar, Sumodh, Ramesh, MR, Balan, ASS, Doddamani, Mrityunjay (2024). "A comprehensive characterization of 3D printable poly ether ketone ketone." *Journal of the Mechanical Behavior of Biomedical Materials*, 150, 106243.
- Patankar, S., Das, A., Kranov, Y. J. C. P. A. A. S. and Manufacturing. (2009). "Interface engineering via compatibilization in HDPE composite reinforced with sodium borosilicate hollow glass microspheres." 40(6-7), 897-903.
- Patankar, S., Kranov, Y. J. M. S. and A, E. (2010). "Hollow glass microsphere HDPE composites for low energy sustainability." 527(6), 1361-1366.
- Patil, B., Kumar, B. B., Bontha, S., Balla, V. K., Powar, S., Kumar, V. H., Suresha, S., Doddamani, M. J. C. S. and Technology. (2019). "Eco-friendly lightweight filament synthesis and mechanical characterization of additively manufactured closed cell foams." 183, 107816.
- Patil, B., Kumar, B. B. and Doddamani, M. J. M. L. (2019). "Compressive behavior of fly ash based 3D printed syntactic foam composite." 254, 246-249.
- Patil, B., Kumar, BR Bharath, Bontha, Srikanth, Balla, Vamsi Krishna, Powar, Satvasheel, Kumar, V Hemanth, Suresha, SN, Doddamani, Mrityunjay. (2019). "Eco-friendly lightweight filament synthesis and mechanical characterization of additively manufactured closed cell foams." *Composites Science and Technology*, 183, 107816.
- Porter, D. A., Hoang, T. V. and Berfield, T. A. (2017). "Effects of in-situ poling and process parameters on fused filament fabrication printed PVDF sheet mechanical and electrical properties." *Additive Manufacturing*, 13, 81-92.
- Pötschke, P., Villmow, Tobias, Krause, Beate (2013). "Melt mixed PCL/MWCNT composites prepared at different rotation speeds: Characterization of rheological, thermal, and electrical properties, molecular weight, MWCNT macrodispersion, and MWCNT length distribution." *Polymer*, 54(12), 3071-3078.
- Przybytek, A., Gubańska, I., Kucińska-Lipka, J., Janik, H. J. F. and Europe, T. i. E. (2018). "Polyurethanes as a potential medical-grade filament for use in fused deposition modeling 3D printers—a brief review."
- Rabbi, M. F. and Chalivendra, V. (2020). "Strain and damage sensing in additively manufactured CB/ABS polymer composites." *Polymer Testing*, 90, 106688.

Rahim, T. N. A. T., Abdullah, A. M. and Md Akil, H. J. P. R. (2019). "Recent developments in fused deposition modeling-based 3D printing of polymers and their composites." 59(4), 589-624.

Rajesh, M., Pitchaimani, Jeyaraj (2017). "Experimental investigation on buckling and free vibration behavior of woven natural fiber fabric composite under axial compression." *Composite Structures*, 163, 302-311.

Rajeshwari, P. (2015). "Microstructure and mechanical properties of multiwall carbon nanotubes reinforced polymer composites." *Materials Today: Proceedings*, 2(4-5), 3598-3604.

Raviv, D., Zhao, W., McKnelly, C., Papadopoulou, A., Kadambi, A., Shi, B., Hirsch, S., Dikovskiy, D., Zyracki, M. and Olguin, C. (2014). "Active printed materials for complex self-evolving deformations." *Scientific reports*, 4(1), 1-8.

Riddick, J. C., Haile, M. A., Von Wahlde, R., Cole, D. P., Bamiduro, O. and Johnson, T. E. (2016). "Fractographic analysis of tensile failure of acrylonitrile-butadiene-styrene fabricated by fused deposition modeling." *Additive Manufacturing*, 11, 49-59.

Rizkalla, S., Dawood, M., Schnerch, D. J. C. P. A. A. S. and Manufacturing. (2008). "Development of a carbon fiber reinforced polymer system for strengthening steel structures." 39(2), 388-397.

Saber-Samandari, S., Gross, Karlis A (2009). "Effect of angled indentation on mechanical properties." *Journal of the European Ceramic Society*, 29(12), 2461-2467.  
Sayyad, A. S., Ghugal, Yuwaraj M (2019). "Modeling and analysis of functionally graded sandwich beams: A review." *Mechanics of Advanced Materials and Structures*, 26(21), 1776-1795.

Sepet, H., Tarakcioglu, N. and Misra, R. J. J. o. c. m. (2016). "Investigation of mechanical, thermal and surface properties of nanoclay/HDPE nanocomposites produced industrially by melt mixing approach." 50(22), 3105-3116.

Shutov, F. A., Henrici-Olivé, G. and Olivé, S. (1986). Integral Foam Based on Polyurethanes *Integral/Structural Polymer Foams* (pp. 153-188): Springer.

Shutov, F. A. J. C. f. c. (1986). "Syntactic polymer foams." 63-123.

Silva, M., Pereira, A., Alves, N., Mateus, A. and Malça, C. J. P. M. (2017). "A hybrid processing approach to the manufacturing of polyamide reinforced parts with carbon fibers." 12, 195-202.

Singh, A. K., Patil, B., Hoffmann, N., Saltonstall, B., Doddamani, M. and Gupta, N. J. J. (2018). "Additive manufacturing of syntactic foams: part 1: development, properties, and recycling potential of filaments." 70(3), 303-309.

- Singh, R., Bedi, P., Fraternali, F. and Ahuja, I. (2016). "Effect of single particle size, double particle size and triple particle size Al<sub>2</sub>O<sub>3</sub> in Nylon-6 matrix on mechanical properties of feed stock filament for FDM." *Composites Part B: Engineering*, 106, 20-27.
- Singh, R., Kumar, R. and Kumar, S. (2017). "Polymer waste as fused deposition modeling feed stock filament for industrial applications."
- Singh, R., Singh, S. and Fraternali, F. (2016). "Development of in-house composite wire based feed stock filaments of fused deposition modelling for wear-resistant materials and structures." *Composites Part B: Engineering*, 98, 244-249.
- Singh, R., Singh, S. and Fraternali, F. J. C. P. B. E. (2016). "Development of in-house composite wire based feed stock filaments of fused deposition modelling for wear-resistant materials and structures." 98, 244-249.
- Singh, R., Singh, S. and Mankotia, K. (2016). "Development of ABS based wire as feedstock filament of FDM for industrial applications." *Rapid Prototyping Journal*.
- Sofiyev, A. and Kuruoglu, N. J. T.-W. S. (2014). "Buckling and vibration of shear deformable functionally graded orthotropic cylindrical shells under external pressures." 78, 121-130.
- Sofiyev, A. J. C. S. (2019). "The buckling and vibration analysis of coating-FGM-substrate conical shells under hydrostatic pressure with mixed boundary conditions." 209, 686-693.
- Spoerk, M., Arbeiter, F., Cajner, H., Sapkota, J. and Holzer, C. J. J. o. a. p. s. (2017). "Parametric optimization of intra-and inter-layer strengths in parts produced by extrusion-based additive manufacturing of poly (lactic acid)." 134(41), 45401.
- Sreenivasulu, B., Ramji, B. and Nagaral, M. J. M. T. P. (2018). "A review on graphene reinforced polymer matrix composites." 5(1), 2419-2428.
- Stan, F., Stanciu, N.-V. and Fetecau, C. (2019). *On the 3D Printability of Multi-Walled Carbon Nanotube/High Density Polyethylene Composites*. Paper presented at the International Manufacturing Science and Engineering Conference.
- Stanciu, N.-V., Stan, F., Fetecau, C. and Susac, F. (2019). *On the Feasibility of Printing 3D Composite Objects Based on Polypropylene/Multi-walled Carbon Nanotubes*. Paper presented at the MATEC Web of Conferences.
- Stansbury, J. W. and Idacavage, M. J. J. D. m. (2016). "3D printing with polymers: Challenges among expanding options and opportunities." 32(1), 54-64.

Sui, G., Zhong, W., Ren, X., Wang, X. and Yang, X. (2009). "Structure, mechanical properties and friction behavior of UHMWPE/HDPE/carbon nanofibers." *Materials Chemistry and Physics*, 115(1), 404-412.

Tahir, S. I., Chikh, A., Tounsi, A., Al-Osta, M. A., Al-Dulaijan, S. U. and Al-Zahrani, M. M. J. C. S. (2021). "Wave propagation analysis of a ceramic-metal functionally graded sandwich plate with different porosity distributions in a hygro-thermal environment." 269, 114030.

Tahir, S. I., Chikh, Abdelbaki, Tounsi, Abdelouahed, Al-Osta, Mohammed A, Al-Dulaijan, Salah U, Al-Zahrani, Mesfer M. (2021). "Wave propagation analysis of a ceramic-metal functionally graded sandwich plate with different porosity distributions in a hygro-thermal environment." *Composite Structures*, 269, 114030.

Tang, W., Santare, M. H. and Advani, S. G. (2003). "Melt processing and mechanical property characterization of multi-walled carbon nanotube/high density polyethylene (MWNT/HDPE) composite films." *Carbon*, 41(14), 2779-2785.

Tekinalp, H. L., Kunc, V., Velez-Garcia, G. M., Duty, C. E., Love, L. J., Naskar, A. K., Blue, C. A. and Ozcan, S. (2014). "Highly oriented carbon fiber-polymer composites via additive manufacturing." *Composites Science and Technology*, 105, 144-150.

Tellis, B., Szivek, J., Bliss, C., Margolis, D., Vaidyanathan, R., Calvert, P. J. M. S. and C, E. (2008). "Trabecular scaffolds created using micro CT guided fused deposition modeling." 28(1), 171-178.

Tian, X., Liu, T., Wang, Q., Dilmurat, A., Li, D. and Ziegmann, G. (2017). "Recycling and remanufacturing of 3D printed continuous carbon fiber reinforced PLA composites." *Journal of cleaner production*, 142, 1609-1618.

Toutanji, H. A. and Saafi, M. J. S. J. (2000). "Flexural behavior of concrete beams reinforced with glass fiber-reinforced polymer (GFRP) bars." 97(5), 712-719.

Tuan Rahim, T. N. A., Abdullah, A. M., Md Akil, H., Mohamad, D. and Rajion, Z. A. (2015). "Preparation and characterization of a newly developed polyamide composite utilising an affordable 3D printer." *Journal of reinforced plastics and composites*, 34(19), 1628-1638.

Tucker, K., Tucker, D., Eastham, J., Gibson, E., Varma, S. and Daim, T. (2014). "Network based technology roadmapping for future markets: Case of 3D printing." *Technology and Investment*, 2014.

Venkatesan, N., Bhaskar, G., Pazhanivel, K. and Poyyathappan, K. (2014). *Reinforcing effect of montmorillonite nanoclay on mechanical properties of high density polyethylene nanocomposites*. Paper presented at the Applied Mechanics and Materials.

- Verma, D., Gope, P., Shandilya, A. and Gupta, A. J. T. o. t. I. I. o. M. (2014). "Mechanical-thermal-electrical and morphological properties of graphene reinforced polymer composites: a review." 67(6), 803-816.
- Waddar, S., Jeyaraj, P, Doddamani, Mrityunjay (2018). "Influence of axial compressive loads on buckling and free vibration response of surface-modified fly ash cenosphere/epoxy syntactic foams." *Journal of composite materials*, 52(19), 2621-2630.
- Wang, L. and Gardner, D. J. (2017). "Effect of fused layer modeling (FLM) processing parameters on impact strength of cellular polypropylene." *Polymer*, 113, 74-80.
- Weng, Z., Wang, J., Senthil, T. and Wu, L. (2016). "Mechanical and thermal properties of ABS/montmorillonite nanocomposites for fused deposition modeling 3D printing." *Materials & Design*, 102, 276-283.
- Xiang, D., Harkin-Jones, E. and Linton, D. J. R. A. (2014). "Processability, structural evolution and properties of melt processed biaxially stretched HDPE/MWCNT nanocomposites." 4(83), 44130-44140.
- Xiang, D., Harkin-Jones, E., Linton, D. and Martin, P. J. J. o. A. P. S. (2015). "Structure, mechanical, and electrical properties of high-density polyethylene/multi-walled carbon nanotube composites processed by compression molding and blown film extrusion." 132(42).
- Yao, X., Luan, C., Zhang, D., Lan, L. and Fu, J. (2017). "Evaluation of carbon fiber-embedded 3D printed structures for strengthening and structural-health monitoring." *Materials & Design*, 114, 424-432.
- Yu, S.-H., Yeh, J.-T., Huang, B.-C., Huang, K.-S. J. P.-P. T. and Engineering. (2010). "Preparation of a HDPE/carbon nanotube composite." 49(15), 1534-1539.
- Yuan, Q., Bateman, S. A. and Wu, D. J. J. o. T. C. M. (2010). "Mechanical and conductive properties of carbon black-filled high-density polyethylene, low-density polyethylene, and linear low-density polyethylene." 23(4), 459-471.
- Zaldivar, R., Witkin, D., McLouth, T., Patel, D., Schmitt, K. and Nokes, J. (2017). "Influence of processing and orientation print effects on the mechanical and thermal behavior of 3D-Printed ULTEM® 9085 Material." *Additive Manufacturing*, 13, 71-80.
- Zeng, Y., Lu, G., Wang, H., Du, J., Ying, Z. and Liu, C. (2014). "Positive temperature coefficient thermistors based on carbon nanotube/polymer composites." *Scientific reports*, 4(1), 1-7.

Zeng, Y., Lu, Guixia, Wang, Han, Du, Jinhong, Ying, Zhe, Liu, Chang (2014). "Positive temperature coefficient thermistors based on carbon nanotube/polymer composites." *Scientific reports*, 4(1), 1-7.

Zhang, W., Wu, A. S., Sun, J., Quan, Z., Gu, B., Sun, B., Cotton, C., Heider, D. and Chou, T.-W. (2017). "Characterization of residual stress and deformation in additively manufactured ABS polymer and composite specimens." *Composites Science and Technology*, 150, 102-110.

Zhang, X., Xu, Y., Zhang, X., Wu, H., Shen, J., Chen, R., Xiong, Y., Li, J. and Guo, S. (2019). "Progress on the layer-by-layer assembly of multilayered polymer composites: Strategy, structural control and applications." *Progress in Polymer Science*, 89, 76-107.

Zhao, G., Liu, Hong-Yuan, Cui, Xiaoyu, Du, Xusheng, Zhou, Helezi, Mai, Yiu-Wing, Jia, Yuan-Yuan, Yan, Wenyi (2022). "Tensile properties of 3D-printed CNT-SGF reinforced PLA composites." *Composites science and technology*, 109333.

Zou, R., Xia, Y., Liu, S., Hu, P., Hou, W., Hu, Q. and Shan, C. (2016). "Isotropic and anisotropic elasticity and yielding of 3D printed material." *Composites Part B: Engineering*, 99, 506-513.

## LIST OF PUBLICATIONS

### INTERNATIONAL JOURNALS

1. **Sumodh Kumar**, Ramesh M.R., and Mrityunjay Doddamani, (2024) “3D printing of functionally graded nanocomposites: An investigation of microstructural, rheological, and mechanical behaviour”. *Polymer Engineering & Science*. (Wiley, Scopus, IF-3.2), [10.1002/pen.26873](https://doi.org/10.1002/pen.26873).
2. **Sumodh Kumar**, M. R. Ramesh, P. Jeyaraj, Satvasheel Powar, Mrityunjay Doddamani, (2023) “Buckling behavior of non-uniformly heated 3D printed plain and functionally graded nanocomposites”. *Polymer Composites*, 44, 5450-5463. (Wiley, SCI, IF-5.2), [10.1002/pc.27500](https://doi.org/10.1002/pc.27500).
3. **Sumodh Kumar**, Ramesh M.R., and Mrityunjay Doddamani, (2023) “Investigation on hardness, impact, and compression responses of additively manufactured functionally graded nanocomposites”. *Composites Communications*, 39, 101545. (Elsevier, SCI, IF-8), [10.1016/j.coco.2023.101545](https://doi.org/10.1016/j.coco.2023.101545).
4. **Sumodh Kumar**, Ramesh M.R., and Mrityunjay Doddamani, (2023) “Recycling potential of MWCNTs/HDPE nanocomposite filament: 3D printing and mechanical characterization”. *Journal of Material Cycles and Waste Management*, 25, 1168-1178. (Springer, SCIE, IF-3.1), [10.1007/s10163-023-01607-w](https://doi.org/10.1007/s10163-023-01607-w).
5. **Sumodh Kumar**, Ramesh M.R., Mrityunjay Doddamani, Sanjay Mavinkere Rangappa, and Suchart Siengchin, (2022) “Mechanical characterization of 3D printed MWCNTs/HDPE nanocomposites”. *Polymer Testing*, 114, 107703. (Elsevier, SCI, I.F.-5.1), [10.1016/j.polymertesting.2022.107703](https://doi.org/10.1016/j.polymertesting.2022.107703).
6. **Sumodh Kumar**, Ramesh M.R., and Mrityunjay Doddamani, (2022) “Compressive behavior of 3D printed MWCNT/HDPE nanocomposites”. *Composites Communications*, 35, 101317. (Elsevier, SCI, I.F.-8), [10.1016/j.coco.2022.101317](https://doi.org/10.1016/j.coco.2022.101317).
7. **Sumodh Kumar**, Ramesh M.R., P. Jeyaraj, and Mrityunjay Doddamani, (2023) “Buckling and dynamic responses of 3D printed nanocomposites and

their graded variants”. *Composite Structures*, 316, 117031. (Elsevier, SCI, I.F.-6.3), [10.1016/j.compstruct.2023.117031](https://doi.org/10.1016/j.compstruct.2023.117031).

## INTERNATIONAL CONFERENCES

1. **Sumodh Kumar**, Ramesh M.R., and Mrityunjay Doddamani, (2023) “3D printing of nanocomposites and flexural investigations therein”. *International Conference on Digitization and Advancements in Materials and Metallurgical Industries*, held on 19th & 20th August, 2023, Venue: Engineers Bhawan, IEI RSC, Tonk Road, Jaipur, 302015.

## BIO-DATA

1. Name : Sumodh Kumar
2. Father's Name : Rampukar Ram
3. Date of Birth : 05<sup>th</sup> June 1992
4. Nationality : Indian
5. Marital Status : Married
6. Address : Department of Mechanical Engineering,  
National Institute of Technology Karnataka,  
Surathkal, P.O.-Srinivasnagar-575 025,  
Karnataka, India.
7. Mobile Number : +91 9507783023
8. E-mail id. : *rajbabu357@gmail.com*
9. Educational Qualification :

Qualification	University/Board	Year of Passing
Ph.D. (Mechanical Engineering)	National Institute of Technology Karnataka	Pursuing
M.Tech. (Mechanical Engineering)	National Institute of Technology Karnataka	2018
B. E. (Mechanical Engineering)	Anna University, Chennai	2015